Aspects of QCD and the Photon Structure

Christer Friberg

Lund University

Department of Theoretical Physics

Aspects of QCD and the Photon Structure

Christer Friberg

Department of Theoretical Physics
Lund University, Sweden

Thesis for the degree of Doctor of Philosophy

Thesis Advisor: Torbjörn Sjöstrand

Faculty Opponent: Jeffrey R. Forshaw

To be presented, with the permission of
the Faculty of Mathematics and Natural Sciences of Lund University,
for public criticism
in Lecture Hall F of the Department of Theoretical Physics
on Friday, the 6th of October 2000, at 10.15 a.m.

Organization LUND UNIVERSITY Department of Theoretical Physics Sölvegatan 14A SE-223 62 LUND	Document Name DOCTORAL DISSERTATION Date of issue August 2000 CODEN:
Author(s) Christer Friberg	Sponsoring organization

Title and subtitle

Aspects of QCD and the Photon Structure

Abstract

In a single theoretical framework, real and virtual photon interactions are modeled for γp and $\gamma\gamma$ collisions. The description covers aspects from the production of jets to total cross sections, where special emphasis is put on the range of uncertainty in the modeling of a resolved photon component. Our approach extends on a model for photoproduction, where the total cross section is subdivided into three distinct event classes: direct, VMD and anomalous. It provides a smooth transition between the region of real and highly virtual photons. In jet production, photon flux factors are convoluted with matrix elements involving either direct or resolved photons and, for the latter, with parton distributions of the photon. Effects of resolved longitudinal photons are estimated by simple multiplicative factors on the resolved transverse-photon contributions and their impact on some representative distributions are investigated. Complete events are generated with Monte Carlo methods and results are confronted with data from specifically HERA and LEP2. By the breakdown into different event classes, we aim for a complete picture of all event properties in γp and $\gamma\gamma$ collisions.

When there are identical colour charges in a parton cascade, there are several ways to stretch a string, or a cluster chain, in the subsequent hadronization phase. In particular, the possibility that a colour singlet gluon system hadronizes isolated from the remainder of the system in hadronic Z^0 decays is studied.

QCD aspects of leptoquark production at HERA are discussed with focus on initial- and final-state QCD radiation. By taking into account corrections to this, in mass reconstructions of a leptoquark, a narrower mass peak and a better average mass value is obtained.

Key words

Photons, QCD, Monte Carlo Event Generator, Colour Connections, Leptoquarks

Classification system and/or index terms (if any)

Supplementary bibliographical information	Language English
ISSN and key title	ISBN 91-7874-058-4
Recipient's notes	Number of pages 212 / Price
	Security classification

Distribution by (name and address)

Christer Friberg, Dept. of Theoretical Physics, Sölvegatan 14A, SE-223 62 LUND

I, the undersigned, being the copyright owner of the abstract of the above-mentioned dissertation, hereby grant to all reference sources the permission to publish and disseminate the abstract of the above-mentioned dissertation.

Signature _____ Date 2000-08-25

DOKUMENTDATABLAD enl SIS 61 41 21

By PSRate package, (C) Bo Söderberg 1998

To Anneli

This thesis is based on the following publications:

I C. Friberg, G. Gustafson and J. Häkkinen
Colour Connections in e^+e^--annihilation
Nuclear Physics **B490** (1997) 289

II C. Friberg, E. Norrbin and T. Sjöstrand
QCD Aspects of Leptoquark Production at HERA
Physics Letters **B403** (1997) 329

III C. Friberg and T. Sjöstrand
Jet Production by Virtual Photons
European Physical Journal **C13** (2000) 151

IV C. Friberg and T. Sjöstrand
Total Cross Sections and Event Properties from Real to Virtual Photons
LU TP 00–29 (Submitted to *Journal of High Energy Physics*)

V C. Friberg and T. Sjöstrand
Effects of Longitudinal Photons
LU TP 00–31 (Submitted to *Physics Letters* **B**)

VI T. Sjöstrand, P. Edén, C. Friberg, L. Lönnblad, G. Miu, S. Mrenna and E. Norrbin
High-Energy-Physics Event Generation with PYTHIA 6.1
LU TP 00–30 (To be submitted to *Computer Physics Commun.*)

Contents

Introduction **1**
Survey of Particle Physics Phenomenology 1
Matter Within the Range of Vision 3
Photons and QCD 6
Experiments 11
Event Generators 13
The Papers 20
Acknowledgments 22

1 Colour Connections in e^+e^--annihilation **25**

2 QCD Aspects of Leptoquark Production at HERA **45**

3 Jet Production by Virtual Photons **59**

4 Total Cross Sections and Event Properties from Real to Virtual Photons **103**

5 Effects of Longitudinal Photons **151**

6 High-Energy-Physics Event Generation with PYTHIA 6.1 **171**

Introduction

'It is all Greek to me!' If this was your first impression, while reading the title of this thesis, it is actually a good starting point! The word physics comes from a Greek term meaning nature, of which a certain subject will be focused on in this work, namely high-energy physics. The intention with this introduction, is exactly to introduce you to the subject, starting at a very basic level and ending at a more professional one. It is primarily with my family and friends in mind I write this introduction, so hopefully, at least reading this part of the thesis will be worth the effort for all categories of readers, not only scientists.

The first two sections will set particle physics in a perspective where most people can feel comfortable. The subsequent section briefly describe two currently running high-energy physics experiments. All physics investigations and models presented in this thesis have ultimately used an event generator as a test-ground or platform for reasonableness estimations and powerful comparisons with experimental data. Consequently, a separate section has been devoted to event generators and illustrates at the same time many aspects addressed in particle physics phenomenology. Towards the end of this introduction, the papers upon which this thesis is based, will be summarized.

Survey of Particle Physics Phenomenology

Originally, physics was the denomination for all natural sciences. Certain branches of physics turned into separate sciences, i.e. chemistry, biology and geology, after which the objective of physics became the understanding of basic components of matter and their mutual interactions. Therefore it provides the basic conceptual and theoretical framework on which the other natural sciences are founded. High-energy physics or, equivalently, particle physics is dedicated to the understanding of the smallest objects of matter. The connection between high-energy physics and the study of small objects will be explained in the next section.

The forces of nature as we know them today, can be divided into gravitational, electromagnetic, weak and strong forces. The weak force being responsible for radioactive decays and the strong force for the formation of atomic

nuclei. When dealing with distances much smaller than sizes of atomic nuclei, which are typical distances in particle physics, the gravitational force normally has a negligible impact on the studied reactions. It is because of the dominance of the strong force and for the smallness of the particle masses involved. Comparing the strengths of the forces at these distances, they are in the following relation to each other; strong : electromagnetic : weak : gravitational $= 1 : 10^{-2} : 10^{-7} : 10^{-36}$. Evidently, the gravitational force is extremely weak in comparison and will, from a particle physics point of view, be ignored from here on and only be mentioned to give a clear overall picture.

The origin of forces are believed to come from symmetries of nature. This is the case for the four fundamental forces discussed above. The gravitational force has the symmetry of the space-time itself whereas the others exhibit symmetries in internal spaces not directly accessible to our senses. The electromagnetic, weak and strong interactions can all be formulated as what are called *quantum field theories*. The field quanta, which are treated as fundamental particles, are the mediators of forces and are exchanged between particles upon which the forces are acting. We will have reasons to come back to these issues and they will be described in simple terms.

The bulk properties in high-energy particle collisions is due to the influence of the strong force. The understanding of strong interactions is far from complete. So sensible models need to be constructed based on relations previously established. With mathematical techniques, deductive and logical reasoning can be applied. Finally, maybe some phenomenon not yet observed can be predicted or, when compared to experimental measurements, relations can be verified. If the model fails to reproduce experimental data or predictions are not in agreement with new data, it clearly needs to be refined and developed further. In brief, this is the methodology in particle physics phenomenology where theories are based on observed phenomena rather than on any philosophical assumptions on the underlying cause of them. Many people are involved in the field and the progress is mainly a result of teamwork between theorists and experimentalists.

Some of what we can consider as simple calculations today, were not solvable, say, 30 years ago but great theoretical innovations and experimental discoveries during the last decades have taken us to a very detailed understanding of very complicated particle collisions involving hundreds to thousands of particles. Although some calculations can be made by hand on a sheet of paper, realistic studies often involves numerical calculations to some degree, ultimately performed on a computer. One reason is that the complexity of a problem increases rapidly with the number of particles involved and becomes untraceable unless systematized in some way. This is, perhaps, most easily done in a computer code where, in addition, the initial conditions of a particle collision (particle types, collision energy, etc.) are easily changed. Special techniques

Radiation	**Wavelength (m)**	**Energy (eV)**	**Objects**
radio waves	$10^{3} - 10^{-3}$	$10^{-9} - 10^{-3}$	
infrared (IR) light	$10^{-3} - 10^{-6}$	$10^{-3} - 1$	molecules
visible light	$10^{-6} - 10^{-7}$	$1 - 10$	atoms
ultra-violet (UV) light	$10^{-7} - 10^{-9}$	$10 - 10^{3}$	
X-rays	$10^{-9} - 10^{-12}$	$10^{3} - 10^{6}$	nuclei
γ-rays	$10^{-10} -$	$10^{4} -$	

Table 1: The spectrum of electromagnetic radiation. The wavelength and corresponding energy are given in metre and electron-Volt, respectively. In the right column, objects responsible for the absorption or emission of the radiation are given.

have been developed to handle such issues and a flavour of it will be given below.

Matter Within the Range of Vision

At present, matter is considered to be made up of a handful of fundamental particles. Depending on the level of which we consider matter, different groupings or arrangements of such particles can be used to describe the components of matter and the forces acting between them. For example, an atom consists of protons and neutrons that are bound together into a nucleus, with a surrounding cloud of electrons. The simplest atom, the hydrogen atom, consists of one proton and one electron. The proton and electron are interacting among themselves in such a way that a stable configuration is obtained. It is at sizes much smaller than that of a hydrogen atom where particle physicists start to be interested and call the objects they study, simply, particles. At the moment, we will continue towards larger objects however.

The composite atoms in turn, are bound together forming molecules, which in turn form macroscopic structures. Over 100 distinct types of atoms have been observed with more than 1000 varieties of them, called isotopes. The number of molecules is extremely large and they exhibit very distinct properties due to the large variation in internal structure. How do we know of the existence of these different complex structures?

In everyday life, we observe things through our senses. Maybe the most important one is the eyesight. Our eyes absorb light which is translated into a perceived picture. The visible light, however, is only a small fraction of the electromagnetic radiation spectrum, see Table 1. Visible light has wavelengths in the range $0.4 - 0.7$ μm (1 μm $= 1$ micrometre $= 1 \cdot 10^{-6}$ m), with violet light in the low end and red light in the upper end of the interval.

Electrically charged particles are surrounded by an electric field which can

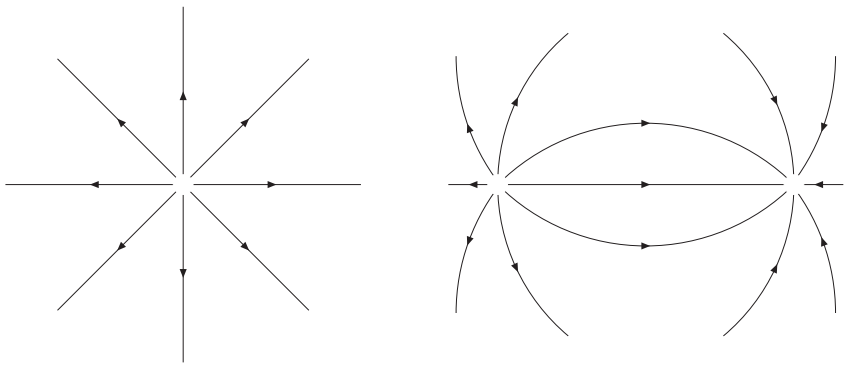

Figure 1: a) Electric field lines for a point charge. b) Electric field lines between two oppositely charged point sources.

be represented by field lines in space, going from positively charged particles to negative ones, Fig. 1. The density of field lines at a specific point will tell the strength of the field and is inversely proportional to the square of the distance from the point charge. The familiar geo-magnetic field has long been used for navigation with the help of compasses (where a needle of a magnetized material points towards the magnetic north pole).

An electric current, electric charges in motion, gives rise to a magnetic field that is perpendicular to the direction of the current. A varying magnetic field will induce an electric field. The two fields can be described by a more general field, the *electromagnetic field*, because of the intimate relation between the two. The fact that an electric field can be generated by a magnetic field and vice versa, implies that changing electric and magnetic fields can exist even without charges. Such mutually sustaining electric and magnetic fields are called electromagnetic waves. Light is an electromagnetic wave and unlike sound waves, can propagate through the vacuum.

The electromagnetic spectrum, which spans over 20 orders of magnitude is divided into different intervals, named after the way the radiation is produced or absorbed, Table 1. The energy of the radiation at different wavelengths are given in electron-volt, 1 eV $= 1.6 \cdot 10^{-19}$ Joule $= 3.8 \cdot 10^{-23}$ kcal. To get a feeling for the smallness of 1 eV, you may put this thesis in your knee — you have just gained about a half Joule (10^{19} eV) from its potential energy difference! (I wish you pick it up again and continue reading however.) We can conclude, from Table 1, that as the wavelength of the radiation decreases the energy increases, there is an inverse proportionality between the two. In the following, we will focus on the short wavelength part of the spectrum.

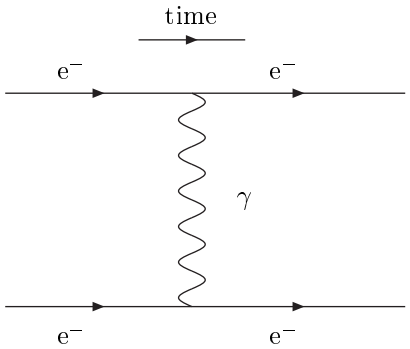

Figure 2: Two electrons (e^-) interact via an exchange of a photon (γ). Time flows to the right and the straight lines represent the motion of the electrons and the wavy line that of the photon.

Thermal radiation, ranging from UV to IR light, can be absorbed and emitted by a molecule as a whole as rotational or vibrational excitations. In atoms, electrons can be bound into different shells which corresponds to different energy levels. Only certain energy levels are available, which is due to the quantum mechanical nature of the electromagnetic interaction at these short distances. The ground state is the configuration where all the inner-most shells, i.e. the lowest bound energy-levels, are filled with electrons. An electron can be excited to a more energetic state by absorbing light, but only specific portions of the electromagnetic field, so called *quanta*, can be absorbed. These quanta have particle-like properties and are refered to as *photons*. In contrast to the classical picture, where light is treated as a continuous wave, it can be seen as electromagnetic *field-particles* being exchanged, transferring energy and momentum, between electrically charged particles, Fig. 2. Photons can also be emitted through de-excitation, i.e. an electron 'jumps' from an outer to an inner available shell. For lighter atoms (with only a few protons and neutrons), this is how visible light can be absorbed and emitted by matter. For heavier atoms, the inner-most shells are filled and short wavelength radiation can normally not be emitted. When bombarded with high-energy particles, energy can be transfered to strike out an electron from the inner-most shells, and subsequently an outer electron can fill its position by radiating *X-rays*. *γ-rays* may, similarly, be emitted from excited atomic nuclei. The excited nucleus may originate from a radioactive decay where the extra energy, stored as kinetic energy by the protons and neutrons, can be emitted in the form of radiation.

The pattern is now clear. We can probe an object by shining light with a certain wavelength on it. Observations of excited states will tell us that it is composite. By choosing a shorter and shorter wavelength of the light, we can probe smaller and smaller constituents of matter. Light acts as a magnifying glass with a variable resolution corresponding to its wavelength. The probing wavelength should be of about the same order of magnitude as the object one would like to study, confer Table 1. A molecule has a typical size of the order of 10^{-9} m, an atom 10^{-10} m and its nucleus $10^{-14} - 10^{-15}$ m. The fundamental building blocks of nature are within the range of vision, although not in the range of visible light, and in the following we shall 'see' even smaller constituents of matter.

Photons and QCD

In this section the meaning of the thesis title will become clear and some of the concepts introduced will be expanded further. One method for probing the structure of an object is through scattering experiments. The principle was mentioned already in the previous section. High-energy particles incident on an atom may transfer energy to it. It was implicitly assumed that charged particles were to be used, so the energy transfer is governed by the emission and absorption of electromagnetic radiation (the photons) between the charged particles and the charged constituents of the atom. An electron is thought to be point-like, i.e. it shows no internal structure. A beam of electrons is then suitable for doing scattering experiments and provide the magnifying glass — the energetic photons.

Consider a scattering experiment with a beam of electrons incident on an atom. For a low-energy beam, corresponding to a low resolution (i.e. exposing the atom with long-wavelength radiation, Table 1), the atom as a whole will appear transparent. Or in other words, it would appear electrically neutral. The long-wavelength photons will not resolve the constituents of the atom, the nucleus and the electrons. Hence, the electron beam will pass through the atom more or less unaffected.

To increase the resolution of the magnifying glass, a smaller wavelength of the photons is required which is obtained by increasing the energy of the electron beam. Now the electrons in the atom can be resolved and may jump to a higher energy level by absorbing a photon, or the atom may even become ionized (one electron will get enough energy to escape from the bound energy levels). When the target remains unchanged, it is referred to as *elastic scattering*, but when it is broken into fragments it is called *inelastic scattering*, e.g. when the atom is ionized. The excitation levels are specific for the particular element used in the target, which can thus be identified, if not known.

When an electron in the beam emits a photon, which is finally absorbed by

$$\begin{pmatrix} \mathrm{u} \\ \mathrm{d} \end{pmatrix} \begin{pmatrix} \mathrm{c} \\ \mathrm{s} \end{pmatrix} \begin{pmatrix} \mathrm{t} \\ \mathrm{b} \end{pmatrix} \qquad \begin{pmatrix} \nu_{\mathrm{e}} \\ \mathrm{e}^- \end{pmatrix} \begin{pmatrix} \nu_{\mu} \\ \mu^- \end{pmatrix} \begin{pmatrix} \nu_{\tau} \\ \tau^- \end{pmatrix}$$

Table 2: The families of quarks and leptons, to the left and right respectively. For the quarks, the top row (up, charm and top) has electric charge $+\frac{2}{3}e$ and the bottom row (down, strange and bottom) has $-\frac{1}{3}e$, where e is the magnitude of the electric charge of the electron. The electron, muon and tau (e, μ and τ resp.) have electric charge $-e$ whereas their neutral counterparts, the neutrinos, are uncharged.

one of the constituents in the atom, it will get a recoil and the electron beam will be deflected. The observed scattering angle and energy of a deflected electron will give additional information about the target atom. The angular distribution depends on the size of the beam and the target, as well as the force acting between them. If we increase the energy of the electron beam further, the nucleus may become excited and reveal its structure. Continuing to even higher energies, we will finally break the nucleus of bound protons and neutrons into fragments, giving new combinations of protons and neutrons. What will happen if we continue increasing the resolution?

In elastic electron scattering from a proton, Fig. 3, the angular distribution of the scattered electron show that the proton has a size corresponding to a radius of $\sim 10^{-15}$ m. The fact that it has a finite size tells us that it is composite. In inelastic electron-proton scattering [1], which breaks up the proton, we see little variation with respect to the electron scattering angle — as if the scattering is taking place from something point-like in the proton! More detailed studies show that there are three point-like particles in both protons and neutrons. They are called *quarks*. The quarks appear in six different flavours, all have been experimentally verified, and can be subdivided into three families, Table 2. The relatively heavy particles in the second and third families (from the left) decay into the lighter ones in the first family. Therefore only the stable light particles in the first family appear naturally in ordinary matter. The proton and the neutron consist of the combinations (uud) and (udd), respectively. The electron is the lightest of the three charged *lepton* flavours, see Table 2 for details.

As discussed above, photons are the exchange particles for the electromagnetic force. The corresponding exchange particles for the strong force are called *gluons*. By exchanging gluons between each other, the quarks are bound together forming protons and neutrons. The quarks and gluons obey a threefold symmetry where a quark carries an additional quantum number which for simplicity has been called *colour charge*. A quark can have three different colours:

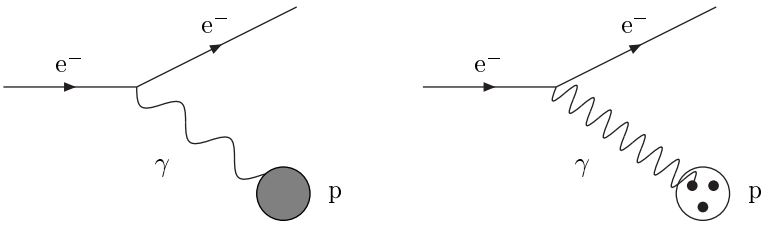

Figure 3: a) Elastic electron scattering from a proton (p). The photon do not resolve the proton which interact as an extended object. b) Inelastic electron scattering from a proton. A short-wavelength photon resolve charged point-like particles inside a proton.

red, green and blue (like the primary colours of natural light). A property of the symmetry of the strong interaction is that the quarks can only be combined into colourless objects called *hadrons*. (Natural light, consisting of the above primary colours is colourless, explaining the choice of colour as the name of the additional quantum number for quarks and gluons.) The colour field outside protons and neutrons make them form stable atomic nuclei, just like the electric field outside neutral atoms binds them together into molecules. Although the strong force is short-ranged, within distances of an atomic nucleus it overcomes the much weaker electromagnetic force which is repulsive between the electrically charged protons.

Another consequence of a symmetry in nature is the existence of *antiparticles*. Each particle has an antiparticle with identical properties except for having opposite quantum numbers. For example, the *positron* is the electron's antiparticle and is positively charged and the antiquark carries an anti-colour. A quark and its corresponding antiquark can be combined to obtain another kind of colourless hadron, $(q\overline{q})$ where q is a quark and $\overline{q}$ is an antiquark. In total we have two classes of hadrons: $(qq'q'')$ and $(q\overline{q})$, where q, q′ and q″ can be any of the six flavours given in Table 2.

Thus, the gluons are the field quanta of the colour force field, but unlike photons, the gluons themselves carry charge — the colour charge. It is then possible to have a gluon exchanged between two gluons. A feature which makes the colour force, acting between e.g. a quark and an antiquark, increasing in strength with separation, just the opposite of the behaviour of the electromagnetic force. As we will see, it has consequences for the sizes of hadrons. The theory of the strong interaction is called Quantum Chromo Dynamics (QCD) and deals with the coloured particles, the quarks and the gluons. The electromagnetic equivalent is called Quantum Electro Dynamics (QED).

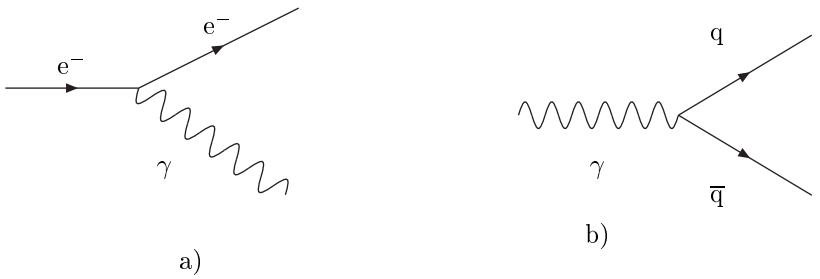

Figure 4: a) A photon is emitted by an electron. b) A photon may fluctuate into a quark (q) and an antiquark ($\overline{\mathrm{q}}$).

In fact, the electromagnetic and the weak interactions can be unified into one *electroweak* theory. Now, the photon is one of the mediators of the electroweak force, the others are called W^+, W^- and Z^0 (with their electric charges indicated as superscript). Whereas the latter three particles have masses close to 100 times the proton mass, the photon is massless. The weak interaction is responsible for radioactive β-decays of atomic nuclei where a neutron is converted into a proton by the emission of a W^- which subsequently decays into an electron and the antiparticle of its neutral counterpart, the (anti)electroneutrino. (Formally, $\mathrm{d} \to \mathrm{u} + \mathrm{W}^- \to \mathrm{u} + \mathrm{e} + \bar{\nu_\mathrm{e}}$.)

Before continuing, it is suitable to reflect upon the masses of some particles discussed until now. The mass of the proton is 10^{-27} kg and that of the electron 10^{-31} kg. They are indeed small numbers, wherefore particle physicists introduce other units which are more appropriate. For instance, the speed of light (c) is set to one. Einstein's equation relates the energy (E) and the mass (m) of a particle, which for a particle at rest reads: $E = mc^2 = m$. The last equality comes from setting $c = 1$. We can now quote particle masses in eV's. Thus the proton mass is 1 GeV ($1\ \mathrm{GeV} = 10^9$ eV) and the electron mass 10^{-3} GeV. The potential energy difference obtained by lifting this thesis a few decimetres then corresponds to the rest energy of 10^{10} protons.

Properties of the Photon

Earlier the photon was described as an exchange particle for the electromagnetic interaction (or generally, the electroweak interaction). In Fig. 2, two electrons are interacting by the exchange of a photon. Energy and momentum are conserved separately in the process if we compare the summed energy and momentum of the two electrons before and after the exchange of the photon. But if we consider a process where a massless photon is emitted by an electron, like in Fig. 4a, it violates energy and momentum conservation. Energy or mo-

mentum can be conserved but not both. It contradicts our classical ideas but it is fully consistent with quantum mechanics. According to the uncertainty principle, energy and time (as well as momentum and position) are complementary quantities and both cannot be determined exactly in simultaneous measurements. For example, the precision of (in this case) the photon energy can only be defined within an uncertainty which is inversely proportional to the life-time of the photon. Consequently, energy can be 'borrowed' during a short time interval in order to conserve energy and momentum. Hence, the photon emitted in Fig. 4a is a short-lived *virtual* state and may either be absorbed by the same electron or by another electrically charged particle. In the latter case, the scenario in Fig. 2 can be imagined, where the virtual photon acts as an exchange particle and in the former case, it is a process that gives rise to a cloud of photons, continuously emitted and absorbed by the electron.

Another approach is to require both energy and momentum conservation in Fig. 4a, but then the photon has to be assigned a non-zero mass. The photon mass can then be seen as a measure of how 'virtual' the photon is. The virtuality spectrum of photons emitted from an electron with a certain energy is peaked in the low end where it can be considered almost massless, i.e. *real*.

The non-zero mass of a virtual photon requires it also to have one longitudinal polarization state. A massless particle only has two transverse polarization states. Recall the discussion about electromagnetic radiation, in an electromagnetic wave the electric and magnetic fields are perpendicular to each other and to the direction of propagation, corresponding to the two transverse polarization states.

At high energies a photon may fluctuate into an electrically charged particle-antiparticle pair, e.g. a $q\overline{q}$-pair as in Fig. 4b. Now the quark and the antiquark are considered virtual and can only exist for a short time and eventually annihilate into a photon again. Due to the presence of the coloured quark and antiquark, the fluctuation may interact with the coloured particles in a hadron via the strong force.

In *Deep Inelastic electron Scattering* (DIS) of a proton, a highly virtual photon is absorbed by a quark in the proton. The spectrum of photon virtualities is peaked in the low end, i.e. the exchange of highly virtual photons are suppressed and DIS processes occur at low rates. A virtual photon may also fluctuate into a $q\overline{q}$-pair. But since the photon itself is virtual and therefore has a limited life-time, its fluctuation has an even shorter life-time. Hence, in DIS a highly virtual photon is not likely to fluctuate, it remains as a fundamental exchange particle — without any internal structure.

On the contrary, a real photon incident on a hadron may fluctuate into a $q\overline{q}$-pair and thereafter interact via the strong force, giving rise to, for example, $qq' \rightarrow qq'$ scattering with an exchange of a gluon. In the latter case, the photon is said to be *resolved* in the collision. The fluctuations can be seen as

being a part of the *photon structure*. Although we still think of the photon as a fundamental structureless particle, we talk about the structure of the photon due to the possibility of having fluctuations into an electrically charged particle-antiparticle pair.

Going one step further, we may probe the structure of a photon directly by inelastic electron scattering of a photon. Both the probing and target photon can be provided by an electron or a positron beam, but probing the structure of a virtual photon suffers from low event rates.

In the region of rather small photon virtualities, say photon masses of a few GeV, a complex picture of photon interactions cannot be avoided. Both the structureless and the resolved photon picture is needed. It is in this region, that the model of photon interactions presented in this thesis apply. It interpolates between the properties of a real and a very virtual photon. The phenomenological importance of resolved longitudinally polarized photons is largely unknown, and are thus modeled to estimate their effects.

Experiments

With no intention of being complete, only two of the current high-energy physics experiments in use will be mentioned, the Large Electron-Positron (LEP) collider at CERN, Geneva, and the electron-proton collider HERA at DESY, Hamburg [2, 3]. (HERA = Hadron-Electron Ring Accelerator.) The obvious reason is that the results of this thesis is directly applicable to physics studied at these experiments. After some general remarks about current particle physics experiments, a brief summary of the above two laboratories will be given.

Physics, like all other sciences, depends on observations. Cosmic rays were one of the first sources for doing particle physics experiments. Unfortunately, the conditions under which some reactions occur spontaneously in nature are rare, so studying natural phenomena does not offer enough variation and flexibility. Nowadays, almost exclusively, particles are made to gain speed in accelerators because they give very intense, collimated beams of controlled energy. With electric and magnetic fields, charged particles can be accelerated and deflected to obtain the desired energy and direction just before they collide. The design of accelerators varies greatly with their use. In high-energy experiments, particles need to exist for seconds in order to obtain a useful acceleration and rules out all but the stable particles, the electron and the proton, and their antiparticles.

The simplest way to accelerate an electrically charged particle is to 'drop' it through a constant electric potential difference. If the particle has a charge e (equal to the charge of the electron) and if a voltage of 1 Volt is applied, the kinetic energy acquired is 1 eV. There are two kinds of accelerators, linear

and circular, both with their pros and cons. In principle, the longer a linear accelerator is, the more energy can be acquired by the beam. As an example can be mentioned a future linear electron-positron collider, which is only a proposal so far, proposed to have a length of 33 km that can provide 500 GeV in collision energy. Usually, a linear collider has only one interaction region, where the detector is located, and the accelerated beam of particles can be used only once.

In circular accelerators, magnets are used to bend the particles to follow a circular path. Two oppositely charged beams can be accelerated in opposite directions and the particles which do not collide in the interaction regions can in principle be recycled. The beam collects energy with each lap, but charged particles radiate energy as their paths bend and the amount of energy lost in this way increases both with the energy of the particles themselves and with the curvature of the path. In order to reduce radiation losses it is therefore desirable to have as small curvature as possible. The accelerators LEP and HERA are both of the circular type.

It is quite ironic that the detectors used for measuring the small particles are of sizes comparable to normal buildings. Most detectors are enclosed in a large magnet, so that charged particle tracks are curved and their momenta can be determined. The detector is composed of a large number of separate parts located in different layers, designed to handle specific kinds of particles.

In order to do comparisons between theory and experiment, uniquely defined observables are needed. One such observable is the total *cross section* of a collision which is the probability of a scattering to occur between the particles involved in the collision. It is measured in units of square metre but is more often stated in terms of barns, 1 barn = 1 b = $1 \cdot 10^{-24}$ m^2. Typical cross sections are of the order 1 pb to 1 mb ($10^{-12} - 10^{-3}$b) depending on the collision energy and the particle types colliding. Further insight into a collision is gained by studying *partial* or *differential* cross sections. For example, the probability to measure a scattered electron at a certain angle θ per unit scattering angle is given by the distribution $\mathrm{d}\sigma/\mathrm{d}\theta$ which generally depends on the scattering angle. If integrated over all angles, the total cross section of the reaction studied is obtained.

CERN

The French acronym CERN stands for European Organization for Nuclear Research and was founded in 1954 [2]. It is situated in Geneva, Switzerland. The first operating accelerator at CERN is now used to feed other accelerators with particles. Electrons and positrons are accelerated in stages before entering the LEP ring, with a circumference of 27 km, where they continue traveling in opposite directions. There are four interaction zones for collision experiments. The detectors are ALEPH, DELPHI, OPAL and L3. Each experimental collab-

oration has emphasized on certain characteristics of the detector. The collision energy has increased over the years, from about 100 GeV, when LEP started running in 1989, to currently 200 GeV. The next big machine to be built at CERN is the Large Hadron Collider. It will use the existing underground ring, colliding protons with each other, and is planned to start operating in 2005.

DESY

DESY — Deutches Elektronen SYnchrotron laboratory, is a publicly funded national research center in Hamburg, Germany [3]. It was founded in 1959 and the current experiments have been operated since 1992. Electrons and protons are accelerated in a ring, with a circumference of 6 km, to 30 and 920 GeV, respectively. There are four interaction zones, two collision experiments H1 and ZEUS and two fixed target experiments HERMES and HERA-B (the target is at rest in the laboratory frame). A possible future for the particle physics program at DESY is to build the proposed linear electron-positron collider mentioned above.

Event Generators

The objective of an event generator is to artificially simulate processes in the same way as they appear in nature, i.e. as measured in an experiment. In the LEP and HERA experiments, discussed in the previous section, tens to hundreds of particles are detected in each event. The complexity of a collision makes a specific class of numerical methods particularly well suited for solving these problems, namely the *Monte Carlo* (MC) methods. MC methods are stochastic techniques, meaning they are based on the use of random numbers and probability statistics to investigate problems. (The use of randomness gives the connection to the games of chance in the casinos of Monte Carlo, and hence the name.) The quantum mechanical nature of high-energy particle collisions gives fluctuations between one event and the next. With MC techniques randomness is ensured in the simulated event generation. MC methods are now used routinely in many diverse fields, from economics to particle physics to regulating the flow of traffic — but, of course, the way they are applied varies widely.

Monte Carlo Methods

As an example of a simple MC method, we will illustrate the concept by calculating the value of π based on a 'hit and miss' integration. If you are a very poor dart player, it is easy to imagine throwing darts randomly at Fig. 5, and it should be apparent that of the total number of darts that hit within the big

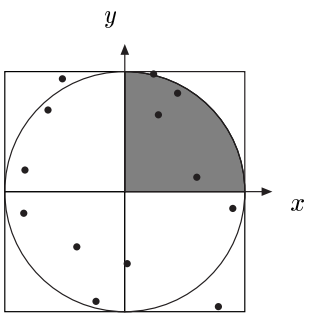

Figure 5: The value of π can be calculated by Monte Carlo methods or by throwing darts randomly on a circle inscribed in a square.

square, or the number of darts that hit within the circle is proportional to the area of that part. If each dart thrown lands somewhere inside the big square, the ratio of 'hits' (in the circle) to 'throws' will be an estimate of $\pi/4$. But it takes a very large number of throws to get a decent value of π. Instead of throwing darts, we can have computers generate random numbers.

Let us concentrate on the upper right square and the shaded area of the circle. For each throw we can generate two random numbers, an x and a y coordinate, which can be used to calculate the distance from the origin of the circle. If the distance from the origin is less than or equal to the radius of the circle, it is within the shaded area and counts as a hit. If this is repeated several times, an estimate of the value of π will be obtained. How good it is depends on how many iterations (throws) are done, and to a lesser extent on the quality of the random number generator.

The above example illustrated how a MC method could be used as a numerical integration method, where the arc of the shaded area represented the function to be integrated. If the function being integrated is a positive definite probability density, it can be converted to a simulation of a physical process, i.e. an event generator. The distribution of photon energies and virtualities from the process $\mathrm{e} \to \mathrm{e}\gamma$ of Fig. 4a can easily be generated with this method, giving a correct (according to the distribution put in) energy and virtuality of the photon which varies randomly between one event and the next.

In this thesis, the above process has been implemented into the MC event generator PYTHIA [4], to provide the photon exchanged between the electron and the proton, when simulating processes as measured at HERA [3]. The two-photon processes, as measured in $\mathrm{e^+e^-}$ collisions at LEP [2], make use of the same routine, but twice — one for each lepton.

A disadvantage of MC methods is the slow convergence in few dimensions. On the other hand, in high-energy physics events, many particles are involved

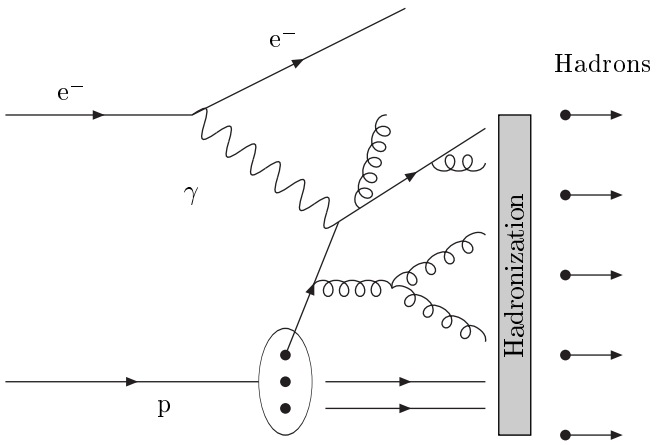

Figure 6: Deeply inelastic electron-proton scattering. Gluons are represented by winding lines.

leading to many dimensions (phase space has three dimensions per particle). But as compared to other methods, MC has fast convergence in many dimensions. Other advantages are, for example, that arbitrarily complex integration regions can be used and only a few generated values are needed to get a first estimate.

Hard Scattering

The purpose of an event generator is of course to build in as many aspects of relevant physics as possible. This is not an easy task, however. One may start to subdivide the problem into smaller components, each one more or less isolated from the other, and try to solve each part as accurately as possible. The fact that the interactions in a high-energy collision occur between fundamental particles, such as quarks and leptons, suggests that the event should be built up from these basic interactions and then to be 'dressed' with other necessary aspects to achieve a realistic description.

Let us return to the Deep Inelastic Scattering (DIS) of an electron from a proton, Fig. 6, for a specific example. The process can be subdivided into three main phases, a *hard scattering*, *parton showers* and *hadronization*. This classification is quite general and need not necessarily be associated with event generators. The borders between the different phases are not absolute and introduce uncertainties when trying to combine the different pictures.

The hard scattering process of Fig. 6 is the $e^-q \to e^-q$ process, where a photon is exchanged between the electron and a quark in the proton. It is refered to as the hard scattering process because the photon is the particle with highest virtuality in the collision. Remember that the photon may fluctuate into a $q\overline{q}$-pair and, for example, the antiquark may interact with one of the quarks in the proton via a gluon exchange. The gluon can then be the particle with highest virtuality in the collision, arriving with the $\overline{q}q \to \overline{q}q$ process as the hard process.

Hard processes can be calculated with a particular method called *perturbation theory*, where the quantum mechanical amplitude for the scattering is calculated, obtaining a result which tells how likely a process is to occur (in terms of differential cross sections). It may depend on particle types, collision energy, scattering angles etc. As a first approximation, only the simplest processes, like $e^-q \to e^-q$, need to be considered since this gives the dominant contribution to the amplitude. Corrections to the simplest processes then involve diagrams with extra gluons or photons, emitted or exchanged. In certain cases comparisons can be made with data already at this level. If the particles involved in the hard interaction scatter at large angles, so called *jets* of particles can be found with approximately the energies and angles of the scattered particles. Hence, the calculations from perturbation theory can be compared with the experimentally observed jets of particles.

Collectively the quarks, antiquarks and gluons are called *partons*. Since the proton not only contains quarks, but also gluons which like photons may split into a $q\overline{q}$-pair, any of these partons may participate in a hard scattering process. It is assumed that when a photon is interacting with a proton it can be viewed as a sum of interactions between the photon and the individual partons in the proton, each carrying a momentum fraction x of the proton's total momentum, with a certain probability for each parton flavour. The distribution of partons also depends on the virtuality of the photon probing the proton. The so called *parton distributions* then give the probability of finding a certain parton at a given x and photon virtuality. The photon-proton scattering cross section will then be proportional to the constituent cross sections for the individual partons times the parton distribution of that kind. There are a number of constraints on parton distributions and when combined with experimental measurements, suitable parameterizations can be obtained.

Several partonic subprocesses, e.g. the DIS process $\gamma^*q \to q$ (the γ^* indicates a virtual photon), have been implemented into the PYTHIA MC event generator [4] for the modeling of virtual photons. They are in turn combined with virtual photon parton distributions (where appropriate).

Parton Showers

We have seen that accelerated electric charges radiate photons. Similarly, accelerated coloured particles radiate gluons, and therefore a shower of partons may be produced in a collision. A parton shower scheme offers a systematic way of taking into account corrections to the over-simplified picture of the hard scattering discussed above. This is important for a number of measurable quantities which depend on multi-parton configurations. Since the quarks are electrically charged, photon emissions also need to be considered. But the weakness of the electromagnetic coupling will suppress them in favour of the QCD parton radiation.

The principle is the following: starting with an energetic initial parton, e.g. a scattered quark, it may radiate a gluon, $q \to qg$. Subsequently, both the gluon and the quark, now with reduced energy due to the radiation, may radiate separately. Hence, both partons can now be considered as initiators of a new shower but with less energy to their disposal. This is continued iteratively until the energy of the partons are of the order of typical hadron masses, $m_{\mathrm{proton}} \simeq 1$ GeV. This scheme is an approximation which is accurate for not so well separated partons, so that the quark and gluon from the splitting $q \to qg$ are relatively close in angular separation. As mentioned above, corrections can also be calculated in connection with the hard scattering, where all configurations giving the same final state of partons contribute and need to be considered together. For multi-parton configurations the calculations rapidly become messy however, and the results become infinite (i.e. should not be trusted) in the limit where two partons are traveling parallel to each other. It is in this limit where the parton shower approach is derived, i.e. gives a good approximation. But on the other hand, it is not so accurate for well separated parton configurations as the other approach is. It is therefore natural to try to combine the two pictures, attaching a parton shower to the hard scattering process.

The parton shower scheme described above was limited to the so called final-state radiation. In the DIS process above, the gluons emitted by the scattered quark, after the photon exchange with the electron, belong to this class. The gluons emitted by the quark before the photon exchange are then part of the initial-state radiation. A similar technique can be used here, but instead you start with the hard process and evolve the parton shower backwards [5]. For instance, by assigning energy and momenta to the initial quark and the final gluon in the parton splitting $q \to qg$, where the final quark exchanged the photon in Fig. 6.

An e^+e^- pair may annihilate into a virtual photon which in turn can produce a $q\overline{q}$-pair. In a subsequent parton shower, identical colour charges can be produced and interference effects may be important. In Paper I of this thesis, a certain parton shower description is improved during these circumstances [6, 7].

A particular observable is suggested, to see the effects of this.

Hadronization

How the coloured partons are transformed into colourless hadrons, the *hadronization* or *fragmentation* process, is not understood from first principles and has to be based on models. The hadronization process has to occur with unit probability however, because only colourless hadrons are observed, never free quarks.

At short distances the strong force is relatively weak and say, between a quark and an antiquark, the one gluon exchange dominates and can be expressed as an attractive $1/r$ potential, where r is the distance between the quark and the antiquark. (The well known Coloumb interaction between two electrically charged particles can be described as a $1/r$ potential. However, the factor in front will differ so it is still much weaker than the QCD potential.) At larger distances, multi-gluon exchange dominates, eventually leading to confinement of quarks (and antiquarks) into hadrons. The colour field is said to be self-interacting since the carriers of the strong interaction, the gluons, may interact among themselves. This leads to a long-range component of the potential which is linear in r.

The colour field between a quark and an antiquark can be pictured as lines of force which are self-attracting and therefore the lowest lying energy configuration of this field is a colour flux tube of fixed cross-section between the quark and the antiquark, Fig. 7. Remember the lines of force for the electromagnetic field which fill the whole space around two electric charges. As the partons move apart the tube gets longer only and the potential energy increases linearly with separation. Consequently, it costs an infinite amount of energy to separate a quark from an antiquark and hence no free quarks have ever been observed, i.e. quarks and gluons are confined into hadrons.

In the *string* fragmentation model [8, 9], the hadronization of partons is based on a colour flux tube (the string) interpretation of the colour field. In a hard scattering, a quark may be moving rapidly away from the quark partners (or antiquark partner) in a hadron, like the DIS process above. (Leaving the gluons from the hard phase behind for a moment.) As the separation increases, the energy in the string increases and the kinetic energy is converted into potential energy of the string. At some separation, when the energy stored in the string is large enough, it becomes possible to form a $q\overline{q}$ pair in the colour field, leaving a region where the colour field cancels — breaking the string into two strings. One string is now stretched between the remnant quarks of the first hadron and the new quark, and the other string is between the new antiquark and the initially scattered quark. This can be continued iteratively for each string piece separately until the energy stored in them is too small to produce a new $q\overline{q}$-pair.

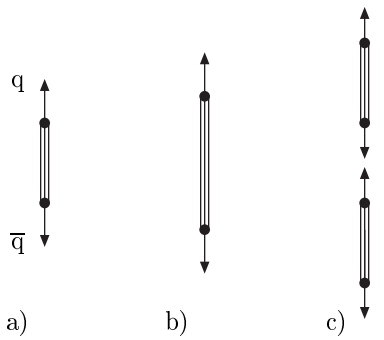

Figure 7: a) A colour flux tube connects a quark and an antiquark. b) As they move apart, the energy in the colour flux tube increases. c) At a certain stage, it is possible to form a new $q\overline{q}$-pair, breaking the colour flux tube. This will continue until the size of each string piece is of typical hadronic sizes.

Instead, when the kinetic energy has been converted into potential energy of the string, the colour and anticolour will turn and be pulled towards each other, resulting in a yo-yo motion of the system. The distance between the turning points is of typical hadronic sizes, i.e. $\sim 10^{-15}$ m. What finally remains after all the string break-ups are ordinary hadrons. Some of them may be unstable and will finally decay into stable hadrons. Other models exist for describing the hadronization process [10] and what they have in common is that they are all based on a phenomenological description.

The gluons from the hard phase of the process will appear as excitations, or kinks, on the string. A gluon will then connect two string ends. It has become standard practice to attach fragmentation models at the end of a parton showering. The possibility of having identical colour charges makes the stretching of the string ambiguous. In Paper I, its consequences are investigated, together with the same problem discussed in the previous section, where a certain measure is used to pick the most relevant configuration.

The Papers

Paper I and II will be summarized separately and Paper III–VI will be presented together since they all treat a model of high-energy photon interactions in photon-proton (γp) and photon-photon ($\gamma\gamma$) collisions.

Paper I

In e^+e^- annihilation, a virtual γ or Z^0 can be produced which may decay into a $q\overline{q}$-pair. In a (possible) subsequent cascade of partons, it was investigated how colours can be connected. In particular, when there are several identical colour charges, we studied the possibility of obtaining a colourless system of gluons fragmenting into hadrons isolated from the other partons in the event. With the ARIADNE event generator [6, 7], an enhancement of the probability of finding fewer particles in a central region was observed as compared to not forming the colourless gluon system. If this type of states appear in Z^0 decays it may also be an indication that colour connections may appear between $q\overline{q}'$ decays of two W's, which would be important for precision measurements of the W mass.

Paper II

Attempts have been done to construct models unifying quarks and leptons, i.e. a model where they are treated on equal footing. Several ways turn out to be possible. In common is that new exchange particles appear as one extend to a theory with a larger symmetry. The exchange particles for the interactions of such a unification are sometimes referred to as *leptoquarks*.

About three years ago, a number of unexpected events were observed at HERA. As a possible explanation, the production of leptoquarks as resonances were discussed and we investigated some QCD aspects of such a scenario. As the name indicates, a leptoquark carries the quantum numbers of a lepton and a quark, i.e. it is both electrically charged and coloured and thereby it may radiate photons and gluons. Depending on the life-time of the leptoquark, it may form a leptoquark-hadron before decaying. By studying how different observables depend on the leptoquark decay angle, something can be said about the leptoquark life-time.

It is important to stress that there is no direct evidence for the existence of leptoquarks, so it should be viewed as a hypothetical particle. Its phenomenological consequences can be investigated however. The arguments and conclusions are quite general and easily applicable to other, similar, situations. By investigating QCD effects in the production and decay of a leptoquark, we found that the largest individual source of smearing, for reconstructing the mass of a leptoquark, is the final state QCD radiation. By taking into account

corrections to this, in mass reconstructions of a leptoquark, a narrower mass peak and a better average mass value was obtained.

Paper III-VI

The model of high-energy photon interactions is based on an existing model for the treatment of real photons in γp and $\gamma\gamma$ events [11]. It is implemented in the event generator PYTHIA [4] which has been developed over a long time and contains a tremendous amount of processes that can be studied under varying conditions and at different colliders. Paper II–V in this thesis have only contributed to a small fraction of its physics content and are summarized in Paper VI together with other new aspects with respect to the previously published versions of the program.

The photon itself is a very complicated object to describe. In the DIS region it can be viewed as an elementary particle without any internal structure. For a real photon this is only one of its components, the *direct* photon. Instead, the interactions are dominated by fluctuations into a $q\overline{q}$ state. The transition region between these two pictures clearly involves both properties, which are non-trivially mixed. We have studied the concept of a resolved photon and how it fades away with the photon virtuality, simplifying to a structureless, direct photon description in the DIS limit.

The approach has been to subdivide the photon into a resolved and a direct one according to whether or not the photon fluctuates into a $q\overline{q}$ state. Major improvements for processes involving virtual photons are, for instance, the convolution of the distribution of photon energies and virtualities (from an e, a μ or a τ source) with the virtuality dependent hard-scattering subprocess cross sections, summing over the transverse and longitudinal polarization states. The resolved virtual photons are further convoluted with their corresponding parton distributions. The description of total cross sections is based on a parameterization for real photons and is extended to incorporate resolved virtual photons by dipole factors which will dampen the cross sections with increasing photon virtuality.

To estimate the importance of resolved longitudinal photons simple multiplicative factors are applied to the transversely ones. Recently, parton distributions of longitudinal photons has become available and therefore its implications on some results were investigated and compared to the simple factors previously used.

Since the model can be confronted with both HERA and LEP data, stringent tests of model assumptions can be made.

Acknowledgments

First, I want to express my gratitude to Prof. Torbjörn Sjöstrand for his patient and ambitious guidance, and for continuously encouraging me to present our research results on various conferences and work shops. I would like to thank Prof. Gösta Gustafson and Dr. Jari Häkkinen for fruitful cooperation. I am also grateful to the people who have shown interest in my research.

To share office with Emanuel has been a great intellectual and social asset. I thank Emanuel, Erik and Sandipan for helpful comments and corrections to the introduction. I also thank my colleagues at the department for a pleasant atmosphere over the years.

Finally, Anneli, very special thanks for being exactly the person you are. Your understanding and moral support are invaluable.

References

[1] M. Breidenbach et al., *Phys. Rev. Lett.* **23** (1969) 935,
Phys. Rev. Lett. **37** (1976) 76.

[2] CERN
http://www.cern.ch/

[3] DESY
http://www.desy.de/

[4] T. Sjöstrand, *Computer Phys. Commun.* **82** (74) 1994;
http://www.thep.lu.se/∼torbjorn/Pythia.html;
Paper VI this thesis.

[5] T. Sjöstrand, *Phys. Lett.* **157B** (1985) 321.

[6] G. Gustafson, *Phys. Lett.* **B175** (1986) 453;
G. Gustafson, and U. Pettersson, *Nucl. Phys.* **B306** (1988) 746;
B. Andersson, G. Gustafson and L. Lönnblad,
Nucl. Phys. **B399** (1990) 393.

[7] L. Lönnblad, *Computer Phys. Commun.* **71** (1992) 15;
http://www.thep.lu.se/∼leif/

[8] X. Artru and G. Mennessier, *Nucl. Phys.* **B70** (1974) 93;
B. Andersson, G. Gustafson and B. Söderberg, *Z. Phys.* **C20** (1983) 317;
B. Andersson, G. Gustafson, G. Ingelman, and T. Sjöstrand,
Phys. Rept. **97** (1983) 31.

[9] R.D. Field and R.P. Feynman, *Phys. Rev.* **D15** (1977) 2590;
P. Hoyer et al., *Nucl. Phys.* **B161** (1979) 349.

[10] B.R. Webber, *Nucl. Phys.* **B238** (1984) 492;
G. Marchesini and B.R. Webber, *Nucl. Phys.* **B238** (1984) 1.

[11] G.A. Schuler and T. Sjöstrand, Nucl. Phys. **B407** (1993) 539,
Z. Phys. **C73** (1997) 677.

Colour Connections in e^+e^--annihilation

Paper I

Colour Connections in e^+e^--annihilation

Christer Friberg, Gösta Gustafson and Jari Häkkinen

Department of Theoretical Physics,
Lund University, Lund, Sweden

Abstract

We have a very limited knowledge about how the confinement mechanism works in processes like $e^+e^- \to q\overline{q}g\ldots g$, when there are identical colour charges. In this case the partons can be connected by a string or a cluster chain in several different ways. We do not know if in such a situation Nature chooses a particular configuration at random, or if some configuration is dynamically favoured. Also in the perturbative parton cascade we have no well founded recipe for describing the interference effects, which correspond to non planar diagrams and are caused by identical colour charges. We have studied two different models, and are in particular interested in the possibility that a colour singlet gluon system hadronizes isolated from the remainder of the state. Using double tagged events with heavy $c\overline{c}$ or $b\overline{b}$ quarks, it appears to be possible to find a significant signal, if such events appear in Nature.

If this type of (re)connected states appear in Z decays it may also be an indication that reconnection might appear between the decay products of two W's in the reaction $e^+e^- \to W^+W^- \to q_1\overline{q}_2Q_1\overline{Q}_2$ at LEP2. This would be important e.g. for a precision measurement of the W mass.

1.1 Introduction

High energy reactions, e.g. e^+e^--annihilation, are generally described in terms of two phases: First a short time perturbative phase with large momentum transfers, described in terms of quarks and gluons. This initial phase is described by a parton cascade. Secondly a long time soft interaction phase, in which the energy of the partons is transformed into hadrons. This non-perturbative hadronization phase is successfully described by a string model [1] or a cluster model [2]. These two phases are generally assumed to be well separated from each other. The parton cascade has a cutoff of the order 0.5–1GeV corresponding to a timescale of 0.2–0.4fm, while the hadronization time often is assumed to be 1–2fm. It is believed that the reaction cross section is fully determined by the perturbative phase, while in the soft hadronization phase a definite hadron state is chosen with total probability 1.

In both phases a set of approximations is used, where the number of colours is assumed to be large. Assuming infinitely many colours reduces the possible interference effects. Only planar diagrams contribute in the perturbative cascade, and the way to connect the partons by a string or cluster chain becomes unique. A specific colour charge has to be connected to a parton with the corresponding anti-colour, and with infinitely many colours the probability that two (or more) partons have the same colour is zero.

With only three colours, as in Nature, this is no longer the case. The basic problem is that the direct correspondence between the parton states and the string states (or cluster chains) is lost. The parton state is determined by the momenta, polarization and colour of all the quarks and gluons. This is not enough to describe the true states in QCD. Also some topological quantum numbers have to be specified, related to the vacuum condensate and the confinement mechanism. 't Hooft has proposed that these extra quantum numbers correspond to gauge singularities similar to the ones appearing in a superconductor [3]. In the string model they correspond to the string topology; the string state is specified by the momenta carried by the string ends (quarks and anti-quarks) and by the corners (gluons), together with a specification of how they are connected.

The most simple example is shown in Fig. 1.1. With two red quarks and two anti-red anti-quarks there are two different possible string states. The string configuration is in principle an observable (reflected in the momenta of the final state hadrons), which corresponds to excitations in the vacuum condensate. When the coloured partons move apart, the confinement mechanism must give a response in the condensate, such that a particular string state is selected. This selection cannot be determined from perturbative QCD, because the distinction between the two string states in Fig. 1.1b does not correspond to any observable related to the parton state in Fig. 1.1a.

The fact that the present models work so well, indicates that these effects

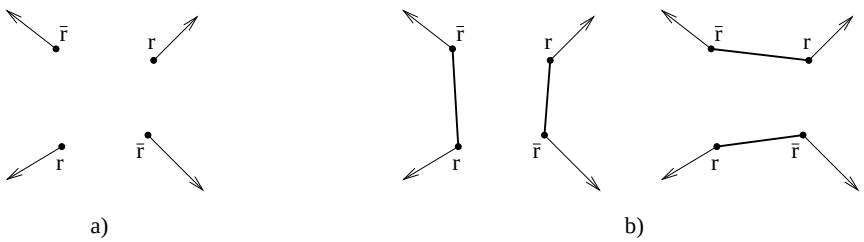

Figure 1.1: When two red and two anti-red colour charges move apart they can be connected by strings or cluster chains in two ways.

are usually small. They are generally of the order $1/N_c^2$, which corresponds to the probability that two gluons have the same colour. They are nevertheless of fundamental importance for our understanding of the confinement mechanism. What determines the response of vacuum to the produced partons, and what is the time scale of the "interface" between the hard and the soft phases? When identical parton charges allow several state topologies, is one topology chosen at random or is some configuration dynamically favoured? Connected to these problems are colour suppressed contributions to the perturbative parton cascade, related to non planar diagrams.

As the problems cannot be solved by perturbative QCD we have to rely on experimental measurements. Thus in this paper we want to study possible effects of the finite number of colours, and observables which are sensitive to these effects. The problem has been studied in refs [4, 5, 6, 7] in connection with the reaction $e^+e^- \to W^+W^- \to q_1\overline{q}_2q_3\overline{q}_4$[1]. At LEP2 the two $q\overline{q}$ pairs originate from points separated by about 0.1fm, which is short compared to the hadronization scale. Here we will study similar effects in the reaction $e^+e^- \to q\overline{q}$ + a number of gluons at LEP1. With few colours it is possible to obtain a gluonic subsystem, which is in a colour singlet state. This system could hadronize independently, decoupled from the remaining state (in the string model as a closed string), and we want in particular to study if it is possible to experimentally identify such gluonic colour singlets. At LEP1 the whole process starts in a single point, and a comparison of the effects in the two reactions would be very valuable.

There are three different problems we want to address in this paper:

- What can we learn about the interface between the hard and the soft phases?
- How does the confinement mechanism work when there are several ways to connect the partons by a string?

[1] In the calculations in [4] the polarization of the W's was neglected. When this is taken into account the reported signal is reduced by approximately a factor 1/2

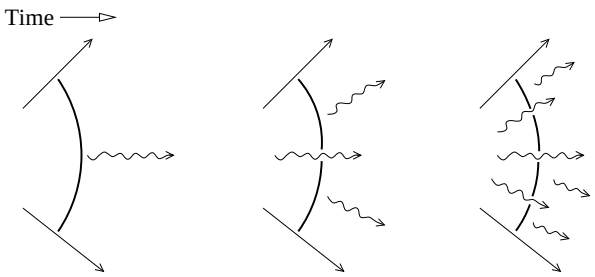

Figure 1.2: The dipole picture of a gluon cascade.

- Is it possible to find a good approximation scheme for the interference effects in the perturbative phase?

These problems will be further discussed in the following sections. The last problem is in principle solvable within perturbative QCD, but this is not the case for the other two problems. We will describe two different models and discuss how these can be experimentally tested. The effects on average event properties are generally small, but it is possible to find an observable signal for special events.

1.2 Interface Between the Hard and Soft Phases

In an e^+e^--annihilation event full perturbative calculations have been performed only to second order in α_s. This is far from sufficient to reproduce experimental data, and different approximation schemes have been developed to approximate the evolution of a parton cascade. In the dipole cascade model [8], an initial colour dipole between a quark and an anti-quark can emit a gluon and thereby split in two dipoles, which can emit further gluons in a cascade as illustrated in Fig. 1.2. The dipoles form a chain where the colour of one gluon is combined with the anti-colour of a neighbouring gluon. The colour and the corresponding anti-colour radiate coherently producing the 'dipole emission'. This effect is often called soft gluon coherence [9], and can be approximated by an angular ordering of the emitted gluons. In the large N_c limit all the dipoles have different colours, and therefore radiate independently, apart from the recoils experienced due to the emission. With only three different colours we must frequently have a situation with e.g. two red and two anti-red charges, which have to interfere in the further gluon emission. In the original dipole cascade model, implemented in the Ariadne MC [10], this interference is neglected, and also in other versions of the parton cascade, e.g. those implemented in the Herwig [11] or the Jetset [12] MC, the only interference included is the one

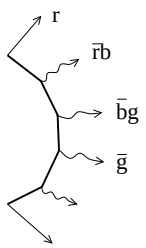

Figure 1.3: In the string model a string-like colour field is stretched from red to anti-red, from blue to anti-blue etc.

from a colour charge and the directly associated anti-charge. One approach to include interference effects, which we will discuss further below, is implemented in the latest version of Ariadne (version 4.07).

Thus in the perturbative cascade a quark-gluon state with well specified colours is produced. Via the confinement mechanism the energy of these partons is transformed into colour singlet hadrons. In the string model a string-like force field is stretched from a quark via a set of gluons to an anti-quark. Thus in the example in Fig. 1.3 the string is stretched from red to anti-red, then from blue to anti-blue etc. With many colours the string configuration corresponds exactly to the chain of dipoles, but if there are more than one red–anti-red pair there may be more than one possible way to stretch the string.

As mentioned in the introduction the string configuration appears as an observable. Even if a certain string state does not correspond uniquely to a definite hadron state, different possible string states produce usually very different hadronic states, and they can therefore be distinguished from each other. We note that in the string model also the direction of a closed string, corresponding to a purely gluonic system, is an observable (with the direction defined e.g. from colour to anti-colour). When the string breaks by the production of an $s\bar{s}$ pair the s and $\bar{s}$ are pulled in opposite directions, which implies a rapidity separation between e.g. a final state K and $\overline{\mathrm{K}}$. This means that e.g. the decay $\Upsilon \to 3g$ can give two differently oriented string loops, which cannot be separated by perturbation theory [13].

Thus the string or cluster chain configuration is an observable, which is not fully determined by the partonic state of coloured quarks and gluons, and the confinement mechanism has to imply that a certain configuration is selected. At which stage in the process is this configuration fixed? Is this fixation purely in the hadronization phase, or does it also affect the initial hard phase. To clarify this problem we will compare with the behaviour of a superconductor, and discuss in more detail the example of Υ decay.

If the vacuum condensate behaves like a type I superconductor, we expect

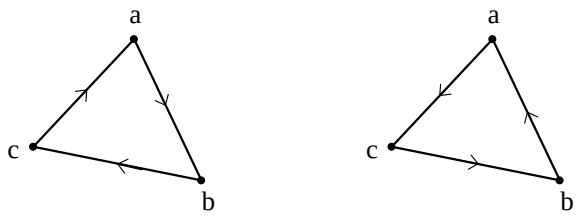

Figure 1.4: Two different string configurations are possible in the decay $\Upsilon \to 3g$. The direction of the string is defined as going from colour to anti-colour.

that the bag model is a good representation of the confinement mechanism, and the string should be more regarded as a flux tube with a radius of the order of 1fm. It is then natural to expect that the topology of the string or cluster chain is not determined until the partons are separated by a similar distance, and that this process is totally separated from the perturbative cascade.

If on the other hand vacuum is more like a type II superconductor the string would be more similar to a vortex line, where the energy is concentrated to a thin core, although the field can be smeared out over a larger region. We can then imagine that the topology is fixed at an earlier stage when the parton separation is of the order of the core radius. In this case the mechanism which determines the string configuration could possibly also affect the early hard phase of the reaction.

As an example let us study the reaction $\Upsilon \to 3g$. The decay amplitude is proportional to the colour factor

$$\frac{1}{2}d^{abc} = \mathrm{Tr}\left[\mathrm{T}^a\mathrm{T}^b\mathrm{T}^c\right] + \mathrm{Tr}\left[\mathrm{T}^c\mathrm{T}^b\mathrm{T}^a\right] \equiv A + B \tag{1.1}$$

where a, b, and c are the colours of the three gluons. The two terms correspond to different orientations of the string (see Fig. 1.4). In the large N_c limit the two amplitudes are orthogonal, and the cross section for the two different string states is given by the colour factors (obtained by summing over all colours)

$$\sum |A|^2 = \sum |B|^2 = \frac{(N_c^2-1)(N_c^2-2)}{8N_c^2} \tag{1.2}$$

For finite N_c there is however also an interference term

$$\sum AB^\dagger = -\frac{N_c^2-1}{4N_c} \tag{1.3}$$

which corresponds to a part of the cross section, for which the orientation of the final state is not determined. An example is when all three gluons

are $r\overline{r}$. Although formally of order $1/N_c^2$ this part is clearly not small; it is negative and for three colours it is a fraction $2/(N_c^2-4) = 40\%$ of the total cross section. Since the two states in Fig. 1.4 are eigenstates to an observable with different eigenvalues, the full amplitudes have to be orthogonal. If the topology is fixed at an early stage of the process, it could conceivably interfere with the perturbative phase and thus influence the cross section [13]. If this would imply that the interference term should be neglected in a calculation of the cross section, a determination of α_s to fit experimental data would give a smaller value, not in agreement with α_s measurements at higher energies [14]. Although not a proof, this is at least an indication that the string configuration is determined at a later stage well separated from the initial hard process, which determines the cross section.

Thus, if the string topology is not determined in the hard phase we must face the following problem: Sometimes the initial perturbative process produces a state with several identical colour charges moving apart. What mechanism selects a specific final state topology? Is the topology chosen at random among those which are possible, or is some topology dynamically favoured? In the next section we will discuss some conceivable models.

1.3 Models

1.3.1 The Hadronization Phase

We first want to discuss a model (called the soft reconnection model) in which the perturbative cascade is unchanged, and only the hadronization phase is modified. Let us assume that the perturbative phase has resulted in a set of partons with colour charges as shown in Fig. 1.5a. These charges can be connected by a string (or cluster chain) in different ways as illustrated in Fig. 1.5b–d. As discussed above we do not know if Nature chooses one configuration at random, or if some particular configuration is dynamically favoured. The same problem is studied in [4, 5, 6, 7] in connection with the reaction $\mathrm{e^+e^-} \to \mathrm{W^+W^-} \to \mathrm{q_1\overline{q}_2q_3\overline{q}_4}$. As in ref. [4] we will here study a model where the confinement mechanism preferentially connects a colour with a corresponding anti-colour in the neighbourhood. This implies that "short" string configurations should be favoured, and to decide what is a "short string" we will, as in [4], use the λ measure defined in [15]. This measure corresponds to an "effective rapidity length" , and is closely correlated to the hadronic multiplicity. For hard gluons it is approximately given by $\lambda \approx \sum \ln\left[(p_i + p_{i+1})^2/m_0^2\right]$ where p_i are the (ordered) parton momenta and the hadronic mass scale m_0 is around 1GeV.

Assume that the ordering in Fig. 1.5b is the one generated in the hard phase. Then the configuration in Fig. 1.5c is possible provided the gluons numbered 1

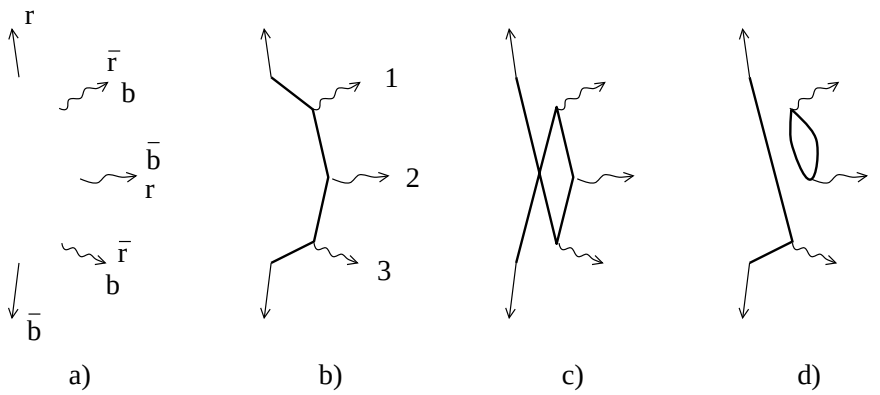

Figure 1.5: The partons in a) can be connected in three different ways as in b), c), and d).

and 3 have identical colours. Similarly the configuration in Fig. 1.5d is possible if the colour of gluon 1 corresponds to the anti-colour of gluon 2. As there are 8 different gluon colours, these possibilities appear in general with probability 1/8. The SU(3) colour algebra will be discussed further in Section 1.4, but the basic property of our model is that a possible colour recoupling of the partons, which results in a smaller value for the λ measure, will be chosen with a probability 1/8. (One constraint is that two or more gluons, which form an isolated colour singlet system as in Fig. 1.5d, must not originate from a single colour octet gluon.)

The possibility to connect the partons as in Fig. 1.5c or 1.5d is often called colour reconnection or recoupling. This is actually an improper terminology. The partons have not been *re*connected. They did not start connected as in Fig. 1.5b, and colour connection would be a better term. This is similar to the use of the term recombination time for the time when electrons and protons first combine to neutral atoms after the Big Bang.

1.3.2 The Hard Phase

In a second model also the hard perturbative phase is modified. In principle this phase is calculable within perturbative QCD. This is not possible in practise, and as mentioned above, in most parton cascade models all non-planar diagrams are neglected. (An exception is the latest version of Ariadne, which we will comment on further below.) This means that essentially only interference effects from e.g. a red and its adjacent anti-red charge in the same dipole is included. Assume that two r$\bar{\text{r}}$ pairs are produced. In principle they would

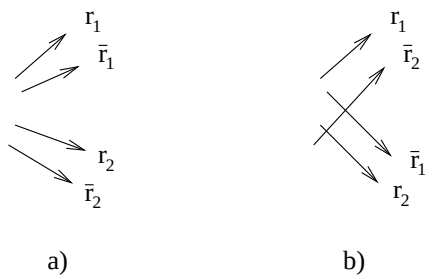

Figure 1.6: a) Usually a colour charge and its associated anti-colour are close in phase space. b) Occasionally a red charge can be closer to an anti-red charge from a different pair.

emit further soft gluons as a quadrupole. In most cases the two partners in one dipole are close in phase space, and therefore appears as a neutral object when viewed from the other dipole, as illustrated in Fig. 1.6a. In these cases the neglected interference between the dipoles should be small. Occasionally this is not true, and the situation can look as in Fig. 1.6b. Here a better approximation would be to include interference within the pairs $r_1\overline{r}_2$ and $r_2\overline{r}_1$, but neglect the interference between these pairs. This means that the emission of softer gluons can correspond to a different ordering of the charges in the dipole chain.

Since a proper inclusion of the interference effects is too complicated, we want to study a rather simple model, assuming that this model can give information about possible qualitative features and the expected order of magnitude of the effects. In the parton cascade it can happen that the colour charges can be arranged in a dipole chain in different ways. In the model we assume that in such cases the emission of softer gluons is better approximated if we reorder the gluons, so that the charges in the dipoles are as close in phase space as possible. As a measure, when we compare two different orderings, we also here use the λ measure discussed above.

As in the soft reconnection model the possibility to have identical gluon colours is taken into account by allowing the reconnection with probability 1/8, if it provides a smaller λ measure.

Thus, at every step in the cascade we check if the gluon chain should be reordered. The colour reconnection of the gluons should be relevant for the emission of softer gluons later in the cascade. The Landau-Pomeranchuk formation time in a gluon emission is related to its transverse momentum, and therefore it is essential that the transverse momentum is used as an ordering parameter in the cascade. For this reason the dipole cascade model, implemented in Ariadne, is particularly convenient, and we will use a modification

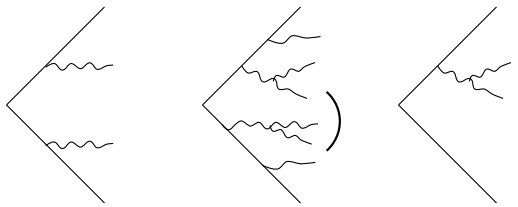

Figure 1.7: a) A pair of gluons emitted from (anti-)quark legs are in a colour singlet state with probability $1/\left[N_c^2-1\right] = 1/8$. b) This is also approximately the case for any connected gluon sub-system. c) An exception is two or more gluons originating from a single gluon parent. Such a system is naturally always a colour octet.

of this program, in spite of the problems discussed below.

A model in which reconnection can occur *both* in the hard phase and in the soft phase will in the following be called the cascade reconnection model.

1.4 Colour Structures and Mother-daughter Relations

1.4.1 Colour Structures

We are particularly interested in the presence of isolated gluonic systems, as in Fig. 1.5d, because such states can possibly be experimentally identified. Such an isolated system must clearly form a colour singlet state. A gluon pair produced as in Fig. 1.7a is a colour singlet with probability $1/(N_c^2-1)$. This is also approximately the case for any connected gluon system, as e.g. the one in Fig. 1.7b. (We note that with 5 gluons, which is the average number in Ariadne at the Z^0-pole, we have 10 different connected gluon systems. If all of these would have the probability 1/8 to form an isolated gluonic system, such systems would not be rare.)

An exception is two or more gluons originating from a single initial gluon as in Fig. 1.7c. Such a system is always a colour octet. Thus it is essential to know if a gluon is emitted by a parent quark or a parent gluon. This is no problem in the cascade schemes implemented in the Herwig or the Jetset MC's. However, in the dipole cascade model a gluon is not emitted from a single parent, but is the result of the separation of a colour charge and anti-charge in a colour dipole. Furthermore colour coherence implies that a gluon

emitted from a dipole between two parent gluons can be effectively emitted from a parent quark (i.e. colour triplet) charge.

This problem was studied in [16] and some results will be discussed in the next subsection. The colour factor for gluon emission from a quark is $C_F = \frac{1}{2}N_c\left[1 - 1/N_c^2\right]$, which is slightly less than half the corresponding factor for emission from a gluon (which is connected to two dipoles), $C_A = N_c$. The aim of ref. [16] was to study how to take into account this colour suppressed contribution to the cascade evolution, but the results can be used also for our purpose analysing the mother-daughter relation.

1.4.2 Mother-daughter Relations in the Dipole Cascade Model

A $q\overline{q}$ pair produced in an e^+e^--annihilation event emits gluons according to the distribution

$$dn = C_F \frac{\alpha_s}{2\pi} \frac{x_1^2 + x_3^2}{(1-x_1)(1-x_3)} dx_1 dx_3 \tag{1.4}$$

where x_1 and x_3 are the conventional scaled quark and anti-quark momenta. For soft gluons this approximately equals the "dipole distribution"

$$dn \approx C_F \frac{\alpha_s}{\pi} d\left[\ln k_\perp^2\right] dy \tag{1.5}$$

where

$$\begin{aligned} k_\perp^2 &= s(1-x_1)(1-x_3) \\ y &= \frac{1}{2}\ln\frac{1-x_3}{1-x_1} \end{aligned} \tag{1.6}$$

The phase space available is approximately a triangular region, $|y| < \frac{1}{2}\left[\ln s - \ln k_\perp^2\right]$, in the $y - \ln k_\perp^2$-plane, cf. Fig. 1.8a.

For the emission of two gluons the hardest one is distributed according to eq. (1.4) or (1.5), while the distribution of the softer gluon corresponds to two independent dipoles spanned between the quark and the gluon and between the gluon and the anti-quark respectively. For fixed $k_{\perp 2}$ of the second gluon, the available rapidity range in the two dipoles is $\ln\left(s_{qg_1}/k_{\perp 2}^2\right)$ and $\ln\left(s_{g_1\overline{q}}/k_{\perp 2}^2\right)$, which results in a total rapidity interval

$$\Delta y = \ln\frac{s_{qg_1}}{k_{\perp 2}^2} + \ln\frac{s_{g_1\overline{q}}}{k_{\perp 2}^2} = \ln\frac{s}{k_{\perp 2}^2} + \ln\frac{k_{\perp 1}^2}{k_{\perp 2}^2}. \tag{1.7}$$

Thus the available phase space for the second gluon is increased and corresponds to the folded surface in Fig. 1.8b. Here the two dipoles correspond

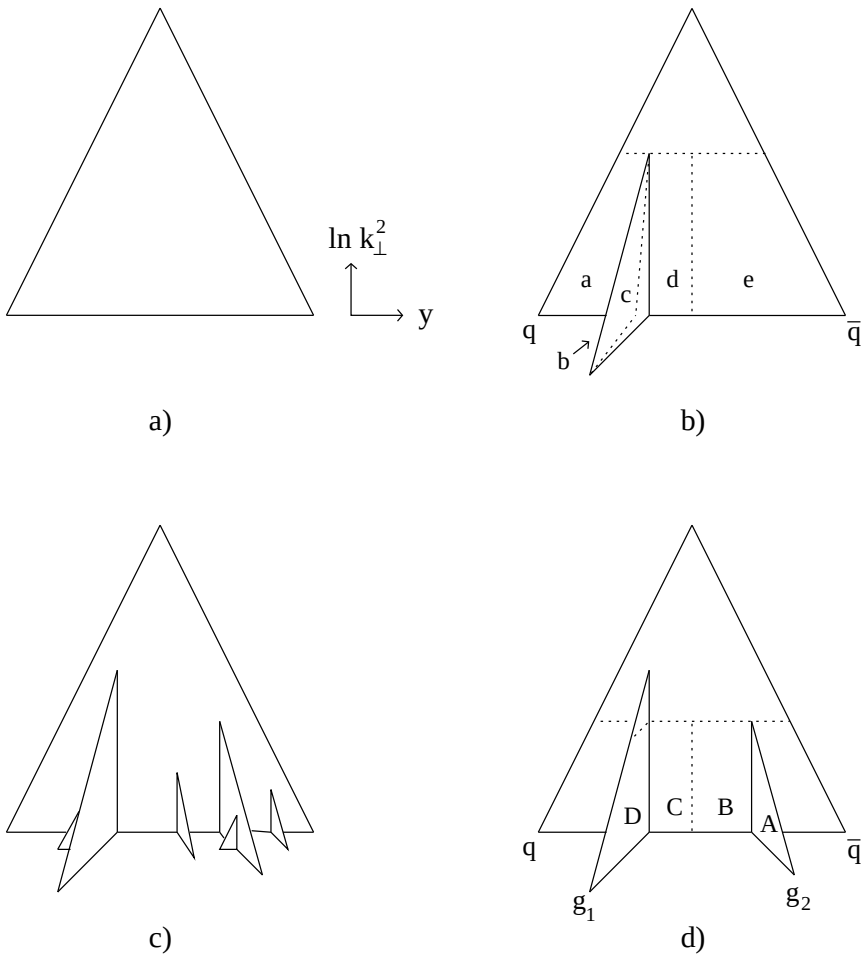

Figure 1.8: a) The phase space for gluon emission from a q$\overline{\text{q}}$ pair is approximately a triangular region in the $y - \ln k_\perp^2$ plane. b) If one gluon is emitted the size of the phase space for emission of softer gluons corresponds to this folded surface. c) Every gluon emission increase the phase space for softer gluons producing a multi-fractal total phase space. d) Gluon emission associated with surfaces B and C corresponds to emission from an effective quark or an anti-quark charge (triplet or anti-triplet).

to the surfaces a+b and c+d+e respectively. The emission density in the two dipoles is proportional to $C_A/2$, but there is also a correction term with a

relative weight $-1/N_c^2$ corresponding to a dipole between the quark and the anti-quark [17]. The result is a density proportional to $C_A/2$ on surfaces b and c and proportional to $C_F = \frac{1}{2}C_A\left[1 - 1/N_c^2\right]$ on surfaces a, d and e. Thus we see that surfaces b and c correspond to emission from the gluon charges (note that this area is determined by the transverse momentum $k_{\perp 1}$ of the first gluon; in the infinite momentum frame this corresponds to the energy times the emission angle) while surfaces a, d and e correspond to emission from a quark (or anti-quark) charge. Here e.g. surfaces a and e can be interpreted as emitted from the quark and the anti-quark. In surface d the quark and the gluon emit coherently as a single triplet charge, due to the soft gluon interference.

In a similar way the emission of a third gluon corresponds to three dipoles etc. Each emission increases the phase space for softer gluons as leading to a multi-fractal structure illustrated in Fig. 1.8c [15]. Consider in particular the emission from a $q\overline{q}g_1g_2$ system as shown in Fig. 1.8d. Here surfaces A, B, C and D correspond to emissions from the dipole between the two gluons. In the same way as above surfaces A and D correspond to emissions from parent gluons, with density $C_A/2$, while in surface C the quark and gluon g_1 emit coherently as a triplet (quark) charge with density C_F. Similarly in surface B the anti-quark and g_2 emit coherently as an anti-triplet charge.

Finally we have to discuss how to associate an emitted gluon (with momentum k) to one of the surfaces in Fig. 1.8d. Assume that the gluon is emitted from the dipole between the gluons g_1 and g_2. Thus it belongs to one of the surfaces A, B, C, or D. We first separate surface A from B+C+D. We then imagine a dipole between gluon g_2 and an effective quark, with momentum $\overline{p}_q + \overline{p}_{g_1} \equiv \overline{P}$. Make a Lorentz boost along $\overline{P}$ such that the momentum $\overline{p}'_{g_2}$ of g_2 in the new frame becomes orthogonal to $\overline{P}$. If the momentum $\overline{k}'$ of the new gluon in this frame is closer to $\overline{p}'_{g_2}$ than to $\overline{P}$ the new gluon should be associated to surface A, otherwise with surface B+C+D. (With closer we mean that the relative angle is smaller.) In the same way we can decide whether the new gluon belongs to surface D or to A+B+C. If it belongs to neither A nor D, it obviously belongs to B+C, and thus is emitted by an effective colour triplet charge. This recipe can obviously be used also for a system with an arbitrary number of gluons.

1.5 MC Implementation

The models presented in Sections 1.3.1 and 1.3.2 are implemented in a modified version of the Ariadne MC. In the "cascade reconnection model" we check after each emission if a reconnection involving the new gluon can give a smaller λ measure. If that is the case this configuration will be used with probability 1/8 in the continuation of the cascade. An exception is when two or more gluons originate from a single parent gluon. Such a system must be a colour

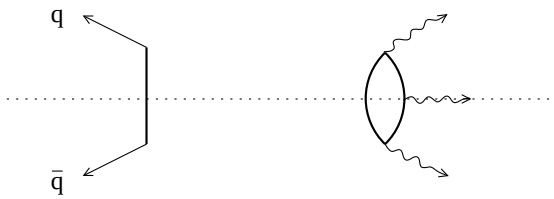

Figure 1.9: We are particularly interested in situations where an isolated gluon system moves away from the remaining system, which may result in a central gap in the hadron distribution.

octet and is therefore not allowed to be separated from the rest of the state. For this reason we keep track of the history of all emissions, as described in Section 1.4.2[2].

In the model where reconnection is only allowed after the perturbative phase (the soft reconnection model) there are generally many gluons and many reconnection possibilities. The probability that a certain reconnection should isolate a gluon system originating from a single gluon parent is therefore very small, and has here been neglected in the MC implementation.

With an implementation of the mother-daughter relation into the MC it is possible to also include the colour suppressed contributions to the emission probabilities. Thus in the MC the emission from an "effective" (anti-)quark charge is suppressed by the factor $2C_F/C_A = 1 - 1/N_c^2$. We have, however, not found any observable which is sensitive to this correction. The effect is small, and can generally be compensated by a retuning of the parameters in the fragmentation model.

1.6 Results

The modifications caused by the colour reconnections are generally small and not observable in average event properties. As in [4] we also here try to find a small corner of phase space, where effects could be visible. The events we want to study are those where an isolated gluon system is moving away from the remaining system, as illustrated in Fig. 1.9. Such states could reveal themselves by a central gap in the rapidity distribution (cf. also ref. [18]).

To know that we have a quark and an anti-quark moving to one side we consider double tagged events with either a $b\overline{b}$ or a $c\overline{c}$ pair. To obtain a sufficient separation between the two parts in Fig. 1.9 we have studied events

[2]A similar reconnection model is developed by Lönnblad and implemented in Ariadne version 4.07. In this model, however, all emissions from a gg dipole are treated as having a gluon parent. Therefore the reconnection effects become smaller than in our calculations.

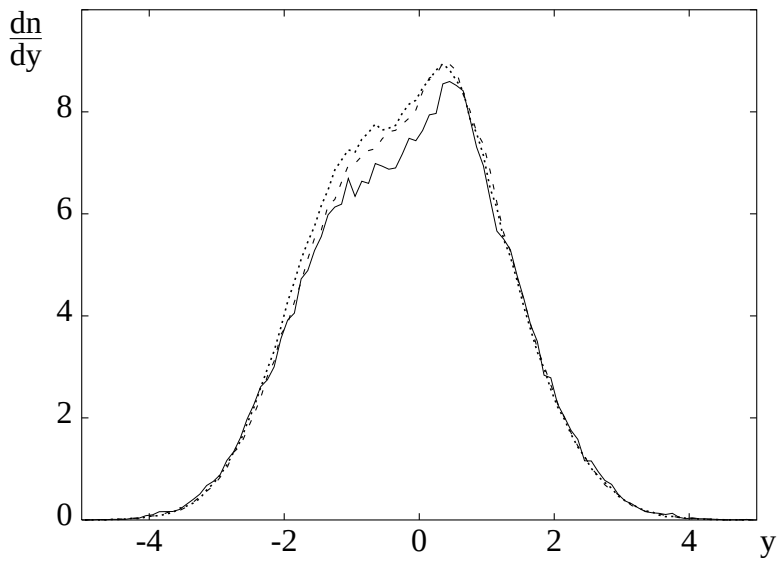

Figure 1.10: Rapidity distribution of charged particles, default Ariadne (dotted line), the soft reconnection model (dashed line), and the cascade reconnection model (solid line). Both models are retuned i.e. for average events they reproduce the expected distributions. One million Z^0 decay events are analyzed. The rapidity is measured along the direction of the added $q\overline{q}$ momenta.

where the angle between the quark and the anti-quark is less than 110°, and the rapidity axis is chosen along the sum of their momenta. In Fig. 1.10 we show the rapidity distribution obtained in the different models; normal Ariadne, the soft connection model, and the cascade reconnection model. Here positive y-values are in the direction of the $q\overline{q}$ pair. The different Monte Carlo's are tuned to reproduce experimental data. We see a dip in the distributions from the reconnection models as compared to normal Ariadne. This difference could be a signal of non trivial effects early in the event.

The difference between the models is enhanced if we study, as in ref. [4], the probability to find an event with no charged particles in a central rapidity interval. Choosing the central rapidity region between -1 and 0 we obtain the distributions in Fig. 1.11, and we see significant difference between the distributions. It is 7 times more probable to find an event with no particles in the central rapidity bin in the cascade reconnection model as compared to normal Ariadne (in the soft reconnection model this factor becomes 3.5). In Fig. 1.11 we see that there is also quite a large difference in the probability to

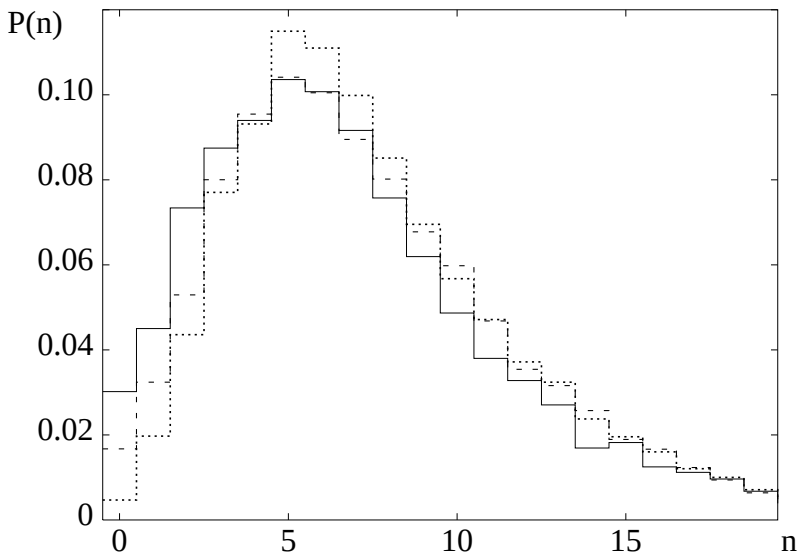

Figure 1.11: Charged multiplicity in the rapidity interval [-1,0], default Ariadne (dotted line), the soft reconnection model (dashed line), and the cascade reconnection model (solid line). Both our models are retuned. The distribution is normalized w.r.t. accepted events.

find events with only 1 or 2 charged particles in the central rapidity bin.

With the probabilities from Fig. 1.11 we can calculate the number of events to be expected to have no charged particles in the central rapidity bin. The results for 3 million Z events at LEP1, assuming 10% double tagging efficiency of the initial heavy quarks, are shown in the table below

Model	Number of events with n_{ch} 0	1	2	Total number of accepted events
Cascade reconnection	103	154	229	32700
Soft reconnection	62	130	220	37700
Background (normal Ariadne)	17	73	162	37100

Table 1.1: Expected number of events with 0, 1, or 2 charged particles in a rapidity interval $-1 < y < 0$. Total events is the number of events which are left after the condition that the angle between the $c\overline{c}$ or $b\overline{b}$ momenta should be less than 110°.

1.7 Conclusions

We have a very limited knowledge about how the confinement mechanism works in processes like $e^+e^- \to q\overline{q}g\ldots g$, when there are several identical colour charges. The transition from a Feynman diagram to a string configuration or a cluster chain is not straight forward, as the partons can be connected in several different ways. We do not know if in such a situation Nature chooses a particular configuration at random, or if some configuration is dynamically favoured. The choice of a configuration which differs from the one initially obtained in the generation procedure is often called colour reconnection or recoupling, although the partons have not been connected before, and thus should not be called reconnected.

Also in the perturbative parton cascade we have no well founded recipe for describing the interference effects, which correspond to non-planar diagrams and are caused by identical colour charges. Although these effects are in principle calculable within perturbative QCD, this is at present not possible in practice.

To learn more about how the confinement mechanism and the interference effects work, we have studied two different models. In these models it is assumed that configurations, where the confining string connects partons which are close in phase space, are dynamically favoured.

We are in particular interested in the possibility that a colour singlet gluon system hadronizes isolated from the remainder of the state. A possible signal for such events is a central rapidity gap in events where the angle between the quark and the anti-quark is relatively small. Using double tagged events with heavy $c\overline{c}$ or $b\overline{b}$ quarks, with a relative angle less than 110°, it is possible to find a significant signal, if such events appear in Nature.

If this type of (re)connected states appear in Z decays it may also be an indication that reconnection might appear between the decay products of two W's in the reaction $e^+e^- \to W^+W^- \to q_1\overline{q}_2Q_1\overline{Q}_2$ at LEP2. This would be important e.g. for a precision measurement of the W mass.

Acknowledgments
We would like to thank dr L. Lönnblad and dr T. Sjöstrand for valuable discussions.

References

[1] B. Andersson, G. Gustafson, G. Ingelman, and T. Sjöstrand, *Phys. Rep.* **97** (1983) 31

[2] B.R. Webber, *Nucl. Phys.* **B238** (1984) 492
G. Marchesini, B.R. Webber, *Nucl. Phys.* **B238** (1984) 1

[3] G. 't Hooft, *Nucl. Phys.* **B190** (1981) 455

[4] G. Gustafson, and J. Häkkinen, *Z. Phys.* **C64** (1994) 659

[5] G. Gustafson, U. Pettersson, and P.M. Zerwas, *Phys. Lett.* **B290** (1988) 90

[6] T. Sjöstrand, and V. Khoze, *Z. Phys.* **C62** (1994) 291
T. Sjöstrand, and V. Khoze, *Phys. Rev. Lett.* **72** (1994) 28

[7] L. Lönnblad, CERN TH/95-218

[8] G. Gustafson, *Phys. Lett.* **B175** (1986) 453
G. Gustafson, and U. Pettersson, *Nucl. Phys.* **B306** (1988) 746
B. Andersson, G. Gustafson, L. Lönnblad, *Nucl. Phys.* **B399** (1990) 393

[9] A.H. Mueller, *Phys. Lett.* **B104** (1981) 161
B.I. Ermolaev, and V.S. Fadin, *JETP Lett.* **33** (1981) 269
A. Bassetto, M. Ciafaloni, G. Marchesini, and A.H. Mueller, *Nucl. Phys.* **B207** (1982) 189
G. Marchesini, and B. Webber, *Nucl. Phys.* **B238** (1984) 1

[10] L. Lönnblad, *Comp. Phys. Comm.* **71** (1992) 15

[11] G. Marchesini, B.R. Webber, G. Abbiendi, I.G. Knowles, M.H. Seymour, and L. Stanco, *Comp. Phys. Comm.* **67** (1992) 465

[12] T. Sjöstrand, *Comp. Phys. Comm.* **82** (1994) 74

[13] G. Gustafson, *Z. Phys.* **C15** (1982) 155

[14] See e.g. M. Schmelling, CERN-PPE/95-129

[15] B. Andersson, P. Dahlqvist, and G. Gustafson, *Phys. Lett.* **B214** (1988) 604
B. Andersson, P. Dahlqvist, and G. Gustafson, *Z. Phys.* **C44** (1989) 455

[16] G. Gustafson, *Nucl. Phys.* **B392** (1993) 251

[17] Ya.I. Azimov, Yu.L. Dokshitzer, V.A. Khoze, and S.I. Troyan, *Phys. Lett.* **B165** (1985) 147

[18] J.D. Bjorken, S.J. Brodsky, and H.J. Lu, *Phys. Lett.* **B286** (1992) 153
H.J. Lu, S.J. Brodsky, and V.A. Khoze, *Phys. Lett.* **B312** (1993) 215

QCD Aspects of Leptoquark Production at HERA

Paper II

QCD Aspects of Leptoquark Production at HERA

Christer Friberg, Emanuel Norrbin and Torbjörn Sjöstrand

Department of Theoretical Physics,
Lund University, Lund, Sweden

Abstract

If a leptoquark is produced at HERA as a narrow resonance, various effects tend to broaden the measurable mass distribution considerably. These effects are discussed here, with special emphasis on initial- and final-state QCD radiation. A proper understanding is important to assess the significance of data and to devise strategies for better mass reconstruction.

Recently, the H1 and ZEUS Collaborations at HERA have presented evidence for an excess of events at large Q^2 and x [1, 2]. This could be nothing but a statistical fluke. Alternatively, it could be the first signal of the production of an s-channel resonance, a leptoquark (LQ). In order to test such a hypothesis, as further data accumulate, it is important to understand the production characteristics of an LQ at HERA. In particular, it should be noted that an expected narrow mass peak will be smeared by various physics and detector effects. In this letter we want to give a brief survey of the physics components that could contribute to this smearing, and estimate the magnitude of each of these effects. Previous studies of a similar kind have been performed with the LEGO generator [3], which is partly based on PYTHIA [4]. We also want to give some examples of how to improve the reconstruction of the LQ mass.

This is not a study on the physics implications of an LQ observation at HERA [5]. Therefore we do not discuss the origin of an LQ in terms of an underlying theory, be that compositeness, supersymmetry or anything else, but stay with a purely phenomenological description of LQ properties [6]. Even so, several options are possible, and we will restrict ourselves further. An LQ may have spin 0 or 1, with differences in the decay angular distribution, but of little importance for the considerations in this letter, so we stay with the spin 0 alternative. An LQ may have net fermion number 0 ($\mathrm{q}\overline{\ell}$ or $\overline{\mathrm{q}}\ell$) or ± 2 ($\mathrm{q}\ell$ or $\overline{\mathrm{q}}\overline{\ell}$). Given that HERA has been running with an e^+ beam in recent years, the latter kind would be disfavoured by requiring a sea antiquark from the proton. It would have been favoured in the earlier HERA runs with e^-, however, where the valence quark distributions could have been accessed. The ratio in parton distributions between valence and sea at $x \approx 0.5$ being larger than the recorded luminosity ratio $\mathrm{e}^+\mathrm{p}/\mathrm{e}^-\mathrm{p}$, the previous non-observation [7] favours LQ's with vanishing fermion number. A leptogluon scenario is not excluded, but is not favoured [8]. QCD consequences of a $\overline{\mathrm{q}}\overline{\ell}$ LQ or a leptogluon are briefly mentioned later.

Phenomenologically, the production cross section for a leptoquark in the process $\mathrm{q} + \ell^+ \to \mathrm{LQ}$ can be written as [6]

$$\sigma = \frac{\pi\lambda^2}{4s} q(x, M_{\mathrm{LQ}}^2) = k\frac{\pi^2\alpha_{\mathrm{em}}}{s} q(x, M_{\mathrm{LQ}}^2) \; . \tag{2.1}$$

Here λ gives the strength of the unknown Yukawa coupling; the alternative k parameter is normalized such that $k = 1$ corresponds to electromagnetic strength of the coupling. To first approximation $x = M_{\mathrm{LQ}}^2/s$ — corrections to this will be a main theme of the letter — and $q(x, M_{\mathrm{LQ}}^2)$ the parton distribution at a scale given by the LQ mass.

The observed handful of candidate events per experiments, for an integrated luminosity of order 15 pb^{-1} and a detection efficiency around 50% (including a cut $Q^2 > 15000$ GeV^2), would suggest a production cross section of the order

of 1 pb. For a ue^+ LQ of around 200 GeV mass this corresponds to $k \sim 0.01$. The width of a scalar LQ,

$$\Gamma_{\mathrm{LQ}} = \frac{\lambda^2}{16\pi} M_{\mathrm{LQ}} = \frac{k\alpha_{\mathrm{em}}}{4} M_{\mathrm{LQ}} \ , \tag{2.2}$$

then becomes only $\Gamma_{\mathrm{LQ}} \sim 4$ MeV. A de^+ LQ would be somewhat broader, but in either case the width is negligibly small on an experimental scale. Unless the total width is enhanced significantly by decays to exotic channels, the LQ is long-lived enough that it will form an LQ-hadron, made up of the LQ and an antiquark or a diquark.

QCD radiation of gluons and QED radiation of photons in principle can occur in the initial state, off the LQ itself, and in the final state. Including all interference terms, a complicated radiation pattern is then possible. The small width here offers a considerable simplification: interference terms and radiation off the LQ are suppressed for radiated energies above Γ_{LQ} [9, 10]. The region $E \lesssim \Gamma_{\mathrm{LQ}} \sim 10$ MeV giving a very small contribution to the total radiated energy, it is therefore sufficient to consider three main classes of corrections, (i) initial-state radiation, (ii) LQ-hadron formation, and (iii) final-state radiation. We will consider these effects one at a time, roughly in order of decreasing importance.

The main effect of final-state radiation is that the hadronic system of the LQ decay acquires a mass in excess of the naive quark one and that, as a consequence, the energy of the recoiling lepton is reduced. The jet mass phenomenology is not very different from experience in hadronic e^+e^- annihilation events. A standard parton-shower description [11] tuned to LEP data predicts an average quark jet mass of about 30 GeV at 200 GeV energy. Taking over the same formalism for the LQ decays then gives an average mass $\langle M_{\mathrm{q}} \rangle \approx 32$ GeV, Fig. 2.1, i.e. somewhat higher since the absence of a radiating final-state partner removes some phase-space competition. In a more detailed study one should include the explicit matrix-element information for the region of well-separated emission, which could introduce some modest dependence on the spin of the leptoquark.

In the rest frame of the LQ the lepton takes an energy

$$E_\ell = \frac{M_{\mathrm{LQ}}}{2} \left(1 - \frac{M_{\mathrm{q}}^2}{M_{\mathrm{LQ}}^2} \right) \ . \tag{2.3}$$

The rest-frame lepton scattering angle θ^* is only very little affected by the QCD radiation [12]. (Furthermore, for a spin 0 leptoquark, the inclusive decay distribution is isotropic in $\cos\theta^*$ in any case.) Even though the standard DIS variables do not have the traditional meaning related to a spacelike boson propagator, they can be defined purely experimentally. The M_{q} term above then propagates to give

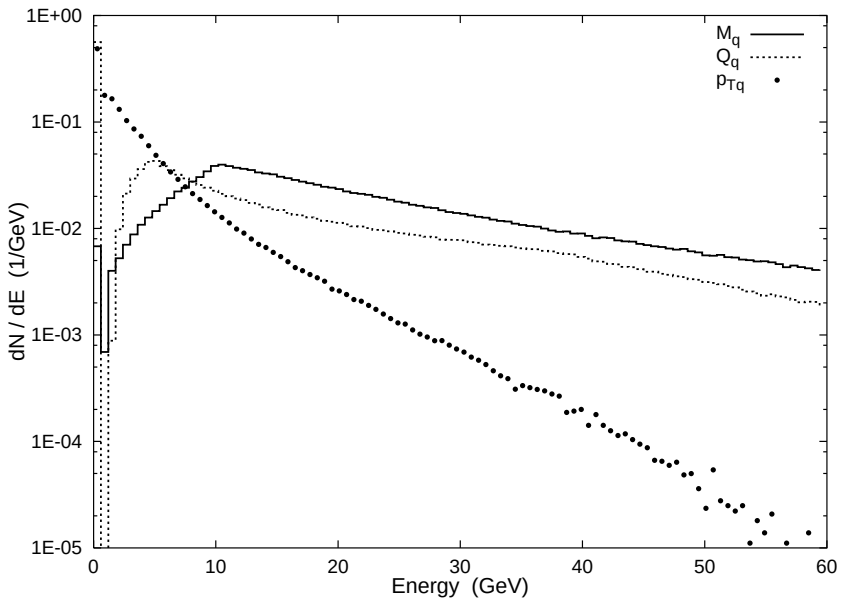

Figure 2.1: Distribution of $M_{\rm q}$ (full), $Q_{\rm q}$ (dashed) and $p_{\perp {\rm q}}$ (dots).

$$Q^2 = \frac{M_{\rm LQ}^2}{2}(1-\cos\theta^*)\left(1-\frac{M_{\rm q}^2}{M_{\rm LQ}^2}\right) , \tag{2.4}$$

$$x_{\rm Bj} = \frac{Q^2}{2Pq} = \frac{M_{\rm LQ}^2}{s}\frac{Q^2}{Q^2+M_{\rm q}^2} . \tag{2.5}$$

Defining τ to be the x value relevant for an LQ mass determination,

$$\tau \equiv \frac{\hat{s}}{s} = \frac{M_{\rm LQ}^2}{s} = x_{\rm Bj}\left(1+\frac{M_{\rm q}^2}{Q^2}\right) , \tag{2.6}$$

one finds that $\tau > x_{\rm Bj}$. In particular note that the denominator of the $M_{\rm q}$ correction factor is Q^2, not $M_{\rm LQ}^2$. This means that low-Q^2 data would not be expected to show any peak in $x_{\rm Bj}$. A typical cut $Q^2 > 15000\,{\rm GeV}^2$ reduces the $\langle M_{\rm q}\rangle$ from 32 GeV to 29 GeV (eq. (2.4)). The $\langle M_{\rm q}^2\rangle \approx 1430\,{\rm GeV}^2$ then gives an average correction factor in eq. (2.6) of somewhat above 5%. If the experimentally reconstructed LQ mass is taken to be $\sqrt{x_{\rm Bj}s}$, the original δ function is smeared as shown in Fig. 2.2. Since $Q^2 = x_{\rm Bj}ys$ is an identity that follows from

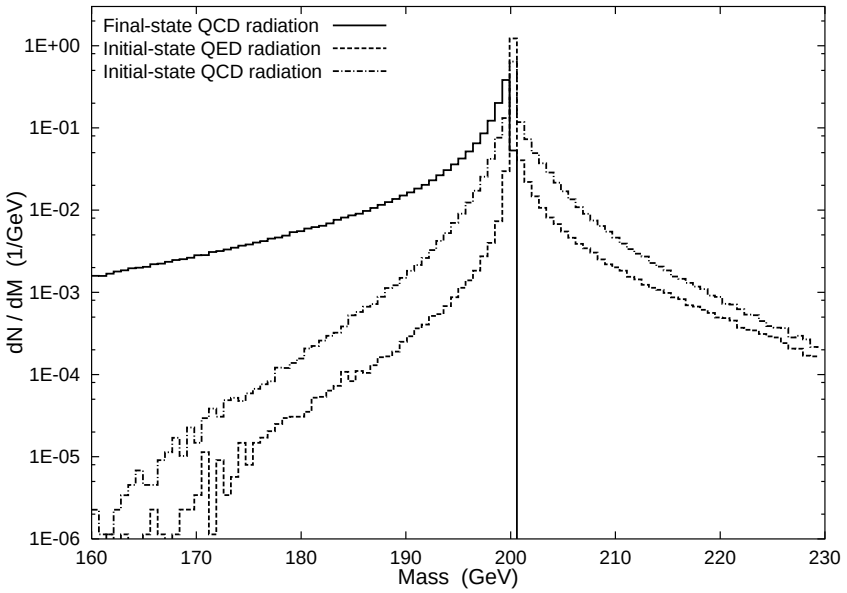

Figure 2.2: The reconstructed LQ mass distribution $m_{\rm recon} = \sqrt{x_{\rm Bj} s}$ for an input mass of 200 GeV, with a simple cut $Q^2 > 15000$ GeV^2 on the leptoquark sample. Results are shown with only one component active at a time: final-state QCD radiation (full), initial-state QED radiation off the positron (dashed) and initial-state QCD radiation (dot-dashed).

the definition of the respective variable, the alternative experimental measure $\sqrt{Q^2/y}$ gives the same smearing.

Also photons may be radiated in the final state, both from the lepton and the quark. Owing to the smaller coupling, the amount of radiation is reduced compared with the QCD case above. Radiation almost collinear with the lepton occurs at a significant rate, but is not resolved by the calorimetric definition of lepton energy and so is of little consequence. In our studies we choose not to resolve final-state photons below a 1 GeV invariant mass cut-off.

We next turn to initial-state radiation, i.e. radiation off the incoming quark and lepton lines. This reduces the longitudinal momentum fraction carried by the reacting quark/lepton, and builds up a $p_\perp$ and a spacelike virtuality for it.

Photon radiation off the lepton line is dominated by the almost collinear one. In this limit, one has that $\tau = x_{\rm q} x_\ell$, where the x_i are the respective momentum fractions. In the leading-log approximation, the positron-inside-

positron distribution is roughly [13]

$$D_{\mathrm{e}}^{\mathrm{e}}(x_\ell, M_{\mathrm{LQ}}^2) \approx \beta(1-x_\ell)^{\beta-1} \quad \text{with} \quad \beta = \frac{\alpha_{\mathrm{em}}}{\pi}\left(\ln\frac{M_{\mathrm{LQ}}^2}{m_{\mathrm{e}}^2} - 1\right) \approx 0.0575. \tag{2.7}$$

The eq. (2.1) is then modified to

$$\sigma = k\frac{\pi^2\alpha_{\mathrm{em}}}{s}\iint \mathrm{d}x_{\mathrm{q}}\,\mathrm{d}x_\ell\; q(x_{\mathrm{q}}, M_{\mathrm{LQ}}^2)\, D_{\mathrm{e}}^{\mathrm{e}}(x_\ell, M_{\mathrm{LQ}}^2)\,\delta(x_{\mathrm{q}}x_\ell - \tau)\ . \tag{2.8}$$

One obtains $\langle x_\ell\rangle \approx 0.99$ or $\langle x_{\mathrm{q}}\rangle \approx 1.01\tau$. The steep fall-off of $q(x_{\mathrm{q}}, M_{\mathrm{LQ}}^2)$ dampens the tail to large $1-x_\ell$. Therefore typical experimental cuts on photon energy lost in the beam pipe do not make a big difference. The relation between the true and reconstructed masses is

$$\tau = x_{\mathrm{Bj}}\,\frac{x_\ell^2}{1-(1-x_\ell)/y}\ , \tag{2.9}$$

so the mass shift may be in either direction, Fig. 2.2.

Radiation of photons and gluons in the initial state leads to a buildup of spacelike virtualities and transverse momenta for the incoming quark and lepton. The largest effects come on the quark side, Fig. 2.1, where $\langle Q_{\mathrm{q}}\rangle \approx 14.3$ GeV and $\langle p_{\perp\mathrm{q}}\rangle \approx 3.6$ GeV, while $\langle Q_\ell\rangle \approx 0.85$ GeV and $\langle p_{\perp\ell}\rangle \approx 0.15$ GeV for the incoming positron, using the spacelike parton-shower formalism of [14]. (Numbers vary a bit depending on choice of parton distribution parametrizations etc.) The spacelike virtualities can be seen as a kinematical consequence of the $p_\perp$ kicks, so the $Q_{\mathrm{q}(\ell)}$ and $p_{\perp\mathrm{q}(\ell)}$ are strongly correlated. Note that $\langle Q_{\mathrm{q}}^2\rangle \ll M_{\mathrm{q}}^2$: spacelike parton-shower evolution is constrained by the limited phase space and the steeply falling parton distributions at large x. That is, the probability that the daughter quark at x_i comes from the branching of a mother quark at $x_{i-1} > x_i$ is related to the ratio $q(x_{i-1})/q(x_i)$ of parton distributions, and the integral of $q(x_{i-1})$ over $x_{i-1} > x_i$ is small. At each branching one has $p_{\perp i}^2 \approx (1-z_i)Q_i^2$, with $z_i = x_i/x_{i-1}$, so from the argument above it is clear why also $\langle p_{\perp\mathrm{q}}^2\rangle \ll \langle Q_{\mathrm{q}}^2\rangle$.

The consequences of nonzero virtualities and transverse momenta can again be traced through the standard DIS variables. Also including the previous effects, i.e. $M_{\mathrm{q}} \neq 0$ and $x_\ell \neq 0$, gives the relation

$$\begin{aligned} \tau &= \frac{b - 2aQ_{\mathrm{q}}^2 + \sqrt{b^2 - 4ax_\ell Q^2\left(Q_{\mathrm{q}}^2 - p_{\perp\mathrm{q}}^2\right)}}{2sa}\ , \\ \text{where}\quad a &= 1 - \frac{1-y}{x_\ell} \\ \text{and}\quad b &= x_\ell Q^2 + M_{\mathrm{q}}^2 + Q_{\mathrm{q}}^2 - 2\overline{p}_{\perp\mathrm{q}}\overline{k}'_\perp\ . \end{aligned} \tag{2.10}$$

(A correction formula in terms of another set of variables is found in [3].) The spacelike virtuality and $p_\perp$ kick may either increase or decrease the estimated LQ mass. In particular, there is an explicit dependence on the azimuthal angle between the $p_{\perp \mathrm{q}}$ of the incoming quark (= $p_{\perp \mathrm{LQ}}$ in this approximation) and the $k'_\perp$ of the outgoing lepton. The resulting spread in reconstructed LQ mass is shown in Fig. 2.2.

A $p_{\perp \mathrm{q}}$ contribution is also given by the primordial $k_\perp$ of the parton-shower initiator inside the proton. This primordial $k_\perp$ is some combination of Fermi motion and initial-state radiation below the soft cut-off of the simulation program. A typical scale for the former would be $\langle k_\perp^2 \rangle \approx 0.25$ GeV^2, but even if this is increased to 1 GeV^2 the net effects are quite negligible, since the $k_\perp$ is added to the much larger $p_\perp$ of the perturbative parton shower. Only in some future study of the LQ $p_\perp$ distribution itself would the low-$p_{\perp \mathrm{LQ}}$ tail be sensitive to the choice.

The effects of LQ-hadron formation are not large, since the LQ is so massive that its motion is not significantly affected by hadronization effects. Data on b and c quarks are consistent with a non-perturbative fragmentation where the LQ-hadron retains an average fraction

$$z \approx \frac{M_{\mathrm{LQ}}}{M_{\mathrm{LQ}} + 1 \text{ GeV}} \approx 0.995 \tag{2.11}$$

of the original LQ momentum, cf. [15]. The antiquark (diquark) contributes a typical fragmentation $p_\perp$ to the net $p_\perp$ of the LQ-hadron. The LQ has some Fermi motion inside the LQ-hadron, of the order of the antiquark constituent mass, that shifts the momentum of the decaying LQ. The net effects of all the hadronization contributions should be a more-or-less random momentum shift at or below the 1 GeV scale, i.e. negligible. A consequence of confinement is that the LQ mass cannot be defined unambiguously, so the detailed effects of hadronization have to be seen in the context of some specific scheme for relating the LQ-hadron mass to the LQ mass itself.

The hadronic system will show some effects of the LQ lifetime. If an LQ-hadron is formed, the hadrons produced from the proton remnant and the initial-state-radiation partons decouple completely from those produced in the decay of the LQ-hadron. This means, e.g., that the charged multiplicity is independent of the LQ decay angle, i.e. of Q^2 (apart from some small trigger-bias effects). By contrast, if the LQ is too short-lived for LQ-hadron formation, the initial- and final-state partons are connected into a common colour string [16]. The string length and hence the multiplicity now depends on the angle between the proton remnant and the LQ hadronic decay products (just like in standard DIS processes, with $W^2 \propto Q^2$ for fixed x_{Bj}). If the initial- and final-state shower effects are neglected, the variation at small Q^2 is significant, but is reduced to $\sim 10\%$ in the $Q^2 > 15000$ GeV^2 region. When showers are

included, however, these tend to dominate the particle production characteristics in a global sense. A memory remains in the soft (low-momentum) region, e.g. defined by $|\mathbf{p}| < \mathbf{1}$ GeV in the longitudinal rest frame of the LQ. (The lab frame is unsuitable, since the LQ motion in this frame introduces large spurious effects.) Over the standard high-Q^2 range, and with full inclusion of parton showers, the variation in charged multiplicity is here over 20%. In the unlikely event that the LQ is very short-lived, coherence effects will also appear in the parton-shower stage, and so the multiplicity variation will spread to all $|\mathbf{p}| \lesssim \Gamma_{\mathrm{LQ}}$. It is therefore possible to conclude from the hadronic final state whether an LQ-hadron is being formed or not, given enough statistics. This situation is quite similar to the one for the top quark [10].

All the physics aspects described above are included in the PYTHIA event generator [4].[1] The net distribution of reconstructed LQ masses is shown in Fig. 2.3, where all effects described above have been included. The bulk of the mass spread is given by the effects in eq. (2.10). After correction with this formula, the remaining mass spread is the result of the $k_\perp$ kick and virtuality of the incoming lepton, the QED radiation off the outgoing lepton, and LQ-hadron formation.

A $\overline{\mathrm{q}}\overline{\ell}$ LQ would share most of the features described above. There is enhanced initial-state QCD radiation in those events where a branching chain $\mathrm{q} \to \mathrm{qg}, \mathrm{g} \to \mathrm{q}\overline{\mathrm{q}}$ occurs. However, most events start with a $\overline{\mathrm{q}}$ at the cut-off scale $Q_0 \approx 1$ GeV, and here gluon radiation off the $\overline{\mathrm{q}}$ is suppressed by the steeply falling $\overline{q}(x)$ distribution. That is, parton-shower histories that allow a $\overline{\mathrm{q}}$ to survive at large x and large Q^2 are biased towards lower activity (a bit more than those of the q), and so the $\langle Q_{\overline{\mathrm{q}}} \rangle \approx 12.4$ GeV rather than the 14.3 GeV of the q. For a leptogluon, an increased radiation in the final state follows directly from the higher colour charge, $\langle M_{\mathrm{g}} \rangle \approx 45$ GeV. In the initial state, there is again a suppression from the steeply falling gluon distribution. About half of the events contain a branching step $\mathrm{q} \to \mathrm{qg}$, and this branching is biased towards higher virtualities since the quark line below the branching scale radiates less than the gluon above. The net result is a fairly large mean, $\langle Q_{\mathrm{g}} \rangle \approx 31$ GeV. A leptogluon would hence give a higher hadronic multiplicity than an LQ.

So far we have concentrated exclusively on one method for LQ mass reconstruction, based on the measurement of the scattered positron (Q^2, x_{Bj} and y). Alternative methods are used by the H1 and ZEUS collaborations. However, they all share some common assumptions, such as massless partons and $p_\perp$ balance between the scattered positron and the recoiling hadronic system, and therefore do not recover the bulk of the smearing effects noted above. The op-

[1] LQ-hadron formation is not part of the standard distribution. Note that `MSTJ(50)=0` and `MSTP(67)=0` should be set to switch off interference between the initial- and final-state radiation.

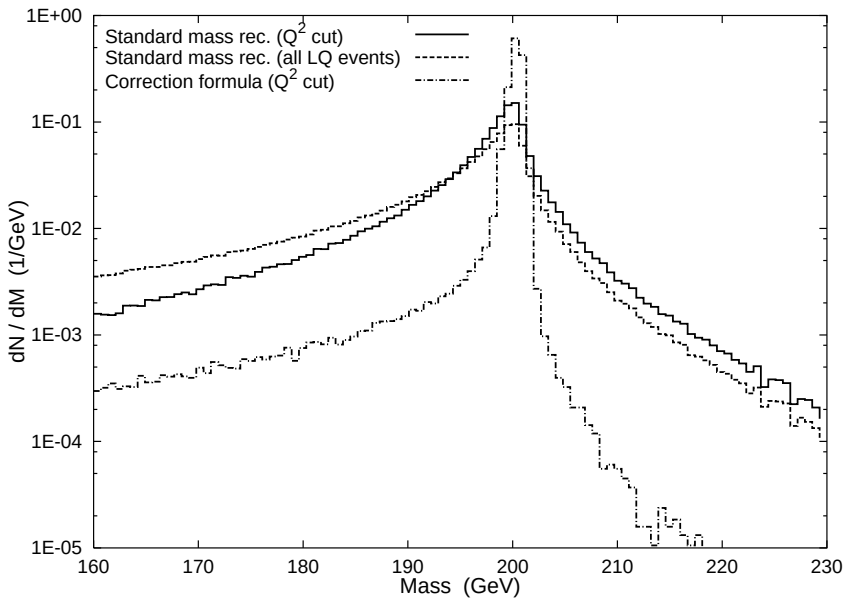

Figure 2.3: The reconstructed LQ mass distribution for an input mass of 200 GeV: all LQ events with $m_{\rm recon} = \sqrt{x_{\rm Bj} s}$ (dashed), $Q^2 > 15000$ GeV^2 with $m_{\rm recon} = \sqrt{x_{\rm Bj} s}$ (full) and $Q^2 > 15000$ GeV^2 with $m_{\rm recon} = \sqrt{\tau s}$, eq. (2.10) (dot-dashed).

timal way to reconstruct a narrow(er) mass peak clearly is detector-dependent, and so must be worked out by the experimental collaborations. We here want to give some very general comments, however.

With an ideal detector, and good separation between the LQ decay products and the hadrons from the proton beam remnant, the four-momentum of the LQ could be reconstructed to give the LQ mass directly. Such an approach suffers from the calorimetric smearing of hadronic momentum measurements. Since the parton-shower activity spreads out hadrons, there is also no clean separation of hadrons. Therefore, alternatively, one could start from the better-measured positron momentum and then add corrections according to eq. (2.10), to give a mass estimate $m_{\rm recon} = \sqrt{\tau s}$. In practice, some of the required terms turn out to be rather difficult to reconstruct from the observable hadronic final state. The most feasible correction is for the final-state QCD radiation, which we have seen to be the largest individual souce of smearing, and which also tends to give a systematic bias in a mass determination. Two alternative methods have been compared for reconstructing $M_{\rm q}$. In the first, all particles

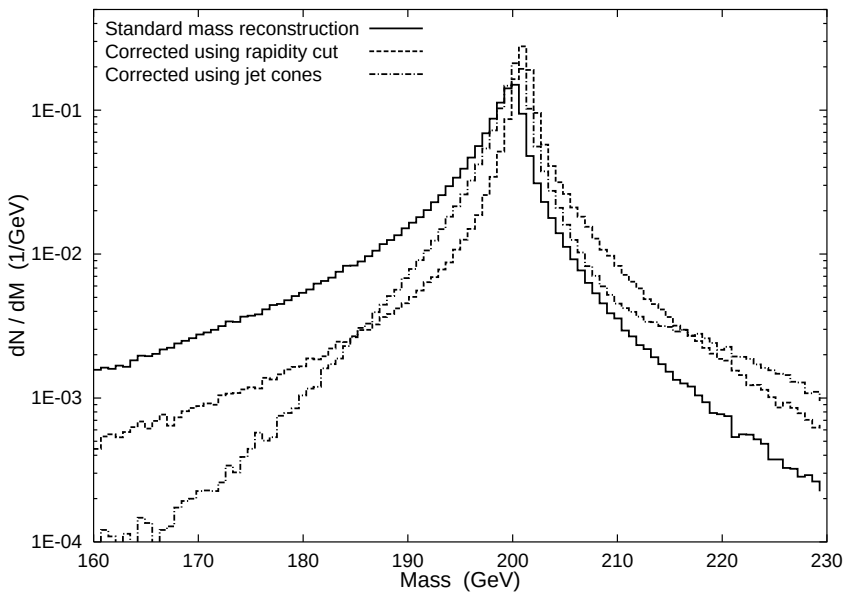

Figure 2.4: The reconstructed LQ mass distribution for an input mass of 200 GeV and with $Q^2 > 15000$ GeV^2. Curves show mass based on x_{Bj} only (full), or corrected for M_{q} either with a pseudorapidity separation (dashed) or a jet-finding strategy (dot-dashed). For details see text.

with a (pseudo)rapidity below 1.7 (except the lepton) are used to calculate an invariant mass that is associated with M_{q}. The cut is selected to minimize the misidentification of particles between the LQ-hadron and the remnant system. In the second method, a jet clustering algorithm [4] is used to find jets with an $E_\perp \geq 10$ GeV inside an $R = \sqrt{(\Delta\eta)^2 + (\Delta\varphi)^2} < 1$ cone, and an invariant mass is calculated for the particles belonging to the jet or jets. The jet threshold is here selected so that initial-state radiation is less likely to give rise to a jet. The reconstructed M_{q} is then used in eq. (2.6) to give a corrected LQ mass estimate. The distributions in Fig. 2.4 show that either correction factor does result in a narrower mass peak (the width is reduced from 11.1 to 8.2 GeV) and one that contains less systematic bias towards underestimating the correct mass (the average is shifted from 195.3 to 200.6 GeV).

In summary, we have shown that several QCD effects are at play in the production and decay of a leptoquark. These effects are fairly well understood from our experience in other areas of high-energy physics. It is therefore possible to describe in detail the production characteristics. This knowledge may be useful to obtain less biased and narrower mass peaks, and also to devise other tests that could help to distinguish between leptoquark production and ordinary DIS phenomena.

References

[1] H1 Collaboration, C. Adloff et al, DESY 97-024.

[2] ZEUS Collaboration, J. Breitweg et al, DESY 97-025.

[3] K. Rosenbauer, thesis RWTH Aachen, PITHA preprint 95/16, http://www.physik.rwth-aachen.de/group/pitha/1995/pitha1995_16.html.

[4] T. Sjöstrand, Comput. Phys. Commun. **82** (1994) 74.

[5] G. Altarelli, J. Ellis, G.F. Giudice, S. Lola and M.L. Mangano, CERN–TH/97–40;
H. Dreiner and P. Morawitz, hep–ph/9703279;
J. Kalinowski, R. Rückl, H. Spiesberger and P.M. Zerwas, DESY 97–038;
V. Barger, K. Cheung, K. Hagiwara and D. Zeppenfeld, MADPH–97–991.

[6] W. Buchmüller, R. Rückl and D. Wyler, Phys. Lett. **B191** (1987) 442.

[7] ZEUS Collaboration, M. Derrick et al, Phys. Rev. Lett. **75** (1995) 1006;
H1 Collaboration, S. Aid et al, Phys. Lett. **B379** (1996) 319.

[8] J. Bijnens, in 'Proceedings of the HERA Workshop', ed. R.D. Peccei (DESY, 1988), Vol. 2, p. 819.

[9] V.A. Khoze, L.H. Orr and W.J. Stirling, Nucl. Phys. **B378** (1992) 413;
V.S. Fadin, V.A. Khoze and A.D. Martin, Phys. Lett. **B320** (1994) 141;
T. Sjöstrand and V.A. Khoze, Z. Phys. **C62** (1994) 281.

[10] V.A. Khoze and T. Sjöstrand, Phys. Lett. **B328** (1994) 466.

[11] M. Bengtsson and T. Sjöstrand, Phys. Lett. **B185** (1987) 435;
Nucl. Phys. **B289** (1987) 810.

[12] R. Kleiss, Phys. Lett. **B180** (1986) 400.

[13] R. Kleiss et al., in 'Z^0 physics at LEP 1', eds. G. Altarelli, R. Kleiss and C. Verzegnassi, CERN 89-08 (Geneva, 1989), Vol. 3, p. 143.

[14] T. Sjöstrand, Phys. Lett. **B157** (1985) 321;
M. Bengtsson, T. Sjöstrand and M. van Zijl, Z. Phys. **C32** (1986) 67.

[15] J.D. Bjorken, Phys. Rev. **D17** (1978) 171.

[16] B. Andersson, G. Gustafson, G. Ingelman and T. Sjöstrand, Phys. Rep. **97** (1983) 31.

Jet Production by Virtual Photons

Paper III

Jet Production by Virtual Photons

Christer Friberg and Torbjörn Sjöstrand

Department of Theoretical Physics,
Lund University, Lund, Sweden

Abstract

The production of jets is studied in collisions of virtual photons, γ^*p and $\gamma^*\gamma^*$, specifically for applications at HERA and LEP2. Photon flux factors are convoluted with matrix elements involving either direct or resolved photons and, for the latter, with parton distributions of the photon. Special emphasis is put on the range of uncertainty in the modeling of the resolved component. The resulting model is compared with existing data.

3.1 Introduction

The photon is a complicated object to describe. In the DIS region, i.e. when it is very virtual, it can be considered as devoid of any internal structure, at least to first approximation. In the other extreme, the total cross section for real photons is dominated by the resolved component of the wave function, where the photon has fluctuated into a $q\overline{q}$ state. The nature of this resolved component is still not well understood, especially not the way in which it dies out with increasing photon virtuality. This dampening is likely not to be a simple function of virtuality, but to depend on the physics observable being studied, i.e. on the combination of subprocesses singled out.

Since our current understanding of QCD does not allow complete predictability, one sensible approach is to base ourselves on QCD-motivated models, where a plausible range of uncertainty can be explored. Hopefully comparisons with data may then help constrain the correct behaviour. The ultimate goal therefore clearly is to have a testable model for all aspects of the physics of γ^*p and $\gamma^*\gamma^*$ collisions. As a stepping stone towards constructing such a framework, in this paper we explore the physics associated with the production of 'high-$p_\perp$' jets in the collision. That is, we here avoid the processes that only produce activity along the γ^*p or $\gamma^*\gamma^*$ collision axis. For resolved photons this corresponds to the 'soft' or 'low-$p_\perp$' events of the hadronic physics analogy, for direct ones to the lowest-order DIS process $\gamma^*q \to q$.

The processes that we will study here instead can be exemplified by $\gamma^*\gamma^* \to q\overline{q}$ (direct), $\gamma^*g \to q\overline{q}$ (single-resolved for $\gamma^*\gamma^*$, direct for γ^*p) and $gg \to q\overline{q}$ (double-resolved for $\gamma^*\gamma^*$, (single-)resolved for γ^*p), where the gluons come from the parton content of a resolved virtual photon or from the proton. Note that these are multi-scale processes, at least involving the virtuality Q_i^2 of either photon ($i = 1, 2$) and the $p_\perp^2$ of the hard subprocess. (In $\gamma^*\gamma^*$ physics the notation P^2 is often used instead of Q^2, especially for the less virtual of the two photons; here we will use Q^2 throughout, however.) For a resolved photon, the relative transverse momentum $k_\perp$ of the initial $\gamma^* \to q\overline{q}$ branching provides a further scale, at least in our framework. This plethora of scales clearly is a challenge to any model builder, but in principle it also offers the opportunity to explore QCD in a more differential fashion than is normally possible.

At large photon virtualities, a possible strategy would be to express the cross sections entirely in terms of processes involving the photon directly, i.e. to include branchings such as $\gamma^* \to q'\overline{q}'$ and $q' \to q'g$ in the Feynman graphs calculated to describe the process, so that e.g. the γ^*p process $gg \to q\overline{q}$ is calculated as $\gamma^*g \to q'\overline{q}'q\overline{q}$. With decreasing virtuality of the photon, such a fixed-order approach is increasingly deficient by its lack of the large logarithmic corrections generated by collinear and soft gluon emission, however. Furthermore, almost real photons allow long-lived $\gamma^* \to q\overline{q}$ fluctuations, that then take on the properties of non-perturbative hadronic states, specifically of vec-

tor mesons such as the ρ^0. It is therefore that an effective description in terms of parton distributions becomes necessary. Hence the resolved component of the photon, as opposed to the direct one.

That such a subdivision is more than a technical construct is excellently illustrated by the x_γ^{obs} plots from HERA [1]. This variable sums up the fraction of the original photon light-cone momentum carried by the two highest-$E_\perp$ jets. A clear two-component structure is visible. The peak close to $x_\gamma^{\mathrm{obs}} = 1$ can be viewed as a smeared footprint of the direct photon, with all the energy partaking in the hard interaction, while the broad spectrum at lower x_γ^{obs} is consistent with the resolved photon, where much of the energy remains in a beam jet. The distinction between the two is not unique when higher-order effects are included, but it is always possible to make a functional separation that avoids double-counting or gaps.

The resolved photon can be further subdivided into low-virtuality fluctuations, which then are of a nonperturbative character and can be represented by a set of vector mesons, and high-virtuality ones that are describable by perturbative $\gamma^* \to \mathrm{q\overline{q}}$ branchings. The former is called the VMD (vector meson dominance) component and the latter the anomalous one. The parton distributions of the VMD component are unknown from first principles, and thus have to be based on reasonable ansätze, while the anomalous ones are perturbatively predictable. This separation is more ambiguous and less well tested than the one between direct and resolved photons. In principle, studies on the structure of the beam remnant, e.g. its $p_\perp$ distribution, should show characteristic patterns. Unfortunately, the naively expected differences are smeared by higher-order QCD corrections (especially initial-state radiation), by the possibility of multiple parton–parton interactions, by hadronization effects, and so on. (Experimentally, gaps in the detector acceptance, e.g. for the beam pipe, is a further major worry.) Many of these areas offer interesting challenges in their own right; e.g. the way in which multiple interactions die out with virtuality, both that of the photon itself and that of the $\mathrm{q\overline{q}}$ pair it fluctuates to. Models for one aspect at the time are therefore likely to be inadequate. Instead we here attempt a combined description of all the relevant physics topics.

The traditional tool for handling such complex issues is the Monte Carlo approach. Our starting point is the model for real photons [2] and the parton distribution parameterizations of real and virtual photons [3] already present in the PYTHIA [4] generator. Several further additions and modifications have been made to model virtual photons, as will be described in the following. Other generators with an overlapping scope include, among others, HERWIG [5], LDC [6], LEPTO [7], PHOJET [8] and RAPGAP [9]. The details of the approaches are different, however, so this gives healthy possibilities to compare and learn. Another alternative is provided by matrix-element calculations [10], that do not provide the same complete overview but can offer superior

descriptions for some purposes.

The plan of this paper is the following. In section 2 the model is described, with special emphasis on those aspects that are new compared with the corresponding description for real photons. Thereafter, in section 3, the dependence of simple observables on model parameters is illustrated. Comparisons are shown with some sets of data from ep and e^+e^- colliders, and this is used to constrain partly the freedom in the model. Based on this experience, some further observables are then proposed and studied, to help shed light on the nature of the virtual photon. Finally, section 4 contains a summary and outlook.

3.2 The Model

The electromagnetic field surrounding a moving electron can be viewed as a flux of photons. Weizsäcker [11] and Williams [12] calculated the spectrum of these photons, neglecting the photon virtualities and terms involving the longitudinal polarization of photons. This approximation is well-known [13] to be a good approximation when the scattered lepton is tagged at small scattering angles.

In the equivalent photon approximation [14], the cross sections for the processes $\mathrm{ep} \to \mathrm{e}\mathbf{X}$ and $\mathrm{ee} \to \mathrm{ee}\mathbf{X}$, where $\mathbf{X}$ is an arbitrary final state, can then be written as the convolutions

$$\mathrm{d}\sigma(\mathrm{ep} \to \mathrm{e}\mathbf{X}) = \int \frac{\mathrm{d}\omega}{\omega}\, N(\omega)\, \mathrm{d}\sigma(\gamma\mathrm{p} \to \mathbf{X}) \tag{3.1}$$

and

$$\mathrm{d}\sigma(\mathrm{ee} \to \mathrm{ee}\mathbf{X}) = \iint \frac{\mathrm{d}\omega_1}{\omega_1}\frac{\mathrm{d}\omega_2}{\omega_2}\, N(\omega_1)N(\omega_2)\, \mathrm{d}\sigma(\gamma\gamma \to \mathbf{X})\ , \tag{3.2}$$

where ω is the energy of the emitted photon. In this approximation, the distribution in photon frequencies $N(\omega)\mathrm{d}\omega/\omega$ is obtained by integrating over the photon virtuality Q^2. The maximum value $Q^2_{\max}$ is usually given by experimental conditions like anti-tagging, i.e. that the scattered lepton is not detected if its scattering angle is too small.

A better approximation, and the one used in our approach, is to keep the Q^2 dependence in the photon flux $f(y, Q^2)$ (with $y \approx \omega/\omega_{\max}$, see below) and in the subprocess cross sections involving the virtual photon(s), $\gamma^*\mathrm{p} \to \mathbf{X}$ and $\gamma^*\gamma^* \to \mathbf{X}$, and to sum over the transverse and longitudinal photon polarizations. Equations (3.1) and (3.2) then modify to

$$\mathrm{d}\sigma(\mathrm{ep} \to \mathrm{e}\mathbf{X}) = \sum_{\xi=\mathrm{T,L}} \iint \mathrm{d}y\, \mathrm{d}Q^2\, f^{\xi}_{\gamma/\mathrm{e}}(y, Q^2)\, \mathrm{d}\sigma(\gamma^*_{\xi}\mathrm{p} \to \mathbf{X}) \tag{3.3}$$

and

$$\begin{aligned} \mathrm{d}\sigma(\mathrm{ee} \to \mathrm{ee}\mathbf{X}) = \sum_{\xi_1,\xi_2=\mathrm{T,L}} \iiiint \mathrm{d}y_1\, \mathrm{d}Q_1^2\, \mathrm{d}y_2\, \mathrm{d}Q_2^2 \times \\ \times\, f_{\gamma/\mathrm{e}}^{\xi_1}(y_1,Q_1^2) f_{\gamma/\mathrm{e}}^{\xi_2}(y_2,Q_2^2)\; \mathrm{d}\sigma(\gamma_{\xi_1}^* \gamma_{\xi_2}^* \to \mathbf{X}) \; . \end{aligned} \tag{3.4}$$

For ep events, this factorized ansatz is perfectly general, so long as azimuthal distributions in the final state are not studied in detail. In $\mathrm{e^+e^-}$ events, it is not a good approximation when the virtualities Q_1^2 and Q_2^2 of both photons become of the order of the squared invariant mass W^2 of the colliding photons [15]. In this region the cross section have terms that depend on the relative azimuthal angle of the scattered leptons, and the transverse and longitudinal polarizations are non-trivially mixed. However, these terms are of order $Q_1^2 Q_2^2/W^2$ and can be neglected whenever at least one of the photons has low virtuality compared to W^2.

3.2.1 The Photon Flux

When Q^2/W^2 is small, one can derive [16, 14, 15]

$$f_{\gamma/l}^{\mathrm{T}}(y,Q^2) = \frac{\alpha_{\mathrm{em}}}{2\pi}\left(\frac{1+(1-y)^2}{y}\frac{1}{Q^2} - \frac{2m_l^2 y}{Q^4}\right) \; , \tag{3.5}$$

$$f_{\gamma/l}^{\mathrm{L}}(y,Q^2) = \frac{\alpha_{\mathrm{em}}}{2\pi}\frac{2(1-y)}{y}\frac{1}{Q^2} \; , \tag{3.6}$$

where $l = \mathrm{e}^{\pm}$, $\mu^{\pm}$ or $\tau^{\pm}$. In $f_{\gamma/l}^{\mathrm{T}}$ the second term, proportional to m_l^2/Q^4, is not leading log and is therefore often omitted. Clearly it is irrelevant at large Q^2, but around the lower cut-off Q_{min}^2 it significantly dampens the small-y rise of the first term. Overall, under realistic conditions, it reduces event rates by 5–10% [15, 17].

The y variable is defined as the light-cone fraction the photon takes of the incoming lepton momentum. For instance, for l^+l^- events, Fig. 3.1,

$$y_i = \frac{q_i k_j}{k_i k_j} \; , \qquad j = 2(1) \text{ for } i = 1(2) \; . \tag{3.7}$$

Alternatively, the energy fraction the photon takes in the rest frame of the collision can be used,

$$x_i = \frac{q_i (k_1+k_2)}{k_i (k_1+k_2)} \; , \qquad i = 1,2 \; . \tag{3.8}$$

The two are simply related,

$$y_i = x_i + \frac{Q_i^2}{s} \; , \tag{3.9}$$

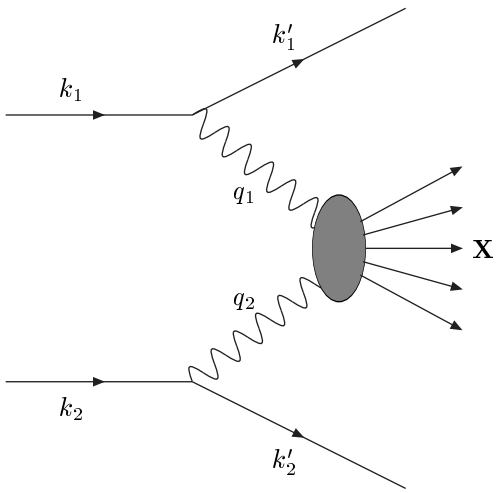

Figure 3.1: Schematic figure of $\gamma\gamma$ processes, illustrating the notation.

with $s = (k_1 + k_2)^2$. (Here and in the following formulae we have omitted the lepton and hadron mass terms when it is not of importance for the argumentation.) Since the Jacobian $\mathrm{d}(y_i, Q_i^2)/\mathrm{d}(x_i, Q_i^2) = 1$, either variable would be an equally valid choice for covering the phase space. Small x_i values will be of less interest for us, since they lead to small W^2 and hence no high-$p_\perp$ jet production, so $y_i/x_i \approx 1$ except in the high-Q^2 tail, and often the two are used interchangeably. Unless special Q^2 cuts are imposed, cross sections obtained with $f_{\gamma/l}^{\mathrm{T,L}}(x, Q^2)\,\mathrm{d}x$ rather than $f_{\gamma/l}^{\mathrm{T,L}}(y, Q^2)\,\mathrm{d}y$ differ only at the per mil level. For comparisons with experimental cuts, it is sometimes relevant to know which of the two is being used in an analysis.

In the ep kinematics, the x and y definitions give that

$$W^2 = xs = ys - Q^2 \ . \tag{3.10}$$

The W^2 expression for l^+l^- is more complicated, especially because of the dependence on the relative azimuthal angle of the scattered leptons, $\varphi_{12} = \varphi_1 - \varphi_2$:

$$\begin{aligned} W^2 &= x_1 x_2 s + \frac{2Q_1^2 Q_2^2}{s} - 2\sqrt{1 - x_1 - \frac{Q_1^2}{s}}\sqrt{1 - x_2 - \frac{Q_2^2}{s}} Q_1 Q_2 \cos\varphi_{12} \\ &= y_1 y_2 s - Q_1^2 - Q_2^2 + \frac{Q_1^2 Q_2^2}{s} - 2\sqrt{1 - y_1}\sqrt{1 - y_2} Q_1 Q_2 \cos\varphi_{12} \ . \end{aligned} \tag{3.11}$$

The lepton scattering angle θ_i is related to Q_i^2 as

$$Q_i^2 = \frac{x_i^2}{1-x_i} m_i^2 + (1-x_i)\left(s - \frac{2}{(1-x_i)^2} m_i^2 - 2m_j^2\right) \sin^2(\theta_i/2)\,, \qquad (3.12)$$

with $m_i^2 = k_i^2 = {k'}_i^2$ and terms of $O(m^4)$ neglected. The kinematical limits thus are

$$(Q_i^2)_{\min} \approx \frac{x_i^2}{1-x_i} m_i^2\,, \qquad (3.13)$$

$$(Q_i^2)_{\max} \approx (1-x_i)s\,, \qquad (3.14)$$

unless experimental conditions reduce the θ_i ranges.

In summary, we will allow the possibility of experimental cuts in the x_i, y_i, Q_i^2, θ_i and W^2 variables. Within the allowed region, the phase space is Monte Carlo sampled according to $\prod_i (\mathrm{d}Q_i^2/Q_i^2)\,(\mathrm{d}x_i/x_i)\,\mathrm{d}\varphi_i$, with the remaining flux factors combined with the cross section factors to give the event weight used for eventual acceptance or rejection.

3.2.2 Photon Processes

The hard-scattering processes are classified according to whether one or both photons are resolved. For completeness we here quote some of the less familiar cross sections.

For the direct process $\gamma^*\gamma^* \to \mathrm{f}\overline{\mathrm{f}}$, f some fermion, the cross sections are [18]

$$\frac{\mathrm{d}\sigma_{\mathrm{TT}}}{\mathrm{d}\hat{t}} = 2\pi\alpha_{\mathrm{em}}^2 N_{\mathrm{f}} e_{\mathrm{f}}^4 \frac{\hat{t}\hat{u} - Q_1^2Q_2^2}{\lambda^2\hat{t}^2\hat{u}^2} \times$$
$$\times \left\{(\hat{t}^2+\hat{u}^2)\,[1-2F(1-F)] - 2Q_1^2Q_2^2F^2\right\}\,, \qquad (3.15)$$

$$\frac{\mathrm{d}\sigma_{\mathrm{TL}}}{\mathrm{d}\hat{t}} = 8\pi\alpha_{\mathrm{em}}^2 N_{\mathrm{f}} e_{\mathrm{f}}^4 \frac{Q_2^2\hat{s}}{\lambda^4\hat{t}^2\hat{u}^2} \times$$
$$\times \left\{2(\hat{t}\hat{u} - Q_1^2Q_2^2)\left[\hat{t}\hat{u} + \frac{Q_1^2\hat{s}(\hat{t}-\hat{u})^2}{\lambda^2}\right] + Q_1^4(\hat{t}-\hat{u})^2\right\}\,, \qquad (3.16)$$

$$\frac{\mathrm{d}\sigma_{\mathrm{LT}}}{\mathrm{d}\hat{t}} = \frac{\mathrm{d}\sigma_{\mathrm{TL}}}{\mathrm{d}\hat{t}}(Q_1^2 \leftrightarrow Q_2^2)\,, \qquad (3.17)$$

$$\frac{\mathrm{d}\sigma_{\mathrm{LL}}}{\mathrm{d}\hat{t}} = 32\pi\alpha_{\mathrm{em}}^2 N_{\mathrm{f}} e_{\mathrm{f}}^4 \frac{Q_1^2Q_2^2\hat{s}^2}{\lambda^6\hat{t}^2\hat{u}^2} \cdot (\hat{t}\hat{u} - Q_1^2Q_2^2)(\hat{t}-\hat{u})^2\,, \qquad (3.18)$$

with $\hat{s} = W^2$,

$$\lambda = \sqrt{(\hat{s}+Q_1^2+Q_2^2)^2 - 4Q_1^2Q_2^2}\,, \qquad (3.19)$$

$$F = \frac{\hat{s}(\hat{s}+Q_1^2+Q_2^2)}{\lambda^2}\,, \qquad (3.20)$$

e_f the electrical charge and N_f the colour factor, 3 for a quark and 1 for a lepton. Remember that $\hat{s} + \hat{t} + \hat{u} = -Q_1^2 - Q_2^2$, neglecting the fermion mass. Note that the cross section for a longitudinal photon vanishes as Q_i^2 in the limit $Q_i^2 \to 0$.

For a resolved photon, the photon virtuality scale is included in the arguments of the parton distribution but, in the spirit of the parton model, the virtuality of the parton inside the photon is not included in the matrix elements. Neither is the possibility of the partons being in longitudinally polarized photons (see below, however). The same subprocess cross sections can therefore be used for direct $\gamma^*\mathrm{p}$ processes and for single-resolved $\gamma^*\gamma^*$ ones. For $\gamma^*\mathrm{q} \to \mathrm{gq}$ one obtains [19]

$$\frac{\mathrm{d}\hat{\sigma}_\mathrm{T}}{\mathrm{d}\hat{t}} = \frac{8}{3}\pi\alpha_\mathrm{s}\alpha_\mathrm{em}e_\mathrm{q}^2 \frac{1}{(\hat{s}+Q_1^2)^2}\left\{\frac{\hat{s}^2+\hat{u}^2-2Q_1^2\hat{t}}{-\hat{s}\hat{u}} - \frac{2Q_1^2\hat{t}}{(\hat{s}+Q_1^2)^2}\right\}, \quad (3.21)$$

$$\frac{\mathrm{d}\hat{\sigma}_\mathrm{L}}{\mathrm{d}\hat{t}} = \frac{8}{3}\pi\alpha_\mathrm{s}\alpha_\mathrm{em}e_\mathrm{q}^2 \frac{-4Q_1^2\hat{t}}{(\hat{s}+Q_1^2)^4}, \quad (3.22)$$

and for $\gamma^*\mathrm{g} \to \mathrm{q\overline{q}}$

$$\frac{\mathrm{d}\hat{\sigma}_\mathrm{T}}{\mathrm{d}\hat{t}} = \pi\alpha_\mathrm{s}\alpha_\mathrm{em}e_\mathrm{q}^2 \frac{1}{(\hat{s}+Q_1^2)^2}\frac{\hat{t}^2+\hat{u}^2}{\hat{t}\hat{u}}\left[1 - \frac{2Q_1^2\hat{s}}{(\hat{s}+Q_1^2)^2}\right], \quad (3.23)$$

$$\frac{\mathrm{d}\hat{\sigma}_\mathrm{L}}{\mathrm{d}\hat{t}} = \pi\alpha_\mathrm{s}\alpha_\mathrm{em}e_\mathrm{q}^2 \frac{8Q_1^2\hat{s}}{(\hat{s}+Q_1^2)^4}. \quad (3.24)$$

Convolution with parton distributions gives

$$\mathrm{d}\sigma(\gamma^*\mathrm{p} \to \mathbf{X}) = \iint \mathrm{d}\hat{x}_2\,\mathrm{d}\hat{t}\, f_i^\mathrm{p}(\hat{x}_2,\mu^2)\,\frac{\mathrm{d}\hat{\sigma}}{\mathrm{d}\hat{t}}(\hat{s}=\hat{x}_2W^2), \quad (3.25)$$

$$\mathrm{d}\sigma(\gamma^*\gamma^* \to \mathbf{X}) = \iint \mathrm{d}\hat{x}_2\,\mathrm{d}\hat{t}\, f_i^{\gamma^*}(\hat{x}_2,\mu^2,Q_2^2)\,\frac{\mathrm{d}\hat{\sigma}}{\mathrm{d}\hat{t}}(\hat{s}=\hat{x}_2W^2), \quad (3.26)$$

where μ^2 is the scale of the hard-scattering subprocess.

Finally we come to resolved processes in $\gamma^*\mathrm{p}$ and doubly-resolved ones in $\gamma^*\gamma^*$. There are six basic QCD cross sections, $\mathrm{qq}' \to \mathrm{qq}'$, $\mathrm{q\overline{q}} \to \mathrm{q'\overline{q}'}$, $\mathrm{q\overline{q}} \to \mathrm{gg}$, $\mathrm{qg} \to \mathrm{qg}$, $\mathrm{gg} \to \mathrm{gg}$ and $\mathrm{gg} \to \mathrm{q\overline{q}}$. Since again parton virtualities are not included, these are the expressions familiar from pp physics [20] and are not

listed here. Again a convolution with parton distributions is necessary,

$$\begin{aligned} \mathrm{d}\sigma(\gamma^*\mathrm{p} \to \mathbf{X}) &= \iiint \mathrm{d}\hat{x}_1\,\mathrm{d}\hat{x}_2\,\mathrm{d}\hat{t}\ \times \\ &\times\ f_i^{\gamma^*}(\hat{x}_1,\mu^2,Q_1^2)\, f_j^{\mathrm{p}}(\hat{x}_2,\mu^2)\,\frac{\mathrm{d}\hat{\sigma}}{\mathrm{d}\hat{t}}(\hat{s}=\hat{x}_1\hat{x}_2W^2)\,, \qquad (3.27) \\ \mathrm{d}\sigma(\gamma^*\gamma^* \to \mathbf{X}) &= \iiint \mathrm{d}\hat{x}_1\,\mathrm{d}\hat{x}_2\,\mathrm{d}\hat{t}\ \times \\ &\times\ f_i^{\gamma^*}(\hat{x}_1,\mu^2,Q_1^2)\, f_j^{\gamma^*}(\hat{x}_2,\mu^2,Q_2^2)\,\frac{\mathrm{d}\hat{\sigma}}{\mathrm{d}\hat{t}}(\hat{s}=\hat{x}_1\hat{x}_2W^2)\,. \qquad (3.28) \end{aligned}$$

In line with the neglect of parton masses, also the $\hat{s}$ expression for $\gamma^*\gamma^*$ is simpler than its W^2 analogue in eq. (3.11). When initial-state radiation is subsequently included, both transverse momenta and spacelike parton virtualities are generated, but in such a way that the relation $\hat{s} = \hat{x}_1\hat{x}_2W^2$ is maintained [21]. Differences between alternative $\hat{s}$ definitions being subleading, they are beyond our standard QCD accuracy.

3.2.3 Parton Distributions

One major element of model dependence enters via the choice of parton distributions for a resolved virtual photon. These distributions contain a hadronic component that is not perturbatively calculable. It is therefore necessary to parameterize the solution with input from experimental data, which mainly is available for (almost) real photons. In the following we will use the SaS distributions [3], which are the ones best suited for our formalism. Another set of distributions is provided by GRS [22], while a simpler recipe for suppression factors relative to real photons has been proposed by DG [23].

The SaS distributions for a real photon can be written as

$$\begin{aligned} f_a^{\gamma}(x,\mu^2) = &\sum_V \frac{4\pi\alpha_{\mathrm{em}}}{f_V^2} f_a^{\gamma,V}(x,\mu^2;Q_0^2) + \\ &+ \frac{\alpha_{\mathrm{em}}}{2\pi}\sum_{\mathrm{q}} 2e_{\mathrm{q}}^2 \int_{Q_0^2}^{\mu^2} \frac{\mathrm{d}k^2}{k^2}\, f_a^{\gamma,\mathrm{q}\overline{\mathrm{q}}}(x,\mu^2;k^2)\,. \end{aligned} \qquad (3.29)$$

Here the sum is over a set of vector mesons $V = \rho^0, \omega, \phi, \mathrm{J}/\psi$ according to a vector-meson-dominance ansatz for low-virtuality fluctuations of the photon, with experimentally determined couplings $4\pi\alpha_{\mathrm{em}}/f_V^2$. The higher-virtuality, perturbative, fluctuations are represented by an integral over the virtuality k^2 and a sum over quark species. We will refer to the first part as the VMD one and the second as the anomalous one. Each component $f^{\gamma,V}$ and $f^{\gamma,\mathrm{q}\overline{\mathrm{q}}}$ obeys a unit momentum sum rule, and also obeys normal QCD evolution equations.

The $f^{\gamma,V}(x,Q_0^2)$ have to be determined by a tune to $F_2^\gamma(x,\mu^2)$ data, while $f^{\gamma,\mathrm{q}\overline{\mathrm{q}}}$ evolve from the boundary condition

$$f_a^{\gamma,\mathrm{q}\overline{\mathrm{q}}}(x,k^2;k^2) = \frac{3}{2}\left(x^2+(1-x)^2\right)\left(\delta_{a\mathrm{q}}+\delta_{a\overline{\mathrm{q}}}\right) . \tag{3.30}$$

The μ^2 dependence enter both via the evolution of each component and via the upper limit of the $\mathrm{d}k^2$ integral. It is the latter dependence that generates the so-called anomalous term of the photon distribution evolution equations, from which the terminology has been taken over for the related event class.

From the above ansatz, the extension to a virtual photon is given by the introduction of a dipole dampening factor for each component,

$$\begin{aligned} f_a^{\gamma^*}(x,\mu^2,Q^2) = &\sum_V \frac{4\pi\alpha_{\mathrm{em}}}{f_V^2}\left(\frac{m_V^2}{m_V^2+Q^2}\right)^2 f_a^{\gamma,V}(x,\mu^2;\tilde{Q}_0^2) \\ &+ \frac{\alpha_{\mathrm{em}}}{2\pi}\sum_{\mathrm{q}} 2e_{\mathrm{q}}^2 \int_{Q_0^2}^{\mu^2}\frac{\mathrm{d}k^2}{k^2}\left(\frac{k^2}{k^2+Q^2}\right)^2 f_a^{\gamma,\mathrm{q}\overline{\mathrm{q}}}(x,\mu^2;k^2) . \end{aligned} \tag{3.31}$$

Thus, with increasing Q^2, the VMD components die away faster than the anomalous ones, and within the latter the low-k^2 ones faster than the high-k^2 ones. In the VMD component, the effective evolution range is reduced by the introduction of a $\tilde{Q}_0^2 = Q_{\mathrm{int}}^2 = Q_0 Q_{\mathrm{eff}} > Q_0^2$, with

$$Q_{\mathrm{eff}}^2 = \mu^2\,\frac{Q_0^2+Q^2}{\mu^2+Q^2}\,\exp\left\{\frac{Q^2(\mu^2-Q_0^2)}{(\mu^2+Q^2)(Q_0^2+Q^2)}\right\} . \tag{3.32}$$

As a technical trick, the handling of the k^2 integral is made more tractable by replacing the dipole factor by a k^2-independent multiplicative factor and an increased lower limit Q_{int}^2 of the integral, in such a way that both the momentum sum and the average evolution range is unchanged. Finally, correction factors are introduced to ensure that $f_a^{\gamma^*}(x,\mu^2,Q^2) \to 0$ for $\mu^2 \to Q^2$: in the region $Q^2 > \mu^2$ a fixed-order perturbative description is more appropriate than the leading-log description in terms of a resolved photon. We then arrive at the so-called modified P_{int} scheme, which is the one used here.

Since the probed real photon is purely transverse, the above ansatz does not address the issue of parton distributions of the longitudinal virtual photons. One could imagine an ansatz based on longitudinally polarized vector mesons, and branchings $\gamma_{\mathrm{L}}^* \to \mathrm{q}\overline{\mathrm{q}}$, but currently no parameterization exists along these lines. We will therefore content ourselves by exploring alternatives based on applying simple multiplicative factors R to the results obtained for a resolved transverse photon. As usual, processes involving longitudinal photons should vanish in the limit $Q^2 \to 0$. To study two extremes, the region with a linear rise in Q^2 is defined either by $Q^2 < \mu^2$ or by $Q^2 < m_\rho^2$, where the former represents

the perturbative and the latter some non-perturbative scale. Also the high-Q^2 limit is not well constrained; we will compare two different alternatives, one with an asymptotic fall-off like $1/Q^2$ and another which approaches a constant ratio, both with respect to the transverse resolved photon. (Since we put $f_a^{\gamma^*}(x, \mu^2, Q^2) = 0$ for $Q^2 > \mu^2$, the R value will actually not be used for large Q^2, so the choice is not so crucial.) We therefore study the alternative ansätze

$$R_1(y, Q^2, \mu^2) = 1 + a \frac{4\mu^2 Q^2}{(\mu^2 + Q^2)^2} \frac{f_{\gamma/l}^{\mathrm{L}}(y, Q^2)}{f_{\gamma/l}^{\mathrm{T}}(y, Q^2)} , \tag{3.33}$$

$$R_2(y, Q^2, \mu^2) = 1 + a \frac{4Q^2}{(\mu^2 + Q^2)} \frac{f_{\gamma/l}^{\mathrm{L}}(y, Q^2)}{f_{\gamma/l}^{\mathrm{T}}(y, Q^2)} , \tag{3.34}$$

$$R_3(y, Q^2, \mu^2) = 1 + a \frac{4Q^2}{(m_\rho^2 + Q^2)} \frac{f_{\gamma/l}^{\mathrm{L}}(y, Q^2)}{f_{\gamma/l}^{\mathrm{T}}(y, Q^2)} \tag{3.35}$$

with $a = 1$ as main contrast to the default $a = 0$. The y dependence compensates for the difference in photon flux between transverse and longitudinal photons. R_1 and R_2 have the same onset at low Q^2 but different asymptotic behaviour; for the former case the longitudinal part vanishes and for the latter it approaches a constant (w.r.t. the transverse case). For the third case the onset is governed by a non-perturbative parameter m_ρ and it has the same asymptotic limit as R_2. In a more sophisticated treatment, presumably also the k^2 scale of the $\gamma^* \to \mathrm{q\overline{q}}$ fluctuation would enter. In double-resolved $\gamma^*\gamma^*$ events one R factor is applied for each side.

Another ambiguity is the choice of μ^2 scale in parton distributions. For a process such as $\gamma\gamma \to \mathrm{q\overline{q}}$, with real photons, conventional wisdom is that $\mu^2 = -\hat{t}$ is the proper scale in the limit $\hat{t} \to 0$, where t-channel graphs dominate the cross sections, and $\mu^2 = -\hat{u}$ in the limit $\hat{u} \to 0$. The combination $\mu^2 = \hat{t}\hat{u}/\hat{s} = p_\perp^2$ interpolates between these limits and thus is a traditional choice, sometimes multiplied by some constant factor. When the incoming (or outgoing) photons/partons are not massless, $\hat{t}\hat{u}/\hat{s} \neq p_\perp^2$. A possible generalization for a direct virtual photon, $Q_1^2 \neq 0$, is

$$\mu^2 = -\frac{\hat{t}\hat{u}}{\hat{t} + \hat{u}} = \frac{\hat{t}\hat{u}}{\hat{s} + Q_1^2} = p_\perp^2 \frac{\hat{s} + Q_1^2}{\hat{s}} . \tag{3.36}$$

For a corresponding t-channel graph involving the quark from a resolved photon, in principle the same relation should hold, with the quark virtuality $\hat{Q}_1^2$ substituting for the photon Q_1^2 one. Inside PYTHIA, however, all incoming partons are assumed massless in the selection of hard-scattering kinematics. When, later on, the $\gamma^* \to \mathrm{q\overline{q}}$ branching is included, the $\hat{s}$ and the rest-frame scattering angle are left unaffected. Thus also $p_\perp^2$ is unchanged, while $\hat{t}$ and $\hat{u}$ are not. Using the corrected values, one obtains the same final expression

as in eq. (3.36), with $\hat{Q}_1^2$ instead of Q_1^2. Kinematics provides the constraint $\hat{Q}_1^2 > x_1 Q_1^2$ at the $\gamma^* \to \mathrm{q}\overline{\mathrm{q}}$ branching. The lower bound is a rather conservative estimate of the actual value of $\hat{Q}_1^2$, however, and more typically one obtains $\hat{Q}_1^2 \approx Q_1^2$ from the $\gamma^* \to \mathrm{q}\overline{\mathrm{q}}$ branching. (Further branchings are included in the standard QCD parton-shower description. By analogy with the description of other QCD processes, we here disregard these shower virtualities.) A scale choice like in eq. (3.36) therefore should be a sensible one both for direct and resolved photons.

When both incoming photons are virtual, the relation between μ^2 and $p_\perp^2$ becomes more complicated, but in the limit that terms of order $Q_1^2 Q_2^2/\hat{s}^2$ are neglected, they simplify to

$$\mu^2 = p_\perp^2 \, \frac{\hat{s} + Q_1^2 + Q_2^2}{\hat{s}} \; . \tag{3.37}$$

This expression does not guarantee that $\mu^2 > Q_1^2 + Q_2^2$. Sometimes such an inequality is assumed [24], so in order to cover a broader range of scale choices, below we will be comparing six different alternatives. In (almost) increasing order these are

$$\mu_1^2 = p_\perp^2 \; , \tag{3.38}$$

$$\mu_2^2 = p_\perp^2 \, \frac{\hat{s} + x_1 Q_1^2 + x_2 Q_2^2}{\hat{s}} \; , \tag{3.39}$$

$$\mu_3^2 = p_\perp^2 \, \frac{\hat{s} + Q_1^2 + Q_2^2}{\hat{s}} \; , \tag{3.40}$$

$$\mu_4^2 = p_\perp^2 + \frac{Q_1^2 + Q_2^2}{2} \; , \tag{3.41}$$

$$\mu_5^2 = p_\perp^2 + Q_1^2 + Q_2^2 \; , \tag{3.42}$$

$$\mu_6^2 = 2\mu_3^2 \; . \tag{3.43}$$

Only the fifth alternative ensures $f_a^{\gamma^*}(x, \mu^2, Q^2) > 0$ for arbitrarily large Q^2; in all other alternatives the resolved contribution (at fixed $p_\perp$) vanish above some Q^2 scale. The last alternative exploits the well-known freedom of including some multiplicative factor in any (leading-order) scale choice. When nothing is mentioned explicitly below, the choice μ_3^2 is used. We should note that the expressions in the program also contain a dependence on final-state masses, e.g. for the production of massive quarks, but this is left out here since it is not a topic studied in this paper. (It will enter briefly in the following, however.)

None of the scales proposed above are unreasonable, although some are more easily motivated than others. In principle, theoretical input on an optimal scale choice could be provided from the results of higher-order calculations. However, such exercises are less than trivial already for hadron–hadron collisions, since different convergence criteria may be applied and since results can depend on

the observable picked. In photon-induced processes, the higher-order ambiguity between direct and resolved processes, and the presence of several scales in the process, is not likely to make the task any easier. This would therefore be an interesting study in its own right, but is not the purpose of the current one.

3.2.4 Other Model Aspects

The issues discussed above are the main ones that distinguish the description of processes involving virtual photons from those induced by real photons or by hadrons in general. In common for the tree is the need to consider the buildup of more complicated partonic configurations from the lowest-order 'skeletons' defined above, (*i*) by parton showers, (*ii*) by multiple parton–parton interactions and beam remnants, where applicable, and (*iii*) by the subsequent transformation of these partons into the observable hadrons. The latter, hadronization stage can be described by the standard string fragmentation framework [25], followed by the decays of unstable primary hadrons, and is not further discussed here. In the following we comment on the shower, multiple-interaction and beam-remnant aspects.

The parton-shower description is conveniently subdivided into initial- and final-state radiation. For wide-angle emissions such a classification is not unambiguous, and it is necessary to consider interference effects in order to describe the data [26]. A direct photon is not associated with any initial-state QCD radiation.

In the hadronic environment, initial-state radiation normally means an evolution of a spacelike branch of partons, from an initially vanishing virtuality up to the scale of the hard process. The 'backwards evolution' strategy [21] allows this cascade to be reconstructed in reverse order. That is, from a parton b coming in to the hard scattering, the branching $a \to bc$ that produced b is first reconstructed, thereafter the branching that produced a, and so on, down to the lower cutoff scale Q_0^{sh}, in practice of the order of 1 GeV. Inclusively, the effect of parton-shower histories is already taken into account by the μ^2 dependence of the parton distributions used to select the hard scattering, so what this procedure does is to associate an exclusive set of initial-state-radiation partons to each hard scattering.

For a real photon, the VMD part is assumed to behave like a hadron, while the lower parton-shower cut-off Q_0^{sh} has to be considered further for the anomalous component. In the spirit of the ansatz for parton distributions, eq. (3.29), the k^2 value of the $\gamma \to \mathrm{q}\overline{\mathrm{q}}$ branching is distributed like $\mathrm{d}k^2/k^2$. In principle, for a given physical process, there would be a further 'trigger bias' effect to this distribution: at large (small) x values a large (small) k^2 would be favoured since it would be associated with a small (large) evolution range. As a first approximation, this bias is neglected here, i.e. k^2 is picked flat in a logarithmic scale between Q_0^2 and μ^2. When this k is larger than the default

value of $Q_0^{\rm sh}$, the shower cut-off is increased to instead be given by k. Thus there is no shower evolution below the k scale of the $\gamma \to \mathrm{q\overline{q}}$ branching. Thereby the amount of collinear emission along the incoming photon direction is reduced for high-virtuality fluctuations.

As a technical aside, we note that the default value $Q_0 = 0.6$ GeV is smaller than $Q_0^{\rm sh} = 1$ GeV. First, it should be made clear that k^2 and the Q^2 virtuality variable of the spacelike shower evolution are not defined in precisely the same way and therefore very well can differ by factors of order unity, so that also the lower cut-offs may differ. However, also disregarding this, there is no reason why the two cut-offs should agree. Whereas Q_0 is severely constrained e.g. by F_2^γ data, $Q_0^{\rm sh}$ is just a crude estimate of where emitted partons in the cascade are so collinear that their effect may be safely neglected. That is, we do not exclude the possibility of parton emissions in the range between Q_0 and $Q_0^{\rm sh}$, but also do not believe that their inclusion or not is essential for a description of final-state properties. The effects of an increased shower cut-off only show up for $\gamma \to \mathrm{q\overline{q}}$ branchings with $k \gtrsim 2$ GeV, in terms of a reduced parton emission rate along the incoming photon direction.

The generalization to a virtual photon is now straightforward, given the extension of f_a^γ to $f_a^{\gamma^*}$, cf. eqs. (3.29) and (3.31). For the VMD piece, the shower cut-off is selected to be the larger of $Q_{\rm int}$ and $Q_0^{\rm sh}$. For the anomalous piece, a k^2 is picked flat in a logarithmic scale between $Q_{\rm int}^2$ and μ^2, and the shower cut-off is the larger of this k and $Q_0^{\rm sh}$.

Final-state radiation from the scattered partons of the hard interaction follow the same pattern as in hadron–hadron collisions, and so need not be discussed here. Also time-like partons on the 'side branches' of an initial-state cascade can undergo final-state evolution, as part of the conventional shower description. The new aspect concerns the $\overline{\mathrm{q}}$ 'beam remnant' parton of an anomalous $\gamma^* \to \mathrm{q\overline{q}}$ branching, where the q is the initiator of the spacelike cascade. This parton can undergo a shower evolution from the $\gamma^* \to \mathrm{q\overline{q}}$ branching scale k down to the timelike shower cut-off $m_0^{\rm sh} \approx 1$ GeV, provided k is above the cut-off. For the VMD part of the photon, the beam remnant is assumed not to radiate.

In general, a beam remnant contains the flavours 'left behind' when one parton initiates the spacelike shower that leads up to the hard interaction. Momentum conservation gives its kinematics. This includes both a longitudinal momentum fraction $1 - x$, if the initiator takes x, and a transverse 'primordial $k_\perp$' recoil. For the VMD components of the photon this transverse momentum should be of a nonperturbative character and small, ~ 0.5 GeV, although there are indications of much larger values in data [27]. A Gaussian ansatz is used to pick a $k_\perp$ vector. For the anomalous part of the photon, we associate its $k_\perp$ with the k scale that already figured prominently above.

Multiple parton–parton interactions [28, 2] could be viewed as a further so-

phistication of the beam-remnant description. The basic idea is that hadronic states contain many partons and that therefore several perturbative interactions may occur in a hadron–hadron collision. Usually (at most) one of these give rise to visible high-$p_\perp$ jets, while the rest only add to the underlying event activity. This additional component is vitally needed in order to reproduce the observed multiplicity and $E_\perp$ flow in high-energy $\mathrm{p\overline{p}}$ collisions, at least if string hadronization is supposed to be universal, i.e. have its parameters constrained by $\mathrm{e^+e^-}$ data. The main unknown parameter in this approach is $p_{\perp\mathrm{min}}^{\mathrm{MI}} \approx 2$ GeV, the scale below which perturbation theory is assumed not to be applied anymore. Physically, this scale can be viewed as related to an effective colour screening phenomenon: gluons with a wavelength larger than $1/p_{\perp\mathrm{min}}^{\mathrm{MI}}$ do not resolve the colour structure inside the hadron wave function and therefore decouple. Of course, this screening should set in gradually, so $p_{\perp\mathrm{min}}^{\mathrm{MI}}$ is only an effective parameter. To first approximation, the average number of interactions per event is the ratio of the jet cross section above $p_{\perp\mathrm{min}}^{\mathrm{MI}}$ to the total inelastic cross section. By now there exist convincing evidence in favour of multiple interactions also in the HERA data [29].

Almost by definition, direct and single-resolved processes do not lead to multiple interactions. Furthermore, within the spectrum of resolved components of a real photon, one would expect a close-to hadronlike behaviour for the VMD part and then a gradual fading-away of multiple interactions as the k^2 scale of an anomalous fluctuation is increased. This may partly be seen as a consequence of that the number of partons (above some fixed x_0) decrease with increasing k^2. Furthermore, the physical size of an anomalous fluctuation should scale like $1/k$, so the screening argument above would lead to a scaling-up of $p_{\perp\mathrm{min}}^{\mathrm{MI}}$ roughly by a factor k/Q_0. This in part would be compensated by an expected decrease in the total cross section of an anomalous fluctuation, about like $1/k^2$ based on the size scaling argument, but in total there should still be a rather rapid fall-off with k. As a first approximation, we follow the route adopted in [2], namely to allow multiple interactions for VMD states to the same extent as for hadrons, and not at all for the anomalous states.

When generalizing to virtual photons, the same arguments as used above for the anomalous component would suggest a fall-off of multiple interactions in the VMD component with increasing Q^2 scale. As a first guess, we have here chosen to scale up $p_{\perp\mathrm{min}}^{\mathrm{MI}}$ like $\sqrt{1 + Q^2/m_V^2}$, while the normalizing total cross section is scaled down like $m_V^4/(m_V^2 + Q^2)^2$ in accordance with the dipole ansatz.

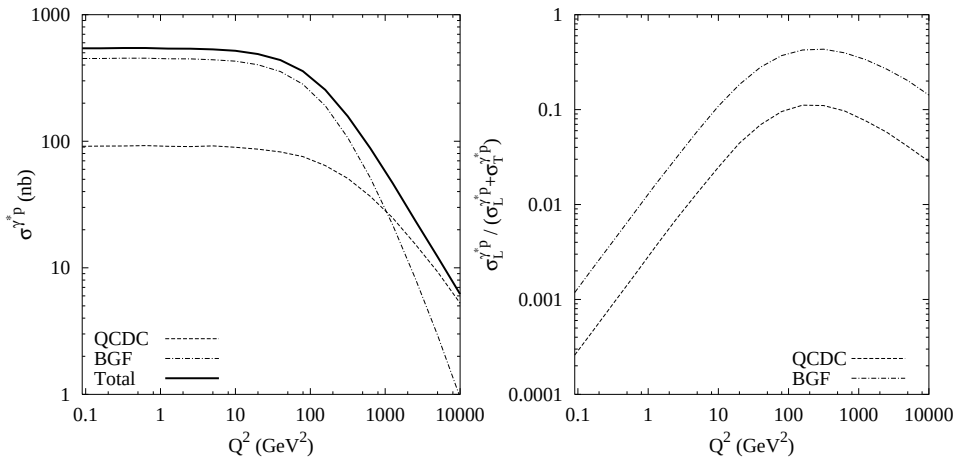

Figure 3.2: Summed transverse and longitudinal contributions from the QCD Compton and boson–gluon fusion processes, equations (3.21)–(3.24), to the $\sigma^{\gamma^* \mathrm{p}}$ parton cross section, $p_\perp^{\mathrm{parton}} > 5$ GeV and $W_{\gamma^* \mathrm{p}} = 200$ GeV. To the right, for each process, is the fraction of the longitudinal contribution.

3.3 Results

3.3.1 Basic Distributions

γ^*p Partonic Cross Sections

The contribution to the $\sigma_{\gamma^* \mathrm{p}}$ parton cross section from the different direct components in equations (3.21)–(3.24), the boson–gluon fusion and the QCD Compton processes, are shown in Fig. 3.2 as a function of the photon virtuality, Q^2. The partons produced in the $2 \to 2$ hard scattering subprocess are restricted to have transverse momenta $p_\perp$ larger than 5 GeV and the hadronic centre of mass energy $W = \sqrt{s_{\gamma^* \mathrm{p}}}$ is equal to 200 GeV.

In the limit $Q^2 \to 0$ the cross section vanishes for the processes involving a longitudinal photon. In the same limit the boson–gluon fusion process with a transverse photon, $\gamma_{\mathrm{T}}^* \mathrm{g} \to \mathrm{q}\overline{\mathrm{q}}$, is more important than the QCD Compton counterpart, $\gamma_{\mathrm{T}}^* \mathrm{q} \to \mathrm{gq}$; this kinematic region permits the gluon/quark from the proton to have a small fraction x of the proton momentum, $x = (\hat{s} + Q^2)/(W^2 + Q^2)$. At large Q^2, the opposite is true; x is large and the QCD Compton process, involving an initial quark from the proton, is more important than the boson–gluon fusion process. Both processes are suppressed by the $1/(\hat{s} + Q^2)^2$ factor

that provides the main dampening at large Q^2. The longitudinal processes, $\gamma_L^* q \to gq$ and $\gamma_L^* g \to q\overline{q}$ have maximal cross sections when $Q^2 \sim \hat{s}$, since $\hat{s} \geq 4p_{\perp \min}$ this occurs for Q^2 around 100 GeV^2.

The proton structure function used to produce Fig. 3.2 was GRV 94 LO, which is the default in PYTHIA. A different choice of structure function would only change the details but not the conclusions made from these results. In the following the GRV 94 LO will be used as the proton parton distribution except where otherwise stated.

When studying jet production with low photon virtualities it is likely that the photon is resolved. The photon fluctuates then into a quark-antiquark pair that develops into a multiparton state and finally one of these partons scatters off a parton from the proton. The virtual photon parton distributions used for modeling the resolved components are the SaS 1D and 2D distributions. The dipole factors in eq. (3.31) will dampen the resolved components with increasing photon virtualities.

The relative importance of the direct components compared to the resolved components — the VMD and anomalous fluctuations — are shown in Fig. 3.3. The direct contribution is the sum of the transverse QCD Compton and boson–gluon fusion processes studied in Fig. 3.2. As expected, the VMD components die away faster than the anomalous ones which in turn die away faster than the sum of the direct components. Here we also see the difference between the SaS 1D and SaS 2D distributions, with SaS 2D having a higher cut-off for the separation between the VMD component and the anomalous component. This is reflected by the larger contribution from the SaS 2D VMD component compared to the SaS 1D one, and vice versa for the anomalous component.

Longitudinal resolved components are simulated with an extra factor of $R_1(y, Q^2, \mu^2)$, eq. (3.33), for the transverse resolved components. In Fig. 3.3 an a-parameter equal to 1 has been used together with the SaS 1D photon parton distribution. The y value is set equal to 0.44 with HERA energies in mind. A noticeable difference is seen in the total jet cross section for Q^2 around 10 GeV^2, since, in this ansatz, the maximal contribution for the longitudinal component is obtained at $Q^2 = \mu^2$, and the direct and the anomalous component is of the same order in this region. With $a = 1$ the sum of the resolved components can be almost a factor of two larger than with $a = 0$, the case with pure transverse resolved photons. There is nothing special with the choice $a = 1$ except that it models a longitudinal resolved component that is of the same order of magnitude as the transverse component at intermediate Q^2 values; this is the same behaviour as seen for the direct components.

$\gamma^*\gamma^*$ Partonic Cross Sections

In Fig. 3.4 the processes $\gamma_{T,L}^* \gamma_{T,L}^* \to q\overline{q}$, equations (3.15)–(3.18), have been generated at a centre of mass energy $W = \sqrt{s_{\gamma^*\gamma^*}}$ of 100 GeV. For simplicity,

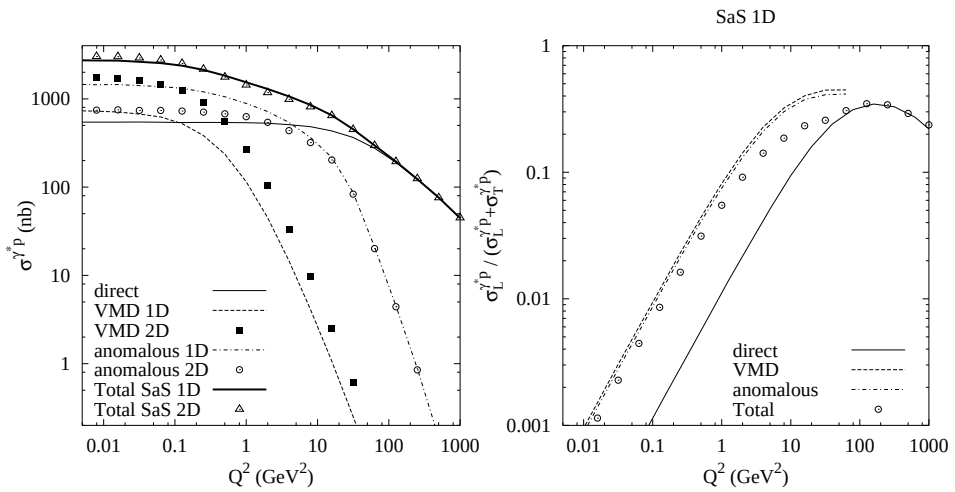

Figure 3.3: Contributions to the $\sigma^{\gamma^*\mathrm{p}}$ parton cross section from events involving a direct, a VMD and an anomalous photon, $p_\perp^{\mathrm{parton}} > 5$ GeV and $\sqrt{s_{\gamma^*\mathrm{p}}} = 200$ GeV. To the left, the SaS 1D and SaS 2D parton distributions was used. To the right, the fraction of the longitudinal contribution is shown. The SaS 1D distribution was used and longitudinal resolved photons is modeled with $a = 1$ and $y = 0.44$ (see text). The longitudinal fraction for the resolved components at high-Q^2 is not shown due to the small cross sections.

one of the photons was kept at a fixed virtuality of 0.1 GeV^2. The transverse momenta for the partons in the hard scattering was restricted to be larger than 5 GeV.

Clearly, the dominant process is $\gamma_T^*\gamma_T^* \to \mathrm{q\overline{q}}$ but, as the virtuality Q_1^2 increases, the contribution from the longitudinal processes becomes more and more important. From eq. (3.15)–(3.18) we notice that the $\gamma_T^*\gamma_L^*$, $\gamma_L^*\gamma_T^*$ and $\gamma_L^*\gamma_L^*$ direct cross sections have a maximum at $Q_1^2 \sim \hat{s} = s_{\gamma^*\gamma^*}$ (for $Q_2^2 \ll \hat{s}$). The $\gamma_L^*\gamma_L^*$ process is bounded to never be larger than twice the $\gamma_T^*\gamma_L^*$ or $\gamma_L^*\gamma_T^*$ process. The $\gamma_L^*\gamma_T^*$ and $\gamma_L^*\gamma_L^*$ processes clearly go to zero as $Q_1^2 \to 0$, the $\gamma_T^*\gamma_L^*$ process remains finite and approaches the expression for the $\gamma_L^*\mathrm{g}$ matrix element, eq. (3.24), with appropriate factors exchanged (and $Q_2^2 \to Q_1^2$). As for the case with direct processes in $\gamma^*\mathrm{p}$, the $\gamma_{\xi_1}^*\gamma_{\xi_2}^* \to \mathrm{q\overline{q}}$ processes (ξ_i =T, L) are suppressed by the $1/\lambda^2$ factor for high Q_i^2.

With the possibility of having resolved photons, nine event classes is obtained. They are illustrated in Fig. 3.5 for the SaS 1D and SaS 2D parton

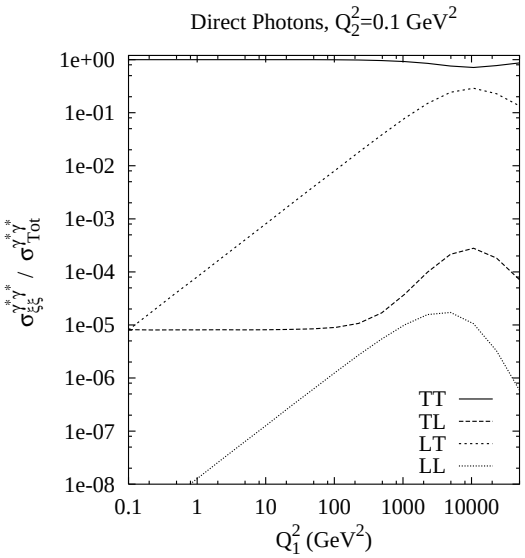

Figure 3.4: The partonic cross sections $\sigma_{\xi\xi}^{\gamma^*\gamma^*}$ for the subprocesses in equations (3.15)–(3.18) normalized w.r.t. the sum of them, $p_\perp^{\text{parton}} > 5$ GeV and $\sqrt{s_{\gamma^*\gamma^*}} = 100$ GeV. The Q_1^2 of the first photon is varied while the second photon is kept at the fixed virtuality $Q_2^2 = 0.1$ GeV^2.

distributions, with the second photon having the fixed virtuality $Q_2^2 = 1$ GeV^2. Generally, as Q_1^2 increases, the VMD components (of the first photon) drops first, then the anomalous components and at very high Q_1^2 remains the direct components (direct–direct, direct–VMD and direct–anomalous). Particularly, with the choice $Q_2^2 = 1$ GeV^2, the anomalous–anomalous events dominates at low Q_1^2 for the SaS 1D case, whereas for the SaS 2D case, the VMD components dominate. In this ansatz, the Q_{int} scheme, the parton distribution for the anomalous component $f_a^{\gamma^*}(x, \mu^2, Q^2) = 0$ when $\mu^2 < Q^2$.

x_γ Distributions

In ep collisions the variable x_γ^{obs} is defined as [1]

$$x_\gamma^{\text{obs}} = \frac{E_{\perp,1}\mathrm{e}^{-\eta_1} + E_{\perp,2}\mathrm{e}^{-\eta_2}}{2E_\gamma} \tag{3.44}$$

where $E_{\perp,i}$ is the transverse energy and η_i is the rapidity of the two jets with the highest transverse energy. E_γ is the energy of the photon. x_γ^{obs} is then

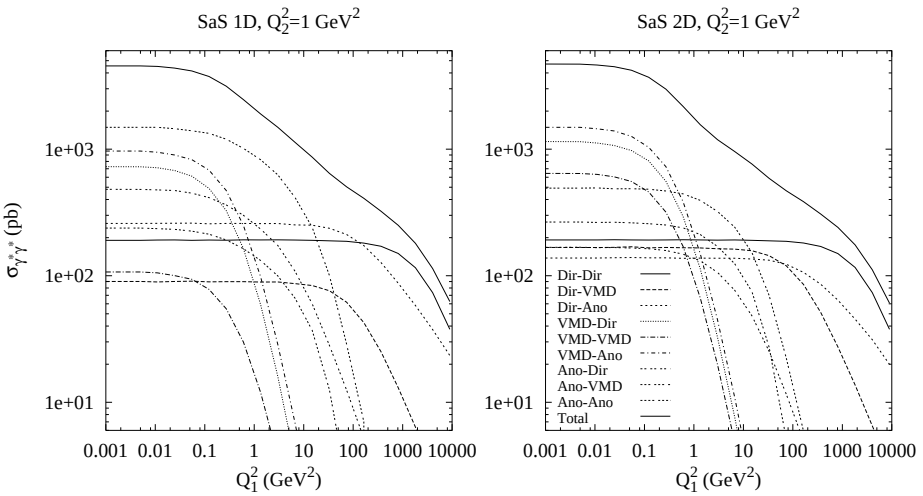

Figure 3.5: Contributions to the $\sigma_{\gamma^*\gamma^*}$ parton cross section from the nine different event classes, $p_\perp^{\rm parton} > 5$ GeV and $\sqrt{s_{\gamma^*\gamma^*}} = 100$ GeV. The Q_1^2 variation is for the first photon; the second photon is kept at fixed virtuality $Q_2^2 = 1$ GeV^2.

the fraction of the photon energy (or better, light-cone momentum) that goes into the production of the two highest transverse energy jets, and therefore reflects the parton distributions of the photon. In Fig. 3.6 the $x_\gamma^{\rm obs}$ distribution is shown for the different photon components. A cone jet algorithm with cone radius $R = 1$ is used for jet finding. The partons in the hard scattering are restricted to have transverse momenta larger than 3 GeV and the jets to have a transverse energy larger than 6 GeV. Note that $p_{\perp\rm min}^{\rm parton} < p_{\perp\rm min}^{\rm jet}$ has been used since migration from $p_\perp < p_{\perp\rm min}^{\rm jet}$ is likely to happen due to various effects; this is discussed further in section 3.3.2. The $x_\gamma^{\rm obs}$ distribution was generated for a Q^2 interval 0.9–1.1 GeV^2. An $x_\gamma^{\rm obs}$ value of 0.7–0.8 will separate most of the direct events from the resolved events. The SaS 2D parton distribution gives less resolved events at large $x_\gamma^{\rm obs}$ as compared to SaS 1D. This is because the VMD component, which is more important in SaS 2D, is dampened faster with increasing Q^2 than the anomalous one. For high Q^2, this difference is not there, since the two anomalous components are approaching each other at high Q^2, and the VMD pieces are vanishingly small.

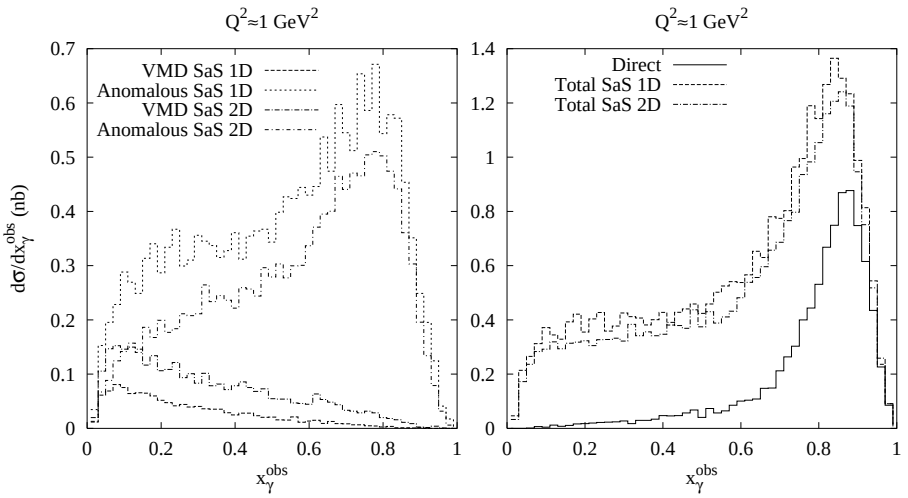

Figure 3.6: The $x_\gamma^{\rm obs}$ distribution for the different photon components. $p_\perp^{\rm parton} > 3$ GeV, $E_\perp^{\rm jet} > 6$ GeV, $0.01 < y < 0.99$ and $\sqrt{s_{\rm ep}} \simeq 300$ GeV.

In e^+e^- collisions the variables x_γ^+ and x_γ^- are defined as [30]

$$x_\gamma^\pm = \frac{\sum_{\rm jets}(E \pm p_z)}{\sum_{\rm particles}(E \pm p_z)} \tag{3.45}$$

where p_z is the momentum component along the z–axis of the e^+e^- collision and E is the energy of the jets or particles. The sum over jets runs over all jets in the event but is limited to the two hardest jets for dijet studies. The different direct and resolved components are shown in Fig. 3.7 for $Q_i^2 < 0.8$ GeV^2; each combination of components will not be shown here. For these symmetric cuts the $x_\gamma^\pm$ distributions are identical, the direct–resolved events for one case corresponds to the resolved–direct for the other. As expected, direct events are concentrated at large $x_\gamma^\pm$, direct–resolved (resolved–direct) are compatible with direct events in ep, and double–resolved are concentrated at small $x_\gamma^\pm$ — suggesting a cut at low x_γ^+ and x_γ^- to separate double–resolved from single–resolved events.

The SaS 2D distribution gives, with $Q_{1,2}^2 < 0.8$ GeV^2, a large double–resolved contribution, dominated by the VMD–VMD events. Similarly, direct–VMD events dominate the single–resolved contribution. The effective parameter $p_{\perp\rm min}^{\rm MI}$ sets the amount of multiple interactions for the VMD component. The results shown in this section are sensitive to the choice of $p_{\perp\rm min}^{\rm MI}$, here chosen to 1.4 GeV, which is the default in PYTHIA.

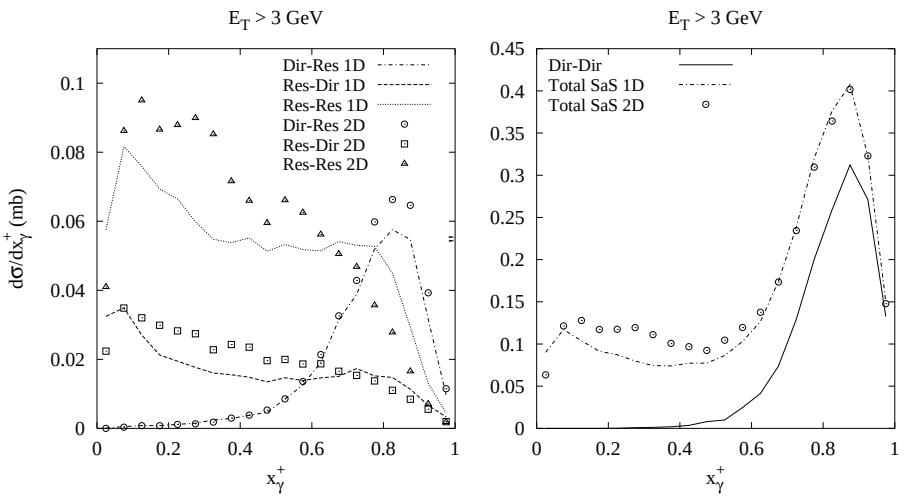

Figure 3.7: The x_γ^+ distribution for the direct and resolved photon components. $p_\perp^{\rm parton} = 1.5$ GeV, $E_\perp^{\rm jet} > 3$ GeV, $0.01 < y_{1,2} < 0.99$, $Q^2_{1,2} < 0.8$ GeV^2 and $\sqrt{s_{\rm e^+e^-}} = 133$ GeV.

Scale Choice in Parton Distributions

To show the dependence on the choice of scale μ^2 in parton distributions we will study ep events, with direct and resolved events treated separately. Three extreme choices of scales $\mu_1^2 = p_\perp^2$, $\mu_5^2 = p_\perp^2 + Q^2$ and $\mu_6^2 \approx 2p_\perp^2$ are compared. For simplicity, we stay with the $p_\perp$ distribution of the hard scattering $2 \to 2$ subprocess, i.e. avoid hadronization, multiple interactions, initial- and final-state bremsstrahlung and jet clustering effects.

In Fig. 3.8, the $\mathrm{d}\sigma_{\rm ep}/\mathrm{d}\log_{10}(p_\perp/(1\mathrm{GeV}))^2$ distribution for the different scale choices are compared at two different photon virtualities, $Q^2 \approx 1$ GeV^2 and $Q^2 \approx 10$ GeV^2. In these distributions, the various scale choices for the direct events do not give a significant difference for the results, and are therefore not shown. For the low-Q^2 case, the results for the resolved events are in decreasing order in accordance with the scale choice; μ_6, μ_5 and μ_1. Here the anomalous component is the dominant one, explaining the difference between the SaS 1D and the SaS 2D distributions. For direct events, only a rather mild scale-breaking of the proton distributions enters. Since small-x values dominate, where distributions increase with μ^2, the μ_6 scale should give the largest result but the difference from the other two are within errors for this distribution.

For $Q^2 \approx 10$ GeV^2, direct events dominate. The resolved results can be

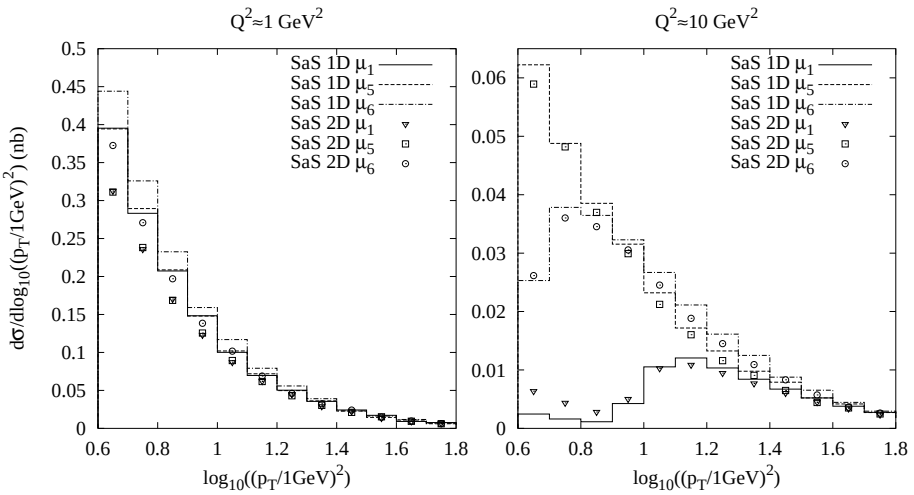

Figure 3.8: The $\mathrm{d}\sigma_{\mathrm{ep}}/\mathrm{d}\log_{10}(p_\perp/(1\mathrm{GeV}))^2$ cross section for different μ_i scales with $Q^2 \approx 1$ GeV^2 and $Q^2 \approx 10$ GeV^2, $\sqrt{s_{\mathrm{ep}}} \simeq 300$ GeV. Only the resolved photon contribution is shown.

divided into two regions; $p_\perp^2 < Q^2$ and $p_\perp^2 > Q^2$. Remember that the μ_5 scale imply that the resolved component will not vanish even when $p_\perp^2 < Q^2$ as can be seen in Fig. 3.8. With the μ_6 scale, the evolution range decreases with $p_\perp^2$ and finally suppresses resolved photons. The μ_1 scale does not allow resolved photons when $p_\perp^2 < Q^2$. (The tiny tail of such events comes from charm production, where actually $\mu_1^2 = p_\perp^2 + m_c^2$ is used rather than only $p_\perp^2$.) The results with the μ_5 and μ_6 scales are, of course, in agreement when $p_\perp^2 \approx Q^2$ and in the tail of the $p_\perp$ distribution the μ_6 scale gives the bigger cross section. At large Q^2 values, the difference between the two photon parton distributions are reduced. For direct events the μ_5 scale is larger than the μ_6 one at low $p_\perp^2$ but smaller at high $p_\perp^2$; a corresponding pattern is expected to be seen in the cross section (again, small-x values dominate). However, differences are small for these distributions.

3.3.2 Comparisons with Data

In this section the model is compared with data. We will not make a detailed analysis of experimental results but use it to point out model dependences and to constrain some model parameters. Where applicable, the HzTool [32] routines will be used for the comparison with data.

$2 \to 2$ parton interactions normally give rise to 2–jet events. In leading–

order QCD, the jets are balanced in transverse momenta in the centre of mass frame of the $\gamma^*\mathrm{p}/\gamma^*\gamma^*$ subsystem. Various effects, such as primordial $k_\perp$, initial- and final-state bremsstrahlung, etc., tend to spoil this picture. This increases the $\mathrm{d}\sigma/\mathrm{d}p_\perp$ spectrum at any fixed $p_\perp$, since jets can be boosted up from lower $p_\perp$. It is here important to remember that $\mathrm{d}\sigma/\mathrm{d}p_\perp$ is dropping steeply with increasing $p_\perp$, since the matrix elements described in section 3.2.2 are divergent for $p_\perp \to 0$. Even a symmetric smearing of jet $p_\perp$, i.e. with shifts $+\delta p_\perp$ and $-\delta p_\perp$ equally probable, would thus increase $\mathrm{d}\sigma/\mathrm{d}p_\perp$: the jets shifted upwards would migrate into a region less populated than those shifted downwards, and therefore proportionately have a larger impact. Additionally, the smearing is not symmetric, but normally shifts one jet upwards while the other may be shifted in either direction. (This holds for primordial $k_\perp$ and initial-state radiation, while final-state radiation tends to shift both jets downwards.) In the generation procedure, the divergences are avoided by the introduction of a lower cut, $p_{\perp\mathrm{min}}^{\mathrm{parton}}$, below which parton scatterings are not considered. In order to study jets above some $p_{\perp\mathrm{min}}^{\mathrm{jet}}$, a $p_{\perp\mathrm{min}}^{\mathrm{parton}} < p_{\perp\mathrm{min}}^{\mathrm{jet}}$ is required. Stable results are obtained when a hard scattering with $p_\perp^{\mathrm{parton}} = p_{\perp\mathrm{min}}^{\mathrm{parton}}$ for the incoming partons do not produce any jets with $p_\perp$ above $p_{\perp\mathrm{min}}^{\mathrm{jet}}$. Typically $p_{\perp\mathrm{min}}^{\mathrm{parton}} = \frac{1}{2} p_{\perp\mathrm{min}}^{\mathrm{jet}}$ or less is required.

Dijets at HERA

Dijet angular distributions in photoproduction and deep inelastic scattering have been studied at HERA [31]. In the center of mass system of the two highest transverse energy jets (which are restricted to have a transverse energy above a certain value) the angle θ^* between the jets and the beam axis is expected to be distributed differently depending on whether or not the photon is resolved. The leading–order direct QCD graphs, boson–gluon fusion and QCD Compton, have spin–1/2 quark propagators leading to an angular dependence proportional to $1/\hat{t} \propto (1 - |\cos\theta^*|)^{-1}$. (The jets are generally not distinguishable so the absolute value of $\cos\theta^*$ cannot be measured.) On the contrary, the resolved processes are dominated by *Rutherford type* scatterings involving a t–channel gluon: $\mathrm{qq}' \to \mathrm{qq}'$, $\mathrm{qg} \to \mathrm{qg}$ and $\mathrm{gg} \to \mathrm{gg}$. These thus give an angular dependence proportional to $1/\hat{t}^2 \propto (1 - |\cos\theta^*|)^{-2}$ i.e. the dijet angular distribution is expected to rise steeper with $|\cos\theta^*|$ for resolved processes than for direct ones.

As discussed in the introduction and in section 3.3.1, with a cut in x_γ^{obs} it is possible to make a separation between events that are likely to be direct from those that are likely to be resolved events. An example of this is shown in Fig. 3.9 where direct and resolved events generated by PYTHIA is compared with results presented by the ZEUS Collaboration [31], with a good agreement in the shape of the distributions. The plots were produced by using the HzTool

package.

In the analysis of the ZEUS Collaboration a cut $x_\gamma^{\rm obs} < 0.75$ was used to classify the photon as resolved while for $x_\gamma^{\rm obs} > 0.75$ it was classified as a direct photon. Of the events classified as having a direct photon a significant contribution comes from events with an anomalous fluctuation of the photon. This is well understood since, in this component, the quark (antiquark) often carries a large fraction of the original photon momentum. The two jets are then likely to be produced at small scattering angles θ^* as described by the matrix elements with gluon exchange. Using the SaS 1D parton distribution, the anomalous component is important for either classification, whereas the VMD part is highly suppressed and negligible by the $x_\gamma^{\rm obs} > 0.75$ cut. For SaS 2D, the VMD contribution is small for events classified as direct but of equal importance as the anomalous part for $x_\gamma^{\rm obs} < 0.75$. The choice of scale μ_i is not crucial at this low Q^2 values, the μ_3 scale is used and the results with μ_5 are within errors.

In the lower part of Fig. 3.9, the cross sections for events classified as resolved and direct have been multiplied by a factor $(1 - |\cos\theta^*|)^2$ and $(1 - |\cos\theta^*|)$, respectively. This confirms that the resolved events, $x_\gamma^{\rm obs} < 0.75$, indeed are dominated by a t–channel gluon exchange since the distribution is rather flat. Moreover, the result is not contaminated by the misclassified pure direct photon events. On the contrary, the direct distribution, $x_\gamma^{\rm obs} > 0.75$, is increasing slightly with $|\cos\theta^*|$, illustrating the importance of including resolved photons in order to explain data classified as originating from direct photon events. (The pure direct events give a flat distribution.)

The possibility for the incoming electron to emit extra photons, that may go undetected, is not taken into account by the model. This effect decreases the lepton energy; hence the photon energy calculated here would be overestimated. A simple estimation of these effects give corrections to the photon energy at the percent level. The consequence would be that the given $x_\gamma^{\rm obs}$ distribution will be shifted towards higher values. An inclusion of such effects would shuffle some of our resolved events into the direct category, thus improving the description of the relative amounts. This could be solved by using lepton-inside-lepton structure functions, though the implementation of it is postponed for the future.

From these observations it is tempting to conclude that a cut in $x_\gamma^{\rm obs}$ does not so much separate events with the resolved anomalous component (perturbatively calculable fluctuation) of the photon from the direct component, but rather separates it from the VMD component (non-perturbative fluctuation) of the photon. This statement is true to leading order but the anomalous fluctuation contain pieces that a next-to-leading-order calculation of the direct component would give. Hence, in this sense also anomalous events can be considered as a contribution from the direct component making the $x_\gamma^{\rm obs}$ well suited to separate the direct from the resolved component. Nevertheless,

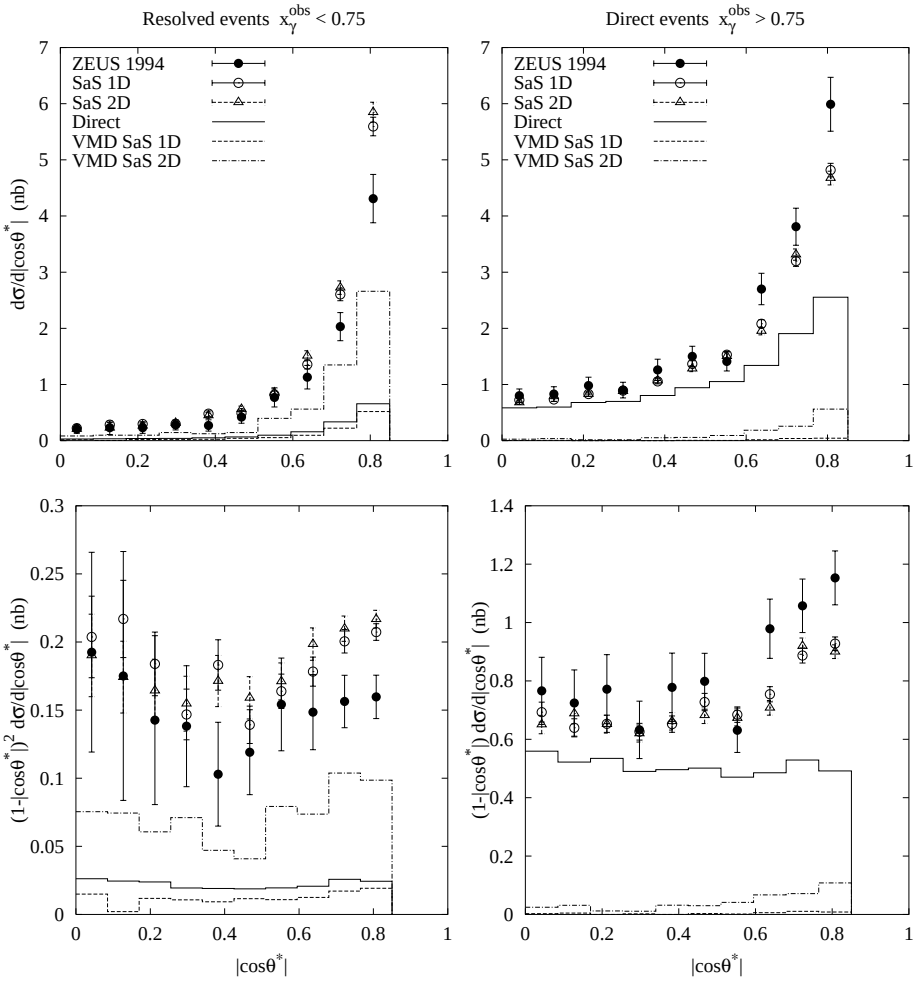

Figure 3.9: The dijet angular cross section $\mathrm{d}\sigma/\mathrm{d}|\cos\theta^*|$ for resolved ($x_\gamma^{\mathrm{obs}} < 0.75$) and direct ($x_\gamma^{\mathrm{obs}} > 0.75$) processes. θ^* is the jet scattering angle w.r.t. the beam axis measured in the dijet centre of mass system. $Q^2 < 4$ GeV^2 and $0.25 < y < 0.8$. The SaS 1D and SaS 2D curves give the total contribution from the resolved and direct components; the VMD and direct components are also shown separately. The anomalous contribution can be obtained by subtracting the direct and the VMD contribution from the full one. In the lower figures, the cross sections for events classified as resolved and direct have been multiplied with a factor $(1 - |\cos\theta^*|)^2$ and $(1 - |\cos\theta^*|)$, respectively.

the classification of the photon into different components used throughout in this paper is based on the leading order description, viewing the anomalous fluctuation as a resolved photon.

Inclusive ep **Jet Cross Sections**

Inclusive ep jet cross sections have been measured by the H1 collaboration [33] in the kinematical range $0 < Q^2 < 49\,\mathrm{GeV}^2$ and $0.3 < y < 0.6$. The differential jet cross section $\mathrm{d}\sigma_{\mathrm{ep}}/\mathrm{d}E^*_\perp$ and the inclusive γ^*p jet cross section in Fig. 3.10 and 3.11 respectively, were produced with the HzTool package. The $E^*_\perp$ and η^* are calculated in the γ^*p centre of mass frame where the incident proton direction corresponds to positive η^*.

For $\mathrm{d}\sigma_{\mathrm{ep}}/\mathrm{d}E^*_\perp$, data is available in nine different Q^2 bins, four of them are shown here with similar results for the intermediate bins. The SaS 1D parton distribution together with a few different μ_i scales; μ_1, μ_3, μ_5 and μ_6, are used to model the resolved photon component. The other choices of scales, μ_2 and μ_4, interpolates between these results.

In the highest Q^2 bin the direct component is the dominant contribution; the virtuality of the photon is for most events of the order of or larger than the transverse momenta squared, $Q^2 \gtrsim p^2_\perp$. However, the resolved component is not negligible and all the scales μ_i, except μ_1, depend on the photon virtuality. This gives a larger resolved component in this region as compared to the the conventional choice, $\mu_1 = p_\perp$. In the low-Q^2 bin the μ_i scales do not differ much from $p_\perp$, i.e. the results are not sensitive to the scale choice μ_i. The exception is μ_6, which there overshoots the data. The $\mu_4^2 = p^2_\perp + Q^2/2$ scale (not shown) gives nice agreement with data for all different Q^2 bins.

Since the VMD part dies out quickly with increasing photon virtuality, multiple interactions will only be visible at low Q^2 (multiple interactions for the anomalous component is not in the model so far). The anomalous component dominates over the VMD component already at 1 GeV^2. Therefore, multiple interactions for the VMD component can safely be neglected for the distributions shown in this section.

Changing the photon parton distribution from SaS 1D to SaS 2D will give a slightly lower result for the low-Q^2 bins, Fig. 3.12. The GRS LO [22] parton distribution gives a similar result as the other two. It has a restricted regime of validity, $Q^2 \ll \mu^2$ (implemented as $5Q^2 < \mu^2$) and $Q^2 < 10\,\mathrm{GeV}^2$. Therefore, it is absent in the high-Q^2 bin, and some regions of phase space are cut out in the low-$E^*_\perp$ bins. One could imagine larger differences for virtual-photon parton distributions that from the onset are more different, so the good SaS/GRS agreement is somewhat fortuitous. Using a parton distribution for a real photon cannot describe the Q^2 dampening in the distributions shown in this section. As an example of this the GRV LO [34] distribution has been used; the change here is solely from the photon flux.

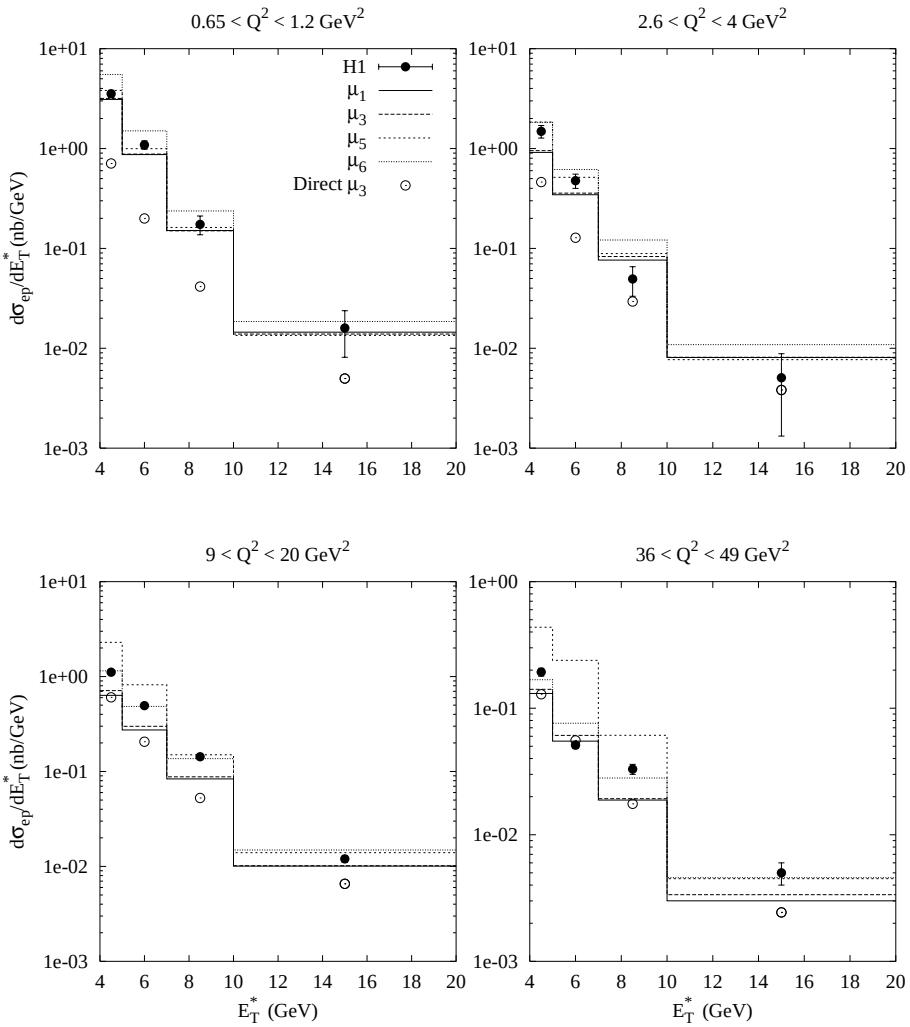

Figure 3.10: The differential jet cross section $\mathrm{d}\sigma_{\mathrm{ep}}/\mathrm{d}E^*_\perp$ for jets with $-2.5 < \eta^* < -0.5$ and $0.3 < y < 0.6$.

Using CTEQ 3L instead of GRV 94 LO as the proton parton distribution reduces the result in some $E^*_\perp$ bins by half, Fig. 3.13. The GRV 94 HO parton distribution give a slightly lower result (as compared to GRV 94 LO). The differences mainly come from the gluon distributions, that are not yet so well constrained from data. In the modeling of the parton distributions, it is a

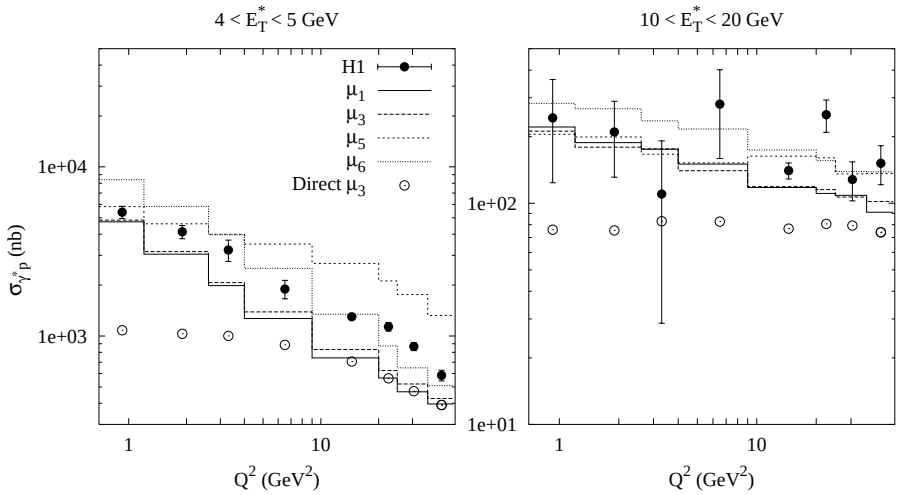

Figure 3.11: The inclusive γ^*p jet cross section $\sigma_{\gamma^*\mathrm{p}}$ for jets with $-2.5 < \eta^* < -0.5$ and $0.3 < y < 0.6$.

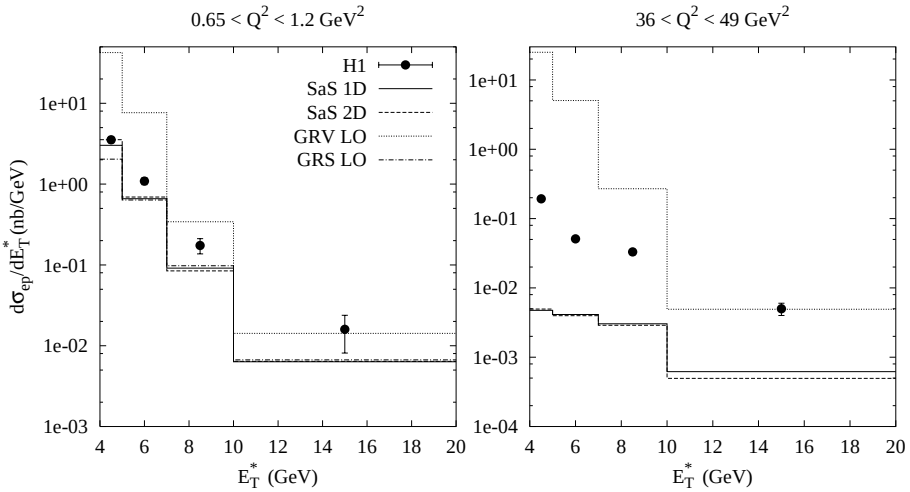

Figure 3.12: The differential jet cross sections $\mathrm{d}\sigma_{\mathrm{ep}}/\mathrm{d}E^*_\perp$ and $\mathrm{d}\sigma_{\mathrm{ep}}/\mathrm{d}\eta^*$ for jets with $-2.5 < \eta^* < -0.5$ and $0.3 < y < 0.6$. Only resolved events are used to show the sensitivity to the photon parton distribution.

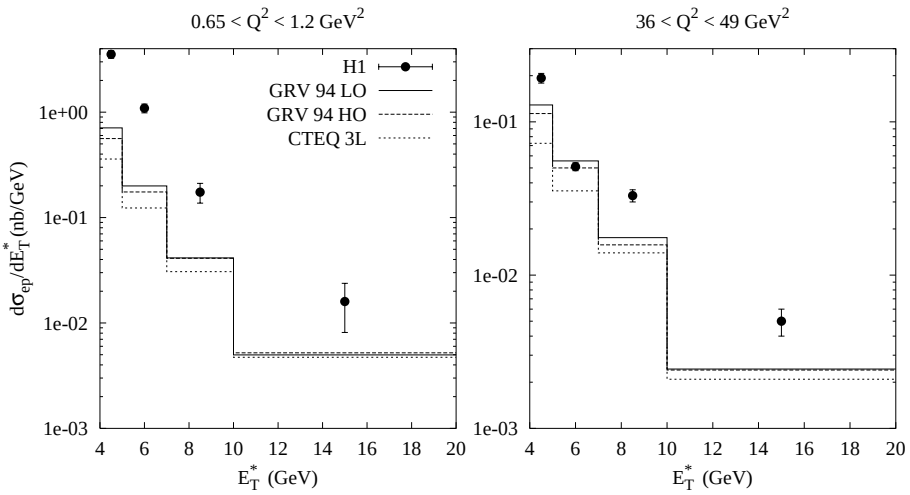

Figure 3.13: The differential jet cross sections $\mathrm{d}\sigma_{\mathrm{ep}}/\mathrm{d}E^*_\perp$ and $\mathrm{d}\sigma_{\mathrm{ep}}/\mathrm{d}\eta^*$ for jets with $-2.5 < \eta^* < -0.5$ and $0.3 < y < 0.6$. Only direct events are used to show the sensitivity to the proton parton distribution.

deceptive accident that the more well-known proton parton distribution gives a larger uncertainty than the photon one. It offers a simple example that also phenomenology of other areas may directly influence the interpretation of photon data.

Inclusive $\gamma^*\gamma^*$ Jet Cross Sections

The OPAL collaboration has measured inclusive one–jet cross sections in the range $|\eta^{\mathrm{jet}}| < 1$ and requiring $E_\perp^{\mathrm{jet}}$ to be larger than 3 GeV [35]. The centre of mass energies were 130 and 136 GeV. In the analysis, a cone jet algorithm was used with a cone radius $R = 1$ and $E_{\perp,\mathrm{min}}^{\mathrm{jet}} = 2$ GeV; differences in the application of this algorithm may affect the results (we used the PXCONE algorithm from HzTool). In Figs. 3.14–3.15, the inclusive jet cross sections as a function of $E_\perp^{\mathrm{jet}}$ or η^{jet} are shown, with events generated at $\sqrt{s_{\mathrm{ee}}} = 133$ GeV. The anti–tagging conditions at this energy corresponds to a $Q^2_{\mathrm{max}} = 0.8$ GeV^2. Due to migration effects $p_{\perp\mathrm{min}}^{\mathrm{parton}}$ was chosen to 1.5 GeV, and $p_{\perp\mathrm{min}}^{\mathrm{MI}} = 1.4$ GeV. The symmetric cuts used gives no difference between the two single–resolved contributions, instead the direct–VMD (VMD–direct) and direct–anomalous (anomalous–direct) contributions are shown together with the direct and double–resolved ones.

At low $E_\perp^{\mathrm{jet}}$ the double–resolved events are dominating and at larger $E_\perp^{\mathrm{jet}}$ it is

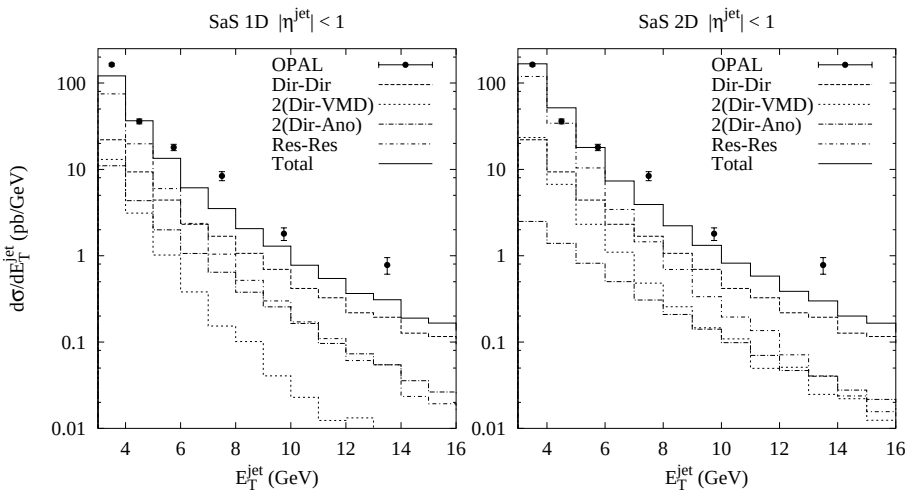

Figure 3.14: The inclusive one–jet cross section as a function of $E_\perp^{\rm jet}$ at the centre of mass energies $\sqrt{s_{\rm e^+e^-}} = 130$ and 136 GeV, $|\eta^{\rm jet}| < 1$. The events were generated at a fixed energy of $\sqrt{s_{\rm e^+e^-}} = 133$ GeV, $Q^2_{\rm max} = 0.8\,{\rm GeV}^2$, $p^{\rm parton}_{\perp{\rm min}} = 1.5$ GeV and $p^{\rm MI}_{\perp{\rm min}} = 1.4$ GeV.

the direct processes since more energy goes into the hard scattering in the latter case. For single–resolved events, the SaS 1D VMD component dies out much quicker with increasing $E_\perp^{\rm jet}$ than the SaS 2D one which is comparable with the direct–anomalous events at high $E_\perp^{\rm jet}$. For both cases, at high $E_\perp^{\rm jet}$, the direct–anomalous components give the same order of magnitude contribution to the cross section as the double–resolved events. The biggest difference between the two parton distributions can be seen at low $E_\perp^{\rm jet}$ and for the $|\eta^{\rm jet}|$ distributions, where the double–resolved events dominates; it is a reflection of the difference in normalization among the contributions. For the SaS 2D case, this kinematical region makes the VMD component more important than the anomalous one; as a consequence multiple interactions play an important role. The double–resolved contribution for SaS 2D without multiple interaction is half of the one shown here. Clearly, for the SaS 1D case the opposite is true: the importance of the components are reversed. In the region of high $E_\perp^{\rm jet}$, where the direct events dominate, the model is undershooting data. On the other hand, there is nice agreement with data for the $|\eta^{\rm jet}|$ distribution when using SaS 2D.

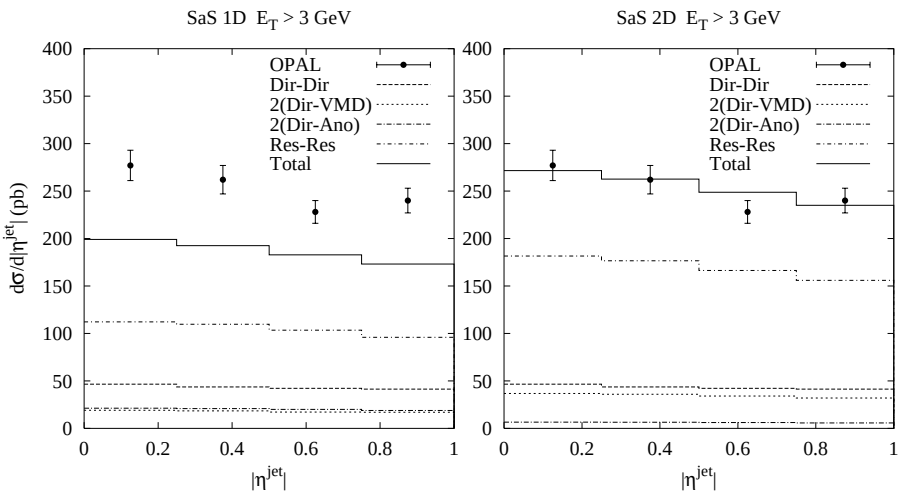

Figure 3.15: The inclusive one–jet cross section as a function of $\eta^{\rm jet}$ at the centre of mass energies $\sqrt{s_{\rm e^+e^-}} = 130$ and 136 GeV, $E_\perp^{\rm jet} > 3$ GeV. The events were generated at a fixed energy of $\sqrt{s_{\rm e^+e^-}} = 133$ GeV, $Q^2_{\rm max} = 0.8$ GeV^2, $p_{\perp\rm min}^{\rm parton} = 1.5$ GeV and $p_{\perp\rm min}^{\rm MI} = 1.4$ GeV.

Forward Jets in ep

Jet cross sections as a function of Bjorken-x, $x_{\rm Bj}$, for forward jet production (in the proton direction) have been measured at HERA [36]. The objective is to probe the dynamics of the QCD cascade at small $x_{\rm Bj}$. The forward jet is restricted in polar angle w.r.t. the proton and the transverse momenta $p_\perp^{\rm jet}$ should be of the same order as the virtuality of the photon, suppressing an evolution in transverse momenta. If the jet has a large energy fraction of the proton, there will be a big difference in x between the jet and the photon vertex, $x_{\rm Bj} \ll x_{\rm jet}$, allowing an evolution in x. The above restrictions will not eliminate the possibility of having a resolved photon, although the large Q^2 values are not in favour of it.

The HzTool routines were used to obtain the results in Fig. 3.16. Five different scales μ_i are shown. A larger forward jet cross section is obtained with a stronger Q^2 dependence, with the scale $\mu_5^2 = p_\perp^2 + Q^2$ in best agreement with data, in general agreement with the conclusions in [24][1]. The constraint

[1] However, we note a not complete agreement in the description of the inclusive jet cross sections. In [24] a different option of the SaS extension to virtual photons was used than here, but we have checked that this cannot be the main reason for the discrepancy.

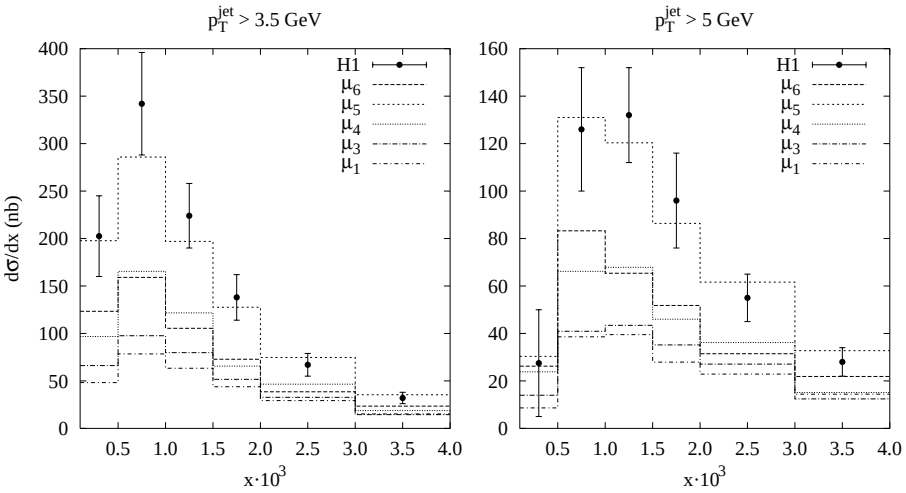

Figure 3.16: Forward jet cross section as a function of x compared with H1 data (with statistical and systematic uncertainties added in quadrature). Five different scales are shown at two different $p_\perp^{\rm jet}$ cuts, 3.5 and 5 GeV. $x_{\rm jet} > 0.035$, $0.5 < (p_\perp^{\rm jet})^2/Q^2 < 2$ and $7^\circ < \theta_{\rm jet} < 20^\circ$.

$(p_\perp^{\rm jet})^2 \simeq Q^2$ gives a large enhancement for the μ_4 and μ_5 scales, which are combinations of $(p_\perp^{\rm parton})^2$ and Q^2, whereas μ_2 and μ_3 have a Q^2 dependence that are scaled down by $\hat{s}$. The choice of scale does not only affect the resolved photon contribution but also the direct photon, as seen in Fig. 3.17. The available evolution ranges for the parton showers are related to the choice of μ scale and responsible for the major part of the difference between the two scales. Also the scale dependence in the proton parton distribution gives a contribution, but it is small. As a check for the direct component, a simple comparison was made between PYTHIA, using the $\mu_1 = p_\perp$ scale and the direct processes, and LEPTO [7], without soft colour interactions, giving similar results. The rather large Q^2 values, $Q^2 \simeq (p_\perp^{\rm jet})^2$, suppresses VMD photons and favours the SaS 1D distribution which is the one used here, though the difference is small.

Note that the μ_6 scale undershoots the forward jet cross section data and overshoots the inclusive jet distributions at low Q^2, so it is not a real alternative. As a further check, with more data accumulated and analyzed, the $(p_\perp^{\rm jet})^2/Q^2$ interval could be split into several subranges which hopefully would help to discriminate between scale choices.

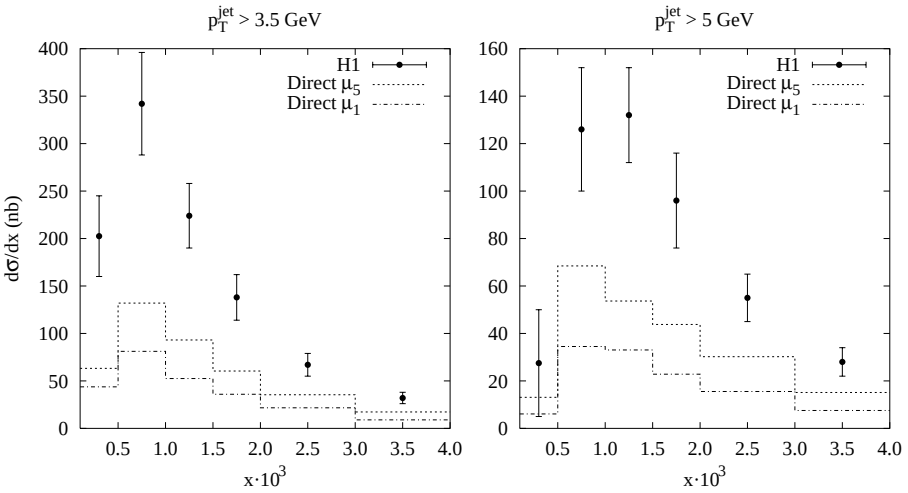

Figure 3.17: Same as in Fig. 3.16 but only the direct component is compared with data for two different scale choices.

Importance of Longitudinal Resolved Photons

In this section we will study the importance of longitudinal resolved photons. The different R-factors described in section 3.2.3 will be used to provide some estimates. Of those distributions studied so far, we will concentrate on the $\mathrm{d}\sigma_{\mathrm{ep}}/\mathrm{d}E_\perp^*$ distributions for inclusive jets and the $\mathrm{d}\sigma_{\mathrm{ep}}/\mathrm{d}x$ for forward jet cross sections. A sensible Q^2–dependent scale choice, μ_3, together with the SaS 1D distribution will be used throughout.

With $a = 1$ the different alternatives are shown in Fig. 3.18 for the $\mathrm{d}\sigma_{\mathrm{ep}}/\mathrm{d}E_\perp^*$ distributions together with the result from pure transverse photons, i.e. $a = 0$. The importance of the resolved contributions decreases with increasing Q^2, see Fig. 3.10, which makes the asymptotic behaviour less crucial. The onset of longitudinal photons governed by the R_1 and R_2 alternatives are favoured whereas the R_3 one overshoots data in the context of the other model choices made here.

In Fig. 3.19 the same alternatives are shown for the forward jet cross sections. With this scale choice, μ_3, none of the longitudinal resolved components (together with the direct contribution) are sufficient to describe the forward jet cross section. The resolved contribution with R_3 is about the same as the one obtained with the scale $\mu_5^2 = p_\perp^2 + Q^2$ (without longitudinal contribution); the difference in the total results originates from the difference in the direct contributions, see Fig. 3.17. With R_1 and $a = 1$, the μ_5 scale (not shown)

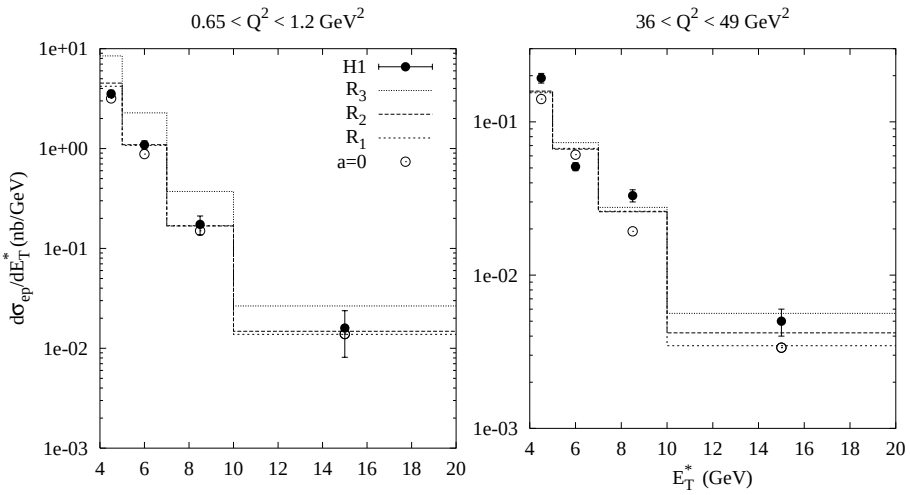

Figure 3.18: The differential jet cross section $\mathrm{d}\sigma_{\mathrm{ep}}/\mathrm{d}E^*_\perp$ for jets with $-2.5 < \eta^* < -0.5$ and $0.3 < y < 0.6$.

overshoots the data, but undershoots in combination with μ_4. The μ_4 scale in combination with R_3 and $a = 1$ is in nice agreement with data. However, with these model choices, R_3 together with the μ_3 scale was ruled out for the inclusive jet distributions studied above, and this is even more so for μ_4.

The above study indicates, as expected, that longitudinal resolved photons are important for detailed descriptions of various distributions. It cannot by itself explain the forward jet cross section, but may give a significant contribution. Combined with other effects, for example, different scale choices, parton distributions, underlying events, etc. it could give a reasonable description. The model(s) so far does not take into account the difference in x distribution or the k^2 scale (of the $\gamma^* \to \mathrm{q\overline{q}}$ fluctuations) between transverse and longitudinal photons. As long as the distributions under study allow a large interval in x the average description may be reasonable. In a more sophisticated treatment these aspects have to be considered in more detail.

3.3.3 Example of Further Tests: Forward Jets in $\mathrm{e^+e^-}$

With the experience of forward jets at HERA, we suggest a similar study at LEP. The optimal kinematical and forward jet constraints have to be set by each collaboration itself; the study here will give the order of magnitude for the cross section and point out uncertainties in the model.

Comparing with forward jets at HERA, one of the leptons will play the role

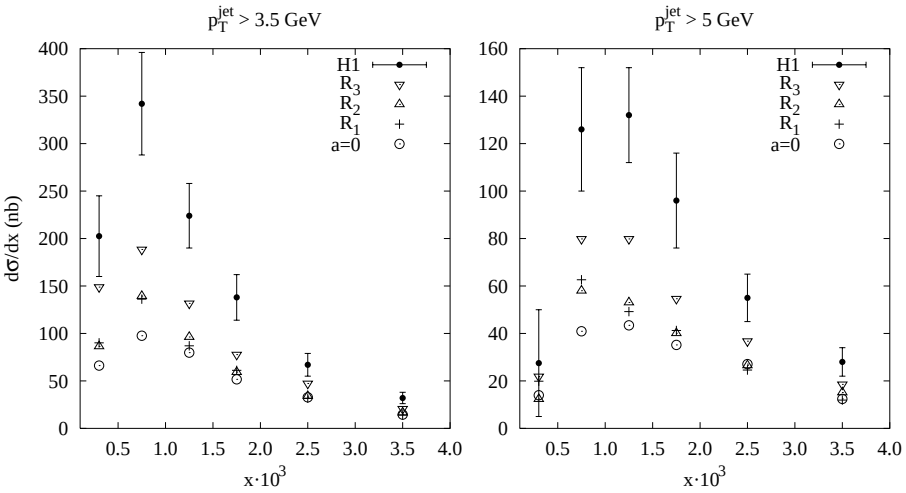

Figure 3.19: Forward jet cross section as a function of x.

of the proton. Some of the constraints will be taken over directly, kinematic cuts:

$$y > 0.1, \quad E'_e > 11 \text{ GeV}, \tag{3.46}$$

and jet selection:

$$p_\perp^{\text{jet}} > 3.5 \text{ GeV} \tag{3.47}$$

$$x_{\text{jet}} = \frac{E_{\text{jet}}}{E_{\text{e}}} > 0.035 \tag{3.48}$$

$$0.5 < \frac{(p_\perp^{\text{jet}})^2}{Q^2} < 2 \tag{3.49}$$

$$3^\circ < \theta_{\text{jet}} < 20^\circ \tag{3.50}$$

To fulfill the jet selection one of the leptons has to be tagged in order to know the virtuality of the photon. To obtain a reasonable number of events the other lepton is not tagged, imposing a Q^2_{max}, here chosen to 1.5 GeV^2. With a centre of mass energy of 200 GeV, the smallest accessible $x_{\text{Bj}} = \frac{Q^2}{ys}$ is around 10^{-4}, where Q^2 and y is calculated from the tagged electron, omitting the virtuality of the other photon. In a more sophisticated treatment also double–tagged events are analyzed; then one of the photons plays the role of a proton and the forward jet should be defined with respect to one of the photons.

A cone jet algorithm with cone radius $R = 1$ and $E_{\perp,\min}^{\text{jet}} = 2$ GeV is used for jet finding. As for the case at HERA, the μ_5 scale gives the largest forward jet cross section, about twice as large as with the μ_2 scale, Fig. 3.20. Most of the differences arise from the double–resolved events. Double–resolved and single–resolved events, where the resolved photon give rise to the forward jet, dominate the forward jet cross section, Fig. 3.20 and 3.21. At low x, for the μ_5 scale, the double–resolved contribution is close to an order of magnitude larger than the direct one. For the μ_2 scale it is about a factor of four. As for the case at HERA, the rise of the forward jet cross section at small x is dominated by resolved photons. A study like this at LEP could be an important cross check for the understanding of resolved photons and that of small-x dynamics.

3.4 Summary and Outlook

The field of photon physics is rapidly expanding, not least by the impact of new data from HERA and LEP. The prospects of building a Linear Collider, with its objective of high-precision measurements and to search for possible new physics, requires an accurate description of photon processes. The plan here is to have a complete description of the main physics aspects in γp and $\gamma\gamma$ collisions, which will allow important cross checks to test universality of certain model assumptions. As a step forward, we have in this article concentrated on those that are of importance for the production of jets by virtual photons, and are absent in the real-photon case. While we believe in the basic machinery developed and presented here, we have to acknowledge the many unknowns — scale choices, parton distribution sets (also those of the proton), longitudinal contributions, underlying events, etc. — that all give non-negligible effects. To make a simultaneous detailed tuning of all these aspects was not the aim here, but rather to point out model dependences that arise from a virtual photon.

When Q^2 is not small, naively only the direct component needs to be treated, but in practice a rather large contribution arises from resolved photons. For example, for high-Q^2 studies like forward jet cross sections, Fig. 3.16–3.17, or inclusive differential jet cross sections, Fig. 3.10–3.11. Resolved longitudinal photons are poorly understood and the model presented here can be used to estimate their importance and get a reasonable global description. The three different alternatives, together with other sound model choices, can explain the inclusive jet cross sections (for a wide range of photon virtualities) and the forward jet cross sections measured at HERA. With our conservative estimates, longitudinal effects are in most cases small but of importance for some particular distributions and for fine–tuning. Since some exclusive processes have strikingly large longitudinal contributions [37], effects larger than shown here should not be excluded.

The inclusive jet cross sections [33] were used to point out that the gluon

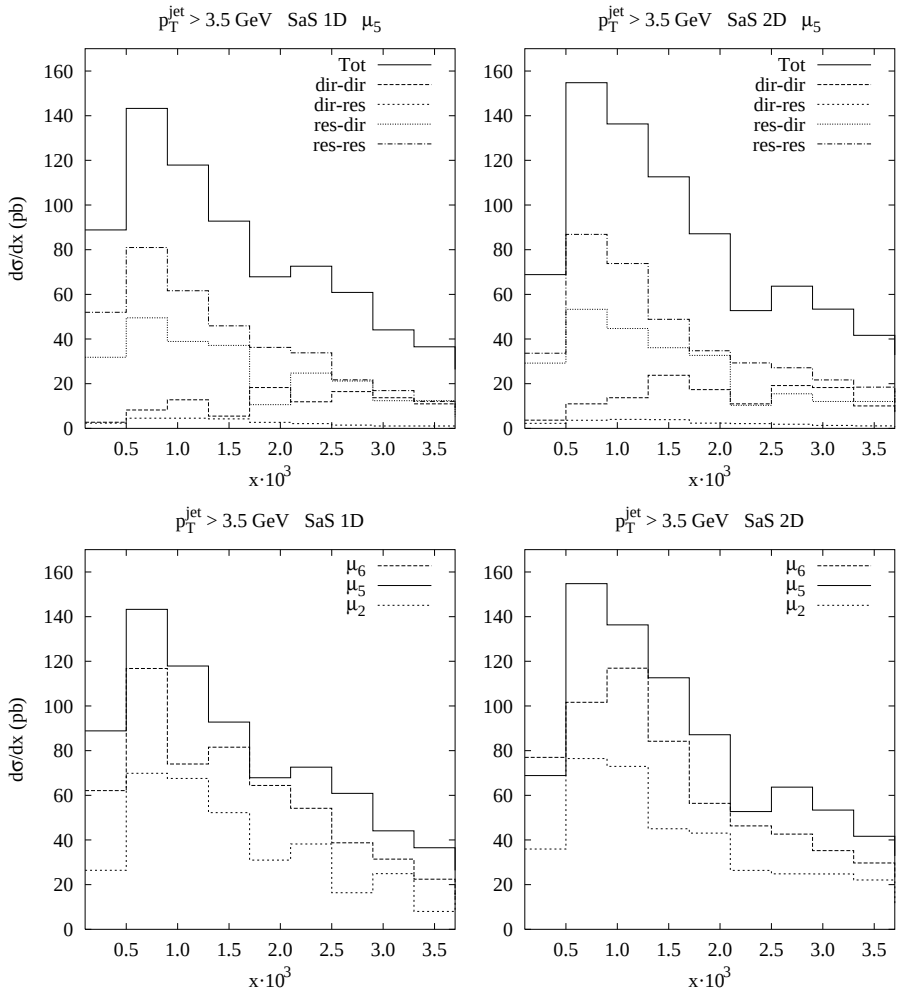

Figure 3.20: Forward jet cross section as a function of x. $p_\perp^{\rm jet} > 3.5$ GeV, $x_{\rm jet} > 0.035$, $0.5 < (p_\perp^{\rm jet})^2/Q^2 < 2$ and $3^\circ < \theta_{\rm jet} < 20^\circ$.

distribution of the proton may, of times, contribute more to the overall uncertainty than the virtual photon ones. A real photon parton distribution is ruled out already at small photon virtualities.

In the study of the dijet angular distributions in photoproduction [31] the relative amount of direct and resolved events is not so well described by the

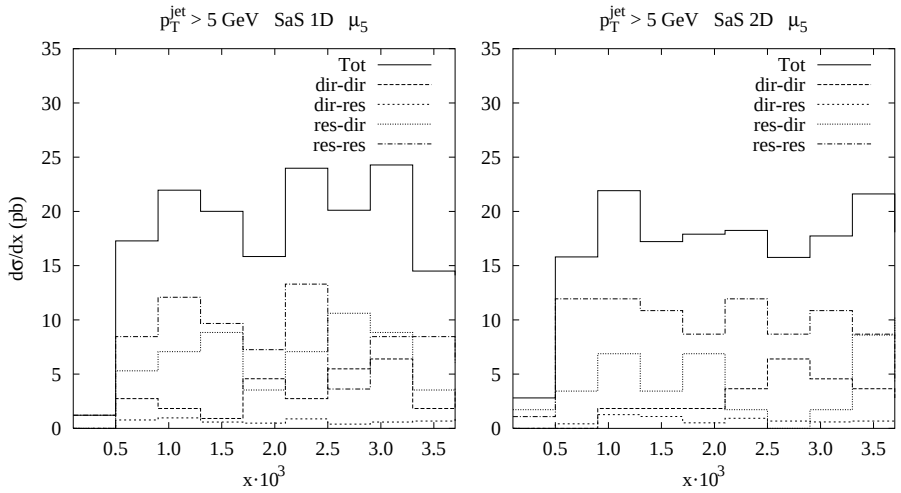

Figure 3.21: Forward jet cross section as a function of x. $p_\perp^{\rm jet} > 5$ GeV, $x_{\rm jet} > 0.035$, $0.5 < (p_\perp^{\rm jet})^2/Q^2 < 2$ and $3^\circ < \theta_{\rm jet} < 20^\circ$.

model. In the future, this could be improved by using lepton-inside-lepton structure functions. In order to describe the direct distribution, $x_\gamma > 0.75$, a resolved photon component is needed to explain the rise with $|\cos\theta^*|$, which is steeper than the $1/(1-|\cos\theta^*|)$ rise expected from the pure direct component.

The inclusive $\gamma^*\gamma^*$ one-jet cross sections [35] are well described except for the high $E_\perp^{\rm jet}$ region of the $E_\perp^{\rm jet}$ distribution. In this region, the direct events are dominating. Currently, owing to the lesser flexibility in the modeling of the direct component, we do not see any simple way to improve the model. The factorized ansatz made for the photon flux is expected to be valid in this kinematical range; interference terms are suppressed by $Q_1^2Q_2^2/W^2_{\gamma^*\gamma^*}$. However, differences in the application of the cone jet algorithm may affect the results.

The forward jet cross section presented by H1 [36] is well described by an ordinary parton shower prescription including the possibility of having resolved photons. The criteria that the $p_\perp^{\rm jet}$ should be of the same order as Q^2, makes the scale choice crucial and $\mu_5^2 = p_\perp^2 + Q^2$ is favoured by data, as concluded in [24]. However, we found this scale to be incompatible with inclusive jet cross sections: it overshoots data in the high-Q^2 bins. Longitudinal resolved photons modeled with a more restrictive scale choice, i.e. $\mu^2 \simeq p_\perp^2$, give a similar resolved photon contribution but less contribution from the direct component (due to different available evolution ranges in the parton showers and the scale dependence in the proton parton distribution). With more data accumulated and analyzed,

the $(p_\perp^{\rm jet})^2/Q^2$ interval could be split into several subranges, which hopefully would help to discriminate between different scale choices. With the experience of forward jets at HERA, we predict the forward jet cross section to be obtained at LEP.

Multiple interactions for the anomalous component are not yet included, and is not expected to be of same importance as in the VMD case. However, for low k^2 fluctuations it may be important, especially for SaS 1D, and need to be investigated.

After this study of jet production by virtual photons it is natural to extend the modeling to low–$p_\perp$ events. Clearly, a smooth transition from perturbative to non-perturbative physics is wanted. One idea is to make use of a parameterization of the total γp and $\gamma\gamma$ cross section in terms of a pomeron and a reggeon exchange. Starting from the real-photon case, dipole dampening factors are introduced for the generalization to virtual photons. For example, the γp cross section is divided into a VMD, an anomalous, a direct and a DIS $\gamma^*\mathrm{q} \to \mathrm{q}$ process part. In the limit $Q^2 \to 0$, the first three event classes remain. On the contrary, when Q^2 increases from zero to high Q^2; the resolved processes dies out (as given by the dipole factors), the direct also drops and finally only the DIS process remain. At intermediate Q^2 values, the direct processes and the DIS (+parton showers) process overlap, since, in some regions of phase space, they are equally valid descriptions of the same physics. It thus becomes necessary to avoid double-counting, e.g. by introducing Sudakov style form factors for the DIS process, suppressing those parton configurations covered by the direct processes. We intend to return to this issue in a future publication.

Acknowledgements

We acknowledge helpful conversations with, among others, Jon Butterworth, Jiri Chýla, Gerhard Schuler, Hannes Jung, Leif Jönsson, Ralph Engel and Tancredi Carli.

References

[1] ZEUS Collaboration, M. Derrick et al., *Phys. Lett.* **B322** (287) 1994;
H1 Collaboration, T. Ahmed et al., *Nucl. Phys.* **B445** (195) 1995.

[2] G.A. Schuler and T. Sjöstrand, *Nucl. Phys.* **B407** (539) 1993;
Z. Phys. **C73** (677) 1997.

[3] G.A. Schuler and T. Sjöstrand, *Z. Phys.* **C68** (607) 1995;
Phys. Lett. **B376** (193) 1996.

[4] T. Sjöstrand, *Computer Phys. Commun.* **82** (74) 1994;
http://www.thep.lu.se/∼torbjorn/Pythia.html.

[5] G. Marchesini, B.R. Webber, G. Abbiendi, I.G. Knowles, M.H. Seymour and L. Stanco, *Computer Phys. Commun.* **67** (465) 1992.

[6] H. Kharraziha and L. Lönnblad, *J. High Energy Phys.* **03** (006) 1998.

[7] G. Ingelman, A. Edin and J. Rathsman, *Computer Phys. Commun.* **101** (108) 1997.

[8] R. Engel and J. Ranft, *Phys. Rev.* **D54** (4244) 1996.

[9] H. Jung, *Computer Phys. Commun.* **86** (147) 1995.

[10] M. Glück, E. Reya and M. Stratmann, *Phys. Rev.* **D54** (5515) 1996; D. de Florian, C. Garcia Canal and R. Sassot, *Z. Phys.* **C75** (265) 1997; M. Klasen, G. Kramer and B. Pötter, *Eur. Phys. J.* **C1** (261) 1998.

[11] C.F. von Weiszäcker, *Z. Phys.* **88** (612) 1934.

[12] E.J. Williams, *Phys. Rev.* **45** (729) 1934.

[13] M. Klasen, G. Kramer and S.G. Salesch, *Z. Phys.* **C68** (113) 1995.

[14] V.M. Budnev, I.F. Ginzburg, G.V. Meledin and V.G. Serbo, *Phys. Rept.* **15** (181) 1975.

[15] G.A. Schuler, *Computer Phys. Commun.* **108** (279) 1998.

[16] G. Bonneau, M. Gourdin and F. Martin, *Nucl. Phys.* **B54** (573) 1973.

[17] S. Frixione, M.L. Mangano, P. Nason and G. Ridolfi, *Phys. Lett.* **B319** (339) 1993.

[18] V.N. Baier, E.A. Kuraev, V.S. Fadin and V.A. Khoze, *Phys. Rept.* **78** (293) 1981.

[19] G. Altarelli and G. Martinelli, *Phys. Lett.* **76B** (89) 1978; A. Mendéz, *Nucl. Phys.* **B145** (199) 1978; R. Peccei and R. Rückl, *Nucl. Phys.* **B162** (125) 1980; Ch. Rumpf, G. Kramer and J. Willrodt, *Z. Phys.* **C7** (337) 1981.

[20] B.L. Combridge, J. Kripfganz and J. Ranft, *Phys. Lett.* **70B** (234) 1977; R. Cutler and D. Sivers, *Phys. Rev.* **D17** (196) 1978.

[21] T. Sjöstrand, *Phys. Lett.* **157B** (321) 1985; M. Bengtsson, T. Sjöstrand and M. van Zijl, *Z. Phys.* **C32** (67) 1986.

[22] M. Glück, E. Reya and M. Stratmann, *Phys. Rev.* **D51** (3220) 1995.

[23] F.M. Borzumati and G.A. Schuler, *Z. Phys.* **C58** (139) 1993;
M. Drees and R.M. Godbole, *Phys. Rev.* **D50** (3124) 1994.

[24] H. Jung, L. Jönsson and H. Kuster, DESY 98-051 (hep-ph/9805396);
Eur. Phys. J. **C9** (383) 1999.

[25] B. Andersson, G. Gustafson, G. Ingelman and T. Sjöstrand,
Phys. Rept. **97** (31) 1983.

[26] CDF Collaboration, F. Abe et al., *Phys. Rev.* **D50** (5562) 1994.

[27] S. Frixione, M.L. Mangano, P. Nason and G. Ridolfi,
Nucl. Phys. **B431** (453) 1994;
L. Apanasevich et al., *Phys. Rev.* **D59** (074007) 1999;
G. Miu and T. Sjöstrand, *Phys. Lett.* **B449** (313) 1999.

[28] T. Sjöstrand and M. van Zijl, *Phys. Rev.* **D36** (2019) 1987.

[29] H1 Collaboration, S. Aid et al., *Z. Phys.* **C70** (17) 1996.

[30] L. Lönnblad and M. Seymour (convenors),
$\gamma\gamma$ *Event Generators*, in "Physics at LEP2", CERN 96-01,
Eds. G. Altarelli, T. Sjöstrand and F. Zwirner, Vol. 2 (1996) 187.

[31] ZEUS Collaboration, M. Derrick et al., *Phys. Lett.* **B384** (401) 1996.

[32] J. Bromley et al., HzTool — A Package for Monte Carlo Generator – Data
Comparison at HERA, http://www-h1.desy.de/∼h01rtc/hztool.html

[33] H1 Collaboration, C. Adloff et al., *Phys. Lett.* **B415** (418) 1997.

[34] M. Glück, E. Reya and A. Vogt, *Phys. Rev.* **D46** (1973) 1992;
Phys. Rev. **D45** (3986) 1992.

[35] OPAL Collaboration, K. Ackerstaff et al., *Z. Phys.* **C73** (433) 1997.

[36] H1 Collaboration, C. Adloff et al., *Nucl. Phys.* **B538** (3) 1998;
H1 Collaboration, S. Aid et al., *Phys. Lett.* **B356** (118) 1995;
ZEUS Collaboration, J. Breitweg et al., *Eur. Phys. J.* **C6** (239) 1998.

[37] H1 Collaboration, C. Adloff et al., DESY 99-010 (hep-ex/9902019),
to appear in *Eur. Phys. J.* **C**;
ZEUS Collaboration, J. Breitweg et al., *Eur. Phys. J.* **C6** (603) 1999.

Total Cross Sections and Event Properties from Real to Virtual Photons

Paper IV

Total Cross Sections and Event Properties from Real to Virtual Photons

Christer Friberg and Torbjörn Sjöstrand

Department of Theoretical Physics,
Lund University, Lund, Sweden

Abstract

A model for total cross sections with virtual photons is presented. In particular γ^*p and $\gamma^*\gamma^*$ cross sections are considered. Our approach extends on a model for photoproduction, where the total cross section is subdivided into three distinct event classes: direct, VMD and anomalous. With increasing photon virtuality, the latter two decrease in importance. Instead Deep Inelastic Scattering dominates, with the direct class being the $\mathcal{O}(\alpha_s)$ correction thereof. Hence, the model provides a smooth transition between the two regions. By the breakdown into different event classes, one may aim for a complete picture of all event properties.

4.1 Introduction

Traditionally, different descriptions are used for virtual (γ^*) and real (γ) photons. Virtual photons in the DIS (Deeply Inelastic Scattering) region are normally described as devoid of any structure, while for the real ones, the possibility of hadronic-like fluctuations play an important rôle. In the region of intermediate Q^2, it should be possible to find a description starting from either extreme. Then the language may not always be unique, i.e. a given Feynman diagram may be classified in different ways.

Several paths are possible; one is to have an explicit description in terms of higher-order Feynman diagrams [1], which then may contain several hard scales. However, in this article a main point is to obtain a smooth transition to soft physics, beyond the region of validity of perturbation theory, and then it is convenient to be able to consider transitions in one scale at a time. In the following, we will therefore develop one specific approach, where the main principle is to characterize events by a set of standard scales, such as the photon virtuality (or virtualities for $\gamma^*\gamma^*$), the photon resolution scale(s), and the hard scale of a partonic subprocess. Here the photon resolution scale is a measure of the virtuality of a hadronic fluctuation (separate from that of the photon itself), e.g. m_ρ when a photon fluctuates to a ρ meson. Depending on the relative ordering of these scales, events are classified in different categories. Special emphasis is normally put on the hardest scale of the event. This may determine e.g. whether an event is classified as a DIS or a resolved photon one. Matrix elements are defined to lowest required order only, and higher-order corrections are approximated by parton showers. For instance, if the hard scale is larger than the resolution scale of the photon, a partonic evolution is allowed between the two scales. The DGLAP equations are then suitable for this evolution [2] and are to be combined with the appropriate leading-order matrix elements, responsible for the hard scattering. In a γ^*p event, the photon resolution scale may well be smaller than both the photon virtuality and the hard-scattering scale. In this way, partly unordered evolutions in $p_\perp$ are accounted for. This is still less complete than allowed by the CCFM equations [3, 4], where the ordering may be broken in several steps, but could well provide the bulk of non-ordering effects at current energies.

The classification used here is not an economical route, however, since it leads to many event classes. For studies e.g. of the total cross section in the intermediate-Q^2 region, it is cumbersome and not necessarily better than existing approaches [5]. However, by the breakdown into distinct event classes, the road is open to provide a (more or less) complete picture of all event properties. It is this latter aspect that has then guided the model development.

As an example, the γ^*p cross section is divided into a VMD, an anomalous, a direct and a DIS component. In the limit $Q^2 \to 0$, the DIS process $\gamma^*\mathrm{q} \to \mathrm{q}$ becomes kinematically forbidden and only the first three event classes remain,

reproducing the result from the photoproduction model (except for some improvements). On the contrary, when Q^2 increases from zero to high values, the resolved processes decrease in importance (as given by dipole dampening factors for each mass component individually), the direct ones also drops (by Q^2 dependence and a shrinking phase space) and finally only the DIS process remain. At intermediate Q^2 values, the direct processes and the DIS (+parton showers) process overlap, since, in some regions of phase space, they are equally valid descriptions of the same physics. It thus becomes necessary to avoid double-counting, e.g. by introducing Sudakov style form factors for the DIS process, suppressing those parton configurations covered by the direct processes.

Based on the study of jet production by virtual photons [6] we extend the modeling to low–$p_\perp$ events. Clearly, a smooth transition from perturbative to non-perturbative physics is desired, and is achieved partly by allowing for multiple parton–parton scatterings. These are needed to explain the underlying event activity seen in the data in hadron–hadron collisions [7], and the ideas will be taken over to the hadronic resolved photon components. At the same time, the multiple parton–parton interactions unitarize the jet cross sections, a necessity for a decent growth of the total cross section with increasing energy.

The outline of the paper is as follows. First, the different event classes are presented, including an extension to virtual photons of a model for photoproduction. How the event classes are combined, in order to avoid double-counting but still to cover the whole phase space, is described in detail. Then, results of the model are presented, with some comparisons to available data. In particular, total cross sections with virtual photons are shown with emphasis on the importance of the different event classes at various photon virtualities. Some distributions of event properties are shown to vary significantly with the photon virtuality, others less so, illustrating a complex model working smoothly between the regions of real and highly virtual photons. Similarities in γp and $\gamma\gamma$ events will be pointed out where appropriate. Finally, a summary and an outlook is given.

4.2 Event Classes

In the following, we begin by a reminder on the models for DIS and photoproduction, before embarking on the generalization also to intermediate virtualities in γ^*p processes. The $\gamma\gamma$, $\gamma^*\gamma$ and $\gamma^*\gamma^*$ processes thereafter follow by an application of the same rules.

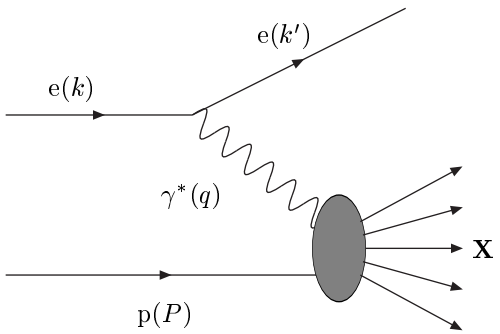

Figure 4.1: Deeply inelastic charged lepton-hadron scattering. (The four-momenta are given in parentheses.)

4.2.1 Deeply Inelastic Scattering

The Deeply Inelastic Scattering of a high-energy charged lepton off a proton target, Fig. 4.1, involves a single electroweak boson exchange between a beam lepton and a target quark. At not too large Q^2 only photon exchange need be considered. Then the double-differential ep cross-section for DIS can be expressed in terms of the total cross-section for virtual transverse (T) and longitudinal (L) photons [8]:

$$\frac{\mathrm{d}^2\sigma(\mathrm{ep}\to\mathrm{e}\mathbf{X})}{\mathrm{d}y\,\mathrm{d}Q^2} = f^{\mathrm{T}}_{\gamma/\mathrm{e}}(y,Q^2)\sigma_{\mathrm{T}}(y,Q^2) + f^{\mathrm{L}}_{\gamma/\mathrm{e}}(y,Q^2)\sigma_{\mathrm{L}}(y,Q^2)\ , \tag{4.1}$$

with the fluxes

$$f^{\mathrm{T}}_{\gamma/\mathrm{e}}(y,Q^2) = \frac{\alpha_{\mathrm{em}}}{2\pi}\left(\frac{1+(1-y)^2}{y}\frac{1}{Q^2} - \frac{2m_{\mathrm{e}}^2 y}{Q^4}\right)\ , \tag{4.2}$$

$$f^{\mathrm{L}}_{\gamma/\mathrm{e}}(y,Q^2) = \frac{\alpha_{\mathrm{em}}}{2\pi}\frac{2(1-y)}{y}\frac{1}{Q^2}\ . \tag{4.3}$$

The conventional DIS variables

$$y = \frac{qP}{kP}\ , \qquad x = \frac{Q^2}{2qP} = \frac{Q^2}{Q^2+W^2-m_{\mathrm{p}}^2}\ ,$$
$$Q^2 = -q^2\ , \qquad W^2 = (q+P)^2\ , \tag{4.4}$$

are related e.g. by

$$Q^2 = xy\,2kP\ , \qquad W^2 = (1-x)y\,2kP + m_{\mathrm{p}}^2\ , \tag{4.5}$$

where $2kP \approx (k+P)^2 = s$. Thus there are only two kinematical degrees of freedom.

The cross-sections can be related to the proton structure functions F_2 and F_L by [9, 10]

$$\begin{aligned} F_2(x,Q^2) &= \frac{Q^2}{4\pi^2\alpha_\mathrm{em}} \frac{(1-x)Q^2}{(Q^2+4m_\mathrm{p}^2x^2)} (\sigma_\mathrm{T}+\sigma_\mathrm{L}) \,, \\ F_\mathrm{L}(x,Q^2) &= \frac{Q^2}{4\pi^2\alpha_\mathrm{em}} \frac{(1-x)Q^2}{(Q^2+4m_\mathrm{p}^2x^2)} \sigma_\mathrm{L} \end{aligned} \tag{4.6}$$

and the total virtual photon-proton cross section by

$$\begin{aligned} \sigma_\mathrm{tot}^{\gamma^*\mathrm{p}} \equiv \sigma_\mathrm{T}+\sigma_\mathrm{L} &= \frac{4\pi^2\alpha_\mathrm{em}}{Q^2} \frac{(Q^2+4m_\mathrm{p}^2x^2)}{(1-x)Q^2} F_2(x,Q^2) \\ &\simeq \frac{4\pi^2\alpha_\mathrm{em}}{Q^2(1-x)} F_2(x,Q^2) \,. \end{aligned} \tag{4.7}$$

The final, approximate form is valid for $W^2 \gg Q^2$, which is our region of main interest.

In the parton model,

$$F_2(x,Q^2) = \sum_\mathrm{q} e_\mathrm{q}^2 \left\{ xq(x,Q^2) + x\overline{q}(x,Q^2) \right\} \;, \quad F_L(x,Q^2) = 0 \,, \tag{4.8}$$

to lowest order. Such an interpretation is not valid in the limit $Q^2 \to 0$, where gauge invariance requires $F_2(x,Q^2) \to 0$ so that $\sigma_\mathrm{tot}^{\gamma^*\mathrm{p}}$ remains finite. We will replace the DIS description by a photoproduction one in this limit. Hence, at small photon virtualities, the DIS process $\gamma^*\mathrm{q} \to \mathrm{q}$ should be constructed vanishingly small as compared to the contribution from the interaction of the hadronic component of the photon (to be discussed in the next section). To obtain a well-behaved DIS cross section in this limit, a $Q^4/(Q^2+m_\rho^2)^2$ factor is introduced. Here m_ρ is some non-perturbative hadronic parameter, for simplicity identified with the ρ mass. One of the $Q^2/(Q^2+m_\rho^2)$ factors is required already to give finite $\sigma_\mathrm{tot}^{\gamma\mathrm{p}}$ for conventional parton distributions, and could be viewed as a screening of the individual partons at small Q^2. The second factor is chosen to give not only a finite but actually a vanishing $\sigma_\mathrm{DIS}^{\gamma^*\mathrm{p}}$ for $Q^2 \to 0$ in order to retain the pure photoproduction description there. This latter factor thus is more a matter of convenience, and other approaches could have been pursued. Then, in the parton model, eq. (4.7) modifies to a DIS cross section

$$\sigma_\mathrm{DIS}^{\gamma^*\mathrm{p}} \simeq \frac{4\pi^2\alpha_\mathrm{em}Q^2}{(Q^2+m_\rho^2)^2} \sum_\mathrm{q} e_\mathrm{q}^2 \left\{ xq(x,Q^2) + x\overline{q}(x,Q^2) \right\} \,. \tag{4.9}$$

For numerical studies, the available parton distribution parameterizations for the proton have some lower limit of applicability in both x and Q^2. For values below these minimal ones, the parton distributions are frozen at the lower limits.

4.2.2 Photoproduction

To first approximation, the photon is a point-like particle. However, quantum mechanically, it may fluctuate into a (charged) fermion–antifermion pair. The fluctuations $\gamma \leftrightarrow \mathrm{q\overline{q}}$ can interact strongly and therefore turn out to be responsible for the major part of the γp total cross section. The total rate of $\mathrm{q\overline{q}}$ fluctuations is not perturbatively calculable, since low-virtuality fluctuations enter a domain of non-perturbative QCD physics. It is therefore customary to split the spectrum of fluctuations into a low-virtuality and a high-virtuality part. The former part can be approximated by a sum over low-mass vector-meson states, customarily (but not necessarily) restricted to the lowest-lying vector multiplet. Phenomenologically, this Vector Meson Dominance (VMD) ansatz turns out to be very successful in describing a host of data. The high-virtuality part, on the other hand, should be in a perturbatively calculable domain.

In total, the photon wave function can then be written as

$$|\gamma\rangle = c_{\mathrm{bare}}|\gamma_{\mathrm{bare}}\rangle + \sum_{V=\rho^0,\omega,\phi,\mathrm{J}/\psi} c_V|V\rangle + \sum_{\mathrm{q=u,d,s,c,b}} c_{\mathrm{q}}|\mathrm{q\overline{q}}\rangle + \sum_{\ell=\mathrm{e},\mu,\tau} c_\ell|\ell^+\ell^-\rangle \tag{4.10}$$

(neglecting the small contribution from Υ). In general, the coefficients c_i depend on the factorization scale μ used to probe the photon. Thus $c_\ell^2 \approx (\alpha_{\mathrm{em}}/2\pi)(2/3)\ln(\mu^2/m_\ell^2)$. Introducing a cut-off parameter k_0 to separate the low- and high-virtuality parts of the $\mathrm{q\overline{q}}$ fluctuations, one similarly obtains $c_{\mathrm{q}}^2 \approx (\alpha_{\mathrm{em}}/2\pi)2e_{\mathrm{q}}^2\ln(\mu^2/k_0^2)$. The VMD part corresponds to the range of $\mathrm{q\overline{q}}$ fluctuations below k_0 and is thus μ-independent (assuming $\mu > k_0$). In conventional notation $c_V^2 = 4\pi\alpha_{\mathrm{em}}/f_V^2$, with $f_V^2/4\pi$ determined from data to be 2.20 for ρ^0, 23.6 for ω, 18.4 for ϕ and 11.5 for J/ψ [10]. The k_0 parameter is constrained by fits to F_2^γ, i.e. to the parton distributions of the photon, to be $k_0 \simeq 0.6$ GeV [11]. (The fits also contain other model uncertainties, and are only logarithmically dependent on k_0, so the precision is not high.) Finally, c_{bare} is given by unitarity: $c_{\mathrm{bare}}^2 \equiv Z_3 = 1 - \sum c_V^2 - \sum c_{\mathrm{q}}^2 - \sum c_\ell^2$. In practice, c_{bare} is always close to unity. Usually the factorization (and renormalization) scale μ is taken to be the transverse momentum of a $2 \to 2$ parton-level process.

The subdivision of the above photon wave function corresponds to the existence of three main event classes in γp events [12], cf. Fig. 4.2:

1. The VMD processes, where the photon turns into a vector meson before

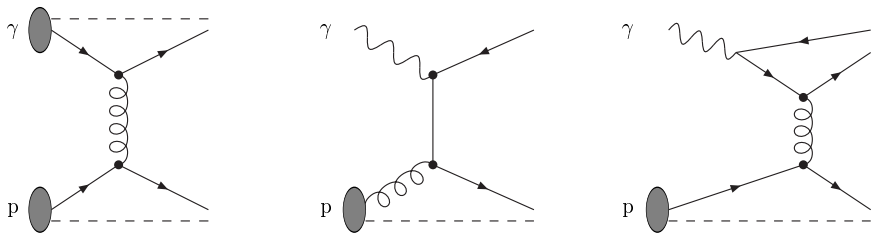

Figure 4.2: Contributions to hard γp interactions: a) VMD, b) direct, and c) anomalous. Only the basic graphs are illustrated; additional partonic activity is allowed in all three processes. The presence of spectator jets has been indicated by dashed lines, while full lines show partons that (may) give rise to high-$p_\perp$ jets.

the interaction, and therefore all processes allowed in hadronic physics may occur. This includes elastic and diffractive scattering as well as low-$p_\perp$ and high-$p_\perp$ non-diffractive events.

2. The direct processes, where a bare photon interacts with a parton from the proton.
3. The anomalous processes, where the photon perturbatively branches into a $\mathrm{q\overline{q}}$ pair, and one of these (or a daughter parton thereof) interacts with a parton from the proton.

All three processes are of $\mathcal{O}(\alpha_{\mathrm{em}})$. However, in the direct contribution the photon structure function is of $\mathcal{O}(1)$ and the hard scattering matrix elements of $\mathcal{O}(\alpha_{\mathrm{em}})$, while the opposite holds for the VMD and the anomalous processes. The $\ell^+\ell^-$ fluctuations are not interesting for us, and there is thus no class associated with them.

The difference between the three classes is reflected in the beam jet structure. The incoming proton always gives a beam jet containing the partons of the proton that did not interact. On the photon side, the direct processes do not give a beam jet at all, since all the energy of the photon is involved in the hard interaction. The VMD ones (leaving aside the elastic and diffractive subprocesses for the moment) give a beam remnant just like the proton, with a moderately small 'primordial $k_\perp$' smearing. The anomalous processes give a beam remnant produced by the $\gamma \to \mathrm{q\overline{q}}$ branching, with a transverse momentum going from k_0 upwards.

Based on the different event classes discussed above, the total photoproduction cross section can be written as

$$\sigma_{\mathrm{tot}}^{\gamma\mathrm{p}} = \sigma_{\mathrm{VMD}}^{\gamma\mathrm{p}} + \sigma_{\mathrm{direct}}^{\gamma\mathrm{p}} + \sigma_{\mathrm{anomalous}}^{\gamma\mathrm{p}} \,. \tag{4.11}$$

Total hadronic cross sections show a characteristic fall-off at low energies

and a slow rise at higher energies. This behaviour can be parameterized by the form

$$\sigma_{\rm tot}^{AB}(s) = X^{AB} s^{\epsilon} + Y^{AB} s^{-\eta} \tag{4.12}$$

for $A + B \to X$. The powers ϵ and η are universal, with fit values [13]

$$\epsilon \approx 0.0808 \; , \qquad \eta \approx 0.4525 \; , \tag{4.13}$$

while the coefficients X^{AB} and Y^{AB} are process-dependent. Equation (4.12) can be interpreted within Regge theory, where the first term corresponds to pomeron exchange and gives the asymptotic rise of the cross section. The second term, the reggeon one, is mainly of interest at low energies. For the purpose of our study we do not have to rely on the Regge interpretation of eq. (4.12), but can merely consider it as a convenient parameterization.

The VMD part of the γp cross section is an obvious candidate for a hadronic description. The diagonal VMD model suggests:

$$\sigma_{\rm VMD}^{\gamma {\rm p}}(s) = \sum_{V=\rho^0,\omega,\phi,{\rm J}/\psi} \frac{4\pi\alpha_{\rm em}}{f_V^2} \, \sigma_{\rm tot}^{V{\rm p}}(s) \; . \tag{4.14}$$

Assuming an additive quark model the Vp cross sections can be parameterized as [12]

$$\begin{aligned}
\sigma_{\rm tot}^{\rho^0 {\rm p}}(s) &\approx \sigma_{\rm tot}^{\omega {\rm p}}(s) \approx \frac{1}{2} \left(\sigma_{\rm tot}^{\pi^+ {\rm p}} + \sigma_{\rm tot}^{\pi^- {\rm p}} \right) \approx 13.63 s^{\epsilon} + 31.79 s^{-\eta} \;\; [{\rm mb}] \; , \\
\sigma_{\rm tot}^{\phi {\rm p}}(s) &\approx \sigma_{\rm tot}^{{\rm K}^+ {\rm p}} + \sigma_{\rm tot}^{{\rm K}^- {\rm p}} - \sigma_{\rm tot}^{\pi^- {\rm p}} \approx 10.01 s^{\epsilon} - 1.52 s^{-\eta} \;\; [{\rm mb}] \; , \\
\sigma_{\rm tot}^{{\rm J}/\psi {\rm p}}(s) &\approx \frac{m_\phi^2}{m_{{\rm J}/\psi}^2} \, \sigma_{\rm tot}^{\phi {\rm p}}(s) \approx \frac{1}{10} \, \sigma_{\rm tot}^{\phi {\rm p}}(s) \; ,
\end{aligned} \tag{4.15}$$

with s in GeV^2. Adding the vector meson contributions, we arrive at

$$\sigma_{\rm VMD}^{\gamma {\rm p}}(s) \approx 53.4 s^{\epsilon} + 115 s^{-\eta} \;\; [\mu{\rm b}] \; . \tag{4.16}$$

There is no compelling reason that such an ansatz should hold also for the total γp cross section, but empirically a parameterization according to

$$\sigma_{\rm tot}^{\gamma {\rm p}}(s) = X^{\gamma {\rm p}} s^{\epsilon} + Y^{\gamma {\rm p}} s^{-\eta} = 67.7 s^{\epsilon} + 129 s^{-\eta} \;\; [\mu{\rm b}] \tag{4.17}$$

does a good job [13]. For instance, these parameter values were used to predict the high-energy behaviour of the cross section, close to what was then measured by H1 and ZEUS. Thus VMD corresponds to approximately 80% of the total γp cross section at high energies, with the remaining 20% then shared among the direct and anomalous event classes.

The anomalous contribution can be written as

$$\sigma^{\gamma \mathrm{p}}_{\mathrm{anomalous}}(s) = \frac{\alpha_{\mathrm{em}}}{2\pi} \sum_{\mathrm{q}} 2\mathrm{e}_{\mathrm{q}}^2 \int_{k_0^2}^{\infty} \frac{\mathrm{d}k_\perp^2}{k_\perp^2} \, \sigma^{\mathrm{q}\overline{\mathrm{q}}\mathrm{p}}(s; k_\perp) \tag{4.18}$$

where the prefactor and integral over $\mathrm{d}k_\perp^2/k_\perp^2$ corresponds to the probability for the photon to split into a $\mathrm{q}\overline{\mathrm{q}}$ state of transverse momenta $\pm k_\perp$. The cross section for this $\mathrm{q}\overline{\mathrm{q}}$ pair to scatter against the proton, $\sigma^{\mathrm{q}\overline{\mathrm{q}}\mathrm{p}}$, need to be modeled. Based only on geometrical scaling arguments (to be discussed in the next section), one could expect a decrease roughly like $1/k_\perp^2$. This suggests an ansatz

$$\sigma^{\mathrm{q}\overline{\mathrm{q}}\mathrm{p}}(s; k_\perp) = \frac{k_{V(\mathrm{q}\overline{\mathrm{q}})}^2}{k_\perp^2} \, \sigma^{V(\mathrm{q}\overline{\mathrm{q}})\mathrm{p}}(s) \; . \tag{4.19}$$

The $k_{V(\mathrm{q}\overline{\mathrm{q}})}$ is a free parameter introduced for dimensional reasons. It could be associated with the typical $k_\perp$ inside the vector meson V formed from a $\mathrm{q}\overline{\mathrm{q}}$ pair: $\rho^0 \approx \omega$ for u and d, ϕ for s, J/ψ for c. As a reasonable ansatz, one could guess $k_{V(\mathrm{q}\overline{\mathrm{q}})} \approx m_V/2 \approx m_\rho/2$. (For heavier quarks, a higher mass scale is indicated, but also a correspondingly larger lower integration limit in $k_\perp^2$, so the two effects cancel more or less.) Fits to the total cross section at not too high energies, with a large VMD and a small direct contributions subtracted, give corresponding numbers, $k_{V(\mathrm{q}\overline{\mathrm{q}})} \approx 0.4$ GeV for a $k_0 \approx 0.5$ GeV. These values are here related to each other: if the latter were to be changed, the former would have to be retuned accordingly. In the following we use this set of numbers. The anomalous cross section can thus be written as

$$\sigma^{\gamma \mathrm{p}}_{\mathrm{anomalous}}(s) = \frac{\alpha_{\mathrm{em}}}{2\pi} \sum_{\mathrm{q}} 2\mathrm{e}_{\mathrm{q}}^2 \int_{k_0^2}^{\infty} \frac{\mathrm{d}k_\perp^2}{k_\perp^2} \, \frac{k_{V(\mathrm{q}\overline{\mathrm{q}})}^2}{k_\perp^2} \, \sigma^{V(\mathrm{q}\overline{\mathrm{q}})\mathrm{p}}(s) \tag{4.20}$$

To leading order, the direct events come in two kinds: QCD Compton $\gamma\mathrm{q} \to \mathrm{qg}$ (QCDC) and boson-gluon fusion $\gamma\mathrm{g} \to \mathrm{q}\overline{\mathrm{q}}$ (BGF). The cross sections are divergent in the limit $k_\perp \to 0$ for the outgoing parton pair. Therefore a lower cut-off is required, but no other specific model assumptions.

4.2.3 Combining the photoproduction processes

The VMD, direct and anomalous classes have so far been considered separately. The complete physics picture presumably would provide smooth transitions between the various possibilities. To understand the relation between the processes, consider the simple graph of Fig. 4.3a. There two transverse momentum scales, $k_\perp$ and $p_\perp$, are introduced. Here $k_\perp$ is related to the $\gamma \to \mathrm{q}\overline{\mathrm{q}}$ vertex while $p_\perp$ is the hardest QCD $2 \to 2$ subprocess of the ladder between the photon and the proton. Further softer partons in the ladder are omitted for

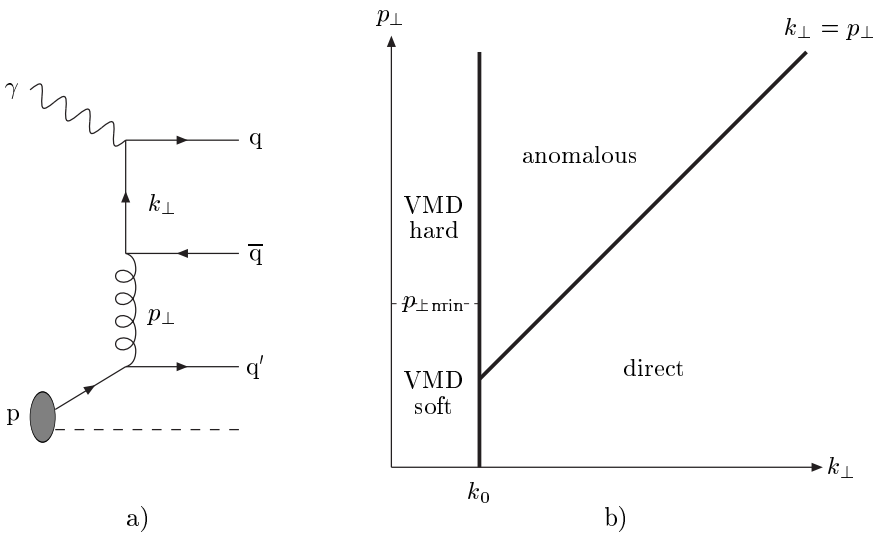

Figure 4.3: (a) Schematic graph for a hard γp process, illustrating the concept of two different scales. (b) The allowed phase space for this process, with one subdivision into event classes.

clarity, i.e. for a large $p_\perp$ one would expect a sequence of intermediate virtualities $k_\perp < p_{\perp 1} < p_{\perp 2} < \ldots < p_{\perp n} < p_\perp$ on the photon side of the event, and a similar sequence from some nonperturbative cutoff scale Q_0 to $p_\perp$ on the proton side. The allowed phase space can then conveniently be represented by a two-dimensional plane, Fig. 4.3b. The region $k_\perp < k_0$ corresponds to a small transverse momentum at the $\gamma \to \mathrm{q}\overline{\mathrm{q}}$ vertex, and thus to VMD processes. For $k_\perp > k_0$, the events are split along the diagonal $k_\perp = p_\perp$. If $k_\perp > p_\perp$, the hard $2 \to 2$ process of Fig. 4.3a is $\gamma\mathrm{g} \to \mathrm{q}\overline{\mathrm{q}}$, and the lower part of the graph is part of the leading log QCD evolution of the gluon distribution inside the proton. These events are direct ones. If $p_\perp > k_\perp$, on the other hand, the hard process is $\overline{\mathrm{q}}\mathrm{q}' \to \overline{\mathrm{q}}\mathrm{q}'$, and the $\gamma \to \mathrm{q}\overline{\mathrm{q}}$ vertex builds up the quark distribution inside a photon. These events are thus anomalous ones.

It should be remembered that the classification is only simple away from the border regions. When $k_\perp \approx p_\perp$, say, a description either in terms of anomalous or direct interactions would be possible. Also higher-order corrections will blur the picture, although pragmatic separations normally can be found.

A comment on the choice of variables. Instead of the squared transverse momenta $k_\perp^2$ and $p_\perp^2$ one could equally well have imagined the squared virtualities $-k^2$ and $-p^2$. However, in many processes several Feynman graphs contribute, both in the t-, u- and s-channel. The association of $p^2 = \hat{t}$ or $p^2 = \hat{u}$

is then not unique, while $p_\perp^2 = \hat{t}\hat{u}/\hat{s}$ is well-defined and coincides with $-\hat{t}$ or $-\hat{u}$ in the respective singular limit. Whether events are classified by one kind of scale or another should not be relevant, at least so long as one is consistent and stays with a leading-order description. Only for the virtual photon do we use the scale $Q^2 = -q^2 = -\hat{t}$ rather than $q_\perp^2$, in order to stay in line with conventional notation, and because there is no scale choice ambiguity here.

What complicates the picture is that an event may contain several interactions, once one considers an incoming particle as a composite object with several partons that may interact, more or less independently of each other, with partons from the other incoming particle. Such a multiple parton–parton interaction scenario is familiar already from pp physics [7]. Here the jet cross section, above some $p_{\perp\min}$ scale of the order of 2 GeV, increases faster with energy than the total cross section. Above an energy of a few hundred GeV the calculated jet cross section is larger than the observed total one. Multiple interactions offers a solution to this apparent paradox, by squeezing a larger number of jet pairs into the average event, a process called unitarization or eikonalization. The perturbative jet cross section can then be preserved, at least down to $p_{\perp\min}$, but in the reinterpreted inclusive sense. At the same time, the unitarization plays a crucial rôle in taming the growth of the total cross section.

The composite nature of hadrons also fills another function: it regularizes the singularity of perturbative cross sections, such as qg $\to$ qg, in the limit $p_\perp \to 0$. Perturbative calculations assume free colour charges in the initial and final states of the process, while the confinement in hadrons introduces some typical colour neutralization distance. It is the inverse of this scale that appears as some effective cutoff scale $p_{\perp\min} \simeq 2$ GeV, most likely with a slow energy dependence [14]. One possible parameterization is

$$p_{\perp\min}(s) = (1.9\ \text{GeV}) \left(\frac{s}{1\ \text{TeV}^2} \right)^{\epsilon} , \tag{4.21}$$

with the same ϵ as in eq. (4.13), since the rise of the total cross section with energy via Regge theory is related to the small-x behaviour of parton distributions and thus to the density of partons.

Now, if an event contains interactions at several different $p_\perp$ scales, standard practice is to classify this event by its hardest interaction. Several reasons can be given; one is that a softer interaction may be confused with QCD radiation emitted from the harder one, and thus cannot be identified on an exclusive basis. With this prescription, the cross section for an event of scale $p_\perp$ is the naive jet cross section at this $p_\perp$ scale *times* the probability that the event contained no interaction at a scale above $p_\perp$. The latter defines a form factor, related to probability conservation, analogously to but not equivalent with the Sudakov form factor of parton showers. At large $p_\perp$ values the probability of

having an even larger $p_\perp$ is small, i.e. the form factor is close to unity, and the perturbative cross section is directly preserved in the event rate. At lower $p_\perp$ values, the likelihood of a larger $p_\perp$ is increased, i.e. the form factor becomes smaller than unity, and the rate of events classified by this $p_\perp$ scale falls below the perturbative answer.

We expect this picture to hold also for the VMD part of the photon, since this is clearly in the domain of hadronic physics. Thus, in the VMD domain $k_\perp < k_0$, the region of large $p_\perp$ in Fig. 4.3b is populated according to perturbation theory, though with nonperturbative input to the parton distributions. The region of smaller $p_\perp$ is suppressed, since the form factor here drops significantly below unity.

As one moves away from the 'pure' VMD states, such as the ρ^0, much of the same picture could well hold. Interactions at a larger $k_\perp$ value could be described in terms of some ρ' state. The uncertainty relation gives us that a state of virtuality $\simeq k_\perp$ has a maximal size $\simeq 1/k_\perp$ and thus spans an area $\propto 1/k_\perp^2$. In a naive picture, the ρ'p cross section would then drop with increasing $k_\perp$, but flatten out at a value given by the proton size. We know that this is not the scaling observed in nature, however, where e.g. the J/ψp cross section is much below the ϕp one [15]. Rather it appears that the cross section is proportional to the area of the state interacting with the proton, i.e. a (kind of) geometrical scaling. Such a behaviour becomes understandable (but not easily predicted in detail) when one remembers that the colour neutralization distance inside a more virtual photon state is also reduced, so that the interactions in general tend to be weakened by interference effects not included in the simple perturbative cross sections. This could then be the origin for a geometrical scaling like the one in eq. (4.19).

Alternatively to the geometric approach, the anomalous and direct cross sections for such a $k_\perp$ state could be calculated. If these latter are larger than the geometrical scaling answer, one could expect multiple interaction effects to become important and couple the two event classes. That is, the presence of an anomalous interaction of some large $p_\perp$ would preempt the event from being classifiable as a direct one with a lower $p_\perp$, in analogy with the discussion on hadronic physics above. One can even attempt eikonalized descriptions [16], although such require a number of assumptions to be made.

Calculating the perturbative anomalous cross section in the region given by $p_\perp > \max(k_\perp, p_{\perp\min}(s))$, the geometric scaling answer is exceeded for some region $k_\perp \lesssim k_1$, with $k_1 \approx 2 - 4$ GeV (higher for higher energies). Only for $k_\perp > k_1$ is the jet cross section dropping below the geometric scaling one. At these larger $k_\perp$ values, the direct rate dominates over the anomalous. As a convenient but rather arbitrary choice, for subsequent studies we put $k_1 = p_{\perp\min}(s)$, with the latter given by eq. (4.21). This value lies below the crossover point noted above, but the simple modified geometrical scaling picture is not

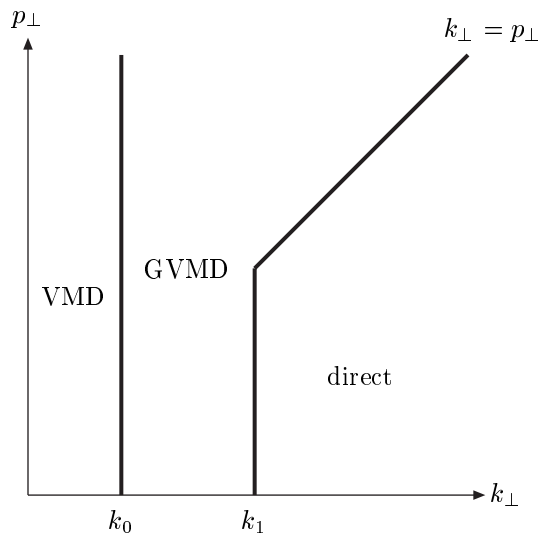

Figure 4.4: An alternative classification of the phase space in Fig. 4.3, which better takes into account unitarization effects.

precise enough that it can be trusted too far, so a separate k_1 parameterization would seem excessive.

The final scenario is illustrated in Fig. 4.4. The bulk of the cross section, in the region $k_\perp < k_1$, is now described by the photon interacting as dense, hadronic states, VMD for $k_\perp \lesssim k_0$ and Generalized VMD (GVMD) for $k_0 \lesssim k_\perp \lesssim k_1$. The total VMD cross section is given by the pomeron-type ansatz, while the jet cross section can be obtained from the parton distributions of the respective vector meson state. Correspondingly, the GVMD states have a total cross section based on Pomeron considerations and a jet cross section now based on the anomalous part of the parton distributions of the photon. In principle, an eikonalization should be performed for each GVMD state separately, but in practice that would be overkill. Instead the whole region is represented by one single state per quark flavour, with a jet production given by the full anomalous part of the photon distributions. By extending this jet rate also to the region $k_\perp > k_1$, one does introduce a small mismatch between the low-$p_\perp$ and high-$p_\perp$ descriptions, but retains the correct full jet rate at high $p_\perp$'s. (This mismatch will increase in the corresponding scenario for a very virtual GVMD photon, but at the same time the GVMD component itself becomes less important, so it is not a major worry.) Implicitly, the presence of a spectrum of $k_\perp$ states can be taken into account by the choice of a

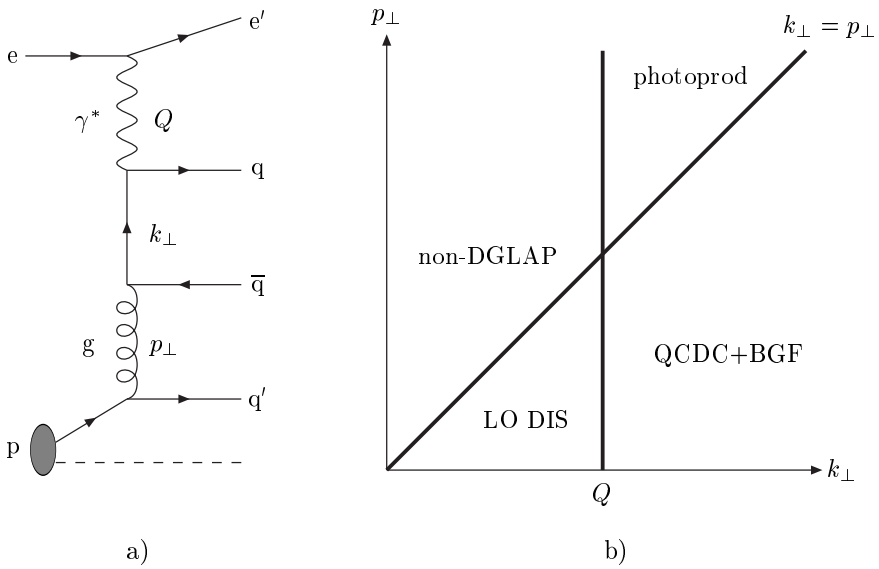

Figure 4.5: (a) Schematic graph for a hard γ^*p process, illustrating the concept of three different scales. (b) Event classification in the large-Q^2 limit.

realistic $p_\perp$ spectrum of the photon beam remnant, maybe still without the full correlation structure between the high-$p_\perp$ and low-$p_\perp$ parts of the individual events.

Thus, post facto, the approximate validity of a Regge theory ansatz for $\sigma_{\rm tot}^{\gamma \rm p}$ is making sense. Above k_1 only the direct cross section need be considered, since here the anomalous one is negligibly small, at least in terms of total cross sections. (As noted above, we have actually chosen to lump it with the other GVMD contributions, so as not to lose the jet rate itself.) Numerically, the recipe of extending the anomalous contribution to infinity according to a GVMD scaling recipe, as is done in eq. (4.20), is about equally good. The latter may involve some double-counting with the direct cross section, but not more than falls within the general uncertainty of the geometric scaling and eikonalization game.

4.2.4 DIS revisited

In DIS, the photon virtuality Q^2 introduces a further scale to the process, i.e. one goes from Fig. 4.3a to Fig. 4.5a. The traditional DIS region is the strongly ordered one, $Q^2 \gg k_\perp^2 \gg p_\perp^2$, where DGLAP-style evolution [2] is responsible

for the event structure. As above, ideology wants strong ordering, while real life normally is based on ordinary ordering $Q^2 > k_\perp^2 > p_\perp^2$. Then the parton-model description of $F_2(x, Q^2)$ in eq. (4.8) is a very good first approximation. The problems come when the ordering is no longer well-defined, i.e. either when the process contains several large scales or when $Q^2 \to 0$. In these regions, an $F_2(x, Q^2)$ may still be defined by eq. (4.7), but its physics interpretation is not obvious.

Let us first consider a large Q^2, where a possible classification is illustrated in Fig. 4.5b. The regions $Q^2 > p_\perp^2 > k_\perp^2$ and $p_\perp^2 > Q^2 > k_\perp^2$ correspond to non-ordered emissions, that then go beyond DGLAP validity and instead have to be described by the BFKL [17] or CCFM [3] equations, see e.g. [4]. Normally one expects such cross sections to be small at large Q^2. The (sparsely populated) region $p_\perp^2 > k_\perp^2 > Q^2$ can be viewed as the interactions of a resolved (anomalous) photon.

The region $k_\perp^2 > Q^2 \gg 0$ and $k_\perp^2 > p_\perp^2$ contains the $\mathcal{O}(\alpha_s)$ corrections to the lowest-order (LO) DIS process $\gamma^*\mathrm{q} \to \mathrm{q}$, namely QCD Compton $\gamma^*\mathrm{q} \to \mathrm{qg}$ and boson-gluon fusion $\gamma^*\mathrm{g} \to \mathrm{q\overline{q}}$. These are nothing but the direct processes $\gamma\mathrm{q} \to \mathrm{qg}$ and $\gamma\mathrm{g} \to \mathrm{q\overline{q}}$ extended to virtual photons. The borderline $k_\perp^2 > Q^2$ is here arbitrary — also processes with $k_\perp^2 < Q^2$ could be described in this language. In the parton model, this whole class of events are implicitly included in F_2, and are related to the logarithmic scaling violations of the parton distributions. The main advantage of a separation at $k_\perp = Q$ thus comes from the matching to photoproduction. Also the exclusive modeling of events, with the attaching of parton showers of scale Q^2 to DIS events, is then fairly natural.

The DIS cross section thus is subdivided into

$$\sigma_{\mathrm{tot}}^{\gamma^*\mathrm{p}} \simeq \frac{4\pi^2\alpha_{\mathrm{em}}Q^2}{(Q^2+m_\rho^2)^2}F_2(x,Q^2) = \sigma_{F_2}^{\gamma^*\mathrm{p}} \simeq \sigma_{\mathrm{DIS}}^{\gamma^*\mathrm{p}} = \sigma_{\mathrm{LO\,DIS}}^{\gamma^*\mathrm{p}} + \sigma_{\mathrm{QCDC}}^{\gamma^*\mathrm{p}} + \sigma_{\mathrm{BGF}}^{\gamma^*\mathrm{p}} \,. \tag{4.22}$$

The $\sigma_{\mathrm{DIS}}^{\gamma^*\mathrm{p}}$ is given by eq. (4.9), while the last two terms are well-defined by an integration of the respective matrix element [6]. When extended to small Q^2, these two terms will increase in importance, and one may eventually encounter a $\sigma_{\mathrm{LO\,DIS}}^{\gamma^*\mathrm{p}} < 0$, if calculated by a subtraction of the QCDC and BGF terms from the total DIS cross section. However, here we expect the correct answer not to be a negative number but an exponentially suppressed one, by a Sudakov form factor. This modifies the cross section:

$$\sigma_{\mathrm{LO\,DIS}}^{\gamma^*\mathrm{p}} = \sigma_{\mathrm{DIS}}^{\gamma^*\mathrm{p}} - \sigma_{\mathrm{QCDC}}^{\gamma^*\mathrm{p}} - \sigma_{\mathrm{BGF}}^{\gamma^*\mathrm{p}} \quad \longrightarrow \quad \sigma_{\mathrm{DIS}}^{\gamma^*\mathrm{p}} \, \exp\left(-\frac{\sigma_{\mathrm{QCDC}}^{\gamma^*\mathrm{p}} + \sigma_{\mathrm{BGF}}^{\gamma^*\mathrm{p}}}{\sigma_{\mathrm{DIS}}^{\gamma^*\mathrm{p}}}\right) \,. \tag{4.23}$$

Since we here are in a region where $\sigma_{\mathrm{DIS}}^{\gamma^*\mathrm{p}} \ll \sigma_{F_2}^{\gamma^*\mathrm{p}}$, i.e. where the DIS cross section is no longer the dominant one, this change of the total DIS cross section

is not essential. Even more, for $Q^2 \to 0$ we know that the direct processes should survive whereas the lowest-order DIS one has to vanish. Since eq. (4.9) ensures that $\sigma_{\mathrm{DIS}}^{\gamma^*\mathrm{p}} \to 0$ in this limit, it also follows that $\sigma_{\mathrm{LO\,DIS}}^{\gamma^*\mathrm{p}}$ does so.

4.2.5 From Real to Virtual Photons

It is now time to try to combine the different aspects of the photon, to provide an answer that smoothly interpolates between the photoproduction and DIS descriptions, in a physically sensible way.

A virtual photon has a reduced probability to fluctuate into a vector meson state, and this state has a reduced interaction probability. This can be modeled with the traditional dipole factors [18]

$$\sigma_{\mathrm{VMD}}^{\gamma^*\mathrm{p}}(s,Q^2) = \sum_{V=\rho^0,\omega,\phi,\mathrm{J}/\psi} \frac{4\pi\alpha_{\mathrm{em}}}{f_V^2} \left(\frac{m_V^2}{m_V^2+Q^2}\right)^2 \sigma_{\mathrm{tot}}^{V\mathrm{p}}(s) \; . \tag{4.24}$$

Similarly, the GVMD states are affected,

$$\sigma_{\mathrm{GVMD}}^{\gamma^*\mathrm{p}}(s,Q^2) = \frac{\alpha_{\mathrm{em}}}{2\pi} \sum_{\mathrm{q}} 2\mathrm{e}_{\mathrm{q}}^2 \int_{k_0^2}^{k_1^2} \frac{\mathrm{d}k_\perp^2}{k_\perp^2} \left(\frac{4k_\perp^2}{4k_\perp^2+Q^2}\right)^2 \frac{k_{V(\mathrm{q}\overline{\mathrm{q}})}^2}{k_\perp^2} \sigma^{V(\mathrm{q}\overline{\mathrm{q}})\mathrm{p}}(s) \; , \tag{4.25}$$

where a relation $2k_\perp \simeq m$ is assumed. Note that the dipole factor here occurs for each mass/$k_\perp$ state individually; after integration over $k_\perp$ the GVMD fall-off with Q^2 is slower than a simple dipole.

The above generalization to virtual photons does not address the issue of longitudinal photons. Their interactions vanish in the limit $Q^2 \to 0$, but can well give a non-negligible contribution at finite Q^2 [19]. A common approach is to attribute the longitudinal cross section with an extra factor of $r_V = a_V Q^2/m_V^2$ relative to the transverse one [20], where a_V is some unknown parameter to be determined from data. Such an ansatz only appears reasonable for moderately small Q^2, however, so following the lines of our previous study of jet production by virtual photons [6], we will try the two alternatives

$$r_1(m_V^2,Q^2) = a\frac{4m_V^2Q^2}{(m_V^2+Q^2)^2} \; , \tag{4.26}$$

$$r_2(m_V^2,Q^2) = a\frac{4Q^2}{(m_V^2+Q^2)} \; . \tag{4.27}$$

While r_1 vanishes for high Q^2, r_2 approaches the constant value a. The above VMD expressions are again extended to GVMD by the identification $m_V \approx$

$2k_\perp$. The cross sections can then be written as

$$\sigma^{\gamma^*\mathrm{p}}_{\mathrm{VMD}}(W^2,Q^2) = \sum_{V=\rho^0,\omega,\phi,\mathrm{J}/\psi} \frac{4\pi\alpha_{\mathrm{em}}}{f_V^2}\left[1+r_i(m_V^2,Q^2)\right] \times \times \left(\frac{m_V^2}{m_V^2+Q^2}\right)^2 \sigma^{V\mathrm{p}}_{\mathrm{tot}}(W^2)\,, \quad (4.28)$$

$$\sigma^{\gamma^*\mathrm{p}}_{\mathrm{GVMD}}(W^2,Q^2) = \frac{\alpha_{\mathrm{em}}}{2\pi}\sum_{\mathrm{q}} 2\mathrm{e}_{\mathrm{q}}^2 \int_{k_0^2}^{k_1^2} \frac{\mathrm{d}k_\perp^2}{k_\perp^2}\left[1+r_i(4k_\perp^2,Q^2)\right] \times \times \left(\frac{4k_\perp^2}{4k_\perp^2+Q^2}\right)^2 \frac{k^2_{V(\mathrm{q}\overline{\mathrm{q}})}}{k_\perp^2}\,\sigma^{V(\mathrm{q}\overline{\mathrm{q}})\mathrm{p}}(W^2)\,. \quad (4.29)$$

Note that we also here replaced s by the conventional DIS variable W^2; obviously both refer to the same γ^*p squared invariant mass.

The extrapolation to $Q^2 > 0$ is trivial for the direct processes, which coincide with the DIS QCDC and BGF processes. The matrix elements contain all the required Q^2 dependence, with a smooth behaviour in the $Q^2 \to 0$ limit. They are to be applied to the region $k_\perp > \max(k_1, Q)$ (and $k_\perp > p_\perp$, as usual).

Remains the LO DIS process. It is here that one could encounter an overlap and thereby double-counting with the VMD and GVMD processes. Comparing Fig. 4.5b with Fig. 4.4, one may note that the region $p_\perp > k_\perp$ involves no problems, since we have made no attempt at a non-DGLAP DIS description but cover this region entirely by the VMD/GVMD descriptions. Also, if $Q > k_1$, then the region $k_1 < k_\perp < Q$ (and $k_\perp > p_\perp$) is covered by the DIS process only. So it is in the corner $k_\perp < k_1$ that the overlap can occur. If Q^2 is very small, the exponential factor in eq. (4.23) makes the DIS contribution too small to worry about. Correspondingly, if Q^2 is very big, the VMD/GVMD contributions are too small to worry about. Furthermore, a large Q^2 implies a Sudakov factor suppression of a small $k_\perp$ in the DIS description. If W^2 is large, the multiple-interaction discussions above are relevant for the VMD/GVMD states: the likelihood of an interaction at large $p_\perp$ will preempt the population of the low-$p_\perp$ region.

In summary, it is only in the region of intermediate Q^2 and rather small W^2 that we have reason to worry about a significant double-counting. As we shall see, it is indeed in this region that the VMD/GVMD contribution does not appear to dampen quite as fast as data indicates. Typically, this is the region where $x \approx Q^2/(Q^2+W^2)$ is not close to zero, and where F_2 is dominated by the valence-quark contribution. The latter behaves roughly $\propto (1-x)^n$, with an n of the order of 3 or 4. Therefore we will introduce a corresponding damping factor to the VMD/GVMD terms. The real damping might be somewhat different but, since small W values are not our prime interest, we rest content with this approximate form.

In total, we have now arrived at our ansatz for all Q^2

$$\begin{aligned}\sigma_{\mathrm{tot}}^{\gamma^*\mathrm{p}} &= \sigma_{\mathrm{DIS}}^{\gamma^*\mathrm{p}} \exp\left(-\frac{\sigma_{\mathrm{QCDC}}^{\gamma^*\mathrm{p}}+\sigma_{\mathrm{BGF}}^{\gamma^*\mathrm{p}}}{\sigma_{\mathrm{DIS}}^{\gamma^*\mathrm{p}}}\right) + \sigma_{\mathrm{QCDC}}^{\gamma^*\mathrm{p}} + \sigma_{\mathrm{BGF}}^{\gamma^*\mathrm{p}} \\ &+ \left(\frac{W^2}{Q^2+W^2}\right)^n \left(\sigma_{\mathrm{VMD}}^{\gamma^*\mathrm{p}} + \sigma_{\mathrm{GVMD}}^{\gamma^*\mathrm{p}}\right) , \end{aligned} \tag{4.30}$$

where the DIS, VMD and GVMD terms are given by eqs. (4.9), (4.28) and (4.29), respectively, and the QCDC and BGF terms by direct integration of the respective matrix elements for the region $k_\perp > \max(k_1, Q)$. To keep the terminology reasonably compact, also for the $\gamma^*\gamma^*$ case below, we will use res as shorthand for the resolved VMD plus GVMD contributions and dir as shorthand for the QCDC and BGF processes. Then eq. (4.30) simplifies to

$$\sigma_{\mathrm{tot}}^{\gamma^*\mathrm{p}} = \sigma_{\mathrm{DIS}}^{\gamma^*\mathrm{p}} \exp\left(-\frac{\sigma_{\mathrm{dir}}^{\gamma^*\mathrm{p}}}{\sigma_{\mathrm{DIS}}^{\gamma^*\mathrm{p}}}\right) + \sigma_{\mathrm{dir}}^{\gamma^*\mathrm{p}} + \left(\frac{W^2}{Q^2+W^2}\right)^n \sigma_{\mathrm{res}}^{\gamma^*\mathrm{p}} . \tag{4.31}$$

4.2.6 Photon–photon collisions

A generalization of the γp picture to $\gamma\gamma$ events is obtained by noting that each of the two incoming photons is described by a wave function of the type given in eq. (4.10). In total, there are therefore three times three event classes. By symmetry, the 'off-diagonal' combinations appear pairwise, so for real photons the number of distinct classes is only six. These are, cf. Fig. 4.6:

1. VMD×VMD: both photons turn into hadrons, and the processes are therefore the same as allowed in hadron–hadron collisions.
2. VMD×direct: a bare photon interacts with the partons of the VMD photon.
3. VMD×anomalous: the anomalous photon perturbatively branches into a $\mathrm{q\overline{q}}$ pair, and one of these (or a daughter parton thereof) interacts with a parton from the VMD photon.
4. Direct×direct: the two photons directly give a quark pair, $\gamma\gamma \to \mathrm{q\overline{q}}$. Also lepton pair production is allowed, $\gamma\gamma \to \ell^+\ell^-$, but will not be considered by us.
5. Direct×anomalous: the anomalous photon perturbatively branches into a $\mathrm{q\overline{q}}$ pair, and one of these (or a daughter parton thereof) directly interacts with the other photon.
6. Anomalous×anomalous: both photons perturbatively branch into $\mathrm{q\overline{q}}$ pairs, and subsequently one parton from each photon undergoes a hard interaction.

Most of the above classes above are pretty much the same as allowed in γp events, since the interactions of a VMD or anomalous photon and those of a proton are about the same. Only the direct×direct class offer a new hard subprocess.

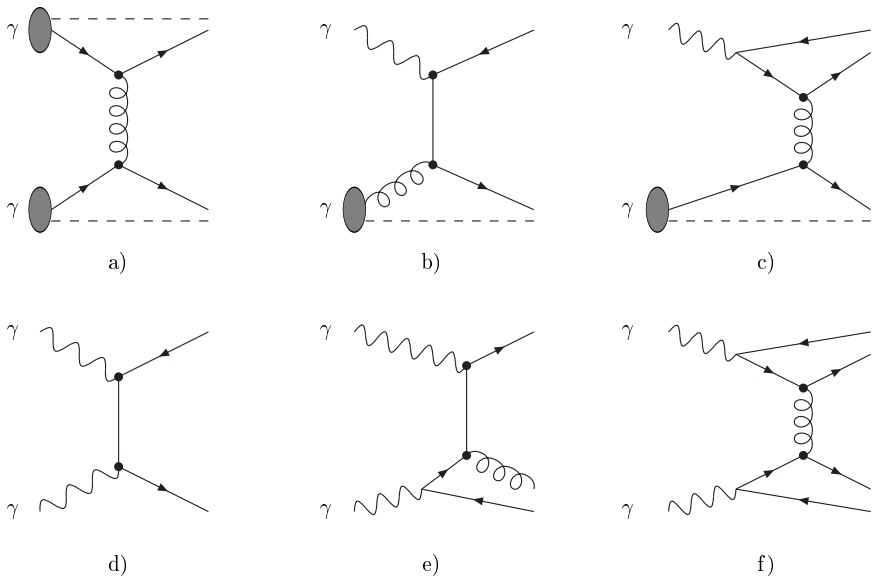

Figure 4.6: Contributions to hard real $\gamma\gamma$ interactions: a) VMD×VMD, b) VMD×direct, c) VMD×anomalous, d) direct×direct, e) direct×anomalous, and f) anomalous×anomalous. Notation as in Fig. 4.2.

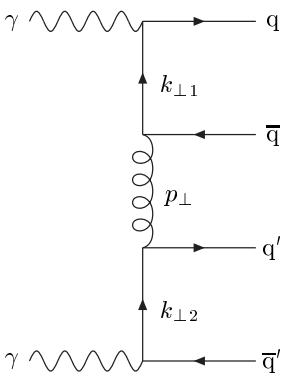

1. VMD×VMD: $k_{\perp 1}, k_{\perp 2} < k_0$, arbitrary $p_\perp$
2. VMD×direct: $k_{\perp 1} < k_0 < p_\perp < k_{\perp 2}$
   + $(1 \leftrightarrow 2)$
3. VMD×anomalous: $k_{\perp 1} < k_0 < k_{\perp 2} < p_\perp$
   + $(1 \leftrightarrow 2)$
4. Direct×direct: $k_0 < k_{\perp 1} = k_{\perp 2}$
5. Direct×anomalous: $k_0 < k_{\perp 1} < p_\perp < k_{\perp 2}$
   + $(1 \leftrightarrow 2)$
6. Anomalous×anomalous: $k_0 < k_{\perp 1}, k_{\perp 2} < p_\perp$

Figure 4.7: Schematic graph for a hard $\gamma\gamma$ process, showing the three different scales. To the right is shown the relation to the six classes in the text.

The main parton-level processes that occur in the above classes are:

- The 'direct' processes $\gamma\gamma \to \mathrm{q\overline{q}}$ only occur in class 4.
- The 'single-resolved' processes $\gamma\mathrm{q} \to \mathrm{qg}$ and $\gamma\mathrm{g} \to \mathrm{q\overline{q}}$ occur in classes 2 and 5.
- The 'double-resolved' processes $\mathrm{qq'} \to \mathrm{qq'}$ (where $\mathrm{q'}$ may also represent an antiquark), $\mathrm{q\overline{q}} \to \mathrm{q'\overline{q}'}$, $\mathrm{q\overline{q}} \to \mathrm{gg}$, $\mathrm{qg} \to \mathrm{qg}$, $\mathrm{gg} \to \mathrm{q\overline{q}}$ and $\mathrm{gg} \to \mathrm{gg}$ occur in classes 1, 3 and 6.

The classification of a generic Feynman diagram by the different possible components is illustrated in Fig. 4.7. The appearance of more scales makes it infeasible to draw diagrams like Fig. 4.3b, but the principles are the same.

Also the extension to virtual photons follows from the $\gamma^*\mathrm{p}$ formalism above, but now with (up to) five scales to keep track of: $p_\perp$, $k_{\perp 1}$, $k_{\perp 2}$, Q_1 and Q_2. First consider the three by three classes present already for real photons, which remain nine distinct ones for $Q_1^2 \neq Q_2^2$. Each VMD or GVMD state is associated with its dipole damping factor and its correction factor for the longitudinal contribution. The QCDC and BGF matrix elements involving one direct photon on a VMD or a GVMD state explicitly contain the dependence on the direct photon virtuality, separately given for the transverse and the longitudinal contributions. Also the direct×direct matrix elements are known for the four possible transverse/longitudinal combinations. Some examples should be enough:

$$\begin{aligned}
\sigma^{\gamma^*\gamma^*}_{\mathrm{VMD}\times\mathrm{GVMD}}(W^2, Q_1^2, Q_2^2) \quad &= \\
&= \sum_{V_1=\rho^0,\omega,\phi,\mathrm{J}/\psi} \frac{4\pi\alpha_{\mathrm{em}}}{f_{V_1}^2} \left[1 + r_i(m_{V_1}^2, Q_1^2)\right] \left(\frac{m_{V_1}^2}{m_{V_1}^2 + Q_1^2}\right)^2 \times \\
&\quad \times \quad \frac{\alpha_{\mathrm{em}}}{2\pi} \sum_{\mathrm{q}} 2\mathrm{e}_{\mathrm{q}}^2 \int_{k_0^2}^{k_1^2} \frac{\mathrm{d}k_\perp^2}{k_\perp^2} \left[1 + r_i(4k_\perp^2, Q_2^2)\right] \\
&\quad \times \quad \left(\frac{4k_\perp^2}{4k_\perp^2 + Q_2^2}\right)^2 \frac{k_{V_2(\mathrm{q\overline{q}})}^2}{k_\perp^2} \sigma^{V_1 V_2(\mathrm{q\overline{q}})}(W^2),
\end{aligned}$$

$$\begin{aligned}
&\sigma^{\gamma^*\gamma^*}_{\mathrm{VMD}\times\mathrm{dir}}(W^2, Q_1^2, Q_2^2) = \\
&\quad = \sum_{V_1=\rho^0,\omega,\phi,\mathrm{J}/\psi} \frac{4\pi\alpha_{\mathrm{em}}}{f_{V_1}^2} \left[1 + r_i(m_{V_1}^2, Q_1^2)\right] \left(\frac{m_{V_1}^2}{m_{V_1}^2 + Q_1^2}\right)^2 \times \\
&\qquad\qquad \times \left(\sigma_{\mathrm{T}}^{V_1\times\mathrm{dir}}(W^2, Q_2^2) + \sigma_{\mathrm{L}}^{V_1\times\mathrm{dir}}(W^2, Q_2^2)\right) .
\end{aligned}$$

To this should be added the new DIS processes that appear for non-vanishing Q^2, when one photon is direct and the other resolved, i.e. VMD or GVMD.

For simplicity, first assume that one of the two photons is real, $Q_2^2 = 0$. For large Q_1^2, this DIS contribution can be given a parton-model interpretation,

$$\begin{aligned}\sigma^{\gamma^*\gamma}_{\mathrm{DIS}\times\mathrm{res}}(Q_1^2) &\simeq \frac{4\pi^2\alpha_{\mathrm{em}}}{Q_1^2}\, F_2^{\gamma}(x,Q_1^2) \\ &\simeq \frac{4\pi^2\alpha_{\mathrm{em}}Q^2}{(Q_1^2+m_\rho^2)^2}\sum_{\mathrm{q}} e_{\mathrm{q}}^2\, \left\{ xq^{\gamma}(x,Q_1^2) + x\overline{q}^{\gamma}(x,Q_1^2)\right\}\ .\end{aligned} \tag{4.32}$$

Note that this is only the resolved part of $\sigma^{\gamma^*\gamma}_{\mathrm{tot}}$. The direct contribution from $\gamma^*\gamma \to \mathrm{q\overline{q}}$ comes in addition, but can be neglected in the leading-order definition of F_2^{γ}. We will therefore use parton distribution parameterizations for the resolved photon, like SaS 1D [11], to define the $\sigma^{\gamma^*\gamma}_{\mathrm{DIS}\times\mathrm{res}}(Q_1^2)$. Then eq. (4.31) generalizes to

$$\begin{aligned}\sigma^{\gamma^*\gamma}_{\mathrm{tot}}(W^2,Q_1^2) &= \sigma^{\gamma^*\gamma}_{\mathrm{DIS}\times\mathrm{res}}\ \exp\left(-\frac{\sigma^{\gamma^*\gamma}_{\mathrm{dir}\times\mathrm{res}}}{\sigma^{\gamma^*\gamma}_{\mathrm{DIS}\times\mathrm{res}}}\right) + \sigma^{\gamma^*\gamma}_{\mathrm{dir}\times\mathrm{res}} \\ &+ \sigma^{\gamma^*\gamma}_{\mathrm{res}\times\mathrm{dir}} + \sigma^{\gamma^*\gamma}_{\mathrm{dir}\times\mathrm{dir}} + \left(\frac{W^2}{Q_1^2+W^2}\right)^n\ \sigma^{\gamma^*\gamma}_{\mathrm{res}\times\mathrm{res}}\ .\end{aligned} \tag{4.33}$$

The large-x behaviour of a resolved photon does not agree with that of the proton, but for simplicity we will stay with $n = 3$.

The generalization to both photons virtual then gives

$$\begin{aligned}\sigma^{\gamma^*\gamma^*}_{\mathrm{tot}}(W^2,Q_1^2,Q_2^2) &= \sigma^{\gamma^*\gamma^*}_{\mathrm{DIS}\times\mathrm{res}}\ \exp\left(-\frac{\sigma^{\gamma^*\gamma^*}_{\mathrm{dir}\times\mathrm{res}}}{\sigma^{\gamma^*\gamma^*}_{\mathrm{DIS}\times\mathrm{res}}}\right) + \sigma^{\gamma^*\gamma^*}_{\mathrm{dir}\times\mathrm{res}} \\ &+ \sigma^{\gamma^*\gamma^*}_{\mathrm{res}\times\mathrm{DIS}}\ \exp\left(-\frac{\sigma^{\gamma^*\gamma^*}_{\mathrm{res}\times\mathrm{dir}}}{\sigma^{\gamma^*\gamma^*}_{\mathrm{res}\times\mathrm{DIS}}}\right) + \sigma^{\gamma^*\gamma^*}_{\mathrm{res}\times\mathrm{dir}} \\ &+ \sigma^{\gamma^*\gamma^*}_{\mathrm{dir}\times\mathrm{dir}} + \left(\frac{W^2}{Q_1^2+Q_2^2+W^2}\right)^n\ \sigma^{\gamma^*\gamma^*}_{\mathrm{res}\times\mathrm{res}}\ ,\end{aligned} \tag{4.34}$$

where the choice of damping factor for the last term again is a simple guess for an extension. When $Q_1^2 \gg Q_2^2$ the expression for $\sigma^{\gamma^*\gamma^*}_{\mathrm{tot}}(W^2,Q_1^2,Q_2^2)$ can be related to the structure function of a virtual photon,
$F_2^{\gamma^*}(x,Q^2 = Q_1^2, P^2 = Q_2^2)$, where $x = Q_1^2/(Q_1^2+Q_2^2+W^2)$.

A comment about the exponential factors suppressing the DIS terms. Properly, each VMD/GVMD state should come with its ratio of direct to DIS cross sections. However, a number of common factors divide out in this ratio: obviously the probability to fluctuate to the state in question, but partly also the form of the parton distributions in the state. Therefore, it is a good approximation to define a common exponential form for all VMD/GVMD state, based on the weighted average, which is equivalent to using the full resolved term in both numerator and denominator.

4.2.7 Other Model Aspects

In the preceding section we have mainly described the model as differential in W (invariant mass of the γ^*p or $\gamma^*\gamma^*$ system) and the hardest scales involved: $p_\perp$, $k_{\perp i}$ and Q_i^2. The discussion about the different processes has been limited to the parton-level only, but it is necessary to add parton showers, beam remnants, hadronization etc. in order to simulate complete events. The model is implemented in the PYTHIA 6.151 event generator [21], which includes the above and many other aspects, and it will be used in the following for the results presented. Clearly, here we can only give a few typical examples; with the help of the generator it is possible to study any specific experimental conditions and observables.

While based on the formalism outlined above, the complete event simulation also involves some more model-specific assumptions. We here present a few of those, to try to complement the overall picture. Further refinements are possible in many places, and some of the known shortcomings are mentioned.

The extension from pp to γ^*p and $\gamma^*\gamma^*$ collisions requires two new aspects to be introduced in the event simulation structure. One is the need to construct the $\mathrm{e} \to \mathrm{e}\gamma^*$ kinematics, and to let the collision description depend not only on the resulting W but also on the selected Q^2 virtuality scale(s) of the photon(s). This part was described in [6].

The other is the necessity to mix all the different reaction processes. The main classification is here into 4 components for γ^*p — VMD, GVMD, direct and DIS — and 13 for $\gamma^*\gamma^*$ — 4-squared except that there is no DIS process on a direct photon or another DIS photon. Each of these components has a set of allowed subprocesses, e.g. $\gamma^*\mathrm{q} \to \mathrm{qg}$ and $\gamma^*\mathrm{g} \to \mathrm{q\overline{q}}$ for direct processes. This set is the same for a VMD and a GVMD photon, but the two are distinguished by the different parton distributions and total cross section parameterizations used. In the Monte Carlo, a choice is first made between the 4/13 components and then, for that component, among the allowed subprocesses, according to maxima estimated at the initialization. Once the kinematics of the event has been fully selected, the ratio of the actual cross section to the assumed one is used to retain the event or to select a new component and subprocess.

The separation of VMD from GVMD requires access to parton distributions where those two components are explicitly made available separately. Effectively this limits the choice to the SaS parameterizations [11], and with the assumed $k_0 \approx 0.5$ GeV to SaS 1D. An almost equivalent formalism could have been constructed in terms of a common resolved class, so that we could have gone from 4/13 to 3/6 categories. While the calculation of partonic processes would have been simplified, aspects related to total cross section processes (elastic, diffractive, low-$p_\perp$, etc.) would not, so we have not yet tried to construct such a complete alternative machinery.

A VMD photon may be classified either as ρ^0, ω, ϕ or J/ψ. The parameter-

izations of total, elastic, single and double diffractive cross sections for Vp and V_1V_2 collisions of real photons are given in [15]. The respective inelastic non-diffractive cross section is obtained by subtraction, and sets the envelope within which the jet cross section is eikonalized. The events are ultimately classified, either by the hardest interaction that occurs, or as a low-$p_\perp$ event if there are no hard interactions. For virtual photons, both the total, elastic, single and double diffractive cross sections are dampened by the same dipole factors, cf. eq. (4.24). The jet cross section is obtained by the virtuality-dependent parton distributions, however, so in the eikonalization procedure the mixture between jet and low-$p_\perp$ events is explicitly Q^2-dependent. For technical reasons, currently it is not possible to mix different dipole factors for the different VMD states, so the ρ/ω mass is used throughout, thus giving a too fast dampening of the (rare) J/ψ events.

For the GVMD states, the mass selection is based on the identification $m \simeq 2k_\perp$ and a $k_\perp$ spectrum e.g. as implied by eq. (4.29). Thus, neglecting the longitudinal-photon factor, one has a mass spectrum like $\mathrm{d}m^2/(m^2+Q^2)^2$ in the range $2k_0 < m < 2p_{\perp\min}(W^2)$. This spectrum begins at 1 GeV, i.e. a bit above m_ρ. Again there is not yet any provision for heavier quarks in the dipole dampening formulae, but the mass of an $\mathrm{s\overline{s}}$ state is shifted by $m_\phi - m_\rho$ and that of an $\mathrm{c\overline{c}}$ by $m_{\mathrm{J}/\psi} - m_\rho$, to ensure that the GVMD spectrum starts above the lowest-lying state. The mass selected above then becomes the final-state mass of an elastically scattered GVMD particle. A diffractively scattered GVMD is assigned an excited mass according to a spectrum stretching from the selected mass and upwards to the kinematical limit, essentially like $\mathrm{d}m^2/m^2$, as described in [15].

An elastic or diffractive GVMD state is in reality no different from a diffractive VMD state of the same mass. A low-mass system is allowed to decay to two hadrons, whereas more massive ones are considered as strings stretched along the event axis, modulo limited transverse-momentum fluctuations. It is assumed that a simple string is stretched between two endpoint quarks half of the time, and a hairpin string arrangement with a gluon pulled back the other half. Clearly this mixture is only a simple first approximation to what is likely to be a more complex structure [22].

The mass of the GVMD state does not enter the description of inelastic non-diffractive events. However, here the $k_\perp \simeq m/2$ does provide a 'primordial $k_\perp$' kick that can be transmitted to the parton of a hard scattering, not only for GVMD×p but also in processes such as DIS×GVMD. The corresponding number ought to be $k_\perp \approx m_\rho/2$ for VMD and $k_\perp \approx m_\mathrm{p}/3 \approx m_\rho/2$ for a proton. However, in hadronic collisions much higher numbers than that are often required to describe data, typically of the order of 1 GeV [23] if a Gaussian parameterization is used. Thus, an interpretation as a purely nonperturbative motion inside a hadron is difficult to maintain.

Instead a likely culprit is the initial-state shower algorithm. This is set up to cover the region of hard emissions, but may miss out on some of the softer activity, which inherently borders on nonperturbative physics. By default, the shower does not evolve down to scales below $Q_0 = 1$ GeV; if the $k_\perp \simeq m/2$ scale of a GVMD photon is above this the evolution is stopped already at the larger scale. (Whether Q_0 should best be compared with m or $m/2$ is an open issue.) Any shortfall in shower activity around or below this cutoff then has to be compensated by the primordial $k_\perp$ source, which thereby largely loses its original meaning.

It could be argued that, while a VMD photon should have the same primordial $k_\perp$ spectrum as a hadron, a GVMD one should receive its main contribution from the perturbative $k_\perp \simeq m/2$ contribution, i.e. have a shape like $\mathrm{d}k_\perp^2/(k_\perp^2 + Q^2/4)^2$ in the range $k_0 < k_\perp < p_{\perp\min}(W^2)$. However, this has the questionable consequence that a low-mass GVMD state would have a smaller average 'primordial $k_\perp$' than a VMD one. While we have retained such a possibility as an option, our default has instead been to go to the other extreme, where the partons in a GVMD state has a $k_\perp$ given by the vector sum of the perturbative power spectrum and the same nonperturbative Gaussian smearing as for hadrons. Comparisons with data on photon remnant jets should eventually shed more light on the appropriate procedure.

In most processes, initial- and final-state shower activity is routinely added to the lowest-order process, thereby providing an approximation to higher-order QCD corrections. An exception is the DIS process $\gamma^*\mathrm{q} \to \mathrm{q}$, where currently only final-state radiation has been implemented. The technical reason why the initial-state radiation algorithm does not work here is that it is based on a definition of the z of the splitting kernel as being the fraction by which the $\hat{s}$ of the hard subprocess is reduced by an emission, and $\hat{s} = 0$ in the DIS process above. The traditional z interpretation is sensible if one remembers that the complete DIS hard process is $\mathrm{eq} \to \mathrm{eq}$ rather than only $\gamma^*\mathrm{q} \to \mathrm{q}$. However, since we have split off the photon flux, the complete process is not trivially available currently. For small Q^2 values, this is no major problem, since events with activity above this scale belong to the direct event class. Therefore the shower is constrained only to populate the region below Q^2. The problem may become more severe in the high-Q^2 domain, where DIS processes provide the dominant event class and there is a large phase space for shower activity. That is not the region of main interest to us here, however.

The choice of a formalism, with the virtual photon flux separated from the hard processes, is there for two reasons. One is that it makes it possible to set up selection criteria for an event sample, e.g. on W and Q^2 or in terms of scattered electron energies and angles, that are consistent across the different photon components. Another is that many nonperturbative physics aspects, such as VMD total cross sections, best are formulated in such terms.

Also a few other areas are not fully developed. One example is multiple interactions, where only the simpler impact-parameter-independent option can be used [7], at least until one has constructed a model of the spatial distribution of partons in a GVMD state. On the positive side, options are available for several of the other aspects discussed in this article, so that one may study the sensitivity to the assumptions made.

4.3 Results

In this section, some examples of event properties will be given, with emphasis on the differences between the direct, VMD and anomalous/GVMD component of the photon. We will concentrate on a few distributions, starting in the photoproduction limit, and then explore how they gradually turn over from being dominated by the resolved processes to finally being dominated by the bare direct and DIS ones as the photon virtuality increases.

Owing to the resolved components of the photon, pp, γp and $\gamma\gamma$ events show similar behaviour for several event properties, such as multiplicity and transverse energy flow. But clearly, differences are expected due to, for example, the additional direct event class in $\gamma\gamma$.

4.3.1 Total Cross Sections

γ^*p Total Cross Section

The SaS 1D photon parton distribution and the CTEQ5L proton parton distribution will be used throughout in this section if not otherwise stated [11, 24]. In Fig. 4.8, the γ^*p cross section at $W_{\gamma^*\mathrm{p}} = 100$ GeV is shown as a function of the photon virtuality Q^2. The VMD and GVMD components contain contributions from resolved longitudinal photons with the r_1 alternative. An implicit y dependence enters the r_i factors, eq. (4.26) and (4.27), to compensate for the difference in photon flux between longitudinally and transversely polarized photons. To estimate the longitudinal contribution to the resolved component in γ^*p cross sections, a fixed y is chosen in order to set the relative amount of transverse and longitudinal photons. The value of y consequently depends on the beam energy, and at HERA $W_{\gamma^*\mathrm{p}} = 100$ GeV would correspond to $y \simeq 0.1$, a value which will be used in the following. The parameter a, appearing in r_i, is unknown and need to be determined by data. As a starting point for the discussion, a is chosen to 0.5.

In the photoproduction limit, the VMD component dominates the total cross section whereas the DIS one has a vanishing cross section by construction, see Fig. 4.8. The GVMD and direct processes share the remaining part, about 20%, of the total cross section. It follows from the introduction of the dipole

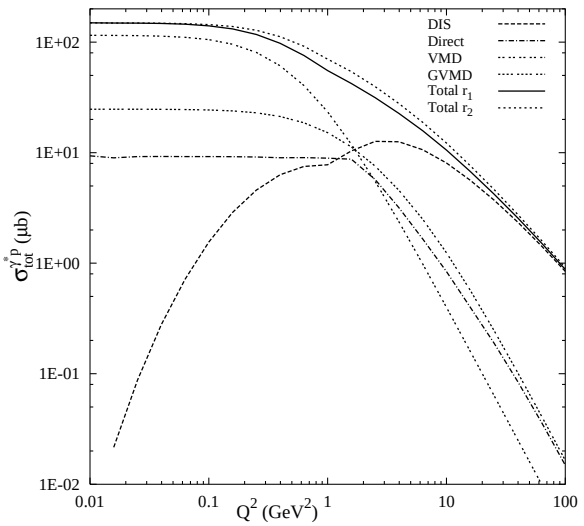

Figure 4.8: The total $\sigma_{\mathrm{tot}}^{\gamma^*\mathrm{p}}$ cross section as function of the photon virtuality at $W_{\gamma^*\mathrm{p}} = 100$ GeV. The resolved components shown are with alternative r_1 for the longitudinal contribution.

factors in eq. (4.24) that, when considering total γ^*p cross sections, the VMD class is the dominating component up to photon virtualities of the order of a vector meson mass. Similarly, the characteristic virtualities for the GVMD class to still be important are of the order of the k_1 parameter discussed in section 4.2.3.

The direct processes are simulated in the region where the hard scale $k_\perp$ of the photon–parton scattering fulfill $k_\perp > \max(k_1, Q)$, cf. Fig. 4.5. At low Q^2 values, the $k_1 = p_{\perp\min}(W^2) \simeq 1.3$ GeV provides a fix limit on the available phase space, but at higher Q^2 the phase space shrinks, explaining the kink in Fig. 4.8 for the direct cross section at $Q^2 = k_1^2$. So it is rather this condition that drives the dampening at large Q^2 than the explicit Q^2 dependence appearing in the matrix elements. A kink can also be seen in the DIS cross section; it is an artifact from the freezing of the parton distributions below their range of applicability (as introduced in section 4.2.1). Hence, the CTEQ5L proton parton distribution has $Q^2_{\mathrm{min}} = 1$ GeV. The factors introduced for the DIS component, eq. (4.9), together with the exponential dampening, eq. (4.23), make the unusual form of the DIS cross section — to be discussed in more detail below.

The proton structure function F_2 has been measured at various x and Q^2

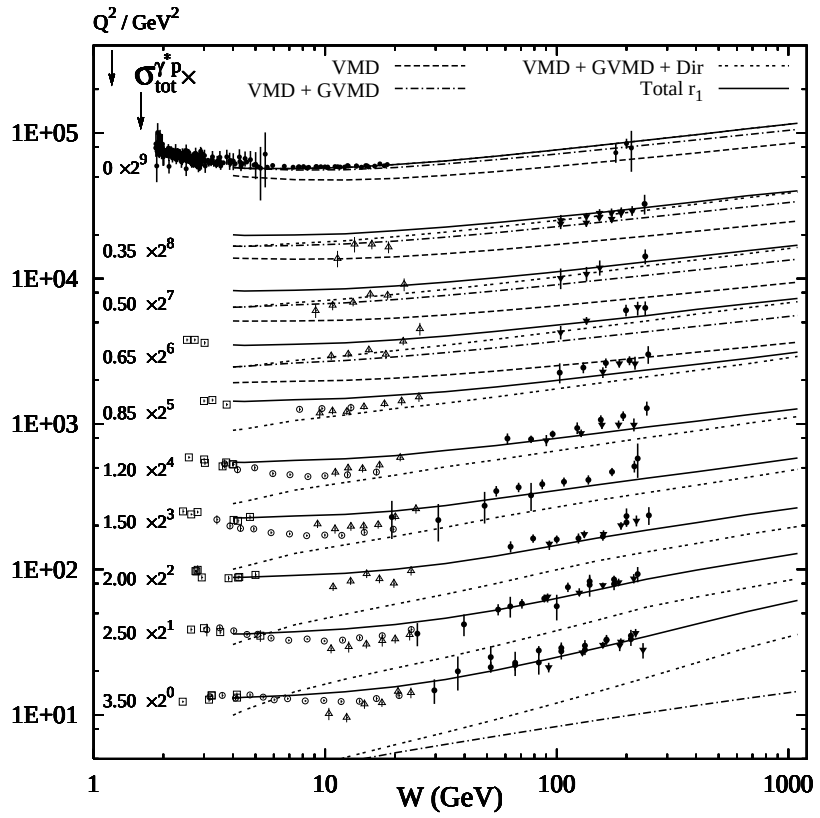

Figure 4.9: Contributions to the total $\sigma_{\rm tot}^{\gamma^*{\rm p}}$ (μb) cross section from the different event classes: direct, VMD, GVMD and DIS. For simplicity, the VMD and VMD+GVMD contributions are not shown for the lines corresponding to Q^2 values in the range $0.85 - 2.5$ GeV^2. See text for details. The legend for the data points can be found in Fig. 4.10.

values [25] and is related to the total virtual photon–proton cross section $\sigma_{\rm tot}^{\gamma^*{\rm p}}$ through eq. (4.7). In Fig. 4.9 and 4.10, $\sigma_{\rm tot}^{\gamma^*{\rm p}}$ is shown from zero Q^2, the total photoproduction cross section [26], to medium Q^2 values as a function of the invariant mass W of the γ^*p-system. Results from the model are compared with data from different fixed-target and HERA experiments. The contribution from the different event classes: direct, VMD, GVMD and DIS are shown in Fig. 4.9, and sum up to the total contribution as given in eq. (4.31). The DIS contribution can be obtained by subtracting the 'VMD+GVMD+Dir' contribution from the 'Total r_1' one. With increasing photon virtuality, the energy

dependence of k_1 makes the GVMD states to be less dampened at large energies as compared to low ones. This is also indicated in Fig. 4.9 by comparing the 'VMD' and 'VMD+GVMD' lines at different Q^2 and W.

In Fig. 4.10, the total contribution obtained with different assumptions of the longitudinal contribution for resolved photons are compared to the case with transverse photons only. With the other model assumptions made, a non-vanishing longitudinal contribution is indicated. The alternative with r_1 gives a good fit to data, but overshoots at low W values for some Q^2 values. In the high Q^2 region, showed in Fig. 4.8 and at the bottom in Fig. 4.11, the choice of longitudinal alternative for the resolved component is irrelevant for the total cross section since the resolved event classes give a negligible contribution. Hence, the parameter a should be tuned at intermediate Q^2 values. At lower Q^2 values, however, the r_2 alternative is overshooting data significantly. Taking $a = 0.5$ as a satisfactory value for the r_1 alternative, the r_2 one require $a = 0.2$ to give an equally good description (not shown).

The direct processes increase with $W_{\gamma^*\mathrm{p}}$ faster than the DIS one, and consequently also the exponential suppression of the DIS term. Therefore they contribute substantially to the total cross section in the large $W_{\gamma^*\mathrm{p}}$ (small x) region, even at photon virtualities up to tens of GeV^2, shown for $W_{\gamma^*\mathrm{p}} = 100\,\mathrm{GeV}$ in Fig. 4.8. The DIS and direct classes are often combined and clearly dominate the total cross section at $Q^2 = 3.5\ \mathrm{GeV}^2$ which is above the m_V^2 and k_1^2 scales of the VMD and GVMD states discussed above. Due to the negligible contribution from the direct processes at $W_{\gamma^*\mathrm{p}} = 10$ GeV, the exponential suppression factor for the DIS term is close to unity — independently of Q^2. Hence, the sum of the direct and DIS contributions reproduce the $\sigma_{\mathrm{DIS}}^{\gamma^*\mathrm{p}}$ cross section, eq. (4.22). For $W_{\gamma^*\mathrm{p}} = 100$ and 1000 GeV this is the case for $Q^2 > 5$ and 8 GeV^2, respectively.

$\gamma^*\gamma$ Total Cross Section

For simplicity, a fixed $y_i = 0.1$ is also used in photon–photon collisions for the calculation of the longitudinal resolved photon contributions. In Fig. 4.12a, the $\sigma_{\mathrm{tot}}^{\gamma^*\gamma}$ at $W_{\gamma^*\gamma} = 100\,\mathrm{GeV}$ is shown as a function of one of the photon virtualities; the other photon is real. The different components are shown separately and sum up to the total contribution with the r_1 alternative. Additionally, relative to the corresponding $\gamma^*\mathrm{p}$ case, the direct cross section enters and starts to be significantly dampened only when $Q_1^2 \simeq W^2$. The kink seen for the single-resolved case can again be explained by the constraint of the hard scale in the scattering process to be larger than the virtuality of the direct photon.

The same distribution is shown for the case of two virtual photons in Fig. 4.12b. The low virtuality end of Q_1^2 of course corresponds to the cross sections at $Q_1^2 = 10\ \mathrm{GeV}^2$ in Fig. 4.12a. The DIS cross section dominates in this region, with the first photon as the target probed by the second one. This

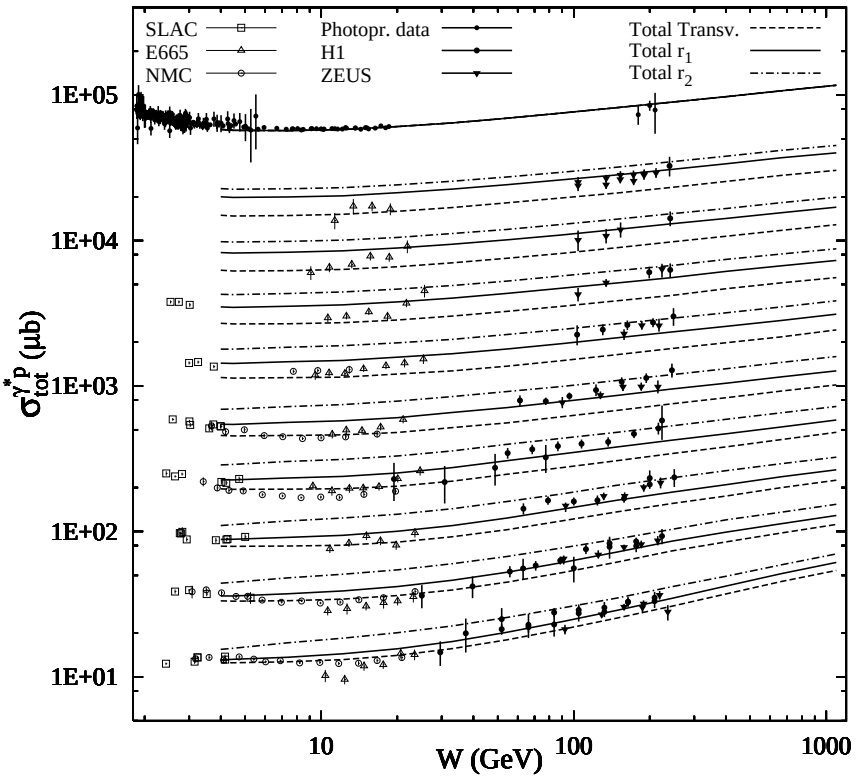

Figure 4.10: The total contribution to $\sigma_{\rm tot}^{\gamma^* {\rm p}}$ from the different event classes. The two different longitudinal alternatives are compared to the case with only transverse photons considered. The data and 'Total r_1' is the same as in Fig. 4.9.

is interchanged for $Q_1^2 \geq Q_2^2$. It is noticeable that all the different processes shown are of about the same importance when Q_1^2 is in the neighbourhood of Q_2^2.

For various reasons, the photon F_2^γ measurements [27] are both less precise and available in a smaller kinematical range than in the proton case. In Fig. 4.13, the $\sigma_{\rm tot}^{\gamma^* \gamma}$ is shown as a function of W for different Q^2 values, similarly to the study in the previous section. With $a = 0.5$ for both alternatives of the longitudinally resolved photons, data does not discriminate between them. The r_1 alternative is below the high-energy end data points for the $Q^2 = 4.04$ and 5.15 GeV^2 lines but the errors and spread in data do not give an unambiguous

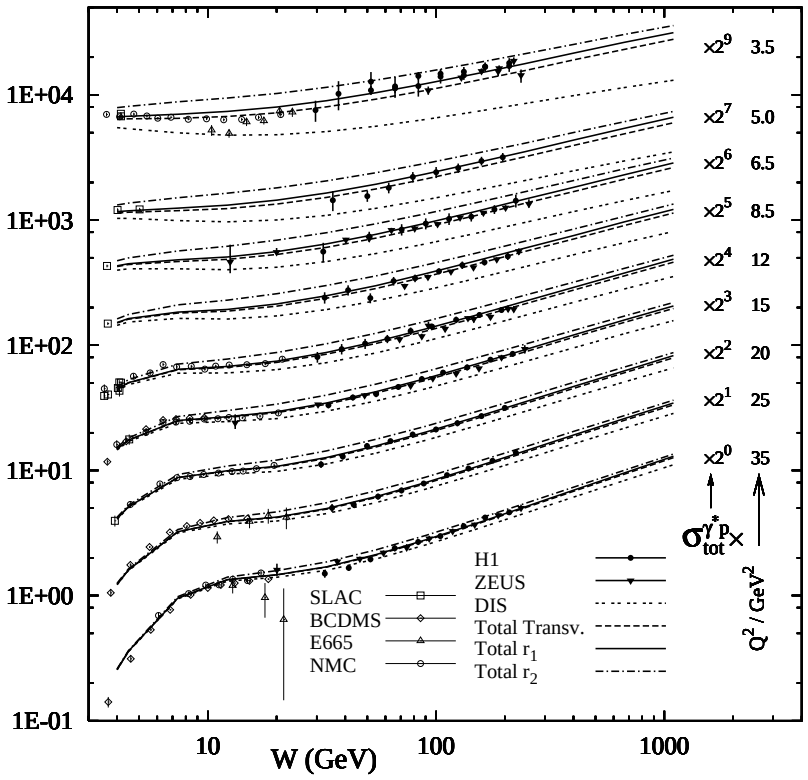

Figure 4.11: $\sigma_{\rm tot}^{\gamma^*\gamma}$ (μb) as in Fig. 4.10 but for a different Q^2 range and also the DIS contribution is shown. For reference, the $Q^2 = 3.5$ GeV^2 lines are the same, however.

conclusion.

Fig. 4.14 shows the contribution to $\sigma_{\rm tot}^{\gamma^*\gamma}$ for some different event classes at $Q^2 = 9.90\,\mathrm{GeV}^2$. The direct and DIS ones are dominating at low $\gamma^*\gamma$ invariant masses whereas the single-resolved ones increase in importance at high $W_{\gamma^*\gamma}$. The direct processes show the characteristic $1/W^2$ fall off [6] and thereby give its major contribution to the region where the valence quarks dominate the contribution to F_2^γ. Again, the single-resolved processes (1-res; cf. direct ones in γ^*p) increase with energy, which therefore dampens the DIS term slightly at large $W_{\gamma^*\gamma}$, a region which is dominated by the gluon content of the photon. As resolved processes in γ^*p, double-resolved ones (2-res) in $\gamma^*\gamma$ increase with $W_{\gamma^*\gamma}$.

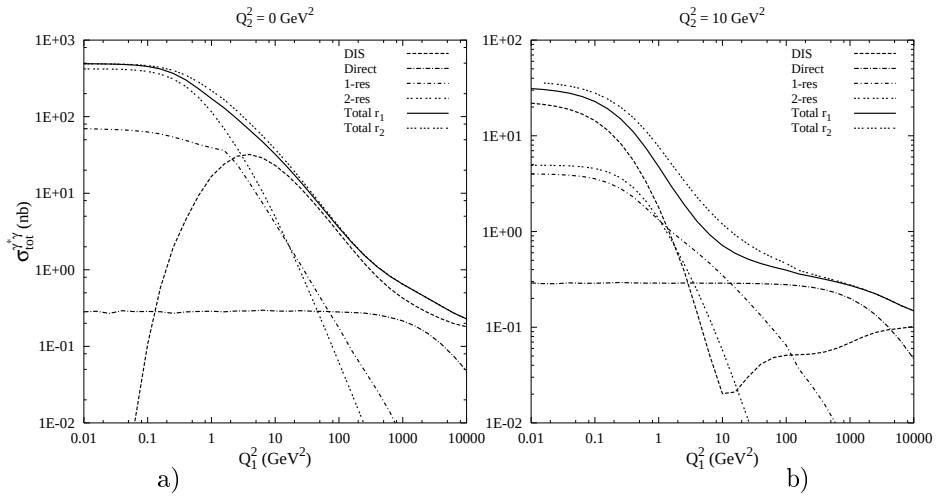

Figure 4.12: a) The $\sigma_{\rm tot}^{\gamma^*\gamma}$ at $W_{\gamma^*\gamma} = 100$ GeV as a function of the photon virtuality Q_1^2 of one of the photons is shown for the DIS, direct, single-resolved (1-res), double-resolved (2-res) and total contribution. The other photon is real, $Q_2^2 = 0$ GeV^2. b) Same as in a) but for $\gamma^*\gamma^*$ with a target photon virtuality $Q_2^2 = 10$ GeV^2.

$\gamma^*\gamma^*$ Total Cross Section

There are hardly any systematic data on $\gamma^*\gamma^*$ cross sections. Prior to the recent and ongoing LEP studies, essentially the only publication is the $F_{\rm eff}$ measurement by PLUTO [28]. A comparison with these data points is found in Fig. 4.15a. The low W values — the first point is in the resonance region — makes the comparison especially precarious, and the second photon is also not all that virtual with its $\langle Q_2^2 \rangle = 0.35$ GeV^2. The main point of the plot is thus not the acceptable agreement with data, but to illustrate the amount of reduction of the cross section relative to the real-photon alternative $Q_2^2 = 0$ and the dependence on assumed longitudinal contributions.

Double-tag two-photon events, $e^+e^- \to e^+e^- +$ hadrons, have been measured by the L3 collaboration [29]. The differential e^+e^- cross section w.r.t. the variable

$$Y = \ln\left(\frac{y_1 y_2 s}{\sqrt{Q_1^2 Q_2^2}}\right) \tag{4.35}$$

is shown in Fig. 4.15b. The two scattered leptons are required to be within the polar angle of $30 < \theta_i < 60$ mrad (with respect to the incoming beams) and to

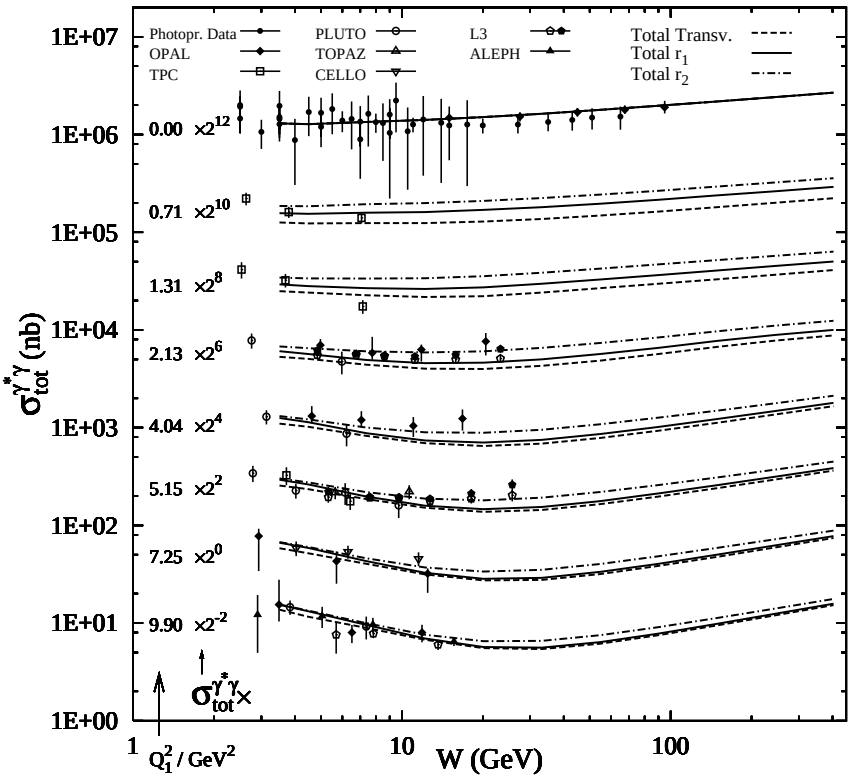

Figure 4.13: Same as in Fig. 4.11 but for $\gamma^*\gamma$ instead of γ^*p.

have an energy larger than 30 GeV. This plot is expected to provide a clean test of the BFKL behaviour, with a cross section increasing at large Y [30], but the data does not support such a behaviour, or at least less of it than expected. Our model agrees with the data at small Y, but tends to fall below at larger values. This is almost entirely dictated by the drop in the dominant direct contribution. The resolved contributions — which are the ones that could be used to represent a BFKL behaviour in our framework — do come up at large Y, but nowhere near enough to make a significant contribution. We remind that the resolved contributions are suppressed in Q^2 by simple dipole factors; a less steep drop and thereby a larger resolved contribution could be motivated e.g. if the eikonalization of the jet cross section is less significant for a virtual photon. Instead of the conventional increase of the VMD cross section like s^ϵ with $\epsilon \approx 0.08$, eq. (4.12), a larger effective value like $\epsilon \approx 0.2 - 0.3$ could thus

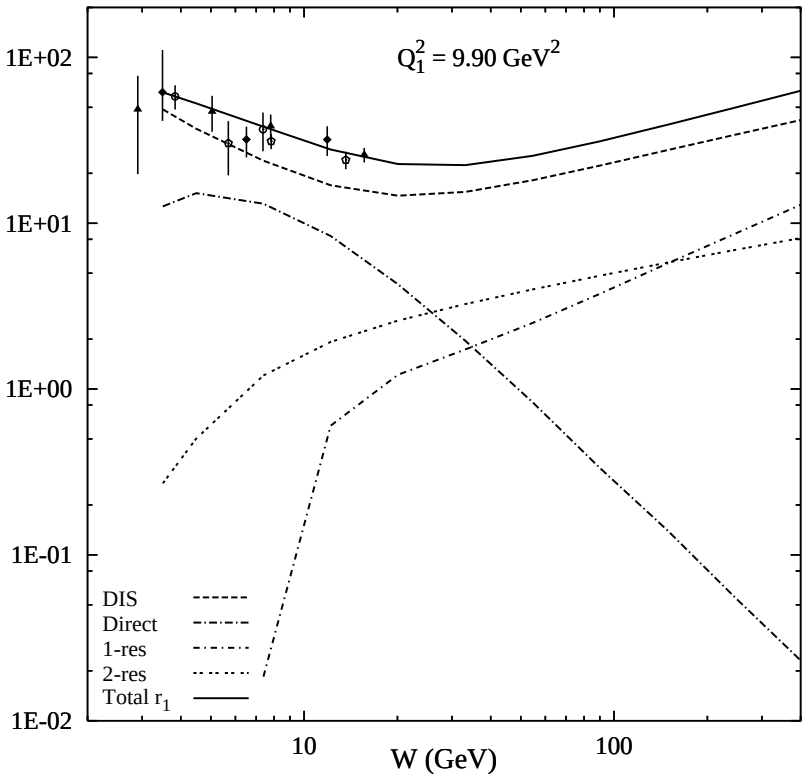

Figure 4.14: The $\sigma_{\rm tot}^{\gamma^*\gamma}$ (nb) as a function of the invariant mass of the $\gamma^*\gamma$ system is shown for the DIS, direct, single-resolved (1-res), double-resolved (2-res) and total contribution.

easily be accommodated for virtual photons [31]. For the moment, however, we prefer to await further experimental data. In particular, more detailed analyses of event properties could provide some insight on the relative mixture of event classes at large Y.

4.3.2 Event Properties

Some event properties are fairly similar between pp, γ^*p and $\gamma^*\gamma^*$, while others differ markedly. The charged multiplicity, Fig. 4.16, is an example of the former, while the jet rate, Fig. 4.17, is of the latter.

Over a wide range of Q^2 values, the γ^*p and $\gamma^*\gamma^*$ events have average

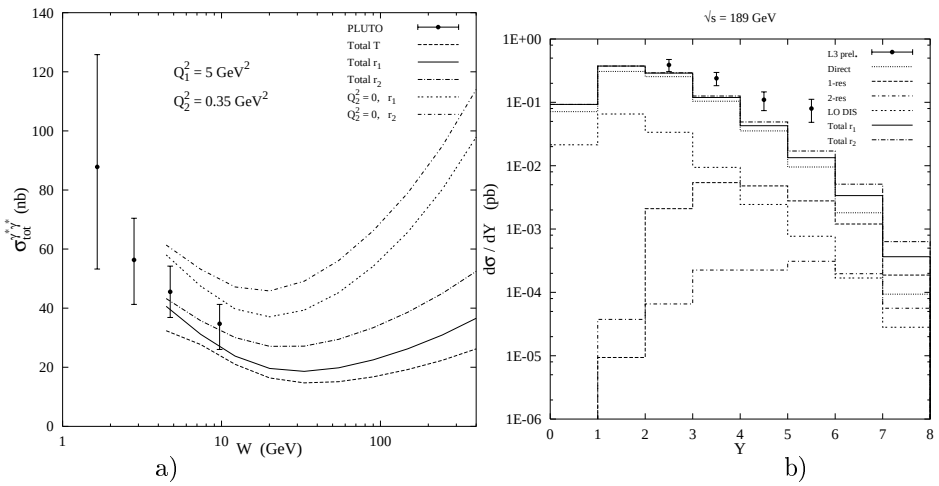

Figure 4.15: a) The $\sigma_{\rm tot}^{\gamma^*\gamma^*}$ cross section as a function of $W_{\gamma^*\gamma^*}$ for a probing and target photon with virtualities 5 and 0.35 GeV^2 respectively. The data points from PLUTO are obtained from the measured $F_{\rm eff}$ through eq. (4.7). For reference, the results with a real photon target is shown, $Q_2^2 = 0$ b) The differential $\rm e^+e^- \to e^+e^- +$ hadrons cross section as a function of $Y = \ln(y_1 y_2 s/\sqrt{Q_1^2 Q_2^2})$. The different components shown add up to the 'Total r_1'.

charged multiplicities within ±20% of the pp value, Fig. 4.16a. (Elastic and diffractive events have not been considered. Their inclusion would reduce average multiplicities and change some details, but leave a similar overall picture.) For γ^*p at small Q^2, this is a consequence of the dominance of VMD events, with the characteristic features of hadronic physics, including such aspects as multiple parton–parton interactions. The VMD multiplicity is fairly Q^2-independent, Fig. 4.16b. The drop to a somewhat lower γ^*p multiplicity around $Q^2 \approx 1 - 10$ GeV^2 instead comes from the transition from VMD dominance to DIS ditto, where the DIS events are cleaner by consisting of only one string piece stretched directly between the kicked-out quark and the beam remnant. Remember that the DIS events here by definition are low-$p_\perp$ ones, with the high-$p_\perp$ part in the direct class, with a higher multiplicity. As the borderline between the two shifts with Q^2, both individually show an increasing multiplicity: the direct by corresponding to a smaller fraction of higher-$p_\perp$ events and the DIS by allowing an increasing admixture of jet events. Figures 4.16c and 4.16d show the corresponding Q_1^2 dependence of the $\gamma^*\gamma^*$ multiplicity, for a fixed $Q_2^2 = 1$ GeV^2, normalized to the number of event of each kind

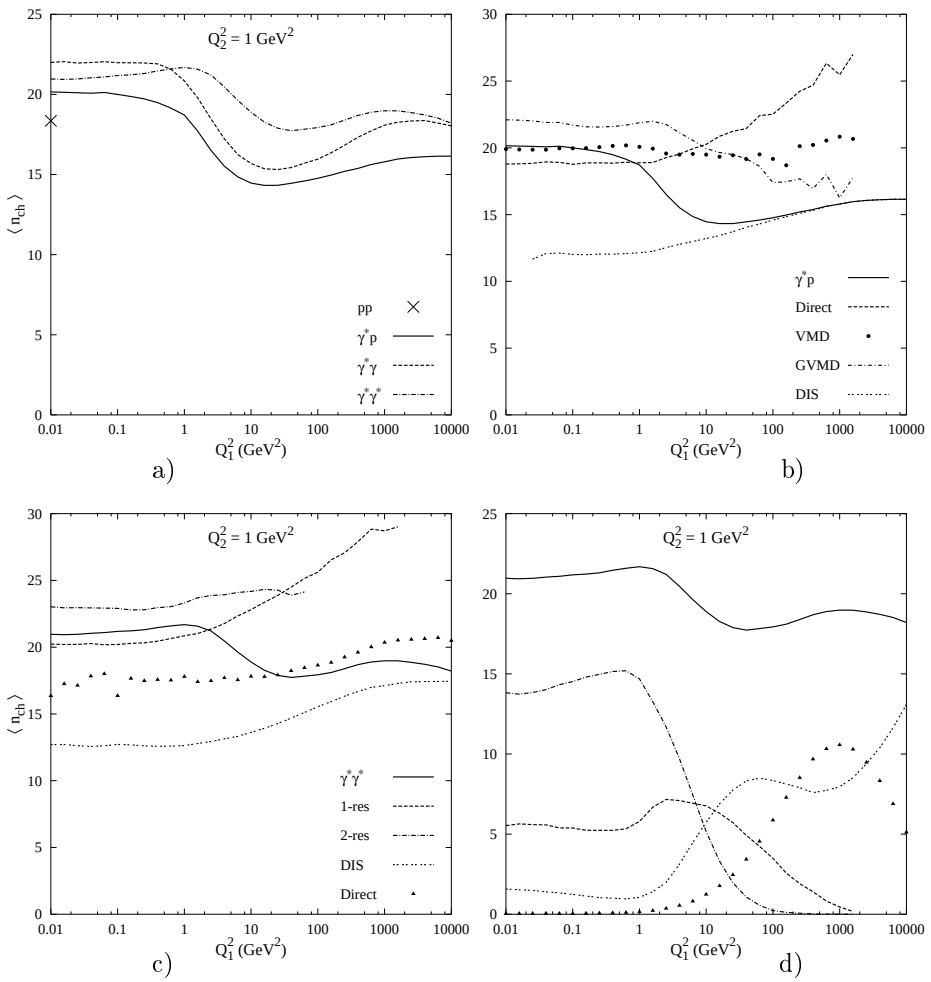

Figure 4.16: a) The average charged multiplicity $\langle n_{\rm ch} \rangle$ as a function of the photon virtuality for γ^*p, $\gamma^*\gamma$ and $\gamma^*\gamma^*$ events at a center of mass energy of 100 GeV. The result from pp events is indicated with a cross on the y-axis. For the $\gamma^*\gamma^*$ events, the other photon virtuality is kept fixed at $Q_2^2 = 1$ GeV^2. (In $\gamma^*\gamma$ $Q_2^2 = 0$ GeV^2.) No diffractive or elastic events are considered. b) The results from the different components in γ^*p, averaged over the number of events of the respective kind. c) The result from different components in $\gamma^*\gamma^*$, averaged over the number of events of the respective kind. d) As in c) but averaged over the total number of $\gamma^*\gamma^*$ events.

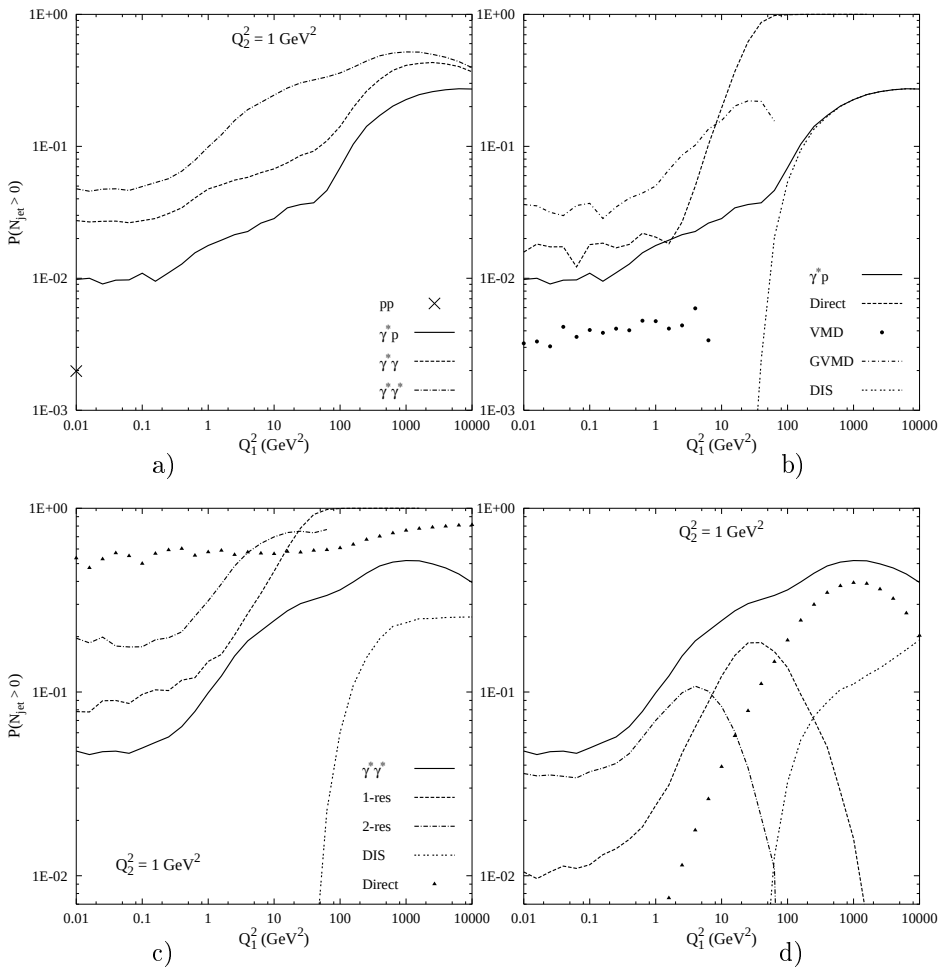

Figure 4.17: a) The fraction of events that contain at least one jet with an $E_\perp > 5$ GeV inside a cone of radius $R = \sqrt{(\Delta y)^2 + (\Delta\phi)^2} < 1$. $W = 100$ GeV in all cases. No diffractive or elastic events are considered. b) The results from the different components in γ^*p, averaged over the number of events of the respective kind. c) The result from different components in $\gamma^*\gamma^*$, averaged over the number of events of the respective kind. d) As in c) but averaged over the total number of $\gamma^*\gamma^*$ events.

and to the total number, respectively. Again the disappearance of the doubly-resolved event class is responsible for a drop in the multiplicity, with the DIS and direct processes taking over. We remind that in $\gamma^*\gamma^*$ the high-$p_\perp$ part of

the DIS process is the single-resolved one, corresponding to the direct one of γ^*p, while the $\gamma^*\gamma^*$ direct class has no correspondence in γ^*p.

When it comes to the fraction of events that contain at least one jet, the differences are orders of magnitude, both with a hierarchy of increasing jet fraction from pp to γ^*p to $\gamma^*\gamma^*$, and with an increase as a function of Q^2, Fig. 4.17a. Again the detailed studies in Figs. 4.17b–d show that the main effect in Q^2 is not in each individual event class but rather in the mixture of the event classes. Thus VMD is similar to pp, with minor differences from parton distributions, while GVMD is higher and direct higher still (at large Q^2). The DIS rate starts vanishing, since events with parton $p_\perp > Q$ are put in the direct class, but eventually comes up for $Q > p_\perp$. In that range, all direct events are required to have jets at lowest order, and only fluctuations in the parton shower and hadronization can occasionally stop jets from being found. For $\gamma^*\gamma^*$ events, shown in Figs. 4.17c and d, the single- and double-resolved processes show the behaviour of the direct and resolved (VMD plus GVMD) ones, respectively, in γ^*p. The additional direct class increase slowly with Q^2, Fig. 4.17c, and dominates the jet rate between the single-resolved and DIS dominated regions, peaking at $Q_1^2 = 1000$ GeV^2, Fig. 4.17d. It is at this point, for this center of mass energy, where the direct matrix elements starts to be suppressed by the large photon virtuality.

The transverse energy flow, as a function of pseudo-rapidity in the center of mass frame of the collision, is shown in Fig. 4.18. (Again, elastic and diffractive events are not considered.) In Fig. 4.18a all photons are real except for $\gamma\gamma^*$ where one of them has the virtuality $Q_2^2 = 1$ GeV^2. Here the most interesting aspect is to see how the events differ in the photon and the proton directions, pp being symmetric as well as $\gamma\gamma$ whereas the γp interpolate between the two with the photon in the $\eta > 0$ direction. Comparing the $\gamma\gamma^*$ with the $\gamma\gamma$ case, the single-resolved processes in $\gamma\gamma^*$ has a larger energy flow in the γ^* direction ($\eta < 0$) due to the increased jet activity. On the other hand, for the double-resolved ones it decreases in both hemispheres but less in the γ^* direction. Additionally, the DIS processes come in to play but add on more or less evenly between the two hemispheres at this low virtuality.

In Fig. 4.18b, the transverse energy flow is shown for three different virtualities in the γ^*p center of mass frame. The major differences again come from the transition of the events from being VMD dominated to being dominated by the DIS processes. This is compensated by an increasing jet activity in the photon direction, giving the rather subtle changes of the total contribution in the photon hemisphere which camouflage the big changes of the relative composition of the different event classes. The different components in γ^*p collisions with $Q_1^2 = 4$ GeV^2 are shown in Fig. 4.18c, normalized to the number of events of the respective kind. The asymmetry is largest in the direct class, where all of the photon energy goes into the two high-$p_\perp$ jets. The typical $p_\perp$ of the jets

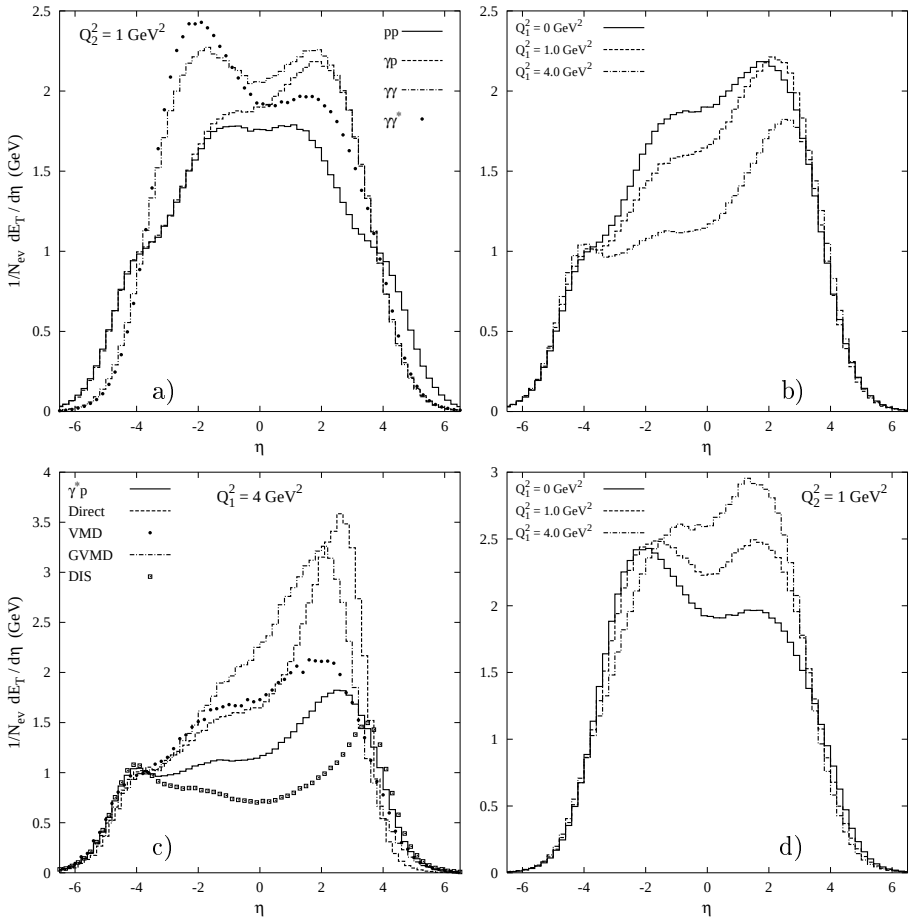

Figure 4.18: a) The transverse energy flow as a function of pseudo-rapidity in the center of mass frame of the collision, $W = 100$ GeV in all cases. No diffractive or elastic events are considered. b) The transverse energy flow as a function of pseudo-rapidity in the γ^*p center of mass frame, normalized to the number of events. Distributions are shown for photon virtualities of 0, 1.0 and 4.0 GeV^2. c) The different components in γ^*p collisions, normalized to the number of events of the respective kind. The photon virtuality is $Q_1^2 = 4$ GeV^2. d) The transverse energy flow as a function of pseudo-rapidity in the $\gamma^*\gamma^*$ center of mass frame, normalized to the number of events. Distributions are shown for photon virtualities Q_1^2 of 0, 1.0 and 4.0 GeV^2, the other photon has the virtuality $Q_2^2 = 1$ GeV^2.

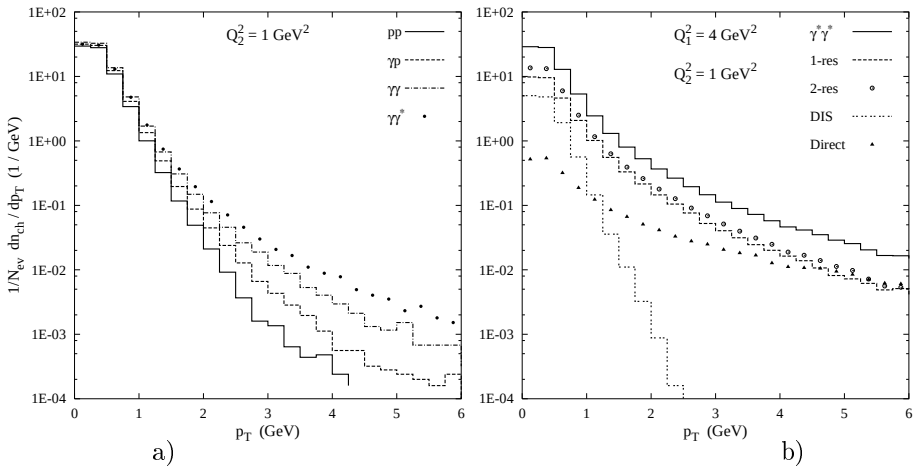

Figure 4.19: a) The transverse momentum spectra of charged particles for different collisions, normalized to the total number of events. The pseudo–rapidity interval is constrained to [0.5,1.5] (corresponding to the γ direction in case of γp, $\gamma\gamma$ and $\gamma\gamma^*$ collisions). For $\gamma\gamma^*$, one photon is real and the other has a virtuality of $Q_2^2 = 1$ GeV^2. b) With $Q_1^2 = 4$ GeV^2 and $Q_2^2 = 1$ GeV^2, the $\gamma^*\gamma^*$ distribution is shown for the different components; single-resolved, double-resolved, DIS and direct. The sum of them, add up to the full line.

is not all that high, however, so at least one of the jets appears at large positive pseudo-rapidities. The VMD and GVMD events are more symmetric, but the virtual photon parton distributions are harder than the corresponding proton one, giving rise to the observed asymmetry. The VMD events are nearly symmetric for the real photon case, whereas for the GVMD ones the asymmetry is still pronounced, as it should be. As expected, the largest contribution in the photon hemisphere is in decreasing order from DIS, direct, GVMD and VMD events, where the direct and GVMD events are of about equal importance.

A slightly asymmetric energy sharing between the two coloured beam remnants in a hadron–hadron kind of collision has been chosen for the results in this section. A more asymmetric energy sharing could also well be imagined, leaving an uncertainty in the model. For example, the energy flow in the VMD events of Fig. 4.18c could well decrease by several percent for a latter case.

In Fig. 4.18d, the transverse energy flow for the collision of two photons is shown. One of the photons is kept at $Q_2^2 = 1$ GeV^2 ($\eta < 0$) and the other has $Q_1^2 = 0$, 1 and 4 GeV^2, all shown separately. The $Q_1^2 = 0$ GeV^2 distribution was discussed earlier in comparison with two real photons, and is built up by (in

order of importance) the asymmetric double- and single-resolved contributions together with a small symmetric DIS contribution — the direct event class is negligible. With both photons having the same virtuality, $Q_i^2 = 1$ GeV^2, the above relative importance between the different components still holds but now all event classes give a symmetric contribution to the $E_\perp$ flow. The last case, with two photons at different virtualities, the single-resolved processes are responsible for most of the asymmetric shape of the total contribution. Now also the direct processes starts to be important with a central plateau of two units in pseudo-rapidity. It is here comparable with the DIS contribution, about 0.25 GeV at central rapidities (normalized to the total number of events).

The transverse momentum spectra of charged particles become harder when going from pp to γp to $\gamma\gamma^*$, Fig. 4.19, which is partly a reflection of the property of the respective parton distributions and the pattern seen in the jet rates. In γp, the VMD processes dominate in the low end of the spectra and the GVMD and direct processes in the high-$p_\perp$ tail. With increasing photon virtuality, the DIS processes enters but is only of importance at low $p_\perp$ due to the constraint $p_\perp < Q$. (The parton shower and hadronization will cause some particles to be found at $p_\perp > Q$, however.) With a photon virtuality of a few GeV^2, a similar spectra is obtained as for $\gamma^*\gamma^*$ in Fig. 4.19b, remembering to associate the γp direct events with the $\gamma^*\gamma^*$ single-resolved ones, and the γp resolved with the $\gamma^*\gamma^*$ double-resolved ones.

With two photons, the direct processes give a tail out at high $p_\perp$ that is comparable to the single- and double-resolved processes, Fig. 4.19b, and contribute to the hardening of the spectra as compared to pp and γp collisions. When both photons have the same virtuality, for example two real photons, the DIS processes are as usual absent. Although the mixture of event classes differs significantly within a certain kind of collision, the low end of the spectra remain approximately the same when the photon virtuality is increased.

4.4 Summary and Outlook

We have in this article tried to outline a scenario that covers 'all' photon interactions, whether real or spacelike virtual, that produces hadronic final states. Part of it relies on previous studies, e.g. on jet production with virtual photons or total cross sections for real photons, but here it is eventually combined to give the overall picture. In doing this, we attempt to integrate various aspects into a reasonably consistent overall picture. It would have been nice if a single very economical ansatz for the photon could be made to cover all relevant phenomenology. We do not exclude that this would be possible, although we could also see problems with such an approach. For instance, it appears likely that there really is a fundamental separation into a 'resolved' and a 'direct' (or 'pointlike') part of the photon, e.g. based on the x_γ distributions observed at

HERA [32]. Even this separation, of course, is only theoretically well-defined to lowest order, and needs to be prescribed in higher orders of perturbation theory. Nevertheless, the 'all orders' data quite nicely show a separation.

Our model takes such an approach one step further. The resolved part of the photon is subdivided into VMD and GVMD, depending on whether the resolved photon is associated with one of the lowest-lying vector mesons or with one in the set of not so well known higher-mass resonances. For a virtual photon, these states then have a dampened cross section given by dipole form factors. The direct sector is somewhat more complicated, since the lowest-order DIS process $\gamma^*\mathrm{q} \to \mathrm{q}$ is not allowed in the limit $Q^2 \to 0$ while the higher-order direct ones $\gamma^*\mathrm{q} \to \mathrm{qg}$ and $\gamma^*\mathrm{g} \to \mathrm{q\overline{q}}$ are. It therefore requires some care to retain only the latter for $Q^2 = 0$ while equating them with the first-order QCD corrections to the DIS process for large Q^2.

The first test that the mixing makes sense comes from a comparison with the total cross sections of $\gamma^*\mathrm{p}$ and $\gamma^*\gamma^*$ interactions. It is possible to obtain a reasonable description of all the data, although with some disagreement for rather small W, where our language is not expected to survive limited phase-space corrections and exclusive final-state effects anyway. Of course, since we have not even attempted to produce our own sets of parton distributions, but taken existing ones, all the possibilities of tuning are not exhausted by far. Also the inclusion of the effects of longitudinal resolved photons remains an area where little is known, and our simpleminded ansatz could be made more sophisticated, e.g. by the use of parton distributions designed to describe the partonic structure of longitudinal virtual photons [33]. However, the model is so far limited to the SaS 1D set of parton distributions. An alternative approach with a common resolved class could have been taken, facilitating the handling of the partonic processes, but probably ending up with a more complicated picture for other aspects such as elastic and diffractive scattering, multiple parton–parton interactions, etc. and at the same time losing the flexibility of having the non-perturbative part of the photon structure separated from the perturbatively calculable one. It is a subject for further studies, however.

More sophisticated tests come from the study of event shapes. We have in this article provided some examples how event properties vary between different initial states and photon virtualities. The examples are mainly chosen as simple illustrations; we look forward to more detailed studies by the experimental community, based on the code we now provide in the PYTHIA event generator. Again one cannot expect perfect agreement, but at least an overall such, where disagreements hopefully could help provide hints in which direction to move for an even better and more complete picture. In this sense, our model could be seen as a straw man, although a rather more sophisticated such than is often the case.

Given the fairly complex description, we do not expect the model to be

competitive in the high-Q^2 region of HERA, say for $Q^2 > 10$ GeV^2. There the simple DIS language provides a powerful starting point, that has been well studied over the years, with many models developed in extensive detail [34]. We are here more interested in the crossover region, $Q^2 \sim 0.5 - 5$ GeV^2, where our model predicts all of the photon components to have comparable cross sections, and we therefore would expect no simple picture to work. In $\gamma^*\gamma^*$ studies at LEP2, it is enough to have one photon in this region for our approach to offer interesting alternatives to other descriptions [35]. For smaller Q^2, it smoothly attaches to the existing PYTHIA model of real-photon interactions, while the high-Q^2 end has no such correspondence.

There are some areas where we already now know that not enough effort has gone in to cover the field. One such is the treatment of heavy flavours and in particular charm production, both open and closed (primarily J/ψ), where mass effects are very important. For the lighter quarks, like the u one, the intrinsic 'current algebra' mass is negligible relative to the 'constituent' one, that sets the scale e.g. of the ρ mass. But for a complete charm description, both the impact of the current algebra mass scale and of the further QCD-induced confinement mass effects have to be considered. Another example of a missing area is that related to rapidity gaps, which are already included in the VMD/GVMD sector within a traditional Regge language, but currently not in the DIS region, in spite of the quite conclusive evidence for this from HERA [36]. The two aspects come together in the W dependence of the production rate of exclusive vector mesons, where data show a steeper rise for J/ψ than lighter mesons, and a steeper rise also at larger Q^2 [31]. On the technical side, initial-state radiation remains to be implemented for the lower-$p_\perp$ DIS process (but is there in the higher-$p_\perp$ direct ones).

Therefore the current model should not be considered as the end of the road, but rather as providing a basic framework that could be further refined. In the end, data will have to tell whether the approach as such is viable or not. In the latter case, a simpler scenario would then be preferable, but more likely an even more complex one would be required.

References

[1] E. Mirkes and D. Zeppenfeld, *Phys. Lett.* **B380** (1996) 105;
S. Frixione and G. Ridolfi, *Nucl. Phys.* **B507** (1997) 315;
M. Klasen, T. Kleinwort and G. Kramer, *Eur. Phys. J.* **C1** (1998) 1;
B.W. Harris and J.F. Owens, *Phys. Rev.* **D57** (1998) 5555;
P. Aurenche, L. Bourhis, M. Fontannaz, J.Ph. Guillet, hep-ph/0006011.

[2] V.N. Gribov and L.N. Lipatov, *Sov. J. Nucl. Phys.* **15** (1972) 438 and 675;
G. Altarelli and G. Parisi, *Nucl. Phys.* **B126** (1977) 298;
Yu.L. Dokshitzer, *Sov. Phys. JETP* **46** (1977) 641.

[3] M. Ciafaloni, *Nucl. Phys.* **B296** (1988) 49;
S. Catani, F. Fiorani and G. Marchesini, *Phys. Lett.* **B234** (1990) 339,
Nucl. Phys. **B336** (1990) 18.

[4] B. Andersson, G. Gustafson and J. Samuelsson,
Nucl. Phys. **B467** (1996) 443;
B. Andersson, G. Gustafson and H. Kharraziha,
Phys. Rev. **D57** (1998) 5543;
H. Kharraziha and L. Lönnblad, *J. High Energy Phys.* **03** (1998) 006.

[5] A. Levy and U. Maor, *Phys. Lett.* **B182** (1986) 108;
H. Abramowicz et al., *Phys. Lett.* **B269** (1991) 465;
B. Badelek and J. Kwiecinski, *Phys. Lett.* **B295** (1992) 263;
A. Donnachie and P.V. Landshoff, *Phys. Lett.* **B437** (1998) 408.

[6] C. Friberg and T. Sjöstrand, *Eur. Phys. J.* **C13** (2000) 151
(hep-ph/9907245), and references therein.

[7] T. Sjöstrand and M. van Zijl, *Phys. Rev.* **D36** (1987) 2019.

[8] L. N. Hand, *Phys. Rev.* **129** (1963) 1834.

[9] V. M. Budnev, I. F. Ginzburg, G. V. Meledin and V. G. Serbo,
Phys. Rept. **15** (1974) 181.

[10] T. H. Bauer et al., *Rev. Mod. Phys.* **50** (1978) 261.

[11] G.A. Schuler and T. Sjöstrand, *Z. Phys.* **C68** (1995) 607,
Phys. Lett. **B376** (1996) 193.

[12] G.A. Schuler and T. Sjöstrand, *Phys. Lett.* **B300** (1993) 169,
Nucl. Phys. **B407** (1993) 539.

[13] A. Donnachie and P.V. Landshoff, *Phys. Lett.* **B296** (1992) 227.

[14] J. Dischler and T. Sjöstrand, in preparation.

[15] G.A. Schuler and T. Sjöstrand, *Z. Phys.* **C73** (1997) 677.

[16] T. Sjöstrand, in 'Multiparticle Dynamics 1994', eds. A. Giovannini et al. (World Scientific, Singapore, 1995), p. 221.

[17] I.I. Balitsky and L.N. Lipatov, *Sov. J. Nucl. Phys.* **28** (1978) 822, *Yad. Fiz.* **28** (1978) 1597;
E.A. Kuraev, L.N. Lipatov and V.S. Fadin,
Sov. Phys. JETP **45** (1977) 199, *Zh. Eksp. Teor. Fiz.* **72** (1977) 377.

[18] H. Fraas and D. Schildknecht, *Nucl. Phys.* **B14** (1969) 543.

[19] BCDMS Collaboration, A.C. Benvenuti et al.,
Phys. Lett. **B223** (1989) 485;
H1 Collaboration, C. Adloff et al., *Phys. Lett.* **B393** (1997) 452;
HERMES Collaboration, K. Ackerstaff et al.,
Phys. Lett. **B475** (2000) 386.

[20] J. J. Sakurai, *Phys. Rev. Lett.* **22** (1969) 981.

[21] T. Sjöstrand, *Computer Phys. Commun.* **82** (1994) 74;
http://www.thep.lu.se/∼torbjorn/Pythia.html.

[22] G. Ingelman and P.E. Schlein, *Phys. Lett.* **152B** (1985) 256.

[23] EMC Collaboration, M. Arneodo et al., *Z. Phys.* **C36** (1987) 527;
L. Apanasevich et al., *Phys. Rev.* **D59** (1999) 074007;
G. Miu and T. Sjöstrand, *Phys. Lett.* **B449** (1999) 313;
C. Bálazs, J. Huston and I. Puljak, hep-ph/0002032.

[24] CTEQ Collaboration, H. L. Lai et al., *Eur. Phys. J.* **C12** (2000) 375.

[25] T. Gehrmann, R.G. Roberts and M.R. Whalley, *J. Phys.* **G25** (1999) A1;
BCDMS Collaboration, A.C. Benvenuti et al.,
Phys. Lett. **223B** (1989) 485;
SLAC Collaboration, L.W. Whitlow et al., *Phys. Lett.* **B282** (1992) 475;
E665 Collaboration, M.R. Adams et al., *Phys. Rev.* **D54** (1996) 3006;
NMC Collaboration, M. Arneodo et al., *Nucl. Phys.* **B483** (1997) 3;
H1 Collaboration, S. Aid et al., *Nucl. Phys.* **B470** (1996) 3,
C. Adloff et al., *Nucl. Phys.* **B497** (1996) 3;
ZEUS Collaboration, M. Derrick et al., *Z. Phys.* **C72** (1996) 399,
J. Brietweg et al., *Phys. Lett.* **B407** (1997) 432,
Eur. Phys. J. **C7** (1999) 609.

[26] Particle Data Group, C. Caso et al., *Eur. Phys. J.* **C3** (1998) 1;
ZEUS Collaboration, M. Derrick et al., *Phys. Lett.* **293B** (1992) 465,
Z. Phys. **C63** (1994) 391;
H1 Collaboration, S. Aid et al., *Z. Phys.* **C69** (1995) 27.

[27] TPC/2γ Collaboration, H. Aihara et al., *Z. Phys.* **C34** (1987) 1,
Phys. Rev. Lett. **58** (1997) 97;
PLUTO Collaboration, Ch. Berger et al., *Z. Phys.* **C26** (1984) 353,
Nucl. Phys. **B281** (1987) 365;
CELLO Collaboration, H.J. Behrend et al., contributed paper to the XXVth Int. Conf. on HEP, Singapore, 1990;
TOPAZ Collaboration, K. Muramatsu et al., *Phys. Lett.* **B332** (1994) 477;
OPAL Collaboration, K. Ackerstaff et al., *Z. Phys.* **C74** (1997) 33,
Phys. Lett. **B411** (1997) 387, *Phys. Lett.* **B412** (1997) 225,
G. Abbiendi et al., *Eur. Phys. J.* **C14** (2000) 199;
L3 Collaboration, M. Acciarri et al., *Phys. Lett.* **B436** (1998) 403,
Phys. Lett. **B447** (1999) 147;
ALEPH Collaboration, R. Barate et al., *Phys. Lett.* **B458** (1999) 152.

[28] PLUTO Collaboration, Ch. Berger et al., *Phys. Lett.* **B142** (1984) 119.

[29] L3 Collaboration, M. Acciarri et al., *Phys. Lett.* **B453** (1999) 333.

[30] J. Bartels, A. De Roeck and H. Lotter, *Phys. Lett.* **B389** (1996) 742;
S.J. Brodsky, F. Hautmann and D.E. Soper, *Phys. Rev.* **D56** (1997) 6957.

[31] B. Waugh, *Nucl. Phys.* **B82** *(Proc. Suppl.)* (2000) 262,
and references therein.

[32] ZEUS Collaboration, M. Derrick et al., *Phys. Lett.* **B322** (1994) 287;
H1 Collaboration, T. Ahmed et al., *Nucl. Phys.* **B445** (1995) 195.

[33] J. Chýla, PRA-HEP 00-03 (hep-ph/0006232).

[34] 'Monte Carlo Generators for HERA Physics', eds. A.T. Doyle, G. Grindhammer, G. Ingelman and H. Jung, DESY-PROC-1999-02.

[35] L. Lönnblad, M. Seymour et al., in 'Physics at LEP2', eds. G. Altarelli, T. Sjöstrand and F. Zwirner, CERN 96-01, Vol. 2, p. 187;
T. Alderweireld et al., 'Event generators for gamma-gamma physics', to appear in the Proceedings of the LEP2 Monte Carlo Workshop.

[36] ZEUS Collaboration, M. Derrick et al., *Phys. Lett.* **B315** (1993) 481;
H1 Collaboration, T. Ahmed et al., *Nucl. Phys.* **B429** (1994) 477.

Effects of Longitudinal Photons

Paper V

Effects of Longitudinal Photons

Christer Friberg and Torbjörn Sjöstrand
Department of Theoretical Physics,
Lund University, Lund, Sweden

Abstract

The description of longitudinal photons is far from trivial, and their phenomenological importance is largely unknown. While the cross section for direct interactions is calculable, an even more important contribution could come from resolved states. In the development of our model for the interactions of (real and) virtual photons, we have modeled resolved longitudinal effects by simple multiplicative factors on the resolved transverse-photon contributions. Recently, a first set of parton distributions for longitudinal virtual photons has been presented by Chýla. We therefore compare their impact on some representative distributions, relative to the simpler approaches.

5.1 Introduction

The interactions of a real photon are nontrivial, since the photon can fluctuate into partly non-perturbative $q\overline{q}$ hadron-like states. These strongly-interacting states actually are responsible for the bulk of the γp and $\gamma\gamma$ cross sections. In the spirit of hadronic physics, it is necessary to introduce parton distribution functions (PDF's) in order to describe jet production, with non-perturbative boundary conditions at some low μ_0^2 scale followed by a perturbatively defined evolution towards larger μ^2. Also like in hadronic physics, a description of total, elastic and diffractive cross sections tends to rely on Regge type phenomenology, but again with many unknowns. The hadron-like interaction types are complemented by the direct interactions of the photons, to form a photoproduction framework.

In moving from the real to the virtual photon, matters do not become any simpler. Granted, once the photon virtuality Q^2 is very large, the deeply inelastic scattering (DIS) language of ep collisions can be used quite successfully, but this language bears little resemblance with the one used for real photons, and cannot be extended to small Q^2. So, in the intermediate region, say $Q^2 \sim m_\rho^2$, physics is at best a bit of each, at worst beyond either of the two frameworks. In a set of two recent articles [1, 2] we have tried to develop a model that should provide a smooth interpolation between the photoproduction and the DIS regions, in the first article studying jet production and in the second the total cross section of events.

A special problem here is the contribution from longitudinal photons. By gauge invariance we know that longitudinal photon interactions must vanish in the limit $Q^2 \to 0$. However, in the few instances where their effects have been measured at nonvanishing Q^2, the contribution has been quite significant, from vector meson polarization in exclusive reactions [3] to the standard DIS analysis of $R = \sigma_{\mathrm{L}}^{\gamma^* \mathrm{p}}/\sigma_{\mathrm{T}}^{\gamma^* \mathrm{p}}$ at small x and Q^2 [4]. Furthermore, in QED processes like $\mathrm{e^+e^-} \to \mathrm{e^+e^-e^+e^-}$ the longitudinal contributions are non-negligible [5, 6, 7]. Some of these contributions can be given a partonic interpretation, so it would be tempting again to use the time-honoured parton-distribution language. This is not a universally accepted route, but we may recall the successes in describing much of the diffractive phenomenology in terms of a partonic structure of the Pomeron [8], a state about as virtual and elusive as the longitudinal photon.

Recently a first set of PDF's for the longitudinal photon was presented by Chýla [5]. While the analysis is sensitive to the non-perturbative input for predictions at small Q^2, this sensitivity is reduced for larger Q^2. Access to sensible PDF's should allow an improved predictivity for a number of observables, compared with our previous approach of using simple Q^2- and μ^2-dependent factors to estimate the potential impact of the longitudinal-photon contribution. It is noteworthy that the total γ^*p and $\gamma^*\gamma^*$ cross sections do contain

low-$p_\perp$ components as well, for which a partonic interpretation is only implicit, and where the need for simpler ansätze remains.

The plan of this letter is the following. In section 2 we summarize the main features of our model for virtual-photon interactions, and in section 3 how the model can be extended to encompass an assumed longitudinal-photon contribution as well. Some comparisons, between the more sophisticated approach of having PDF's for longitudinal photons and the simpler one of x-independent multiplicative factors, are presented in section 4. Finally, some conclusions are drawn in section 5.

5.2 A Model for Photon Interactions

In this section we summarize the model presented in [1, 2]. It starts from the model for real photons in [9], but further develops this model and extends it also to encompass the physics of virtual photons. The physics has been implemented in the PYTHIA generator [10], so that complete events can be studied under realistic conditions.

Photon interactions are complicated since the photon wave function contains so many components, each with its own interactions. To first approximation, it may be subdivided into a direct and a resolved part. (In higher orders, the two parts can mix, so one has to provide sensible physical separations between the two.) In the former the photon acts as a pointlike particle, while in the latter it fluctuates into hadronic states. These fluctuations are of $\mathcal{O}(\alpha_{\mathrm{em}})$, and so correspond to a small fraction of the photon wave function, but this is compensated by the bigger cross sections allowed in strong-interaction processes. For real photons therefore the resolved processes dominate the total cross section, while the pointlike ones take over for virtual photons.

The fluctuations $\gamma \to \mathrm{q\overline{q}}\,(\to \gamma)$ can be characterized by the transverse momentum $k_\perp$ of the quarks, or alternatively by some mass scale $m \simeq 2k_\perp$, with a spectrum of fluctuations $\propto \mathrm{d}k_\perp^2/k_\perp^2$. The low-$k_\perp$ part cannot be calculated perturbatively, but is instead parameterized by experimentally determined couplings to the lowest-lying vector mesons, $V = \rho^0$, ω^0, ϕ^0 and J/ψ, an ansatz called VMD for Vector Meson Dominance. Parton distributions are defined with a unit momentum sum rule within a fluctuation [11], giving rise to total hadronic cross sections, jet activity, multiple interactions and beam remnants as in hadronic interactions. In interactions with a hadron or another resolved photon, jet production occurs by typical parton-scattering processes such as $\mathrm{qq}' \to \mathrm{qq}'$ or $\mathrm{gg} \to \mathrm{gg}$.

States at larger $k_\perp$ are called GVMD or Generalized VMD, and their contributions to the parton distribution of the photon are called anomalous. Given a dividing line $k_0 \simeq 0.5$ GeV to VMD states, the anomalous parton distributions are perturbatively calculable. The total cross section of a state is not,

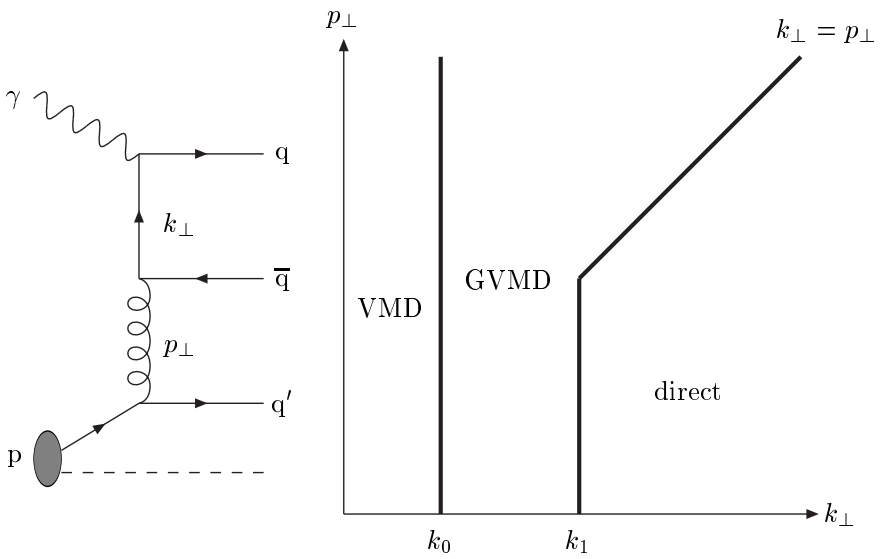

Figure 5.1: (a) Schematic graph for a hard γp process, illustrating the concept of two different scales. (b) The allowed phase space for this process, with one subdivision into event classes.

however, since this involves aspects of soft physics and eikonalization of jet rates. Therefore an ansatz is chosen where the total cross section of a state scales like $k_V^2/k_\perp^2$, where the adjustable parameter $k_V \approx m_\rho/2$ for light quarks. The spectrum of GVMD states is taken to extend over a range $k_0 < k_\perp < k_1$, where k_1 is identified with the $p_{\perp\min}(s)$ cut-off of the perturbative jet spectrum in hadronic interactions, $p_{\perp\min}(s) \approx 1.5$ GeV at typical energies [10]. Above that range, the states are assumed to be sufficiently weakly interacting that no eikonalization procedure is required, so that cross sections can be calculated perturbatively without any recourse to Pomeron phenomenology. There is some arbitrariness in that choice, and some simplifications are required in order to obtain a manageable description.

A real direct photon in a γp collision can interact with the parton content of the proton: $\gamma q \to qg$ (QCD Compton) and $\gamma g \to q\overline{q}$ (Boson Gluon Fusion). The $p_\perp$ in this collision is taken to exceed k_1, in order to avoid double-counting with the interactions of the GVMD states. In γγ, the equivalent situation is called single-resolved, where a direct photon interacts with the partonic component of the other, resolved photon. The γγ direct process $\gamma\gamma \to q\overline{q}$ has no correspondence in γp.

As an illustration of this scenario, the phase space of γp events is shown in Fig. 5.1. (A corresponding plot can be made for $\gamma\gamma$, but then requires three dimensions.) Two transverse momentum scales are introduced, namely the photon resolution scale $k_\perp$ and the hard interaction scale $p_\perp$. Here $k_\perp$ is a measure of the virtuality of a fluctuation of the photon and $p_\perp$ corresponds to the most virtual rung of the ladder, possibly apart from $k_\perp$. As we have discussed above, the low-$k_\perp$ region corresponds to VMD and GVMD states that encompasses both perturbative high-$p_\perp$ and non-perturbative low-$p_\perp$ interactions. Above k_1, the region is split along the line $k_\perp = p_\perp$. When $p_\perp > k_\perp$ the photon is resolved by the hard interaction, as described by the anomalous part of the photon distribution function. This is as in the GVMD sector, except that we should (probably) not worry about multiple parton–parton interactions. In the complementary region $k_\perp > p_\perp$, the $p_\perp$ scale is just part of the traditional evolution of the proton PDF's up to the scale of $k_\perp$, and thus there is no need to introduce an internal structure of the photon. One could imagine the direct class of events as extending below k_1 and there being the low-$p_\perp$ part of the GVMD class, only appearing when a hard interaction at a larger $p_\perp$ scale would not preempt it. This possibility is implicit in the standard cross section framework.

If the photon is virtual, it has a reduced probability to fluctuate into a vector meson state, and this state has a reduced interaction probability. This can be modeled by a traditional dipole factor $(m_V^2/(m_V^2+Q^2))^2$ for a photon of virtuality Q^2, where $m_V \to 2k_\perp$ for a GVMD state. Putting it all together, the cross section of the GVMD sector then scales like

$$\int_{k_0^2}^{k_1^2} \frac{\mathrm{d}k_\perp^2}{k_\perp^2} \frac{k_V^2}{k_\perp^2} \left(\frac{4k_\perp^2}{4k_\perp^2 + Q^2} \right)^2 . \tag{5.1}$$

For a virtual photon the DIS process $\gamma^*\mathrm{q} \to \mathrm{q}$ is also possible, but by gauge invariance its cross section must vanish in the limit $Q^2 \to 0$. At large Q^2, the direct processes can be considered as the $\mathcal{O}(\alpha_\mathrm{s})$ correction to the lowest-order DIS process, but the direct ones survive for $Q^2 \to 0$. There is no unique prescription for a proper combination at all Q^2, but we have attempted an approach that gives the proper limits and minimizes doublecounting. For large Q^2, the DIS γ^*p cross section is proportional to the structure function $F_2(x, Q^2)$ with the Bjorken $x = Q^2/(Q^2 + W^2)$. Since normal parton distribution parameterizations are frozen below some Q_0 scale and therefore do not obey the gauge invariance condition, an ad hoc factor $(Q^2/(Q^2+m_\rho^2))^2$ is introduced for

the conversion from the parameterized $F_2(x,Q^2)$ to a $\sigma_{\mathrm{DIS}}^{\gamma^*\mathrm{p}}$:

$$\begin{aligned}\sigma_{\mathrm{DIS}}^{\gamma^*\mathrm{p}} &\simeq \left(\frac{Q^2}{Q^2+m_\rho^2}\right)^2 \frac{4\pi^2\alpha_{\mathrm{em}}}{Q^2} F_2(x,Q^2) \\ &= \frac{4\pi^2\alpha_{\mathrm{em}}Q^2}{(Q^2+m_\rho^2)^2} \sum_{\mathrm{q}} e_{\mathrm{q}}^2 \left\{ xq(x,Q^2) + x\overline{q}(x,Q^2) \right\} \ .\end{aligned} \tag{5.2}$$

Here m_ρ is some non-perturbative hadronic mass parameter, for simplicity identified with the ρ mass. One of the $Q^2/(Q^2+m_\rho^2)$ factors is required already to give finite $\sigma_{\mathrm{tot}}^{\gamma\mathrm{p}}$ for conventional parton distributions, and could be viewed as a screening of the individual partons at small Q^2. The second factor is chosen to give not only a finite but actually a vanishing $\sigma_{\mathrm{DIS}}^{\gamma^*\mathrm{p}}$ for $Q^2 \to 0$ in order to retain the pure photoproduction description there. This latter factor thus is more a matter of convenience, and other approaches could have been pursued.

In order to avoid double-counting between DIS and direct events, a requirement $p_\perp > \max(k_1, Q)$ is imposed on direct events. In the remaining DIS ones, denoted lowest order (LO) DIS, thus $p_\perp < Q$. This would suggest a subdivision $\sigma_{\mathrm{LO\,DIS}}^{\gamma^*\mathrm{p}} = \sigma_{\mathrm{DIS}}^{\gamma^*\mathrm{p}} - \sigma_{\mathrm{direct}}^{\gamma^*\mathrm{p}}$, with $\sigma_{\mathrm{DIS}}^{\gamma^*\mathrm{p}}$ given by eq. (5.2) and $\sigma_{\mathrm{direct}}^{\gamma^*\mathrm{p}}$ by the perturbative matrix elements. In the limit $Q^2 \to 0$, the DIS cross section is now constructed to vanish while the direct is not, so this would suggest $\sigma_{\mathrm{LO\,DIS}}^{\gamma^*\mathrm{p}} < 0$. However, here we expect the correct answer not to be a negative number but an exponentially suppressed one, by a Sudakov form factor. This modifies the cross section:

$$\sigma_{\mathrm{LO\,DIS}}^{\gamma^*\mathrm{p}} = \sigma_{\mathrm{DIS}}^{\gamma^*\mathrm{p}} - \sigma_{\mathrm{direct}}^{\gamma^*\mathrm{p}} \quad \longrightarrow \quad \sigma_{\mathrm{DIS}}^{\gamma^*\mathrm{p}} \, \exp\left(-\frac{\sigma_{\mathrm{direct}}^{\gamma^*\mathrm{p}}}{\sigma_{\mathrm{DIS}}^{\gamma^*\mathrm{p}}}\right) \ . \tag{5.3}$$

Since we here are in a region where the DIS cross section is no longer the dominant one, this change of the total DIS cross section is not essential.

The overall picture, from a DIS perspective, is illustrated in Fig. 5.2, now with three scales to be kept track of. The traditional DIS region is the strongly ordered one, $Q^2 \gg k_\perp^2 \gg p_\perp^2$, where DGLAP-style evolution [12] is responsible for the event structure. As always, ideology wants strong ordering, while the actual classification is based on ordinary ordering $Q^2 > k_\perp^2 > p_\perp^2$. The region $k_\perp^2 > \max(Q^2, p_\perp^2)$ is also DIS, but of the $\mathcal{O}(\alpha_{\mathrm{s}})$ direct kind. The region where $k_\perp$ is the smallest scale corresponds to non-ordered emissions, that then go beyond DGLAP validity, while the region $p_\perp^2 > k_\perp^2 > Q^2$ cover the interactions of a resolved virtual photon. Comparing Figs. 5.1b and 5.2b, we conclude that the whole region $p_\perp > k_\perp$ involves no doublecounting, since we have made no attempt at a non-DGLAP DIS description but can choose to cover this region entirely by the VMD/GVMD descriptions. Actually, it is only in the corner $p_\perp < k_\perp < \min(k_1, Q)$ that an overlap can occur between the resolved and the

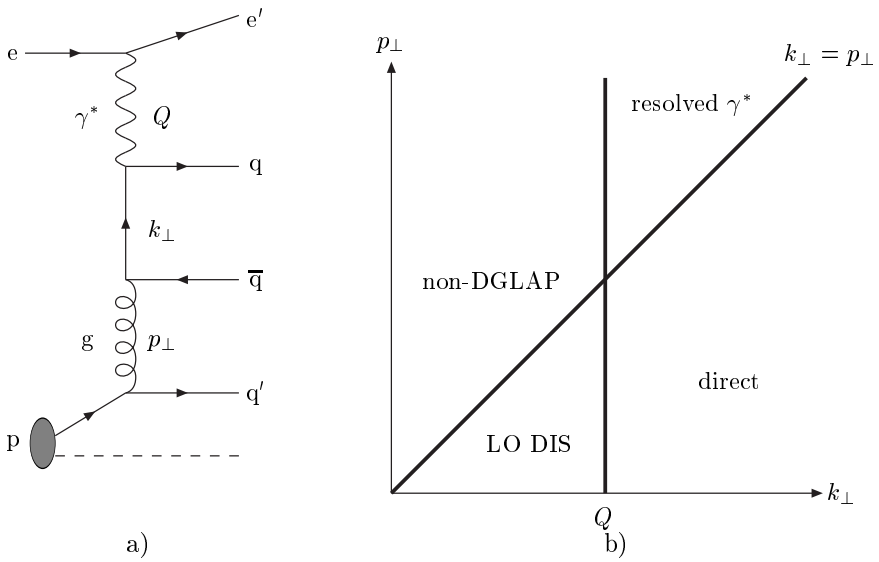

Figure 5.2: (a) Schematic graph for a hard γ^*p process, illustrating the concept of three different scales. (b) Event classification in the large-Q^2 limit.

DIS descriptions. Some further considerations show that usually either of the two is strongly suppressed in this region, except in the range of intermediate Q^2 and rather small W^2. Typically, this is the region where $x \approx Q^2/(Q^2+W^2)$ is not close to zero, and where F_2 is dominated by the valence-quark contribution. The latter behaves roughly $\propto (1-x)^n$, with an n of the order of 3 or 4. Therefore we will introduce a corresponding damping factor to the VMD/GVMD terms.

In total, we have now arrived at our ansatz for all Q^2:

$$\sigma_{\mathrm{tot}}^{\gamma^*\mathrm{p}} = \sigma_{\mathrm{DIS}}^{\gamma^*\mathrm{p}} \exp\left(-\frac{\sigma_{\mathrm{direct}}^{\gamma^*\mathrm{p}}}{\sigma_{\mathrm{DIS}}^{\gamma^*\mathrm{p}}}\right) + \sigma_{\mathrm{direct}}^{\gamma^*\mathrm{p}} + \left(\frac{W^2}{Q^2+W^2}\right)^n \left(\sigma_{\mathrm{VMD}}^{\gamma^*\mathrm{p}} + \sigma_{\mathrm{GVMD}}^{\gamma^*\mathrm{p}}\right) , \tag{5.4}$$

with four main components. Most of these in their turn have a complicated internal structure, as we have seen. The $\gamma^*\gamma^*$ collision between two inequivalent photons contains 13 components: four when the VMD and GVMD states interact with each other (double-resolved), eight with a LO DIS or direct photon interaction on a VMD or GVMD state on either side (single-resolved, including the traditional DIS), and one where two direct photons interact by the process $\gamma^*\gamma^* \to \mathrm{q}\overline{\mathrm{q}}$ (direct, not to be confused with the direct process of γ^*p).

An important note is that the Q^2 dependence of the DIS and direct processes is implemented in the matrix element expressions, i.e. in processes such as $\gamma^*\gamma^* \to \mathrm{q\overline{q}}$ or $\gamma^*\mathrm{q} \to \mathrm{qg}$ the photon virtuality explicitly enters. This is different from VMD/GVMD, where dipole factors are used to reduce the assumed flux of partons inside a virtual photon relative to those of a real one, but the matrix elements themselves contain no dependence on the virtuality either of the partons or of the photon itself. Typically results are obtained with the SaS 1D PDF's for the virtual (transverse) photons [11], since these are well matched to our framework, e.g. allowing a separation of the VMD and GVMD/anomalous components.

5.3 The Longitudinal Photon Contribution

In ep interactions, the cross section can be written as [13]:

$$\frac{\mathrm{d}^2\sigma(\mathrm{ep} \to \mathrm{e}\mathbf{X})}{\mathrm{d}y\,\mathrm{d}Q^2} = f^{\mathrm{T}}_{\gamma/\mathrm{e}}(y,Q^2)\sigma_{\mathrm{T}}(y,Q^2) + f^{\mathrm{L}}_{\gamma/\mathrm{e}}(y,Q^2)\sigma_{\mathrm{L}}(y,Q^2) \ , \tag{5.5}$$

with the fluxes of transverse and longitudinal photons given by

$$f^{\mathrm{T}}_{\gamma/\mathrm{e}}(y,Q^2) = \frac{\alpha_{\mathrm{em}}}{2\pi}\left(\frac{1+(1-y)^2}{y}\frac{1}{Q^2} - \frac{2m_{\mathrm{e}}^2 y}{Q^4}\right) \ , \tag{5.6}$$

$$f^{\mathrm{L}}_{\gamma/\mathrm{e}}(y,Q^2) = \frac{\alpha_{\mathrm{em}}}{2\pi}\frac{2(1-y)}{y}\frac{1}{Q^2} \ . \tag{5.7}$$

Here $y = qP/kP$ is the energy-momentum fraction carried off from the incoming electron by the virtual photon. The y or Q^2 can be traded in for the Bjorken x, but this x can be given an interpretation in terms of the momentum fraction of the struck quark in the proton only in the DIS region of large Q^2. In $\mathrm{e^+e^-}$ events, an $f^{\mathrm{T}}_{\gamma/\mathrm{e}}$ or $f^{\mathrm{L}}_{\gamma/\mathrm{e}}$ occurs on each side, thus giving four terms by simple generalization of eq. (5.5).

The model summarized in the previous section is intended to describe in detail the σ_{T} term, which is composed of all the many different kinds of events. So far, nothing has been said about σ_{L}, except that gauge invariance dictates its vanishing in the limit $Q^2 \to 0$. However, we will assume that quite a similar decomposition can be made of longitudinal photon interactions as was done for the transverse one. To first approximation, this again means a separation into direct and resolved photons. In direct processes, the nature of the photon is explicitly included in the perturbative cross section formulae. Thus, for $\gamma^*\mathrm{q} \to \mathrm{qg}$ and $\gamma^*\mathrm{g} \to \mathrm{q\overline{q}}$, the differential cross sections $\mathrm{d}\hat{\sigma}_{\mathrm{T}}/\mathrm{d}\hat{t}$ and $\mathrm{d}\hat{\sigma}_{\mathrm{L}}/\mathrm{d}\hat{t}$ are separately available [14]. The latter is proportional to Q^2 and thus nicely vanishes in the limit $Q^2 \to 0$. Similarly the $\gamma^*\gamma^* \to \mathrm{q\overline{q}}$ process gives four separate cross section formulae, $\mathrm{d}\hat{\sigma}_{\mathrm{TT,TL,LT,LL}}/\mathrm{d}\hat{t}$ [6]. The DIS, non-direct part

currently contains no explicit description of a longitudinal probing photon, only of a probed one. However, to the extent that PDF's are extracted from $F_2 \propto \sigma_\mathrm{T} + \sigma_\mathrm{L}$ data, effects may be implicitly included. Furthermore, perturbative calculations [15] predict $\sigma_\mathrm{L} \ll \sigma_\mathrm{T}$ in the large-Q^2 region, where this process dominates.

For resolved processes, interactions come in two kinds.
(i) Given a PDF set for the longitudinal photon, jet cross sections can be obtained by the traditional convolution of parton fluxes with the hard-scattering matrix elements. The PDF's are to be evaluated at some factorization scale μ^2 related to the hardness of the scattering, e.g. $\mu^2 = p_\perp^2 = \hat{t}\hat{u}/\hat{s}$ if Q^2 can be neglected.
(ii) In low-$p_\perp$ interactions there is no easily definable perturbative scale μ. The relevant scale instead can be taken as the mass of the state, i.e. m_V for VMD and $2k_\perp$ for GVMD, or m_ρ if one simplifies even further, given that the ρ^0 dominates the VMD/GVMD sector (though less so at large Q^2). Such a choice is not unreasonable also from a partonic point of view: low-$p_\perp$ means no interactions above $k_1 = p_{\perp\min}(s) \approx 2m_\rho$ but certainly allows interactions below this scale, and $k_1/2$ might be a reasonable estimate of the typical order.

In the past, we have studied a few simple multiplicative expressions. Rewriting eq. (5.5) (for the resolved part only) as

$$\frac{\mathrm{d}^2\sigma(\mathrm{ep} \to \mathrm{e}\mathbf{X})}{\mathrm{d}y\,\mathrm{d}Q^2} = f^\mathrm{T}_{\gamma/\mathrm{e}}\sigma_\mathrm{T}\left(1 + \frac{f^\mathrm{L}_{\gamma/\mathrm{e}}}{f^\mathrm{T}_{\gamma/\mathrm{e}}}\frac{\sigma_\mathrm{L}}{\sigma_\mathrm{T}}\right) = f^\mathrm{T}_{\gamma/\mathrm{e}}\sigma_\mathrm{T}\left(1 + \frac{f^\mathrm{L}_{\gamma/\mathrm{e}}}{f^\mathrm{T}_{\gamma/\mathrm{e}}}R\right) \;, \tag{5.8}$$

the forms introduced for jet production were

$$R = R_1(y, Q^2, \mu^2) = a\frac{4\mu^2Q^2}{(\mu^2 + Q^2)^2} \;, \tag{5.9}$$

$$R = R_2(y, Q^2, \mu^2) = a\frac{4Q^2}{(\mu^2 + Q^2)} \;, \tag{5.10}$$

$$R = R_3(y, Q^2, \mu^2) = a\frac{4Q^2}{(m_\rho^2 + Q^2)} \;, \tag{5.11}$$

and for the total cross section processes

$$R = r_1(m_V^2, Q^2) = a\frac{4m_V^2Q^2}{(m_V^2 + Q^2)^2} \;, \tag{5.12}$$

$$R = r_2(m_V^2, Q^2) = a\frac{4Q^2}{(m_V^2 + Q^2)} \;. \tag{5.13}$$

Here a in all cases denotes an unknown number, where the intention was to use $a = 1$ as an extreme contrast to the no-longitudinal-effects $a = 0$, with the truth likely to be somewhere in between. All the expressions were constructed

to vanish like Q^2 for $Q^2 \to 0$. R_1 and r_1 also vanish for large Q^2, while the rest there become Q^2-independent. The μ-independent option R_3 essentially is the same as r_2. In $\gamma^*\gamma^*$ events, the same approach is pursued, with one multiplicative factor for each side with a resolved photon.

It is thus this framework that should be contrasted with what is offered by a set $f_i^{\gamma_{\rm L}^*}(x,\mu^2)$ of PDF's for the longitudinal photon, where the dependence on parton species i and momentum fraction x_i is explicitly given. Assuming that a hard interaction at scale μ^2 is selected for the transverse photon, this entails knowledge of i and x_i. Then a sensible choice would be

$$R = R_{\rm PDF} = \frac{Q^2}{Q^2+m_\rho^2}\,\frac{f_i^{\gamma_{\rm L}^*}(x_i,\mu^2,Q^2)}{f_i^{\gamma_{\rm T}^*}(x_i,\mu^2,Q^2)}\,. \tag{5.14}$$

We have here chosen to introduce one modification for the Chýla $f_i^{\gamma_{\rm L}^*}$, as can be seen. His parameterizations are not intended to be valid for $Q^2 < 1$ GeV^2 or thereabout, since the quark mass effects have not been included, which would provide a dampening in that region. In order to use them below that scale, the ad hoc multiplicative factor $Q^2/(Q^2+m_\rho^2)$ is introduced to ensure the correct limiting behaviour for $Q^2 \to 0$, while rapidly approaching unity for $Q^2 > 1$ GeV^2. The PDF's can then be frozen below the lowest scale for which they can meaningfully be evaluated. In the explicit calculation of $f_i^{\gamma_{\rm L}^*}(x_i,\mu^2,Q^2)$, the relations $0.001 \leq x_i \leq 0.995$ and $1 \leq \ln(\mu^2/\Lambda^2_{\rm QCD})/\ln(Q^2/\Lambda^2_{\rm QCD}) \leq 3.9$ need to be fulfilled and are set to the relevant boundary values if not. It may lead to a negative PDF, however, wherefore the requirement $f_i^{\gamma_{\rm L}^*} \geq 0$ is imposed when calculating $R_{\rm PDF}$.

For the studies in this article, the procedure used is to generate events based on the transverse part of resolved photons only, and then to apply one or several of the R options above as weight for the event. Thus the inclusion of resolved longitudinal-photon effects is not seen as the appearance of any new kinds of hadronic final states, but only as a more or less increased cross section for the already existing transverse-photon ones. This may not be entirely correct — any initial-state radiation would probe $f_i^{\gamma_{\rm L}^*}$ in the region of scales below μ^2 and momentum fractions above x_i, e.g. — but should be a good first approximation, especially in view of all the other uncertainties.

5.4 Some Results

The significance of the longitudinal-photon contribution depends on the $f_i^{\gamma_{\rm L}^*}/f_i^{\gamma_{\rm T}^*}$ ratio, but also on other factors, such as the size of the direct contribution, or the smearing of the parton-level kinematics in realistic observables. We therefore begin by a brief study of $f_i^{\gamma_{\rm L}^*}/f_i^{\gamma_{\rm T}^*}$ itself before illustrating experimental consequences.

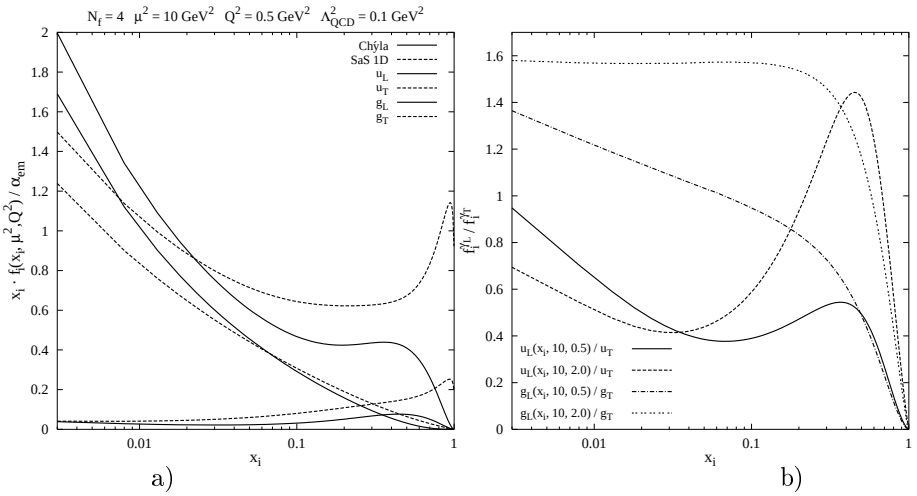

Figure 5.3: a) The x_i-weighted parton distribution functions as given by Chýla and SaS 1D, solid and dashed lines respectively, for a factorization scale $\mu^2 = 10$ GeV^2 and a photon virtuality $Q^2 = 0.5$ GeV^2. x_i is the momentum fraction carried by parton i. In falling order at small x_i the following curves are shown: the sum of the gluon and four lightest flavours (including the respective anti-flavour contribution), the gluon and the u-quark (excluding $\overline{\mathrm{u}}$) contributions. b) The ratio of the Chýla and SaS 1D PDF's as a function of x_i for the u-quark and the gluon at two different photon virtualities, 0.5 and 2 GeV^2, for a fixed factorization scale $\mu^2 = 10$ GeV^2.

The virtual photon PDF used for transversely resolved photons is the SaS 1D one [11]. In Fig. 5.3a it is compared to Chýla's longitudinal photon PDF as a function of the momentum fraction x_i carried by parton i. The down-type quarks give one quarter of the u-quark contribution, due to the difference in electric charge. In Chýla's PDF, no difference is made between u and c, whereas in SaS 1D charm mass effects are included, which dampens the distribution at low photon virtualities. In general, the low-end region in x_i is dominated by the gluon contribution and, with the subdivision made in SaS 1D, the major part comes from the VMD component (at this low photon virtuality). In the high-x_i end, it is instead the valence quarks that dominate and consequently the anomalous, point-like, component of the PDF. The longitudinal PDF's increase faster as compared to the transverse ones when going to lower x_i.

With $\mu^2 = 10$ GeV^2, the u-quark and gluon ratios of the two PDF's are shown in Fig. 5.3b as a function of x_i for two different photon virtualities, 0.5 and 2 GeV^2. At $x_i < 0.5$ the ratios are between 0.4 and 1.6. When increasing

the photon virtuality for a fixed factorization scale μ^2 a non-trivial change in the ratios is obtained due to various effects, for example, shrinking evolution ranges and a faster dampening for the VMD component as compared to the anomalous one.

In Fig. 5.4, the PDF ratio $\sum_i f_i^{\gamma_L^*} / \sum_i f_i^{\gamma_T^*}$ is plotted as a function of the factorization scale μ^2 for different fixed x_i with a photon virtuality of 0.5 GeV^2. Also shown are the different R factors with $a = 0.5$. In the complete event generation, the mass of the fluctuation is used in the r_i factors (eq. (5.12) and (5.13)), i.e. m_V for VMD and $2k_\perp$ for GVMD, but for illustrative purposes the ρ^0 mass has been used for this particular distribution. Therefore, in this plot, r_2 reduces to the simple R_3 alternative. At small and medium x-values the μ^2 dependence is moderate and the μ^2-independent r_2 alternative is a reasonable approximation to $R_{\rm PDF}$. With $Q^2 = 0.5$ GeV^2, the r_1 alternative is about half of the r_2 one. The μ^2-dependent factors, R_1 and R_2, do fall off in agreement with the ratio $f_i^{\gamma_L^*}/f_i^{\gamma_T^*}$ when $x_i = 0.9$, but completely fail at smaller x_i.

We now turn to more realistic distributions, picking one γ^*p and one $\gamma^*\gamma^*$ example, where additionally the former probes jet cross sections and the latter total cross sections. The interesting range of photon virtualities, to study the longitudinal resolved photon effects, is at medium Q^2, say in the interval $m_\rho^2 -$ 4 GeV^2. When approaching $Q^2 = 0$ the longitudinal photon PDF vanish, and at large Q^2 the unresolved events, the direct and DIS ones in our description, take over and dominate the cross sections. In the following, the r_i factors will be used according to eq. (5.12) and (5.13), without the m_ρ approximation.

In γ^*p, a cone jet algorithm was used to find jets with transverse energy $E_\perp^{\rm jet} > 4$ GeV within a radius $R = \sqrt{(\Delta\eta)^2 + (\Delta\phi)^2} < 1$. The invariant mass of the γ^*p system is $W_{\gamma^*{\rm p}} = 200$ GeV and the photon virtuality $Q^2 =$ 1 GeV^2. At HERA $\sqrt{s_{\rm ep}} \simeq 300$ GeV, wherefore a fixed $y = 0.44$ was used when calculating the ratio between the longitudinal and transverse photon fluxes $f_{\gamma/{\rm e}}^{\rm L}(y, Q^2)/f_{\gamma/{\rm e}}^{\rm T}(y, Q^2)$ in eq. (5.8). The proton parton distribution used is the CTEQ5L [17].

The obtained differential jet cross section with at least one jet, with respect to the jet pseudo-rapidity η, is shown in Fig. 5.5a. The photon direction is along the positive y-axes. 'Transverse Resolved' is the total contribution from the sum of the different event classes in our model, but only taking into account the transversely resolved photon contribution. The contribution from direct events, summed over $\sigma_{\rm T,L}$, is shown separately as a reference for the part being unaffected by the different R factors to be applied. The x_i-independent r_1 factor and the $R_{\rm PDF}$ factor give about the same enhancement of the jet cross section. The jet cross section with the r_2 factor is well above the other two. a was for simplicity chosen to 0.5 when calculating r_i. This was the value used in ref. [2] to obtain a nice agreement between data and the model for total γ^*p and $\gamma^*\gamma^*$ cross sections with the r_1 alternative, and also there overshot with

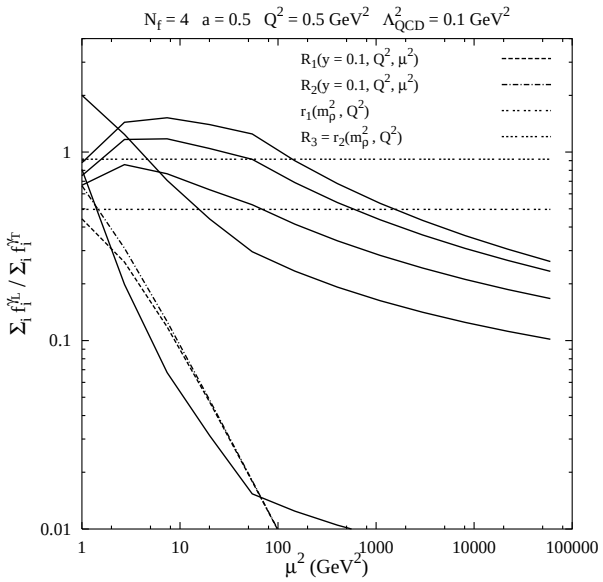

Figure 5.4: The ratio of longitudinal and transverse parton distributions of the photon, $\sum_i f_i^{\gamma^*_{\rm L}} / \sum_i f_i^{\gamma^*_{\rm T}}$, as a function of the factorization scale μ^2 for different fixed parton momentum fractions x_i. The photon virtuality is 0.5 GeV^2. The ratio is between the sum of the gluon and the four lightest flavours contribution for the two PDF's. In decreasing order at high μ^2, x_i is equal to: 0.001, 0.01, 0.1, 0.5 and 0.9. $a = 0.5$ was used to calculate the different R factors.

the r_2 one. The requirement $E_\perp^{\rm jet} > 4$ GeV, i.e. $\mu^2 \gtrsim 16$ GeV^2, suppress the R_1 and R_2 alternatives and give only a small enhancement of the jet cross section for them.

The effects of applying the different R factors above is most pronounced at central rapidities, where the distribution is not so much contaminated by the direct events. With increasing photon virtuality, starting at small but non-negligible Q^2, the jet cross sections obtained with r_1 and r_2 increase faster than the $R_{\rm PDF}$ one (all with respect to the 'Transverse Resolved' jet cross section). At $Q^2 = 1$ GeV^2, as studied above, the r_1 and $R_{\rm PDF}$ agree, with r_2 being above. Continuing to larger virtualities, the $R_{\rm PDF}$ jet cross section will continue increasing relatively to the 'Transverse Resolved', approaching the r_2 one, with the r_1 alternative much below. At large photon virtualities the effect of the R factors will gradually decrease in importance, because the direct cross section will start to dominate the event sample. The main point, however, is that a simple x_i-independent multiplicative factor works well over the whole

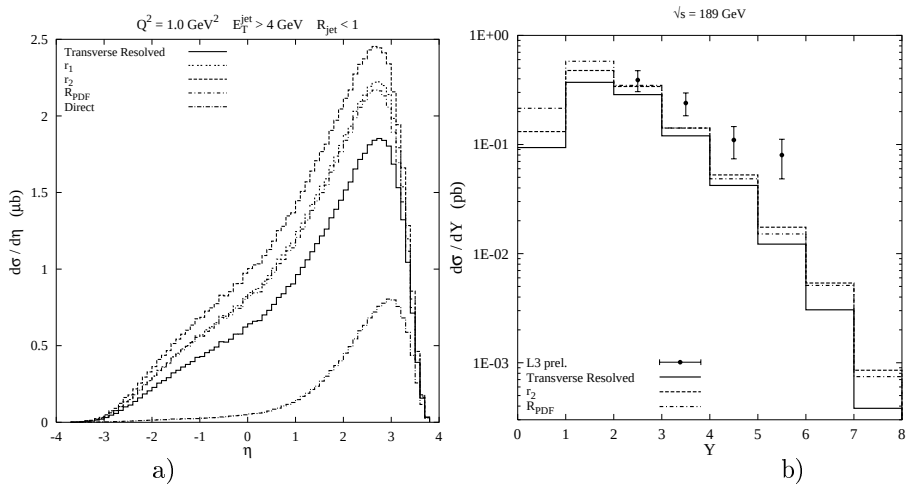

Figure 5.5: a) The γ^*p jet cross section as a function of the pseudo-rapidity η of the jets. 'Direct' shows the contribution from direct events only. The others show the total contribution of all event classes with and without R factors to include (or not include) longitudinal resolved photon effects. $a = 0.5$ is used for r_i. b) The differential $e^+e^- \to e^+e^- +$hadrons cross section as a function of $Y = \ln(y_1 y_2 s/\sqrt{Q_1^2 Q_2^2})$. Same notation as in a).

Q^2 range. This holds also in a simultaneous study of two-jet event properties.

The effects of longitudinal resolved photons can be expected to be important in $\gamma^*\gamma^*$ events, if at least one of the photon virtualities is not too large. Double-tagged two photon events have been measured by the L3 collaboration [18] and is shown with respect to the variable $Y = \ln(y_1 y_2 s/\sqrt{Q_1^2 Q_2^2})$ in Fig. 5.5b, y_i being the energy-momentum fraction carried by photon i, Q_i^2 their respective virtuality and s the CM energy squared of the colliding e^+e^- pair.

As concluded in ref. [2], the direct contribution is the dominant part of the cross section. Again, the 'Transverse Resolved' is the total contribution only taking into account transversely resolved photons. The direct events are included in the total contribution with both transverse and longitudinal cross sections considered. The cross section with the r_2 alternative for estimating the longitudinal resolved photon effects, using $a = 0.5$, give about the same result as with the ratio of the longitudinal and transverse PDF's, $R_{\rm PDF}$. The result with r_1 (not shown) is between the 'Transverse Resolved' and r_2. Elastic, diffractive and low-$p_\perp$ events give a negligible contribution to this $\gamma^*\gamma^*$ cross section. With the hard scale in the processes being relatively large, small factors

R_1 and R_2 are obtained. They disagree with the $R_{\rm PDF}$, which is due to the rather small typical x_i values in the events (cf. Fig. 5.4).

At small Y, corresponding to medium x_i and large Q_i^2, the single- and double-resolved events give small contributions, so the major part of the resolved photon events in this region comes from a photon being resolved by a DIS photon, eq. (5.3) (replacing direct with single-resolved). In our model, the DIS process is simply the $\gamma^*\mathrm{q} \to \mathrm{q}$ one and therefore only the quark part enters the $R_{\rm PDF}$ factor here. Typical x_i values for the lowest Y bins are ~ 0.5, corresponding to the peak region of Fig. 5.3b, where $f_i^{\gamma_{\rm L}^*}/f_i^{\gamma_{\rm T}^*}$ is exceptionally large, and this explains why the r_2 is much below $R_{\rm PDF}$ here. It offers an example of a region where the x_i-dependence of $f_i^{\gamma_{\rm L}^*}/f_i^{\gamma_{\rm T}^*}$ cannot be ignored.

At large Y, x_i and Q_i^2 are smaller (but tagging conditions require $Q_i^2 > 3$ GeV^2), and the single-resolved processes are most important among the resolved ones. The low x_i region is gluon-dominated and $f_i^{\gamma_{\rm L}^*}/f_i^{\gamma_{\rm T}^*}$ vary moderately, wherefore a simple x_i-independent factor can be well approximated for the PDF ratio. While $R_{\rm PDF}$ does increase with Y, already the transversely resolved photon contributions are too small to give a large effect with the R factors included, i.e. the level of the data points is not reached.

5.5 Summary and Outlook

The exploration of the photon structure offers challenges, both for theory and experiment. The theory challenge is to construct a realistic scenario, that covers all the aspects that we know or expect to be there. The experimental challenge is to check each of these aspects separately.

Our photon scenario involves four main components for the real photon — direct, DIS, VMD and GVMD, with the latter two corresponding to a discrete set and a continuum of resolved-photon states, respectively. For $\gamma^*\gamma^*$ interactions, the number of combinations is thirteen. Depending on photon virtualities, these are mixed in varying proportions. Each state can undergo a set of different interactions, that comprise both high-$p_\perp$ jet production and (for most components) low-$p_\perp$ physics. The model has several free parameters, such as parton distributions, μ^2 scales of hard processes, $p_\perp$ cut-off scales, and non-perturbative primordial $k_\perp$ distributions.

Needless to say, the resulting complexity makes experimental tests nontrivial. Any single distribution will receive contributions from several components, states and interactions, usually with so much overlap that it is difficult to distinguish their separate contributions. Some distributions may illuminate a special point, like the separation between direct and resolved photons in the x_γ distribution [16]. Rapidity and $p_\perp$ distributions of jets, underlying event activity, the $p_\perp$ distribution of the beam remnant jet, and elastic and diffractive topolo-

gies are among other measures offering a partial separation. In the future, the simultaneous study of many observables could provide further information, but probably there will be few simple answers.

In this article we have studied one further complication, namely the poorly-known structure of the resolved longitudinal photon. In principle, a separation from transverse photons is provided by the difference in y dependence between $f^{\mathrm{L}}_{\gamma/\mathrm{e}}$ and $f^{\mathrm{T}}_{\gamma/\mathrm{e}}$, but few experiments can offer the range of CM energies and tagging conditions that would allow such a separation. Since the longitudinal-photon interactions vanish in the limit $Q^2 \to 0$, the Q^2 dependence of interaction rates could offer an alternative probe. Assuming that the resolved longitudinal interactions are gradually turned on up to $Q^2 \sim m_\rho^2$, however, over that range also the interactions of the transverse photons partly change character, and furthermore direct longitudinal photons begin to contribute. It is thus not clear to what extent the structure of the longitudinal photon can be probed separately, on top of everything else.

The recent presentation of a set of QCD-evolved parton distributions for the longitudinal photon has allowed a first assessment in this letter. (Other studies, without QCD evolution, were presented in [19].) The x dependence of the Chýla PDF's clearly are different from those of the transverse photons. Therefore the ratio of the two cannot be modeled by simple x-independent factors, the way we have tried in our previous articles. It is then rather disappointing to note that most of these differences are masked in typical experimental quantities. In some instances, the resolved longitudinal-photon contribution itself is rather small relative to other event categories. Even where it is not so small, in quantities like jet rates and total $\gamma^*\gamma^*$ cross sections, the smearing in x and μ^2 is significant.

Thus it comes that a simple factor like our $r_1 = a4m_\rho^2Q^2/(m_\rho^2+Q^2)^2$, with $a \approx 0.5$, gives quite a decent description of the resolved longitudinal effects when photon virtualities are of the order of m_ρ^2. At larger virtualities it is dampened too fast however. (When considering total cross sections, including elastic, diffractive and low-$p_\perp$ events, it was found to agree with data at large photon virtualities [2]. A longitudinal PDF will not give any new insight here however, since no perturbative scale can be associated with the scattering process and, moreover, other descriptions are used.) On the other hand, the $r_2 = a4Q^2/(m_\rho^2+Q^2)$ factor was found to give a decent description of the longitudinal effects in $\gamma^*\gamma^*$ events, characterized by larger Q^2 than the jet studies, while the r_1 failed to do so. A hybrid of the two, e.g. $a4Q^2/(m_\rho^2+bQ^2)$, could accommodate for the r_1 behaviour at $Q^2 \approx m_\rho^2$ ($b \approx 2-3$) and would approach a constant value for large Q^2, similar to r_2. With $R = a4Q^2/(m_V^2+bQ^2)$, $a = 0.5$ and $b = 2$, approximately the same result as r_1 in the γ^*p jet cross section and as r_2 in $\mathrm{e^+e^-} \to \mathrm{e^+e^-} + \mathrm{hadrons}$ ($\gamma^*\gamma^*$) are obtained (Fig. 5.5), i.e. in decent agreement with the parton distribution fraction R_{PDF} for both cases.

It appears likely, but remains to be demonstrated, that a simple factor of this kind could work over a broad kinematical range, for various observables.

The other simple alternatives, R_1 and R_2, are disfavoured. In particular, a significant μ^2 dependence of $f_i^{\gamma_{\rm L}^*}/f_i^{\gamma_{\rm T}^*}$ is only present at large x, and here direct processes may be expected to dominate the data samples.

In summary, the bad news is that the experimental studies of $f_i^{\gamma_{\rm L}^*}(x_i, \mu^2, Q^2)$ may turn out to be very difficult. The good news is that the uncertainty from a non-understanding of the resolved longitudinal photon now can be reduced, which should simplify the task of exploring other aspects of photon physics.

Acknowledgement

We thank J. Chýla for providing the parameterizations of his distributions and for helpful correspondence.

References

[1] C. Friberg and T. Sjöstrand, *Eur. Phys. J.* **C13** (2000) 151 (hep-ph/9907245).

[2] C. Friberg and T. Sjöstrand, LU TP 00–29 (hep-ph/0007314).

[3] CHIO Collaboration, W.D. Shambroom et al., *Phys. Rev.* **D26** (1982) 1;
NMC Collaboration, P. Amaudruz et al., *Z. Phys.* **C54** (1992) 239;
NMC Collaboration, M. Arneodo et al., *Nucl. Phys.* **B429** (1994) 503;
E665 Collaboration, M.R. Adams et al., *Z. Phys.* **C74** (1997) 237;
ZEUS Collaboration, J. Breitweg et al., *Eur. Phys. J.* **C6** (1999) 603, *Eur. Phys. J.* **C12** (2000) 393;
H1 Collaboration, C. Adloff et al., *Eur. Phys. J.* **C13** (2000) 371;
HERMES Collaboration, K. Ackerstaff et al., hep-ex/0002016.

[4] BCDMS Collaboration, A.C. Benvenuti et al., *Phys. Lett.* **B223** (1989) 485;
H1 Collaboration, C. Adloff et al., *Phys. Lett.* **B393** (1997) 452;
HERMES Collaboration, K. Ackerstaff et al., *Phys. Lett.* **B475** (2000) 386.

[5] J. Chýla, PRA-HEP 00-03 (hep-ph/0006232).

[6] V.M. Budnev, I.F. Ginzburg, G.V. Meledin and V.G. Serbo, *Phys. Rept.* **15** (1974) 181;
V.N. Baier, E.A. Kuraev, V.S. Fadin and V.A. Khoze, *Phys. Rept.* **78** (1981) 293.

[7] A.S. Gorski, B.L. Ioffe, A.Yu. Kodjamirian and A. Oganesian, *Z. Phys.* **C44** (1989) 523.

[8] G. Ingelman and P.E. Schlein, *Phys. Lett.* **152B** (1985) 256.

[9] G.A. Schuler and T. Sjöstrand, *Phys. Lett.* **B300** (1993) 169, *Nucl. Phys.* **B407** (1993) 539, *Z. Phys.* **C73** (1997) 677.

[10] T. Sjöstrand, *Computer Phys. Commun.* **82** (1994) 74; T. Sjöstrand et al., in preparation; http://www.thep.lu.se/∼torbjorn/Pythia.html.

[11] G.A. Schuler and T. Sjöstrand, *Z. Phys.* **C68** (1995) 607, *Phys. Lett.* **B376** (1996) 193.

[12] V.N. Gribov and L.N. Lipatov, *Sov. J. Nucl. Phys.* **15** (1972) 438 and 675; G. Altarelli and G. Parisi, *Nucl. Phys.* **B126** (1977) 298; Yu.L. Dokshitzer, *Sov. Phys. JETP* **46** (1977) 641.

[13] L.N. Hand, *Phys. Rev.* **129** (1963) 1834.

[14] G. Altarelli and G. Martinelli, *Phys. Lett.* **76B** (1978) 89; A. Mendéz, *Nucl. Phys.* **B145** (1978) 199; R. Peccei and R. Rückl, *Nucl. Phys.* **B162** (1980) 125; Ch. Rumpf, G. Kramer and J. Willrodt, *Z. Phys.* **C7** (1981) 337.

[15] S. R. Mishra and F. Sciulli, *Phys. Lett.* **B244** (1990) 341.

[16] ZEUS Collaboration, M. Derrick et al., *Phys. Lett.* **B322** (1994) 287; H1 Collaboration, T. Ahmed et al., *Nucl. Phys.* **B445** (1995) 195.

[17] CTEQ Collaboration, H. L. Lai et al., *Eur. Phys. J.* **C12** (2000) 375.

[18] L3 Collaboration, M. Acciarri et al., *Phys. Lett.* **B453** (1999) 333.

[19] J. Chýla and M. Tasevský, PRA-HEP 99-07 (hep-ph/9912514), PRA-HEP 00-01 (hep-ph/0003300).

High-Energy-Physics Event Generation with PYTHIA 6.1

Paper VI

High-Energy-Physics Event Generation with PYTHIA 6.1

Torbjörn Sjöstrand[1], Patrik Edén[2], Christer Friberg[1],
Leif Lönnblad[1], Gabriela Miu[1], Stephen Mrenna[3]
and Emanuel Norrbin[1]

1) Department of Theoretical Physics, Lund University,
Sölvegatan 14A, S-223 62 Lund, Sweden

2) NORDITA, Blegdamsvej 17, DK-2100 Copenhagen, Denmark

3) Physics Department, University of California at Davis,
One Shields Avenue, Davis, CA 95616, USA

Abstract

PYTHIA version 6 represents a merger of the PYTHIA 5, JETSET 7 and SPYTHIA programs, with many improvements. It can be used to generate high-energy-physics 'events', i.e. sets of outgoing particles produced in the interactions between two incoming particles. The objective is to provide as accurate as possible a representation of event properties in a wide range of reactions. The underlying physics is not understood well enough to give an exact description; the programs therefore contain a combination of analytical results and various models. The emphasis in this article is on new aspects, but a few words of general introduction are included. Further documentation is available on the web.

New Version Summary

Title of program: PYTHIA
Version number: 6.152
Catalogue identifier: —
Distribution format: uuencoded compressed tar file
References to most recent previous versions:
Computer Physics Communications **82** (1994) 74 and
Computer Physics Communications **101** (1997) 232, respectively
Catalogue identifiers of most recent previous versions:
ACTU
Authors of most recent previous versions:
T. Sjöstrand, and S. Mrenna, respectively
Does the new version supersede the previous versions?: yes
Computers for which the new program is designed and others on which it has been tested:
Computer:
DELL Precision 210 and any other machine with a Fortran 77 compiler
Installation: Lund University
Operating system under which the new program has been tested:
Linux Red Hat 6.2
Programming language used:
Fortran 77; is also fully compatible with Fortran 90, i.e. does not make use of any obsolescent features of the Fortran 90 standard
Memory required to execute with typical data: about 800 kwords
No. of bits in word: 32 (double precision real uses two words)
No. of processors used: 1
Has the code been vectorized or parallelized?: no
No. of bytes in distributed program: about 1.8 Mb

Keywords:
QCD, standard model, beyond standard model, hard scattering, e^+e^- annihilation, leptoproduction, photoproduction, hadronic processes, high-$p_\perp$ scattering, prompt photons, gauge bosons, Higgs physics, parton distribution functions, jet production, parton showers, fragmentation, hadronization, beam remnants, multiple interactions, particle decays, event measures

Nature of physical problem:
high-energy collisions between elementary particles normally give rise to complex final states, with large multiplicities of hadrons, leptons, neutrinos and photons. The relation between these final states and the underlying physics description is not a simple one, for two main reasons. Firstly, we do not even in principle have a complete understanding of the physics. Secondly, any analytical approach is made intractable by the large multiplicities.

Method of solution:
complete events are generated by Monte Carlo methods. The complexity is mastered by a subdivision of the full problem into a set of simpler separate tasks. All main aspects of the events are simulated, such as hard-process selection, initial- and final-state radiation, beam remnants, fragmentation, decays, and so on. Therefore events should be directly comparable with experimentally observable ones. The programs can be used to extract physics from comparisons with existing data, or to study physics at future experiments.

Restrictions on the complexity of the problem:
depends on the problem studied

Typical running time:
10–1000 events per second, depending on process studied

Unusual features of the program: none

6.1 Introduction

The PYTHIA and JETSET programs [1] are frequently used for event generation in high-energy physics. The emphasis is on multiparticle production in collisions between elementary particles. This in particular means hard interactions in e^+e^-, pp and ep colliders, although also other applications are envisaged. The programs can be used both to compare with existing data, for physics studies or detector corrections, and to explore possibilities at present or future experiments. The programs are intended to generate complete events, in as much detail as experimentally observable ones, within the bounds of our current understanding of the underlying physics. The quantum mechanical variability between events in nature is here replaced by Monte Carlo methods, to obtain 'correctly' both the average behaviour and the amount of fluctuations. Many of the components of the programs represent original research, in the sense that models have been developed and implemented for a number of aspects not covered by standard theory.

Although originally conceived separately, the PYTHIA [2] and JETSET [3] programs today are so often used together that they have here been joined under the PYTHIA header. To this has been added the code of SPYTHIA [4], an extension of PYTHIA that also covers the generation of supersymmetric processes. The current article is not intended to give a complete survey of all the program elements or all the physics — we refer to the long manual and further documentation on the PYTHIA web page

`http://www.thep.lu.se/~torbjorn/Pythia.html`

for this. Instead the objective is to give a survey of new features since the latest official publications, with some minimal amount of background material to tie the story together. Many of the advances are related to physics studies, which are further described in separate articles. Others are of a more technical nature, or have been of too limited a scope to result in individual publications (so far).

Some of the main topics are:

- An improved simulation of supersymmetric physics, with several new processes.
- Many new processes of beyond-the-standard-model physics, in areas such as technicolor and doubly-charged Higgses.
- An expanded description of QCD processes in virtual-photon interactions, combined with a new machinery for the flux of virtual photons from leptons.
- Initial-state parton showers are matched to the next-to-leading order matrix elements for gauge boson production.
- The hadronization description of low-mass strings has been improved, with consequences especially for heavy-flavour production.
- An alternative baryon production model has been introduced.

- Colour rearrangement is included as a new option, and several alternative Bose-Einstein descriptions are added.

Many further examples will be given. In the process, the total size of the program code has almost doubled in the six years since the previous main publication.

The report is subdivided so that the physics news are highlighted in section 2 and the programming ones (plus a few more physics ones) in section 3. Section 4 contains some concluding remarks and an outlook.

6.2 Physics News

For the description of a typical high-energy event, an event generator should contain a simulation of several physics aspects. If we try to follow the evolution of an event in some semblance of a time order, one may arrange these aspects as follows:

1. Initially two beam particles are coming in towards each other. Normally each particle is characterized by a set of parton distributions, which defines the partonic substructure in terms of flavour composition and energy sharing.
2. One shower initiator parton from each beam starts off a sequence of branchings, such as $q \to qg$, which build up an initial-state shower.
3. One incoming parton from each of the two showers enters the hard process, where then a number of outgoing partons are produced, usually two. It is the nature of this process that determines the main characteristics of the event.
4. The hard process may produce a set of short-lived resonances, like the $Z^0/W^{\pm}$ gauge bosons, whose decay to normal partons has to be considered in close association with the hard process itself.
5. The outgoing partons may branch as well, to build up final-state showers.
6. In addition to the hard process considered above, further semihard interactions may occur between the other partons of two incoming hadrons.
7. When a shower initiator is taken out of a beam particle, a beam remnant is left behind. This remnant may have an internal structure, and a net colour charge that relates it to the rest of the final state.
8. The QCD confinement mechanism ensures that the outgoing quarks and gluons are not observable, but instead fragment to colour neutral hadrons.
9. Normally the fragmentation mechanism can be seen as occurring in a set of separate colour singlet subsystems, but interconnection effects such as colour rearrangement or Bose–Einstein may complicate the picture.
10. Many of the produced hadrons are unstable and decay further.

In the following subsections, we will survey updates of the above aspects, not in the same order as given here, but rather in the order in which they appear in the program execution, i.e. starting with the hard process.

Table 6.1: Subprocesses, part 1: standard model, according to the subprocess numbering of PYTHIA.'f' denotes a fermion (quark or lepton), 'Q' a heavy quark and 'F' a heavy fermion.

No.	Subprocess
Hard QCD processes:	
11	$f_i f_j \to f_i f_j$
12	$f_i \bar{f}_i \to f_k \bar{f}_k$
13	$f_i \bar{f}_i \to gg$
28	$f_i g \to f_i g$
53	$gg \to f_k \bar{f}_k$
68	$gg \to gg$
Soft QCD processes:	
91	elastic scattering
92	single diffraction (XB)
93	single diffraction (AX)
94	double diffraction
95	low-$p_\perp$ production
Open heavy flavour: (also fourth generation)	
81	$f_i \bar{f}_i \to Q_k \bar{Q}_k$
82	$gg \to Q_k \bar{Q}_k$
83	$q_i f_j \to Q_k f_l$
84	$g\gamma \to Q_k \bar{Q}_k$
85	$\gamma\gamma \to F_k \bar{F}_k$
Closed heavy flavour:	
86	$gg \to J/\psi g$
87	$gg \to \chi_{0c} g$
88	$gg \to \chi_{1c} g$
89	$gg \to \chi_{2c} g$
104	$gg \to \chi_{0c}$
105	$gg \to \chi_{2c}$
106	$gg \to J/\psi\gamma$
107	$g\gamma \to J/\psi g$
108	$\gamma\gamma \to J/\psi\gamma$

No.	Subprocess
W/Z production:	
1	$f_i \bar{f}_i \to \gamma^*/Z$
2	$f_i \bar{f}_j \to W^\pm$
22	$f_i \bar{f}_i \to Z^0 Z^0$
23	$f_i \bar{f}_j \to Z^0 W^\pm$
25	$f_i \bar{f}_i \to W^+ W^-$
15	$f_i \bar{f}_i \to g Z^0$
16	$f_i \bar{f}_j \to g W^\pm$
30	$f_i g \to f_i Z^0$
31	$f_i g \to f_k W^\pm$
19	$f_i \bar{f}_i \to \gamma Z^0$
20	$f_i \bar{f}_j \to \gamma W^\pm$
35	$f_i \gamma \to f_i Z^0$
36	$f_i \gamma \to f_k W^\pm$
69	$\gamma\gamma \to W^+ W^-$
70	$\gamma W^\pm \to Z^0 W^\pm$
Prompt photons:	
14	$f_i \bar{f}_i \to g\gamma$
18	$f_i \bar{f}_i \to \gamma\gamma$
29	$f_i g \to f_i \gamma$
114	$gg \to \gamma\gamma$
115	$gg \to g\gamma$
Deep inelastic scatt.:	
10	$f_i f_j \to f_i f_j$
99	$\gamma^* f_i \to f_i$
Photon-induced:	
33	$f_i \gamma \to f_i g$
34	$f_i \gamma \to f_i \gamma$
54	$g\gamma \to f_k \bar{f}_k$
58	$\gamma\gamma \to f_k \bar{f}_k$

6.2.1 Physics Subprocesses

Process Classifications

PYTHIA contains a rich selection of physics scenarios, with well above 200 different subprocesses, see Tables 6.1, 6.2, 6.3 and 6.4. The process number

Table 6.2: Subprocesses, part 2: standard model continued and Higgs production in a two-doublet scenario, with notation as above.

No.	Subprocess
131	$f_i\gamma_T^* \to f_i g$
132	$f_i\gamma_L^* \to f_i g$
133	$f_i\gamma_T^* \to f_i \gamma$
134	$f_i\gamma_L^* \to f_i \gamma$
135	$g\gamma_T^* \to f_i \overline{f}_i$
136	$g\gamma_L^* \to f_i \overline{f}_i$
137	$\gamma_T^*\gamma_T^* \to f_i \overline{f}_i$
138	$\gamma_T^*\gamma_L^* \to f_i \overline{f}_i$
139	$\gamma_L^*\gamma_T^* \to f_i \overline{f}_i$
140	$\gamma_L^*\gamma_L^* \to f_i \overline{f}_i$
80	$q_i\gamma \to q_k \pi^{\pm}$
Light SM Higgs:	
3	$f_i \overline{f}_i \to h^0$
24	$f_i \overline{f}_i \to Z^0 h^0$
26	$f_i \overline{f}_j \to W^{\pm} h^0$
102	$gg \to h^0$
103	$\gamma\gamma \to h^0$
110	$f_i \overline{f}_i \to \gamma h^0$
121	$gg \to Q_k \overline{Q}_k h^0$
122	$q_i \overline{q}_i \to Q_k \overline{Q}_k h^0$
123	$f_i f_j \to f_i f_j h^0$
124	$f_i f_j \to f_k f_l h^0$
Heavy SM Higgs:	
5	$Z^0 Z^0 \to h^0$
8	$W^+ W^- \to h^0$
71	$Z_L^0 Z_L^0 \to Z_L^0 Z_L^0$
72	$Z_L^0 Z_L^0 \to W_L^+ W_L^-$
73	$Z_L^0 W_L^{\pm} \to Z_L^0 W_L^{\pm}$
76	$W_L^+ W_L^- \to Z_L^0 Z_L^0$
77	$W_L^{\pm} W_L^{\pm} \to W_L^{\pm} W_L^{\pm}$

No.	Subprocess
BSM Neutral Higgses:	
151	$f_i \overline{f}_i \to H^0$
152	$gg \to H^0$
153	$\gamma\gamma \to H^0$
171	$f_i \overline{f}_i \to Z^0 H^0$
172	$f_i \overline{f}_j \to W^{\pm} H^0$
173	$f_i f_j \to f_i f_j H^0$
174	$f_i f_j \to f_k f_l H^0$
181	$gg \to Q_k \overline{Q}_k H^0$
182	$q_i \overline{q}_i \to Q_k \overline{Q}_k H^0$
156	$f_i \overline{f}_i \to A^0$
157	$gg \to A^0$
158	$\gamma\gamma \to A^0$
176	$f_i \overline{f}_i \to Z^0 A^0$
177	$f_i \overline{f}_j \to W^{\pm} A^0$
178	$f_i f_j \to f_i f_j A^0$
179	$f_i f_j \to f_k f_l A^0$
186	$gg \to Q_k \overline{Q}_k A^0$
187	$q_i \overline{q}_i \to Q_k \overline{Q}_k A^0$
Charged Higgs:	
143	$f_i \overline{f}_j \to H^+$
161	$f_i g \to f_k H^+$
Higgs pairs:	
297	$f_i \overline{f}_j \to H^{\pm} h^0$
298	$f_i \overline{f}_j \to H^{\pm} H^0$
299	$f_i \overline{f}_i \to A^0 h^0$
300	$f_i \overline{f}_i \to A^0 H^0$
301	$f_i \overline{f}_i \to H^+ H^-$

space has tended to become a bit busy, so processes are not always numbered logically. Some processes are closely related variants of the same basic process (e.g. the production of a neutralino pair in processes 216–225), others are alternative formulations (e.g. $Z^0 Z^0 \to h^0$ has to be convoluted with the flux of

Table 6.3: Subprocesses, part 3: beyond the standard model non-SUSY, with notation as above.

No.	Subprocess
New gauge bosons:	
141	$f_i\bar{f}_i \to \gamma/Z^0/Z'^0$
142	$f_i\bar{f}_j \to W'^+$
144	$f_i\bar{f}_j \to R$
Technicolor:	
149	$gg \to \eta_{tc}$
191	$f_i\bar{f}_i \to \rho^0_{tc}$
192	$f_i\bar{f}_j \to \rho^+_{tc}$
193	$f_i\bar{f}_i \to \omega^0_{tc}$
194	$f_i\bar{f}_i \to f_k\bar{f}_k$
195	$f_i\bar{f}_j \to f_k\bar{f}_l$
361	$f_i\bar{f}_i \to W^+_L W^-_L$
362	$f_i\bar{f}_i \to W^\pm_L \pi^\mp_{tc}$
363	$f_i\bar{f}_i \to \pi^+_{tc}\pi^-_{tc}$
364	$f_i\bar{f}_i \to \gamma\pi^0_{tc}$
365	$f_i\bar{f}_i \to \gamma\pi'^0_{tc}$
366	$f_i\bar{f}_i \to Z^0\pi^0_{tc}$
367	$f_i\bar{f}_i \to Z^0\pi'^0_{tc}$
368	$f_i\bar{f}_i \to W^\pm\pi^\mp_{tc}$
370	$f_i\bar{f}_j \to W^\pm_L Z^0_L$
371	$f_i\bar{f}_j \to W^\pm_L \pi^0_{tc}$
372	$f_i\bar{f}_j \to \pi^\pm_{tc} Z^0_L$
373	$f_i\bar{f}_j \to \pi^\pm_{tc}\pi^0_{tc}$
374	$f_i\bar{f}_j \to \gamma\pi^\pm_{tc}$
375	$f_i\bar{f}_j \to Z^0\pi^\pm_{tc}$
376	$f_i\bar{f}_j \to W^\pm\pi^0_{tc}$
377	$f_i\bar{f}_j \to W^\pm\pi'^0_{tc}$

No.	Subprocess
Compositeness:	
146	$e\gamma \to e^*$
147	$dg \to d^*$
148	$ug \to u^*$
167	$q_iq_j \to d^*q_k$
168	$q_iq_j \to u^*q_k$
169	$q_i\bar{q}_i \to e^\pm e^{*\mp}$
165	$f_i\bar{f}_i(\to \gamma^*/Z^0) \to f_k\bar{f}_k$
166	$f_i\bar{f}_j(\to W^\pm) \to f_k\bar{f}_l$
Doubly-charged Higgs:	
341	$\ell_i\ell_j \to H^{\pm\pm}_L$
342	$\ell_i\ell_j \to H^{\pm\pm}_R$
343	$\ell^\pm_i\gamma \to H^{\pm\pm}_L e^\mp$
344	$\ell^\pm_i\gamma \to H^{\pm\pm}_R e^\mp$
345	$\ell^\pm_i\gamma \to H^{\pm\pm}_L \mu^\mp$
346	$\ell^\pm_i\gamma \to H^{\pm\pm}_R \mu^\mp$
347	$\ell^\pm_i\gamma \to H^{\pm\pm}_L \tau^\mp$
348	$\ell^\pm_i\gamma \to H^{\pm\pm}_R \tau^\mp$
349	$f_i\bar{f}_i \to H^{++}_L H^{--}_L$
350	$f_i\bar{f}_i \to H^{++}_R H^{--}_R$
351	$f_if_j \to f_kf_lH^{\pm\pm}_L$
352	$f_if_j \to f_kf_lH^{\pm\pm}_R$
Leptoquarks:	
145	$q_i\ell_j \to L_Q$
162	$qg \to \ell L_Q$
163	$gg \to L_Q\bar{L}_Q$
164	$q_i\bar{q}_i \to L_Q\bar{L}_Q$

Z^0's around fermions, and thus is an approximation to $f_if_j \to f_if_jh^0$; when the latter was implemented the former was still kept). A process may also have hidden further layers of processes (e.g. $H^\pm$ can be produced in top decays, whichever way top is produced).

One classification of the subprocesses is according to the physics scenario. The following major groups may be distinguished:

Table 6.4: Subprocesses, part 4: SUSY, with notation as above. A trailing + on a final state indicates that the charge-conjugated one is included as well.

No.	Subprocess
SUSY:	
201	$f_i\bar{f}_i \to \tilde{e}_L\tilde{e}_L^*$
202	$f_i\bar{f}_i \to \tilde{e}_R\tilde{e}_R^*$
203	$f_i\bar{f}_i \to \tilde{e}_L\tilde{e}_R^*+$
204	$f_i\bar{f}_i \to \tilde{\mu}_L\tilde{\mu}_L^*$
205	$f_i\bar{f}_i \to \tilde{\mu}_R\tilde{\mu}_R^*$
206	$f_i\bar{f}_i \to \tilde{\mu}_L\tilde{\mu}_R^*+$
207	$f_i\bar{f}_i \to \tilde{\tau}_1\tilde{\tau}_1^*$
208	$f_i\bar{f}_i \to \tilde{\tau}_2\tilde{\tau}_2^*$
209	$f_i\bar{f}_i \to \tilde{\tau}_1\tilde{\tau}_2^*+$
210	$f_i\bar{f}_j \to \tilde{\ell}_L\tilde{\nu}_\ell^*+$
211	$f_i\bar{f}_j \to \tilde{\tau}_1\tilde{\nu}_\tau^*+$
212	$f_i\bar{f}_j \to \tilde{\tau}_2\tilde{\nu}_\tau{}^*+$
213	$f_i\bar{f}_i \to \tilde{\nu}_\ell\tilde{\nu}_\ell{}^*$
214	$f_i\bar{f}_i \to \tilde{\nu}_\tau\tilde{\nu}_\tau^*$
216	$f_i\bar{f}_i \to \tilde{\chi}_1\tilde{\chi}_1$
217	$f_i\bar{f}_i \to \tilde{\chi}_2\tilde{\chi}_2$
218	$f_i\bar{f}_i \to \tilde{\chi}_3\tilde{\chi}_3$
219	$f_i\bar{f}_i \to \tilde{\chi}_4\tilde{\chi}_4$
220	$f_i\bar{f}_i \to \tilde{\chi}_1\tilde{\chi}_2$
221	$f_i\bar{f}_i \to \tilde{\chi}_1\tilde{\chi}_3$
222	$f_i\bar{f}_i \to \tilde{\chi}_1\tilde{\chi}_4$
223	$f_i\bar{f}_i \to \tilde{\chi}_2\tilde{\chi}_3$
224	$f_i\bar{f}_i \to \tilde{\chi}_2\tilde{\chi}_4$
225	$f_i\bar{f}_i \to \tilde{\chi}_3\tilde{\chi}_4$
226	$f_i\bar{f}_i \to \tilde{\chi}_1^\pm\tilde{\chi}_1^\mp$
227	$f_i\bar{f}_i \to \tilde{\chi}_2^\pm\tilde{\chi}_2^\mp$
228	$f_i\bar{f}_i \to \tilde{\chi}_1^\pm\tilde{\chi}_2^\mp$
229	$f_i\bar{f}_j \to \tilde{\chi}_1\tilde{\chi}_1^\pm$
230	$f_i\bar{f}_j \to \tilde{\chi}_2\tilde{\chi}_1^\pm$
231	$f_i\bar{f}_j \to \tilde{\chi}_3\tilde{\chi}_1^\pm$
232	$f_i\bar{f}_j \to \tilde{\chi}_4\tilde{\chi}_1^\pm$
233	$f_i\bar{f}_j \to \tilde{\chi}_1\tilde{\chi}_2^\pm$
234	$f_i\bar{f}_j \to \tilde{\chi}_2\tilde{\chi}_2^\pm$
235	$f_i\bar{f}_j \to \tilde{\chi}_3\tilde{\chi}_2^\pm$
236	$f_i\bar{f}_j \to \tilde{\chi}_4\tilde{\chi}_2^\pm$
237	$f_i\bar{f}_i \to \tilde{g}\tilde{\chi}_1$
238	$f_i\bar{f}_i \to \tilde{g}\tilde{\chi}_2$
239	$f_i\bar{f}_i \to \tilde{g}\tilde{\chi}_3$
240	$f_i\bar{f}_i \to \tilde{g}\tilde{\chi}_4$
241	$f_i\bar{f}_j \to \tilde{g}\tilde{\chi}_1^\pm$
242	$f_i\bar{f}_j \to \tilde{g}\tilde{\chi}_2^\pm$
243	$f_i\bar{f}_i \to \tilde{g}\tilde{g}$
244	$gg \to \tilde{g}\tilde{g}$
246	$f_ig \to \tilde{q}_{iL}\tilde{\chi}_1$
247	$f_ig \to \tilde{q}_{iR}\tilde{\chi}_1$
248	$f_ig \to \tilde{q}_{iL}\tilde{\chi}_2$
249	$f_ig \to \tilde{q}_{iR}\tilde{\chi}_2$
250	$f_ig \to \tilde{q}_{iL}\tilde{\chi}_3$
251	$f_ig \to \tilde{q}_{iR}\tilde{\chi}_3$
252	$f_ig \to \tilde{q}_{iL}\tilde{\chi}_4$
253	$f_ig \to \tilde{q}_{iR}\tilde{\chi}_4$
254	$f_ig \to \tilde{q}_{jL}\tilde{\chi}_1^\pm$
256	$f_ig \to \tilde{q}_{jL}\tilde{\chi}_2^\pm$
258	$f_ig \to \tilde{q}_{iL}\tilde{g}$
259	$f_ig \to \tilde{q}_{iR}\tilde{g}$
261	$f_i\bar{f}_i \to \tilde{t}_1\tilde{t}_1^*$
262	$f_i\bar{f}_i \to \tilde{t}_2\tilde{t}_2^*$
263	$f_i\bar{f}_i \to \tilde{t}_1\tilde{t}_2^*+$
264	$gg \to \tilde{t}_1\tilde{t}_1^*$
265	$gg \to \tilde{t}_2\tilde{t}_2^*$
271	$f_if_j \to \tilde{q}_{iL}\tilde{q}_{jL}$
272	$f_if_j \to \tilde{q}_{iR}\tilde{q}_{jR}$
273	$f_if_j \to \tilde{q}_{iL}\tilde{q}_{jR}+$
274	$f_i\bar{f}_j \to \tilde{q}_{iL}\tilde{q}_{jL}^*$
275	$f_i\bar{f}_j \to \tilde{q}_{iR}\tilde{q}_{jR}^*$
276	$f_i\bar{f}_j \to \tilde{q}_{iL}\tilde{q}_{jR}^*+$
277	$f_i\bar{f}_i \to \tilde{q}_{jL}\tilde{q}_{jL}^*$
278	$f_i\bar{f}_i \to \tilde{q}_{jR}\tilde{q}_{jR}^*$
279	$gg \to \tilde{q}_{iL}\tilde{q}_{iL}^*$
280	$gg \to \tilde{q}_{iR}\tilde{q}_{iR}^*$
281	$bq_i \to \tilde{b}_1\tilde{q}_{iL}$
282	$bq_i \to \tilde{b}_2\tilde{q}_{iR}$
283	$bq_i \to \tilde{b}_1\tilde{q}_{iR} + \tilde{b}_2\tilde{q}_{iL}$
284	$b\bar{q}_i \to \tilde{b}_1\tilde{q}_{iL}^*$
285	$b\bar{q}_i \to \tilde{b}_2\tilde{q}_{iR}^*$
286	$b\bar{q}_i \to \tilde{b}_1\tilde{q}_{iR}^* + \tilde{b}_2\tilde{q}_{iL}^*$
287	$q_i\bar{q}_i \to \tilde{b}_1\tilde{b}_1^*$
288	$q_i\bar{q}_i \to \tilde{b}_2\tilde{b}_2^*$
289	$gg \to \tilde{b}_1\tilde{b}_1^*$
290	$gg \to \tilde{b}_2\tilde{b}_2^*$
291	$bb \to \tilde{b}_1\tilde{b}_1$
292	$bb \to \tilde{b}_2\tilde{b}_2$
293	$bb \to \tilde{b}_1\tilde{b}_2$
294	$bg \to \tilde{b}_1\tilde{g}$
295	$bg \to \tilde{b}_2\tilde{g}$
296	$b\bar{b} \to \tilde{b}_1\tilde{b}_2^*+$

- Hard QCD processes, i.e. leading to jet production.
- Soft QCD processes, such as diffractive and elastic scattering, and minimum-bias events. Hidden in this class is also process 96, which is used internally for the merging of soft and hard physics, and for the generation of multiple interactions.

- Heavy-flavour production, both open and hidden (i.e. as bound states like the J/ψ). Hadronization of open heavy flavour will be discussed in section 6.2.4. Some new processes have been added for closed heavy flavour, but we remind that data here are yet not fully understood, and have given rise to models extending on the more conventional PYTHIA treatment [5].
- W/Z production. A first-order process such as $f_i\overline{f}_j \to gW^{\pm}$ is now quite accurately modeled by the initial-state shower acting on $f_i\overline{f}_j \to W^{\pm}$, see section 6.2.2, but the former can still be useful for a dedicated study of the high-$p_\perp$ tail.
- Prompt-photon production.
- Photon-induced processes, including Deep Inelastic Scattering. A completely new machinery for γ^*p and $\gamma^*\gamma^*$ physics has been constructed here, see section 6.2.1.
- Standard model Higgs production, where the Higgs is reasonably light and narrow, and can therefore still be considered as a resonance.
- Gauge boson scattering processes, such as $W_LW_L \to W_LW_L$ (L = longitudinal), when the standard model Higgs is so heavy and broad that resonant and non-resonant contributions have to be considered together.
- Non-standard Higgs particle production, within the framework of a two-Higgs-doublet scenario with three neutral (h^0, H^0 and A^0) and two charged ($H^{\pm}$) Higgs states. Normally associated with SUSY (see below), but does not have to be. The Higgs pair production processes were previously hidden in process 141, but are now included explicitly.
- Production of new gauge bosons, such as a Z′, W′ and R (a horizontal boson, coupling between generations).
- Technicolor production, as an alternative scenario to the standard picture of electroweak symmetry breaking by a fundamental Higgs. Processes 149, 191, 192 and 193 may be considered obsolete, since the other processes now include the decays to the allowed final states of the $\rho_{tc}^0/\omega_{tc}^0/\rho_{tc}^{\pm}$ bosons, also including interferences with $\gamma/Z^0/W^{\pm}$. The default scenario is based on [6].
- Compositeness is a possibility not only in the Higgs sector, but may also apply to fermions, e.g. giving d^* and u^* production. At energies below the threshold for new particle production, contact interactions may still modify the standard behaviour; this is implemented not only for processes 165 and 166, but also for 11, 12 and 20.
- Left–right symmetric models give rise to doubly charged Higgs states, in fact one set belonging to the left and one to the right SU(2) gauge group. Decays involve right-handed W's and neutrinos. The existing scenario is based on [7].
- Leptoquark (L_Q) production is encountered in some beyond-the-standard-model scenarios.

- Supersymmetry (SUSY) is probably the favourite scenario for physics beyond the standard model. A rich set of processes are allowed, even if one obeys R-parity conservation. The supersymmetric machinery and process selection is inherited from SPYTHIA [4], however with many improvements in the event generation chain. Relative to the SPYTHIA process repertoire, the main new additions is sbottom production, where a classification by mass eigenstates is necessary and many Feynman graphs are related to the possibility to have incoming b quarks. Many different SUSY scenarios have been proposed, and the program is flexible enough to allow input from several of these, in addition to the ones provided internally.

Obviously the list is far from exhaustive; it is a major problem to keep up to date with all the new physics scenarios and signals that are proposed and have to be studied. One example of another physics area that has attracted much attention recently is the possibility of extra dimensions on 'macroscopic' scales. Also, a general-purpose program can not be optimized for all kinds of processes. If a generator for some kind of partonic configurations is already available, outside of PYTHIA, there exists the possibility to feed this in for subsequent treatment of showers and hadronization.

Parton Distributions

For cross section calculations, the hard partonic cross section has to be convoluted with the parton distributions of the incoming beam particles. The current default is GRV 94L for protons [8] and SaS 1D for real and virtual photons [9]. Some further parameterizations are available in PYTHIA, such as the recent CTEQ 5 proton ones [10], and a much richer repertoire if the PDFLIB library [11] is linked.

Photon Physics

Since before, a model for the interactions of real photons is available, i.e. for γp and $\gamma\gamma$ events [12]. This has now been improved and extended also to include virtual photons, i.e. γ^*p and $\gamma^*\gamma^*$ events [13]. It is especially geared towards the transition region of rather small photon virtualities $Q^2 \lesssim 10$ GeV^2, where the physics picture is rather complex, while it may be overkill for large Q^2, where the picture again simplifies.

Photon interactions are complicated since the photon wave function contains so many components, each with its own interactions. To first approximation, it may be subdivided into a direct and a resolved part. (In higher orders, the two parts can mix, so one has to provide sensible physical separations between the two.) In the former the photon acts as a pointlike particle, while in the latter it fluctuates into hadronic states. These fluctuations are of $\mathcal{O}(\alpha_{\mathrm{em}})$, and so correspond to a small fraction of the photon wave function, but

this is compensated by the bigger cross sections allowed in strong-interaction processes. For real photons therefore the resolved processes dominate the total cross section, while the pointlike ones take over for virtual photons.

The fluctuations $\gamma \to \mathrm{q}\overline{\mathrm{q}}\,(\to \gamma)$ can be characterized by the transverse momentum $k_\perp$ of the quarks, or alternatively by some mass scale $m \simeq 2k_\perp$, with a spectrum of fluctuations $\propto \mathrm{d}k_\perp^2/k_\perp^2$. The low-$k_\perp$ part cannot be calculated perturbatively, but is instead parameterized by experimentally determined couplings to the lowest-lying vector mesons, $V = \rho^0$, ω^0, ϕ^0 and J/ψ, an ansatz called VMD for Vector Meson Dominance. Parton distributions are defined with a unit momentum sum rule within a fluctuation [9], giving rise to total hadronic cross sections, jet activity, multiple interactions and beam remnants as in hadronic interactions. States at larger $k_\perp$ are called GVMD or Generalized VMD, and their contributions to the parton distribution of the photon are called anomalous. Given a dividing line $k_0 \simeq 0.5$ GeV to VMD states, the parton distributions are perturbatively calculable. The total cross section of a state is not, however, since this involves aspects of soft physics and eikonalization of jet rates. Therefore an ansatz is chosen where the total cross section scales like $k_V^2/k_\perp^2$, where the adjustable parameter $k_V \approx m_\rho/2$ for light quarks. The spectrum of states is taken to extend over a range $k_0 < k_\perp < k_1$, where k_1 is identified with the $p_{\perp\min}(s)$ defined in eq. (6.4) below. There is some arbitrariness in that choice, and for jet rate calculations also contributions to the parton distributions from above this region are included.

If the photon is virtual, it has a reduced probability to fluctuate into a vector meson state, and this state has a reduced interaction probability. This can be modeled by a traditional dipole factor $(m_V^2/(m_V^2+Q^2))^2$ for a photon of virtuality Q^2, where $m_V \to 2k_\perp$ for a GVMD state. Putting it all together, the cross section of the GVMD sector then scales like

$$\int_{k_0^2}^{k_1^2} \frac{\mathrm{d}k_\perp^2}{k_\perp^2} \frac{k_V^2}{k_\perp^2} \left(\frac{4k_\perp^2}{4k_\perp^2 + Q^2} \right)^2 . \tag{6.1}$$

A real direct photon in a γp collision can interact with the parton content of the proton: $\gamma\mathrm{q} \to \mathrm{qg}$ and $\gamma\mathrm{g} \to \mathrm{q}\overline{\mathrm{q}}$. The $p_\perp$ in this collision is taken to exceed k_1, in order to avoid double-counting with the interactions of the GVMD states. For a virtual photon the DIS (deeply inelastic scattering) process $\gamma^*\mathrm{q} \to \mathrm{q}$ is also possible, but by gauge invariance its cross section must vanish in the limit $Q^2 \to 0$. At large Q^2, the direct processes can instead be considered as the $\mathcal{O}(\alpha_\mathrm{s})$ correction to the lowest-order DIS process. The DIS γ^*p cross section is here proportional to the structure function $F_2(x,Q^2)$ with the Bjorken $x = Q^2/(Q^2+W^2)$. Since normal parton distribution parameterizations are frozen below some Q_0 scale and therefore do not obey the gauge invariance condition, an ad hoc factor $(Q^2/(Q^2+m_\rho^2))^2$ is introduced for the conversion from the parameterized $F_2(x,Q^2) = \sum e_\mathrm{q}^2\, q(x,Q^2)$ to a $\sigma_\mathrm{DIS}^{\gamma^*\mathrm{p}}$. In order to avoid double-

counting between DIS and direct events, we decide to introduce a requirement $p_\perp > \max(k_1, Q)$ on direct events. In the remaining DIS ones, thus $p_\perp < Q$. The DIS rate should be reduced accordingly, by a Sudakov form factor giving the probability not to have an interaction above scale Q, which can be approximated by $\exp(-\sigma^{\gamma^*\mathrm{p}}_{\mathrm{direct}}/\sigma^{\gamma^*\mathrm{p}}_{\mathrm{DIS}})$.

Note that the Q^2 dependence of the DIS and direct processes is implemented in the matrix element expressions. This is different from VMD/GVMD, where dipole factors are used to reduce the assumed flux of partons inside a virtual photon relative to those of a real one, but the matrix elements contain no parton virtuality dependence.

After some further minor corrections for double-counting, we arrive at a picture of hadronic γ^*p events as being composed of four main components: VMD, GVMD, direct and DIS. Most of these in their turn have a complicated internal structure, as we have seen. The $\gamma^*\gamma^*$ collision between two inequivalent photons contains 13 components: four when the VMD and GVMD states interact with each other ('double-resolved'), eight with a direct or DIS photon interaction on a VMD or GVMD state on either side ('single-resolved', including the traditional DIS), and one where two direct photons interact by the process $\gamma^*\gamma^* \to \mathrm{q\overline{q}}$ ('direct', not to be confused with the direct process of γ^*p).

Several further aspects can be added to the above machinery. The impact of resolved longitudinal photons is unknown, except that it has to vanish in the limit $Q^2 \to 0$, and can be approximated by some Q^2-dependent enhancement of the normal transverse one. For a complete description of ep events or $\mathrm{e^+e^-}$ two-photon ones, a convolution with the x- and Q^2-dependent flux of virtual photons inside an electron is also now provided.

Supersymmetry

PYTHIA simulates the Minimal Supersymmetric Standard Model (MSSM), based on an effective Lagrangian of softly-broken SUSY with parameters defined at the weak scale, which is typically between m_{Z} and 1 TeV. The MSSM particle spectrum is minimal in the sense that it includes only the partners of all Standard Model particles (presently without massive neutrinos), a two-Higgs doublet — one Higgs $\mathrm{H_u}$ coupling only to up-type fermions and one $\mathrm{H_d}$ coupling only to down-type fermions — and partners, and the gravitino. Once the parameters of the softly-broken SUSY Lagrangian are specified, the interactions are fixed, and the sparticle masses can be calculated [17].

The masses of the scalar partners to fermions, sfermions, depend on soft scalar masses, trilinear couplings, the Higgsino mass μ, and $\tan\beta$, the ratio of Higgs vacuum expectation values $\langle \mathrm{H_u} \rangle / \langle \mathrm{H_d} \rangle$. The masses of the fermion partners to the gauge and Higgs bosons, the neutralinos and charginos, depend on soft gaugino masses, μ, and $\tan\beta$. Finally, the properties of the Higgs scalar sector is calculated from the input pseudoscalar Higgs boson mass m_{A}, $\tan\beta$, μ,

trilinear couplings and the sparticle properties in an effective potential approach [18]. Of course, these calculations also depend on SM parameters (m_t, m_Z, α_s, etc.). Any modifications to these quantities from virtual MSSM effects are not taken into account. In principle, the sparticle masses also acquire loop corrections that depend on all MSSM masses.

R-parity conservation is assumed (at least on the time and distance scale of a typical collider experiment), and only lowest order, sparticle pair production processes are included. Only those processes with $e^+e^-, \mu^+\mu^-$, or quark and gluon initial states are simulated. Likewise, only R-parity conserving decays are allowed, so that one sparticle is stable, either the lightest neutralino, the gravitino, or a sneutrino. SUSY decays of the top quark are included, but all other SM particle decays are unaltered.

Various improvements to the simulation are being implemented in stages. Some of these can have a significant impact on the collider phenomenology. Among these are: the generalization to complex-valued soft SUSY-breaking parameters in the neutralino and chargino sector; the same in the Higgs sector, which removes the possibility of CP-even or CP-odd labels; the calculation of neutralino and chargino decay rates which are accurate for large $\tan\beta$; and matrix element weighting of particle distributions in three-body decays.

Strong Dynamics in Electroweak Symmetry Breaking

The simulation of strong dynamics associated with electroweak symmetry breaking in PYTHIA is based on an effective Lagrangian for the lightest resonances of a technicolor (TC)-like model. In TC, the breaking of a chiral symmetry in a new, strongly interacting gauge theory generates the Goldstone bosons necessary for electroweak symmetry breaking. Bound states of technifermions provide a QCD-like spectrum of technipions (π_{tc}), technirhos (ρ_{tc}), techniomegas (ω_{tc}), etc. The mass hierarchies, however, are unlike QCD because of the behavior of the gauge couplings in realistic models of extended TC (ETC). The difficulties of ETC in explaining the top quark mass while suppressing FCNC's is circumvented by the addition of topcolor interactions, which provide the bulk of m_t.

In ETC models, hard mass contributions to technipion masses make decays like $\rho_{tc} \to \pi_{tc}\pi_{tc}$ kinematically inaccessible. Instead, decays like $\rho_{tc}^{ew} \to \pi_{tc}^{ew} W_L$, for example, dominate, where ew denotes constituent technifermions with only electroweak quantum numbers and W_L is a longitudinal W bosons. As a result, the ew technirho and techniomega tend to have small total widths.

Effective couplings are derived in the valence technifermion approximation, and the techniparticle decays can be calculated directly [6]. Technirhos and techniomegas are produced through kinematic mixing with gauge bosons, leading to final states containing Standard Model particles and/or pseudo-Goldstone bosons (technipions).

As an additional wrinkle, $\mathrm{SU}_c(3)$ non-singlet states are included along with the coloron of topcolor assisted technicolor. In this case, colored technirhos (and the coloron) can have substantial total widths and enhanced couplings to bottom and top quarks.

6.2.2 QCD Radiation

The matrix-element (ME) and parton-shower (PS) approaches to higher-order QCD corrections both have their advantages and disadvantages. The former offers a systematic expansion in orders of α_s, and a powerful machinery to handle multi-parton configurations on the Born level, but loop calculations are tough and lead to messy cancellations at small resolution scales. Resummed matrix elements may circumvent the latter problem for specific quantities, but then do not provide exclusive accompanying events. Parton showers are based on an improved leading-log (almost next-to-leading-log) approximation, and so cannot be accurate for well separated partons, but they offer a simple, process-independent machinery that gives a smooth blending of event classes (by Sudakov form factors) and a sensible match to hadronization. It is therefore natural to try to combine these descriptions, so that ME results are recovered for widely separated partons while the PS sets the sub-jet structure.

For final-state showers in $\mathrm{Z}^0 \to \mathrm{q}\overline{\mathrm{q}}$, where q is assumed essentially massless, such solutions are the standard since long [14], e.g. by letting the shower slightly overpopulate the $\mathrm{q}\overline{\mathrm{q}}\mathrm{g}$ phase space and then using a Monte Carlo veto technique to reduce down to the ME level.

Initial-State Showers

A similar technique is now available for the description of initial-state radiation in the production of a single colour-singlet resonance, such as $\gamma^*/\mathrm{Z}^0/\mathrm{W}^\pm$ [15]. The basic idea is to map the kinematics between the PS and ME descriptions, and to find a correction factor that can be applied to hard emissions in the shower so as to bring agreement with the matrix-element expression. The PYTHIA shower kinematics definitions are based on Q^2 as the spacelike virtuality of the parton produced in a branching and z as the factor by which the $\hat{s}$ of the scattering subsystem is reduced by the branching. Some simple algebra then shows that the two $\mathrm{q}\overline{\mathrm{q}}' \to \mathrm{gW}^\pm$ emission rates disagree by a factor

$$R_{\mathrm{q}\overline{\mathrm{q}}'\to\mathrm{gW}}(\hat{s},\hat{t}) = \frac{(\mathrm{d}\hat{\sigma}/\mathrm{d}\hat{t})_\mathrm{ME}}{(\mathrm{d}\hat{\sigma}/\mathrm{d}\hat{t})_\mathrm{PS}} = \frac{\hat{t}^2+\hat{u}^2+2m_\mathrm{W}^2\hat{s}}{\hat{s}^2+m_\mathrm{W}^4} \;, \tag{6.2}$$

which is always between 1/2 and 1. The shower can therefore be improved in two ways, relative to the old description. Firstly, the maximum virtuality of emissions is raised from $Q^2_\mathrm{max} \approx m^2_\mathrm{W}$ to $Q^2_\mathrm{max} = s$, i.e. the shower is allowed to

populate the full phase space. Secondly, the emission rate for the final (which normally also is the hardest) $q \to qg$ emission on each side is corrected by the factor $R(\hat{s},\hat{t})$ above, so as to bring agreement with the matrix-element rate in the hard-emission region. In the backwards evolution shower algorithm [16], this is the first branching considered.

The other possible $\mathcal{O}(\alpha_s)$ graph is $qg \to q'W^{\pm}$, where the corresponding correction factor is

$$R_{qg\to q'W}(\hat{s},\hat{t}) = \frac{(d\hat{\sigma}/d\hat{t})_{ME}}{(d\hat{\sigma}/d\hat{t})_{PS}} = \frac{\hat{s}^2+\hat{u}^2+2m_W^2\hat{t}}{(\hat{s}-m_W^2)^2+m_W^4} \; , \tag{6.3}$$

which lies between 1 and 3. A probable reason for the lower shower rate here is that the shower does not explicitly simulate the s-channel graph $qg \to q^* \to q'W$. The $g \to q\overline{q}$ branching therefore has to be preweighted by a factor of 3 in the shower, but otherwise the method works the same as above. Obviously, the shower will mix the two alternative branchings, and the correction factor for a final branching is based on the current type.

The reweighting procedure prompts some other changes in the shower. In particular, $\hat{u} < 0$ translates into a constraint on the phase space of allowed branchings, not previously implemented.

Our published comparisons with data on the $p_{\perp W}$ spectrum show quite a good agreement with this improved simulation [15]. A worry was that an unexpectedly large primordial $k_\perp$, around 4 GeV, was required to match the data in the low-$p_{\perp W}$ region. However, at that time we had not realized that the data were not fully unsmeared. The required primordial $k_\perp$ therefore drops by about a factor of two [19].

The method can also be used for initial-state photon emission, e.g. in the process $e^+e^- \to \gamma^*/Z^0$. There the old default $Q^2_{max} = m_Z^2$ allowed no emission at large $p_\perp$, $p_\perp \gtrsim m_Z$ at LEP2. This is now corrected by the increased $Q^2_{max} = s$, and using the R of eq. (6.2) with $m_W \to m_Z$.

The above method does not address the issue of next-to-leading order corrections to the total W cross section, which instead can be studied with more sophisticated matching procedures [20]. Also extensions to other processes can be considered in the future.

There are also some other changes to the initial state radiation algorithm:

- The cut on minimum gluon energy emitted in a branching is modified by an extra factor roughly corresponding to the $1/\gamma$ factor for the boost to the hard subprocess frame. Earlier, when a subsystem was strongly boosted, the minimum energy requirement became quite stringent on the low-energy incoming side, and could cut out much radiation.
- The angular-ordering requirement is now based on ordering $p_\perp/p$ rather than $p_\perp/p_L$, i.e. replacing $\tan\theta$ by $\sin\theta$. Earlier the starting value $(\tan\theta)_{max} = 10$ could actually be violated by some bona fide emissions for strongly boosted

subsystems.

- The Q^2 value of the backwards evolution of a heavy quark like c in a proton beam is by force kept above m_c^2, so as to ensure that the branching $g \to c\overline{c}$ is not 'forgotten' by evolving Q^2 below Q_0^2. Thereby the possibility of having a c in the beam remnant proper is eliminated [21]. The procedure is not forced for a photon beam, where charm occurs as part of the valence flavour content.
- For incoming $\mu^\pm$ (or $\tau^\pm$) beams the kinematical variables are better selected to represent the differences in lepton mass, and the lepton-inside-lepton parton distributions are properly defined.

6.2.3 Beam Remnants and Multiple Interactions

Beam Remnants

In a hadron–hadron collision, the initial-state radiation algorithm reconstructs one shower initiator in each beam, by backwards evolution from the hard scattering. This initiator only takes some fraction of the total beam energy, leaving behind a beam remnant that takes the rest. Since the initiator is coloured, so is the remnant. It is therefore colour-connected to the hard interaction, and forms part of the same fragmenting system. Often the remnant can be complicated, e.g. a g initiator would leave behind a uud proton-remnant system in a colour octet state, which can conveniently be subdivided into a colour triplet quark and a colour antitriplet diquark, each of which are colour-connected to the hard interaction. The energy sharing between these two remnant objects, and their relative transverse momentum, introduces additional nonperturbative degrees of freedom. Some of the default values have recently been updated [21].

One would expect an ep event to have only one beam remnant, and an e^+e^- event none. This is not always correct, e.g. a $\gamma\gamma \to q\overline{q}$ interaction in an e^+e^- event would leave behind the e^+ and e^- as beam remnants. The photons may in their turn leave behind remnants.

It is customary to assign a primordial transverse momentum to the shower initiator, to take into account the motion of quarks inside the original hadron, basically as required by the uncertainty principle. A number of the order of $\langle k_\perp \rangle \approx m_p/3 \approx 300$ MeV could therefore be expected. However, in hadronic collisions much higher numbers than that are often required to describe data, typically of the order of 1 GeV [22, 19] if a Gaussian parameterization is used. (This number is now the default.) Thus, an interpretation as a purely nonperturbative motion inside a hadron is difficult to maintain.

Instead a likely culprit is the initial-state shower algorithm. This is set up to cover the region of hard emissions, but may miss out on some of the softer activity, which inherently borders on nonperturbative physics. By default, the shower does not evolve down to scales below $Q_0 = 1$ GeV. Any shortfall in

shower activity around or below this cutoff then has to be compensated by the primordial $k_\perp$ source, which thereby largely loses its original meaning.

Multiple Interactions

Multiple parton–parton interactions is the concept that, based on the composite nature of hadrons, several parton pairs may interact in a typical hadron–hadron collision [23]. Over the years, evidence for this mechanism has accumulated, such as the recent direct observation by CDF [24]. The occurrences with two parton pairs at reasonably large $p_\perp$ just form the top of the iceberg, however. In the PYTHIA model, most interactions are at lower $p_\perp$, where they are not visible as separate jets but only contribute to the underlying event structure. As such, they are at the origin of a number of key features, like the broad multiplicity distributions, the significant forward–backward multiplicity correlations, and the pedestal effect under jets.

Since the perturbative jet cross section is divergent for $p_\perp \to 0$, it is necessary to regularize it, e.g. by a cut-off at some $p_{\perp\min}$ scale. That such a regularization should occur is clear from the fact that the incoming hadrons are colour singlets — unlike the coloured partons assumed in the divergent perturbative calculations — and that therefore the colour charges should screen each other in the $p_\perp \to 0$ limit. Also other damping mechanisms are possible [25]. Fits to data typically give $p_{\perp\min} \approx 2$ GeV, which then should be interpreted as the inverse of some colour screening length in the hadron.

One key question is the energy-dependence of $p_{\perp\min}$; this may be relevant e.g. for comparisons of jet rates at different Tevatron energies, and even more for any extrapolation to LHC energies. The problem actually is more pressing now than at the time of the original study [23], since nowadays parton distributions are known to be rising more steeply at small x than the flat $xf(x)$ behaviour normally assumed for small Q^2 before HERA. This translates into a more dramatic energy dependence of the multiple-interactions rate for a fixed $p_{\perp\min}$.

The larger number of partons also should increase the amount of screening, however, as confirmed by toy simulations [26]. As a simple first approximation, $p_{\perp\min}$ is assumed to increase in the same way as the total cross section, i.e. with some power $\epsilon \approx 0.08$ [27] that, via reggeon phenomenology, should relate to the behaviour of parton distributions at small x and Q^2. Thus the new default in PYTHIA is

$$p_{\perp\min}(s) = (1.9\ \text{GeV}) \left(\frac{s}{1\ \text{TeV}^2} \right)^{0.08} . \tag{6.4}$$

6.2.4 Fragmentation and Decays

QCD perturbation theory, formulated in terms of quarks and gluons, is valid at short distances. At long distances, QCD becomes strongly interacting and perturbation theory breaks down. In this confinement régime, the coloured partons are transformed into colourless hadrons, a process called either hadronization or fragmentation.

The fragmentation process has yet to be understood from first principles, starting from the QCD Lagrangian. This has left the way clear for the development of a number of different phenomenological models. PYTHIA is intimately connected with string fragmentation, in the form of the time-honoured 'Lund model' [28]. This is the default for all applications. Improvements have been made in some areas, however.

Low-Mass Strings

A hadronic event is conventionally subdivided into sets of partons that form separate colour singlets. These sets are represented by strings, that e.g. stretch from a quark end via a number of intermediate gluons to an antiquark end. Three string mass regions may be distinguished for the hadronization.

1. *Normal string fragmentation.* In the ideal situation, each string has a large invariant mass. Then the standard iterative fragmentation scheme [28, 29] works well. In practice, this approach can be used for all strings above some cut-off mass of a few GeV.
2. *Cluster decay.* If a string is produced with a small invariant mass, maybe only two-body final states are kinematically accessible. The traditional iterative Lund scheme is then not applicable. We call such a low-mass string a cluster, and consider it separately from above. In recent program versions, the modeling has now been improved to give a smooth match on to the standard string scheme in the high-cluster-mass limit [21].
3. *Cluster collapse.* This is the extreme case of the above situation, where the string mass is so small that the cluster cannot decay into two hadrons. It is then assumed to collapse directly into a single hadron, which inherits the flavour content of the string endpoints. The original continuum of string/cluster masses is replaced by a discrete set of hadron masses. Energy and momentum then cannot be conserved inside the cluster, but must be exchanged with the rest of the event. This description has also been improved [21].

String systems below a threshold mass are handled by the cluster machinery. In it, an attempt is first made to produce two hadrons, by having the string break in the middle by the production of a new $q\overline{q}$ pair, with flavours and hadron spins selected according to the normal string rules. If the sum of the hadron masses is larger than the cluster mass, repeated attempts can be made

to find allowed hadrons; the default is two tries. If an allowed set is found, the angular distribution of the decay products in the cluster rest framed is picked isotropically near the threshold, but then gradually more elongated along the string direction, to provide a smooth match to the string description at larger masses. This also includes a forward–backward asymmetry, so that each hadron is preferentially in the same hemisphere as the respective original quark it inherits.

If the attempts to find two hadrons fail, one single hadron is formed from the given flavour content. The basic strategy thereafter is to exchange some minimal amount of energy and momentum between the collapsing cluster and other string pieces in the neighbourhood. The momentum transfer can be in either direction, depending on whether the hadron is lighter or heavier than the cluster it comes from. When lighter, the excess momentum is split off and put as an extra 'gluon' on the nearest string piece, where 'nearest' is defined by a space–time history-based distance measure. When the hadron is heavier, momentum is instead borrowed from the endpoints of the nearest string piece.

The free parameters of the model can be tuned to data, especially to the significant asymmetries observed between the production of D and $\overline{\mathrm{D}}$ mesons in π^-p collisions, with hadrons that share some of the π^- flavour content very much favoured at large x_F in the π^- fragmentation region [30]. These spectra and asymmetries are closely related to the cluster collapse mechanism, and also to other effects of the colour topology of the event ('beam drag') [21]. Also other parameters enter the description, however, such as the effective charm mass and the beam remnant structure.

Baryon Production

A new advanced scheme has been introduced for baryon production with the popcorn mechanism [31], plus some minor changes to the older popcorn scheme [32]. These new features currently only appear as options, with the default unchanged, and can be separated into three parts.

Firstly, an improved implementation of SU(6) weights for baryon production. This should not be regarded as a new model, rather a more correct implementation of the old. However, in order to enable the user to see the effects of the SU(6) weighting separately, both procedures are available as different options. The main change is that, if a step $\mathrm{q} \to \mathrm{B} + \overline{\mathrm{qq}}'$ is SU(6)-rejected, the new try may now instead give a $\mathrm{q} \to \mathrm{M} + \mathrm{q}'$ step (where B stands for baryon, M for meson). The old procedure leads to a slightly faster algorithm and a better interpretation of the input parameter for the diquark-to-quark production rate. However, the probability that a quark will produce a baryon and a antidiquark is then flavour independent, which is not in agreement with the model. Further, for $\mathrm{qq} \to \mathrm{M} + \mathrm{qq}'$, SU(6) symmetry is included in the weights for qq', while qq is kept with unit probability. The procedures for $\mathrm{qq} \to \mathrm{B} + \overline{\mathrm{q}}'$

and a final joining qq + q → B are unchanged.

Secondly, a suppression of diquark vertices occuring at small proper times. This is based on a study of the production dynamics of the three quarks that form a baryon. The main experimental consequence is a suppression of the baryon production rate at large momentum fraction. This in particular implies a smaller rate of first-rank light baryon production, while charm and bottom baryons are less affected (since the production proper time is larger for a heavy hadron than a light one of the same momentum). It thereby substitutes and explains the older brute-force possibility to suppress the production of first-rank baryons.

Thirdly, a completely new flavour algorithm for baryons and popcorn mesons, also using the small-proper-time suppression above. While the old popcorn alternative allowed at most one meson to be produced in between the baryon and the antibaryon, the new model allows an arbitrary number. The new flavour model makes explicit use of the popcorn suppression factor $\exp(-2m_\perp M_\perp/\kappa)$, where $m_\perp$ is the transverse mass of the quark creating the colour fluctuation, $M_\perp$ is the total invariant transverse mass of the popcorn meson system, and κ is the string tension constant. Thus two parameters, representing the mean $2m_\perp/\kappa$ for light quarks and s-quarks, respectively, govern both diquark and popcorn meson production. A corresponding parameter is introduced for the fragmentation of strings that contain diquarks already from the beginning, i.e. baryon remnants. The new procedure therefore requires far fewer parameters than the old one, and still provides a comparable quality in the description of the various baryon production rates. This was investigated in detail in [33]. (The concluding worry of an "improper treatment" was caused by an unfortunate misunderstanding and can be disregarded.) Other features, such as baryon correlations, are also modified.

Several new routines have been added, and the diquark code has been extended with information about the curtain quark flavour, i.e. the $q\overline{q}$ pair that is shared between the baryon and antibaryon, but this is not visible externally. Some parameters are no longer used, while others have to be given modified values, as described in the long writeup.

Interconnection Effects

The widths of the W, Z and t are all of the order of 2 GeV. A standard model Higgs with a mass above 200 GeV, as well as many supersymmetric and other beyond the standard model particles would also have widths in the multi-GeV range. Not far from threshold, the typical decay times $\tau = 1/\Gamma \approx 0.1\,\mathrm{fm} \ll \tau_{\mathrm{had}} \approx 1\,\mathrm{fm}$. Thus hadronic decay systems overlap, between a resonance and the underlying event, or between pairs of resonances, so that the final state may not contain independent resonance decays.

So far, studies have mainly been performed in the context of W pair pro-

duction at LEP2. Pragmatically, one may here distinguish three main eras for such interconnection:

1. Perturbative: this is suppressed for gluon energies $\omega > \Gamma$ by propagator/timescale effects; thus only soft gluons may contribute appreciably.
2. Nonperturbative in the hadroformation process: normally modeled by a colour rearrangement between the partons produced in the two resonance decays and in the subsequent parton showers.
3. Nonperturbative in the purely hadronic phase: best exemplified by Bose–Einstein effects.

The above topics are deeply related to the unsolved problems of strong interactions: confinement dynamics, $1/N_C^2$ effects, quantum mechanical interferences, etc. Thus they offer an opportunity to study the dynamics of unstable particles, and new ways to probe confinement dynamics in space and time [34, 35], *but* they also risk to limit or even spoil precision measurements.

The reconnection scenarios outlined in [35] are now available, plus also an option along the lines suggested in [36]. Currently they can only be invoked in process 25, $e^+e^- \to W^+W^- \to q_1\overline{q}_2q_3\overline{q}_4$, which is the most interesting one for the foreseeable future. (Process 22, $e^+e^- \to \gamma^*/Z^0\ \gamma^*/Z^0 \to q_1\overline{q}_2q_3\overline{q}_4$ can also be used, but the travel distance is calculated based only on the Z^0 propagator part.) If normally the event is considered as consisting of two separate colour singlets, $q_1\overline{q}_2$ from the W^+ and $q_3\overline{q}_4$ from the W^-, a colour rearrangement can give two new colour singlets $q_1\overline{q}_4$ and $q_3\overline{q}_2$. It therefore leads to a different hadronic final state, although differences usually turn out to be subtle and difficult to isolate [37]. When also gluon emission is considered, the number of potential reconnection topologies increases. Apart from the overall rate of reconnection, the scenarios in PYTHIA differ in the relative probability assigned to each of these topologies, based on their properties in momentum space and/or space–time. For instance, scenario I is based on an analogy with type I superconductors, with the colour field represented by extended flux tubes. By contrast, scenario II assumes that narrow vortex lines carry all the topological information, like in type II superconductors, even if the full energy is stored over a wider region.

Bose–Einstein effects are simulated in a simplified manner, by introducing small momentum shifts in identical final-state mesons (primarily $\pi^\pm$ and π^0) so as to bring them closer to each other [38]. The shifts can be chosen to reproduce a desired BE enhancement shape for small relative momentum $Q = \sqrt{m_{ij}^2 - 4m_i^2}$ between identical bosons i and j. Typically the shape is chosen as a Gaussian, $f_2(Q) = 1 + \lambda \exp(-Q^2R^2)$, with λ and R two free parameters. The input is only exactly reproduced in the limit of an isotropic and low-density initial particle distribution; since these conditions are not completely fulfilled in reality, there are distortions [39], for better or worse. (The nontrivial three-particle correlations in data are described qualitatively,

although not quantitatively.)

A major shortcoming of the algorithm is that energy is not automatically conserved, even though three-momentum is. In the original algorithm, this was solved by a uniform rescaling of all three-momenta, with undesirable side effects e.g. when studying BE effects in W^+W^- hadronic final states. In the current version, several new options have been added that, based on different principles, instead shifts pairs apart. The default one, BE_{32}, operates on identical particles, introducing an extra factor

$$1 + \alpha\lambda \exp(-Q^2R^2/9) \left\{1 - \exp(-Q^2R^2/4)\right\} \tag{6.5}$$

to $f_2(Q)$. Here α is a negative number adjusted event by event for overall energy conservation, with $\langle\alpha\rangle \approx -0.25$. This scenario can be viewed as a simplified version of a dampened oscillating correlation function, where only the first peak and dip has been retained. Further new options have also been introduced specifically geared towards studies of W^+W^- hadronic events, e.g. to include the effects of the separated W^+ and W^- decay vertices.

Decays

Two separate decay treatments exist in PYTHIA. One is making use of a set of tables where branching ratios and decay modes are stored, and is used e.g. for hadronic decays, where branching ratios normally cannot be calculated from first principles.

The other treatment is used for a set of fundamental resonances in or beyond the standard model, such as t, Z^0, $W^\pm$, h^0, supersymmetric particles, and many more. Characteristic here is that these resonances have perturbatively calculable widths to each of their decay channels. The decay products are typically quarks, leptons, or other resonances. In decays to quarks, parton showers are automatically added to give a more realistic multijet structure, and one may also allow photon emission off leptons. If the decay products in turn are resonances, further decays are necessary. Often spin information is available in resonance decay matrix elements, leading to nonisotropic decays. This part has been improved in several processes, but is still missing in many others.

The routine used to calculate the partial and total width of resonances (now expressed in GeV throughout), has been expanded for all the new particles and decay modes introduced. Some alternative calculation schemes have also been adopted, e.g. based on a simple rescaling of the on-shell widths rather than a complete recalculation (which may at times not be feasible) based on the current mass.

The width to be used in the denominator of a resonance propagator is only well-defined near the peak. Well away from the peak, an unfortunate choice may lead to a loss of cancellation between resonant and nonresonant

diagrams. A special problem exists for a massive standard model Higgs, where the width $\Gamma_{\rm h} \propto m_{\rm h}^3$ is so large that the choice of $\hat{s}$ dependence of the width significantly influences the resonance peak shape. Following [40], the default now is $\Gamma_{\rm h} \propto m_{\rm h}^2 \sqrt{\hat{s}}$.

6.3 Program News

Essentially all of the basic philosophy and framework remain from the previous PYTHIA and JETSET versions, so no user familiar with these should feel at loss with PYTHIA 6.1. Most of the changes and additions instead are under the surface, and are only visible as new options added to the existing repertoire. However, some changes are fairly obvious, and other less obvious ones still of general interest. These will be covered in this section, in fairly general terms. Again we refer to the PYTHIA web page for a detailed documentation.

6.3.1 Coding conventions

As before, the FORTRAN 77 standard is adhered to. A very few minor extensions may be used in isolated places, like the 7-character names of the PDFLIB routines [11], but are not known to cause problems on any compiler in use.

An obvious consequence of the PYTHIA/JETSET code merging is that the old JETSET routines and commonblocks have been renamed to begin with `PY` (instead of `LU` or `UL`), just like the PYTHIA ones. In most cases, the rest of the name is unchanged, but there are a few exceptions, mainly `RLU`→`PYR`, `KLU`→`PYK`, `PLU`→`PYP` and `LUXTOT`→`PYXTEE`. Three integer functions now begin with `PY`, namely `PYK`, `PYCHGE` and `PYCOMP`, and therefore have to be declared extra. The `LUDATA` block data has been merged into `PYDATA`, and the test routine `LUTEST` into `PYTEST`. For rotations and boosts, the `PYROBO` routine now requires the range of affected entries to be given, like the old `LUDBRB` but unlike `LUROBO` (but 0,0 as range arguments gives back the old `LUROBO` behaviour).

All real variables are now in `DOUBLE PRECISION`, which is assumed to mean 64 bits, and also real constants have been promoted to the higher precision. This is required to ensure proper functioning at currently studied energies, such as the LHC and beyond. To take into account this, all routines begin with the declarations

```
C...Double precision and integer declarations.
      IMPLICIT DOUBLE PRECISION(A-H, O-Z)
      IMPLICIT INTEGER(I-N)
      INTEGER PYK,PYCHGE,PYCOMP
```

and users should do the same in their main programs.

Table 6.5: The current form of the main commonblock declarations.

```
COMMON/PYJETS/N,NPAD,K(4000,5),P(4000,5),V(4000,5)
COMMON/PYDAT1/MSTU(200),PARU(200),MSTJ(200),PARJ(200)
COMMON/PYDAT2/KCHG(500,4),PMAS(500,4),PARF(2000),VCKM(4,4)
COMMON/PYDAT3/MDCY(500,3),MDME(4000,2),BRAT(4000),KFDP(4000,5)
COMMON/PYDAT4/CHAF(500,2)
CHARACTER CHAF*16
COMMON/PYDATR/MRPY(6),RRPY(100)
COMMON/PYSUBS/MSEL,MSELPD,MSUB(500),KFIN(2,-40:40),CKIN(200)
COMMON/PYPARS/MSTP(200),PARP(200),MSTI(200),PARI(200)
COMMON/PYINT1/MINT(400),VINT(400)
COMMON/PYINT2/ISET(500),KFPR(500,2),COEF(500,20),ICOL(40,4,2)
COMMON/PYINT3/XSFX(2,-40:40),ISIG(1000,3),SIGH(1000)
COMMON/PYINT4/MWID(500),WIDS(500,5)
COMMON/PYINT5/NGENPD,NGEN(0:500,3),XSEC(0:500,3)
COMMON/PYINT6/PROC(0:500)
CHARACTER PROC*28
COMMON/PYMSSM/IMSS(0:99),RMSS(0:99)
COMMON/PYUPPR/NUP,KUP(20,7),NFUP,IFUP(10,2),PUP(20,5),Q2UP(0:10)
COMMON/PYBINS/IHIST(4),INDX(1000),BIN(20000)
```

On a machine where `DOUBLE PRECISION` would give 128 bits, it may make sense to use compiler options to revert to 64 bits, since the program is anyway not constructed to make use of 128 bit precision.

The random number generator is the same as in previous versions [41], but has now been expanded to operate with a 48 bit mantissa for the real numbers.

FORTRAN 77 makes no provision for double-precision complex numbers, but since `COMPLEX` is used only sparingly, no problems should be expected from this omission. For the technicolor processes, some variables are declared `COMPLEX*16` in the `PYSIGH` routine. Should the compiler not accept this, that one declaration can be changed to `COMPLEX` with some drop in precision for the affected processes.

Several compilers report problems when an odd number of integers precede a double-precision variable in a commonblock. Therefore an extra integer has been introduced as padding in a few instances (`NPAD`, `MSELPD` and `NGENPD` in Table 6.5).

In order to cater for the increased offering of subprocesses, some arrays in commonblocks have been expanded. A few, such as `PYINT4`, have also been reorganized to represent improvements in the physics modeling. Most com-

Table 6.6: New or modified particle codes or names.

Renamed:	
7	b'
8	t'
17	τ'
18	ν'_τ
25	h^0
35	H^0
Moved:	
100443	ψ'
100553	Υ'
4000001	d^*
4000002	u^*
4000011	e^*
4000012	ν_e^*

Technicolor:	
51	π^0_{tc}
52	π^+_{tc}
53	$\pi'^{\,0}_{\mathrm{tc}}$
54	ρ^0_{tc}
55	ρ^+_{tc}
56	ω^0_{tc}
LR-symmetric:	
61	H_L^{++}
62	H_R^{++}
63	W_R^+
64	$\nu_{R\mathrm{e}}$
65	$\nu_{R\mu}$
66	$\nu_{R\tau}$

SUSY:	
1000001	$\tilde{\mathrm{d}}_L$
1000002	$\tilde{\mathrm{u}}_L$
1000003	$\tilde{\mathrm{s}}_L$
1000004	$\tilde{\mathrm{c}}_L$
1000005	$\tilde{\mathrm{b}}_1$
1000006	$\tilde{\mathrm{t}}_1$
1000011	$\tilde{\mathrm{e}}_L$
1000012	$\tilde{\nu}_{\mathrm{e}L}$
1000013	$\tilde{\mu}_L$
1000014	$\tilde{\nu}_{\mu L}$
1000015	$\tilde{\tau}_1$
1000016	$\tilde{\nu}_{\tau L}$
1000021	$\tilde{\mathrm{g}}$
1000022	$\tilde{\chi}^0_1$
1000023	$\tilde{\chi}^0_2$
1000024	$\tilde{\chi}^+_1$

SUSY:	
2000001	$\tilde{\mathrm{d}}_R$
2000002	$\tilde{\mathrm{u}}_R$
2000003	$\tilde{\mathrm{s}}_R$
2000004	$\tilde{\mathrm{c}}_R$
2000005	$\tilde{\mathrm{b}}_2$
2000006	$\tilde{\mathrm{t}}_2$
2000011	$\tilde{\mathrm{e}}_R$
2000012	$\tilde{\nu}_{\mathrm{e}R}$
2000013	$\tilde{\mu}_R$
2000014	$\tilde{\nu}_{\mu R}$
2000015	$\tilde{\tau}_2$
2000016	$\tilde{\nu}_{\tau R}$
1000025	$\tilde{\chi}^0_3$
1000035	$\tilde{\chi}^0_4$
1000037	$\tilde{\chi}^+_2$
1000039	$\tilde{\mathrm{G}}$

monblocks and commonblock variables are easily recognizable from previous program versions, however. The current complement is given in Table 6.5, omitting some of the less interesting ones.

Since FORTRAN 77 provides no date-and-time routine, `PYTIME` allows a system-specific routine to be interfaced, with some commented-out examples given in the code. This routine is only used for cosmetic improvements of the output, however, so can be left at the default with time 0 given.

For a program written to run PYTHIA 5 and JETSET 7, most of the conversion required for PYTHIA 6 is fairly straightforward, and can be automatized. Both a simple FORTRAN routine and a more sophisticated PERL [42] script exists to this end. Some manual checks and interventions may still be required.

6.3.2 Particle codes and data

A number of new particle codes `KF` have been introduced, or modified, see Table 6.6. Mostly this is based on the PDG-agreed conventions [43, 44], but some not yet standardized codes appear in the 'empty' range 41–80. Furthermore, the fourth generation fermions and neutral scalar Higgs states have been renamed. The two fermion spartners are labelled left and right, except in the third generation, where an expected larger mixing makes the two mass eigenstates a better choice of classification.

The top hadrons are gone. It is now known that top is too short-lived to form hadronic bound states, so a reasonable description is instead to have the top quarks decay before hadronization is considered. The same is now assumed about a hypothetical fourth generation. Should the need ever arise in the future to consider a new long-lived coloured object, an effective description of a hadron as a small string with an ordinary colour-matching flavour at the other end should be sufficient. One such example would be leptoquark-hadrons [45].

Bottom hadrons are now defined individually, e.g. the previous common decay scheme is gone in favour of individual branching ratios for each hadron. On the other hand, given the sketchy knowledge of many branching ratios, the default description is still fairly standardized.

Decay data is mainly based on the 1996 PDG edition [46], but with many 'educated guesses' to fill in missing information.

Since running fermion masses are used in an increasing number of processes, e.g. for Higgs couplings, a function `PYMRUN(KF,Q2)` has been introduced to give the mass as a function of Q^2 scale.

The compressed codes, `KC = PYCOMP(KF)`, are completely changed. We remind that `KF` can range up to seven-digit codes, plus a sign. They therefore cannot be used to directly access information in particle data tables. The `KC` codes range between 1 and 500, and give the index to the particle data arrays. Each `KF` code is now one-to-one associated with a `KC` code; the only ambiguity is that `KC` does not distinguish antiparticles from particles. Whereas `KF` codes below 100 still obey `KF = KC`, the mapping of codes above 100 is completely changed. It is no longer hard-coded in `PYCOMP`, but defined by the fourth component of the `KCHG` array. Therefore it can be changed or expanded during the course of a run, either by `PYUPDA` calls or by direct user intervention.

6.3.3 New Options

A large amount of new options have been added, related to almost all the physics changes above and more, and we here only mention some of the more significant ones.

The inclusion of Susy processes means that all the SPythia `PYMSSM` commonblock switches and parameters are inherited. New parameters are added also for other new physics scenarios, such as technicolor and doubly-charged Higgses.

The extensions to the physics of virtual photons, outlined in section 6.2.1, has resulted in two sets of new possibilities. One is in the description of the virtual-photon flux, where new `CKIN` switches has been introduced, e.g. to set the range of photon x and Q^2. This is available when `PYINIT` is called with `'gamma/lepton'` as beam or target, to denote that the photon flux inside the lepton has to be considered as a new administrative layer, also documented

in the event record. The other is the new physics machinery. Here the main switch is `MSTP(14)` that sets the assumed nature of the photon or photons, e.g. 'a direct photon from the left collides with a VMD one from the right'. The default is the most general mixture, meaning 4 components for γ^*p and 13 for $\gamma^*\gamma^*$. This is the relevant approach for studies of QCD processes. There is no corresponding automatic mixing machinery for other processes, so then the relevant contributing components have to be handled separately and added afterwards. Further options are available for several of the components, e.g. the DIS process dampening in the $Q^2 \to 0$ limit, the relative normalization of the GVMD spectrum, the scale choice for parton distributions, and the possibility to add the effects of a longitudinal resolved contribution.

The matrix-element options for $e^+e^- \to \gamma^*/Z^0 \to 2$, 3 or 4 partons have previously only been available via the `LUEEVT`/`PYEEVT` routine, that suffers from problems of its own in having a rather old-fashioned machinery for QED initial-state radiation and electroweak parameters. Now the QCD matrix-element description is accessible as an option to the shower default for e^+e^- events generated with subprocess 1 of the standard PYTHIA machinery.

6.3.4 Interfaces

While PYTHIA contains an extensive library of subprocesses, it is far from up to all the requirements of the experimental community. Both further processes and a more detailed treatment of the existing ones is required at times. In particular, it is not uncommon with a generator dedicated to one specific process, where also higher-order electroweak corrections, absent in PYTHIA, have been included in the cross section. None of these programs are geared to handle the QCD aspects of parton showers and hadronization, however, so it makes sense to combine the individual strengths.

A generic facility to include external processes exists since long in PYTHIA. Here one can feed in partonic configurations from an external generator, together with some basic information on colour flow and which partons are allowed to radiate, and let PYTHIA construct a complete event based on this information. For the simple configurations encountered in e^+e^- annihilation events, this would often be overkill, since neither the initial-state QCD radiation nor beam-remnant treatment of the generic (hadronic) collision is present.

Based on the concepts presented in the LEP2 workshop [44], a few simpler alternatives are therefore now provided for this kind of tasks:

- `CALL PY2FRM(IRAD,ITAU,ICOM)` allows a parton shower to develop and partons to hadronize from a given two-fermion starting point. `IRAD` sets whether quarks are allowed also to radiate photons or not, `ITAU` whether τ leptons should be decayed or not, and `ICOM` whether the input and output event record is `HEPEVT` or `PYJETS`. An arbitrary number of photons (e.g. from

initial-state radiation) may also be stored with the input.

- `CALL PY4FRM(ATOTSQ,A1SQ,A2SQ,ISTRAT,IRAD,ITAU,ICOM)` allows parton showers to develop and partons to hadronize from a given four-fermion starting point. The extra parameters can be used to select between the two colour pairings allowed for a $q_1\overline{q}_2q_3\overline{q}_4$ state, according to some different strategies when interference terms do not allow unique probabilities to be found.
- `CALL PY6FRM(P12,P13,P21,P23,P31,P32,PTOP,IRAD,ITAU,ICOM)` allows parton showers to develop and partons to hadronize from a given six-fermion starting point. The `Pij` parameters give the relative probabilities for the six colour pairings allowed for a six-quark state, and `PTOP` the probability that the event originates from a $t\overline{t}$ pair (in which case the shower handling has to be different than e.g. in a $Z^0W^+W^-$ event).

The above routines are not set up to handle QCD four-jet events, i.e. events of the types $q\overline{q}gg$ and $q\overline{q}q'\overline{q}'$, with $q'\overline{q}'$ coming from a gluon branching. Such events are generated in normal parton showers, but not necessarily at the right rate (a problem that may be especially interesting for massive quarks like b). Therefore one would like to start a QCD parton shower from a given four-parton configuration. Some time ago, a machinery was developed to handle this kind of occurences [47]. This approach has now been adapted to the current PYTHIA version, in a somewhat modified form. In it, an imagined shower history of two branchings is (re)constructed from the four-parton state, according to relative probabilities derived in the shower language. Thereafter a normal shower is allowed to develop, with branchings chosen at random except for these two predetermined ones. The routine `CALL PY4JET(PMAX,IRAD,ICOM)` takes an original four-parton configuration stored in `HEPEVT` or `PYJETS` and lets a shower develop as described above. `PMAX` can be used to set the maximum virtuality of those parts of the shower not given from the parton configuration itself, either to a fixed value or to the lowest virtuality of the reconstructed shower.

6.3.5 Utilities

The clustering algorithm `PYCLUS` has been extended also to accept the Durham distance measure [48] as an alternative. This is $p_\perp$-based, like the original `LUCLUS` distance measure, but differs in the details.

The `GBOOK` histogramming package was written in 1979 as a lightweight substitute for `HBOOK` [49] before that program was available in FORTRAN 77. The one-dimensional histogram part now appears in the standard distribution, in order to make the sample runs offered on the web a bit more realistic. The main routines are:

- `CALL PYBOOK(ID,TITLE,NX,XL,XU)` to book a one-dimensional histogram with integer identifier `ID` (in the range $1 - 1000$), character title `TITLE` and `NX` bins stretching from `XL` to `XU`.

- `CALL PYFILL(ID,X,W)` to fill histogram `ID` at position `X` with weight `W`.
- `CALL PYFACT(ID,F)` to rescale the contents of histogram `ID` by a factor `F`.
- `CALL PYOPER(ID1,OPER,ID2,ID3,F1,F2)` to perform operations on several histograms, such as adding or dividing them by each other.
- `CALL PYDUMP(MDUMP,LFN,NHI,IHI)` to dump histogram contents to a file from which they could be read in for plotting in another program.
- `CALL PYHIST` to print all histograms in a simple line-printer mode, and thereafter reset histogram contents.

A commonblock of dimension 20000 is used to store the histograms; this size may need to be expanded if many histograms are to be booked.

The `PYUPDA` routine has been expanded with a new option that allows a set of particle data to be read in, in tabular form as before, as an addition to or partial replacement of the existing particle data.

6.4 Summary and Outlook

We have here given a very brief survey of news in the PYTHIA 6.1 program. A more detailed description of physics and programs is available separately [50]. Any serious user should turn to this publication, and to the original physics papers, for further information.

The treasure trove for information is the PYTHIA webpage,

`http://www.thep.lu.se/~torbjorn/Pythia.html` ,

where one may find the current and previous subversions, with documentation, sample main programs, links to related programs, etc.

The PYTHIA program is continuously being developed. We are aware of many physics shortcomings, which hopefully will be addressed in the future. It is in the nature of a program of this kind never to be finished, at least as long as it is of importance for the high-energy physics experimental community.

The main visible change in the future is the transition to C++ as the programming language for PYTHIA 7. Even if much of the physics will be carried over unchanged, none of the existing code will survive. The structure of the event record and the whole administrative apparatus is completely different from the current one, in order to allow a much more general and flexible formulation of the event generation process. Following the formulation of a strategy document [51], a first proof-of-concept version was released recently [52]. So far it only contains one reasonably complete physics module, however, namely that of string fragmentation. More realistic versions should follow, but it will take a long time to convert all important physics components from PYTHIA 6. The two versions therefore will coexist for several years, with the FORTRAN one used for physics 'production' and the C++ one for exploration of the object-oriented approach that will be standard at the LHC.

Acknowledgements

A large number of persons should be thanked for their contributions. Bo Andersson and Gösta Gustafson are the originators of the Lund model, and strongly influenced the early development of the programs. Hans-Uno Bengtsson is the originator of the PYTHIA program. Mats Bengtsson is the original author of the final-state parton-shower algorithm. Several pieces of code have been donated by other persons. Further comments on the programs have been obtained from users too numerous to be mentioned here, but who are all gratefully acknowledged. To write programs of this size and complexity would be impossible without a strong user feedback.

References

[1] T. Sjöstrand, Computer Physics Commun. **82** (1994) 74

[2] H.-U. Bengtsson, Computer Physics Commun. **31** (1984) 323;
H.-U. Bengtsson and G. Ingelman,
Computer Physics Commun. **34** (1985) 251;
H.-U. Bengtsson and T. Sjöstrand,
Computer Physics Commun.**46** (1987) 43

[3] T. Sjöstrand, Computer Physics Commun. **27** (1982) 243;
T. Sjöstrand, Computer Physics Commun. **28** (1983) 227;
T. Sjöstrand, Computer Physics Commun. **39** (1986) 347;
T. Sjöstrand and M. Bengtsson,
Computer Physics Commun. **43** (1987) 367

[4] S. Mrenna, Computer Physics Commun. **101** (1997) 232

[5] B. Cano-Coloma and M.A. Sanchis-Lozano, Nucl. Phys. **B508** (1997) 753;
A. Edin, G. Ingelman and J. Rathsman, Phys. Rev. **D56** (1997) 7317.

[6] K. Lane, Phys.Rev. **D60** (1999) 075007;
S. Mrenna, Phys.Lett. **B461** (1999) 352

[7] K. Huitu, J. Maalampi, A. Pietilä and M. Raidal,
Nucl. Phys. **B487** (1997) 27, and private communication;
G. Barenboim, K. Huitu, J. Maalampi and M. Raidal,
Phys. Lett. **B394** (1997) 132

[8] M. Glück, E. Reya and A. Vogt, Z. Phys. **C67** (1995) 433

[9] G.A. Schuler and T. Sjöstrand, Z. Phys. **C68** (1995) 607,
Phys. Lett. **B376** (1996) 193

[10] CTEQ Collaboration, H.L. Lai et al., Eur.Phys. J. **C12** (2000) 375

[11] H. Plothow-Besch, Computer Physics Commun. **75** (1993) 396

[12] G.A. Schuler and T. Sjöstrand, Nucl. Phys. **B407** (1993) 539,
Z. Phys. **C73** (1997) 677

[13] C. Friberg and T. Sjöstrand, Eur. Phys. J. **C13** (2000) 151,
LU TP 00–29 (hep-ph/0007314)

[14] M. Bengtsson and T. Sjöstrand, Phys. Lett. **B185** (1987) 435,
Nucl. Phys. **B289** (1987) 810

[15] G. Miu and T. Sjöstrand, Phys. Lett. **B449** (1999) 313

[16] T. Sjöstrand, Phys. Lett. **157B** (1985) 321

[17] H.E. Haber and G.L. Kane, Phys. Rep. **117** (1985) 75

[18] M. Carena, J.–R. Espinosa, M. Quiros and C.E.M. Wagner,
Phys. Lett. **B355** (1995) 209;
M. Carena, M. Quiros and C.E.M. Wagner, Nucl. Phys. **B461** (1996) 407

[19] C. Bálazs, J. Huston and I. Puljak, hep-ph/0002032

[20] S. Mrenna, UCD-99-4 (hep-ph/9902471)

[21] E. Norrbin and T. Sjöstrand, Phys. Lett. **B442** (1998) 407,
LUTP 00-16 (hep-ph/0005110), to appear in Eur. Phys. J. **C**

[22] EMC Collaboration, M. Arneodo et al., Z. Physik **C36** (1987) 527;
L. Apanasevich et al., Phys. Rev. **D59** (1999) 074007

[23] T. Sjöstrand and M. van Zijl, Phys. Rev. **D36** (1987) 2019

[24] CDF ollaboration, F. Abe et al., Phys. Rev. Lett. **79** (1997) 584

[25] G. Gustafson and G. Miu, LU TP 99–43

[26] J. Dischler and T. Sjöstrand, LUTP 00-01 (hep-ph/0001237),
in preparation

[27] A. Donnachie and P.V. Landshoff, Phys. Lett. **B296** (1992) 227

[28] B. Andersson, G. Gustafson, G. Ingelman and T. Sjöstrand,
Phys. Rep. **97** (1983) 31

[29] T. Sjöstrand, Nucl. Phys. **B248** (1984) 469

[30] WA82 Collaboration, M. Adamovich et al., Phys. Lett. **B305** (1993) 402;
E769 Collaboration, G.A. Alves et al., Phys. Rev. Lett. **72** (1994) 812;
E791 Collaboration, E.M. Aitala et al., Phys. Lett. **B371** (1996) 157

[31] P. Edén and G. Gustafson, Z. Phys. **C75** (1997) 41;
P. Edén, LUTP 96-29 (hep-ph/9610246)

[32] B. Andersson, G. Gustafson and T. Sjöstrand,
Nucl. Phys. **B197** (1982) 45; Physica Scripta **32** (1985) 574

[33] A. Joly, J. Gascon, P. Taras, Eur. Phys. J. **C6** (1999) 413

[34] G. Gustafson, U. Pettersson and P. Zerwas, Phys. Lett. **B209** (1988) 90

[35] T. Sjöstrand and V.A. Khoze, Z. Phys. **C62** (1994) 281,
Phys. Rev. Lett. **72** (1994) 28

[36] G. Gustafson and J. Häkkinen, Z. Phys. **C64** (1994) 659

[37] E. Norrbin and T. Sjöstrand, Phys. Rev. **D55** (1997) R5;
V.A. Khoze and T. Sjöstrand, Eur. Phys. J. **C6** (1999) 271,
EPJdirect **C1** (2000) 1

[38] L. Lönnblad and T. Sjöstrand, Phys. Lett. **B351** (1995) 293,
Eur. Phys. J. **C2** (1998) 165

[39] R. Muresan, O. Smirnova and B. Lörstad, Eur. Phys. J. **C6** (1999) 629

[40] M. Seymour, Phys. Lett. **B354** (1995) 409

[41] G. Marsaglia, A. Zaman and W.-W- Tsang, Stat. Prob. Lett. **9** (1990) 35;
F. James, Computer Physics Commun. **60** (1990) 329

[42] L. Garren, `http://www-pat.fnal.gov/mcgen/lund/convert.pl`

[43] Particle Data Group, D.E. Groom et al., Eur. Phys. J. **C15** (2000) 1

[44] I.G. Knowles et al., in 'Physics at LEP2', CERN 96-01, eds. G. Altarelli,
T. Sjöstrand and F. Zwirner, Vol. 2, p. 103

[45] C. Friberg, E. Norrbin and T. Sjöstrand, Phys. Lett. **B403** (1997) 329

[46] Particle Data Group, R.M. Barnett et al., Phys. Rev. **D54** (1996) 1

[47] J. André and T. Sjöstrand, Phys. Rev. **D57** (1998) 5767

[48] S. Catani, Yu.L. Dokshitzer, M. Olsson, G. Turnock and B.R. Webber,
Phys. Lett. **B269** (1991) 432

[49] R. Brun et al., CERN Program Library code Y250

[50] T. Sjöstrand, LUTP 95-20 (hep-ph/9508391),
updated version in preparation

[51] L. Lönnblad, Computer Phys. Commun. **118** (1999) 213

[52] M. Bertini, L. Lönnblad and T. Sjöstrand, LUTP 00-23 (hep-ph/0006152)